Analytical Modelling and Analysis of Magnetic Gears and Pseudo Direct Drives for Large Wind Turbines

Andreas Penzkofer

The University Of Sheffield.

A thesis submitted for the degree of

Doctor of Philosophy

Department of Electronic and Electrical Engineering

November 2016

Abstract

The emergence of high energy rare-earth permanent magnets (PMs) led to an increased interest in Magnetic Gears (MGs) in industry and academia. MGs facilitate a contactless torque transmission and may, therefore, offer improvements in efficiency and reliability for applications where mechanical gear boxes are traditionally employed. Furthermore, MGs can also be integrated with a PM machine resulting in electrical machines with high torque densities and high efficiencies. Recently these Pseudo Direct Drives (PDDs) have been considered for many applications, including wind turbines where they may offer an attractive alternative to other drive train solutions.

The MG and the related PDD are fairly new topologies and so far they have mainly been designed, analysed and optimised employing time-consuming Finite Element (FE) methods. Analytical models considering radially magnetised PMs have only been recently proposed for MGs. Therefore, in this thesis an analytical model for the prediction of the flux density distributions in the airgaps and PMs of MGs with arbitrary magnetisation distributions is presented, and is applied for radial and Halbach magnetisation distributions. The developed models are further refined, to take into account of the stator currents in a PDD. Furthermore, in order to predict the efficiency of a PDD, models are developed to predict the flux density distributions in the pole-pieces (PPs) of the MG element and the average flux density distribution in the stator iron of a PDD on no-load and on-load conditions. Predictions from the analytical models are compared to those from 2-dimensional (2D) FE analysis.

The developed models are employed for the analysis and optimisation of MGs and PDDs for a 10MW wind turbine. Design optimisation studies are undertaken in order to determine the effects of the leading design parameters on the key performance indicators (PIs) of the MG and the PDD. It is shown that for a 10MW wind turbine an MG with a PM mass of 13.5 tons, and a PDD with the same PM mass, an efficiency of 98.7% and a total active mass of 50tons, can be achieved. Furthermore,

a 5kNm PDD has been commissioned and built by Magnomatics Ltd. to demonstrate the feasibility of a scaled version of a 10MW PDD, and predictions from the analytical models are also compared with measurements on the demonstrator PDD.

Due to the variability of the PM price and the potential insecurity of supply, the reduction of the PM mass has emerged as an important driver in the design process of drive train solutions for wind turbines. Therefore, in this thesis a PDD, where the high-speed (HS) rotor PMs are replaced by coils, is proposed. The developed models for a PM excited PDD are extended to accommodate for a coil excitation on the HS rotor, and are employed for the optimisation of the coil excited PDD. It it shown that for a 10MW PDD an efficiency of about 95% can be achieved with a total active mass of less than 85tons and a PM mass of only 4.5 tons.

In order to investigate the suitability of the PDD for other wind turbine power ratings the effects of scaling on the masses and efficiencies of the PDD are investigated between 5-20MW.

List of publications

Journal papers

A. Penzkofer, K. Atallah, "Magnetic Gears for High Torque Applications," in IEEE Transactions on Magnetics, vol. 50, no. 11, pp. 1-4, Nov. 2014. (also presented at INTERMAG 2014, Dresden, Germany)

A. Penzkofer, K. Atallah, "Analytical Modeling and Optimization of Pseudo-Direct Drive Permanent Magnet Machines for Large Wind Turbines," in IEEE Transactions on Magnetics, vol. 51, no. 12, pp. 1-14, Dec. 2015.

A. Penzkofer and K. Atallah, "Scaling of Pseudo Direct Drives for Wind Turbine Application," in IEEE Transactions on Magnetics, vol. 52, no. 7, pp. 1-5, July 2016. (also presented at Joint MMM-INTERMAG 2016, San Diego, USA)

A. Penzkofer, G. Cooke, M. Odavic and K. Atallah, "Coil Excited Pseudo Direct Drive Electrical Machines," in IEEE Transactions on Magnetics, vol. 53, no. 1, pp. 1-11, Jan. 2017.

Other publications

A. Penzkofer, K. Atallah, "Optimisation of magnetic gears for large wind turbines," Environment and Electrical Engineering (EEEIC), 2015 IEEE 15th International Conference on, Rome, 2015, pp. 962-967.

A. Penzkofer, K. Atallah, R. S. Dragan, “Deliverable 3.21, Design and PI of PDD generator”, INNWIND.EU, Innovative Wind Conversion Systems (10-20MW) for Offshore Applications, Final report, Feb. 2016.

Acknowledgements

I would like to express my thanks to my supervisor Professor Kais Atallah for his constructive advice and continuous support. In particular I would like to thank him for enabling me to present at multiple conferences, which has contributed significantly to my academic experiences during my studies.

I gratefully acknowledge the financial support provided by the INNWIND.EU project, carried out under the European Union's Seventh Framework Programme, grant agreement No.308974. I would like to thank Magnomatics Ltd for their sponsorship and their support on the experimental measurements and access to a demonstrator PDD. Additionally I would like to thank Radu Stefan Dragan for his collaboration and the constructive discussions on measurements on the demonstrator PDD.

I would like to thank my fellow PhD students and colleagues for countless hours of discussions and whose combined knowledge shaped my understanding of and experiences within the academic environment.

I am grateful to my parents for the love and support that they have provided me with throughout my life. Last but not least, I would like to thank my wife Ava for her outstanding character, endless support and for enabling me to endeavour into this PhD.

Contents

Nomenclature

Abbreviation	Definition
cHM	continuous Halbach magnetisation
dHM	discrete Halbach magnetisation
FE	Finite element
HM	Halbach magnetisation
HS	High-speed
LS	Low-speed (note: the LS rotor in this work has been fixed)
MG	Magnetic gear
PDD	Pseudo Direct Drives
PI	Performance indicator
PM	Permanent magnet
PMDD	Permanent magnet direct drive
PP	Pole-piece
RM	Radial magnetisation
S	Stator
SCDD	Superconducting direct drive

Table 1: Abbreviations in this thesis.

Symbol	Definition	Unit
$\vec{A}$	Vector potential	Tm
A	Axial component of the vector potential	Tm
A_G	General solution of the Poisson equation	Tm
A_P	Particular solution of the Poisson equation	Tm
a	Aspect ratio of the MG	
$a_{pitch,l}$	Ratio of the pole-pitch of the HS rotor PMs to the active axial length	
a_{HS}	Ratio of pole arc to pole pitch for the HS rotor PMs	
$a_{c,HS}$	Ratio of the slot opening angle to the HS rotor pole-pitch	
$\vec{B}$	Magnetic flux density	T
B_{rad}	Radial flux density	T
B_θ	Circumferential flux density	T
B_r	Remanence of the PMs	T
β	PP slot opening angle	deg
β_{mi}	Pole arc of the HS rotor PMs	deg
c_p	Power coefficient of the aerodynamic efficiency	
D	Inner airgap diameter	m
δ	Skin depth in copper	m
f_{out}	Output frequency / Electrical frequency in the stator	Hz
$f_{PP,el}$	Electrical frequency in the PPs	Hz
$f_{out,R}$	Rated output frequency	Hz
G	Gear ratio	
$\vec{H}$	Magnetic field strength	A/m
H_θ	Circumferential magnetic field strength	A/m
θ	Circumferential coordinate	deg
θ_i	Circumferential position of the i-th PP	deg
θ_{PP}	Circumferential dimension of a PP	deg
Θ_E	Load angle	deg
Θ_{HS}	Angular offset of the HS rotor PMs	deg
Θ_{PP}	PP rotor angle	deg
Θ_S	Angular offset of the stator PMs	deg
Θ_T	Angle of the turbine shaft	deg
I_{HS}	Current in a coil on the HS rotor	A
I_{rms}	rms current in a coil on the stator	A
i_{HS}	Current density in the copper of the HS rotor coils	A/mm^2
i_{rms}	Current density in the copper of the stator coils	A_{rms}/mm^2
$i_{HS,R}$	Rated current density in the copper of the HS rotor coils	A/mm^2
$i_{rms,R}$	Rated current density in the copper of the stator coils	A_{rms}/mm^2
J_{HS}	Inertia of the HS rotor	kgm^2
J_{PP}	Inertia of the PP rotor	kgm^2

Table 2: Symbols used in this thesis.

Symbol	Definition	Unit
J_T	Inertia of the turbine shaft and the components connected to it	kgm^2
j_{HS}	Current sheet representing the HS rotor windings	
j_S	Current sheet representing the stator windings	
K	Number of identical sections	
k_w	Winding factor	
L	Average circumferential dimension of a PP	mm
l_a	Active axial length	m
$l_{e,HS}$	Length of end windings on HS rotor	m
$l_{e,S}$	Length of end windings of stator coils	m
l_{gi}	Length of inner airgap	mm
l_{go}	Length of outer airgap	mm
$\vec{M}$	Residual magnetisation	A/m
M_{rad}	Radial residual magnetisation	A/m
M_θ	Circumferential residual magnetisation	A/m
m_{HS}	Halbach segments on the HS rotor	
m_S	Halbach segments on the LS rotor / stator	
m_{air}	Mass density of air	kg/m^3
m_{Cu}	Mass density of copper	kg/m^3
m_L	Mass density of laminated steel	kg/m^3
m_{PM}	Mass density of PMs	kg/m^3
M_{Cu}	Mass of copper	$tons$
$M_{Cu,S}$	Mass of copper on the stator	$tons$
$M_{Cu,HS}$	Mass of copper on the HS rotor	$tons$
M_L	Mass of laminated steel	$tons$
M_{PM}	Mass of PMs	$tons$
μ_0	Permeability of free space	Tm/A
μ_r	Relative permeability of the PMs	
N	Number of highest harmonic order of the Fourier series of the vector potential in the airgap and PM regions before symmetry considerations	
N_{eff}	Number of highest harmonic order of the Fourier series of the vector potential in the airgap and PM regions after symmetry considerations	
N_Q	Number of highest harmonic order of the Fourier series of the vector potential in the PP air regions	
ω_{PP}	Rotational speed of the PP rotor	rpm
ω_{HS}	Rotational speed of the HS rotor	rpm
$P_{Cu,HS}$	Copper losses in the HS rotor windings	W
$P_{Cu,S}$	Copper losses in the stator windings	W
P_E	Operating power	W

Table 3: Symbols used in this thesis.

Symbol	Definition	Unit
P_R	Rated power	W
P_W	Shaft power of a wind turbine	W
p_{HS}	Pole-pairs on HS rotor	
p_S	Pole-pairs on LS rotor / stator	
Q	Pole-pieces on PP rotor	
Q_{rms}	Current loading at the stator	A_{rms}/m
$Q_{rms,R}$	Rated current loading at the stator	A_{rms}/m
Q_{HS}	Current loading at the HS rotor	A/m
$Q_{HS,R}$	Rated current loading at the HS rotor	A/m
r	Radial coordinate	m
R_{blade}	Wind turbine rotor radius	m
R_{HS}	Radius at the interface to the HS rotor back-iron	m
R_{mi}	Radius at the interface between HS rotor PM region and inner airgap	m
R_{PPi}	Radius at the interface between inner airgap and PP region	m
R_{PPo}	Radius at the interface between inner airgap and PP region	m
R_{mo}	Radius at the interface between LS rotor / stator PM region and outer airgap	m
R_S	Radius at the interface between the PMs and the LS rotor / stator back-iron	m
ρ_{Cu}	Resistivity of copper	Ω/m
s	Scaling factor	
σ	Equivalent shear stress	Pa
σ_i	Shear stress in the inner airgap	Pa
σ_o	Shear stress in the outer airgap	Pa
σ_{pull}	Equivalent shear stress at pullout torque	Pa
T_i	Torque in the inner airgap	Nm
T_o	Torque in the outer airgap	Nm
T_E	Electromagnetic torque produced by the interaction of stator winding and the HS rotor	Nm
T_R	Rated torque	Nm
T_W	Load torque	Nm
T_{HS}	Torque on HS rotor	Nm
T_{PP}	Torque on PP rotor	Nm
T_{pull}	Pullout torque	Nm
v_w	Wind speed	m/s
w_{mi}	Radial thickness of magnets on HS rotor	mm
w_{mo}	Radial thickness of magnets on LS rotor	mm
w_{PP}	Radial thickness of PP segments	mm

Table 4: Symbols used in this thesis.

Chapter 1

Introduction

1.1 Motivation

Wind turbines are a rapidly growing electrical energy source accounting for 44.2% of all power capacity installations in 2015 in Europe [1]. The capacity of wind turbines is forecast to expand from 129GW in 2014 to 320GW in 2030, potentially providing 24.4% of the EU's electricity demand [2]. In order to achieve such ambitious growth a significant part of the wind energy market may be located offshore, but the need for offshore wind turbines would require new innovative technologies as well as upscaling of wind turbine dimensions. However, in all cases the primary target is the reduction of the cost of energy of the wind turbine [3].

Electrical machines in series with gearboxes are used extensively to produce cost effective and light weight drive train solutions for applications in which a high-torque low-speed is required, such as in wind turbines [4]. The gearbox component transfers the low-speed high-torque input into high-speed (HS) low-torque output and thereby allows for a significant size reduction compared to direct drive solutions. Mechanical gears are often employed for this purpose, however, they are subject to inherent issues such as damage in over-load situation, noise, periodic lubrication and high maintenance. The associated issues with reliability and cost with their failure made drive train topologies which completely eliminate mechanical gearboxes or reduce their complexities through reducing the number of gearbox

stages, an attractive alternative [4, 5]. Furthermore, with increasing size of the wind turbine simplistic scaling analysis indicates, that direct drive topologies face an ever increasing challenge of decreasing power volumetric/mass density with increasing power rating which would lead to prohibitively large designs [6, 7]. Drive-train solutions employing mechanical gearboxes would also be subject to similar scaling laws, which may lead to very large mechanical gearboxes.

Magnetic gears (MG) may offer an attractive alternative to mechanical gears and have recently received increased interest, both from industry and research [8]. A MG topology capable of a high torque-density has been investigated in [9, 10, 5]. It exhibits contact less torque transmission, inherent overload protection, redundancy of lubrication of the gearing, and reduced mechanical vibrations, and therefore has the potential to overcome the issues associated with mechanical gears. The MG can also be mechanically and magnetically integrated with a permanent magnet (PM) machine, thereby reducing the number of mechanical gearbox stages or completely eliminating the gearbox [11, 12]. MG integrated PM machines are also capable of exhibiting torque densities larger than that of equivalent radial-field PM direct drive machines and, therefore, could enable the realisation of light-weight and cost-effective wind turbine drive train solutions [7].

1.2 Magnetic gears and magnetic gear integrated machines

Generally the gearing effect in MGs is enabled through the contact less magnetic interaction of a set of magnetic poles with another set of magnetic poles. The earliest patent for an MG can be traced back to 1901 [13, 8]. The proposed electromagnetic external spur gear is comprised of two rotors, one of which employs a coil excitation to produce a multipole field, and a second rotor with a higher number of ferromagnetic teeth to interact with the electromagnetic poles and enable the gearing effect, Fig. 1.1.

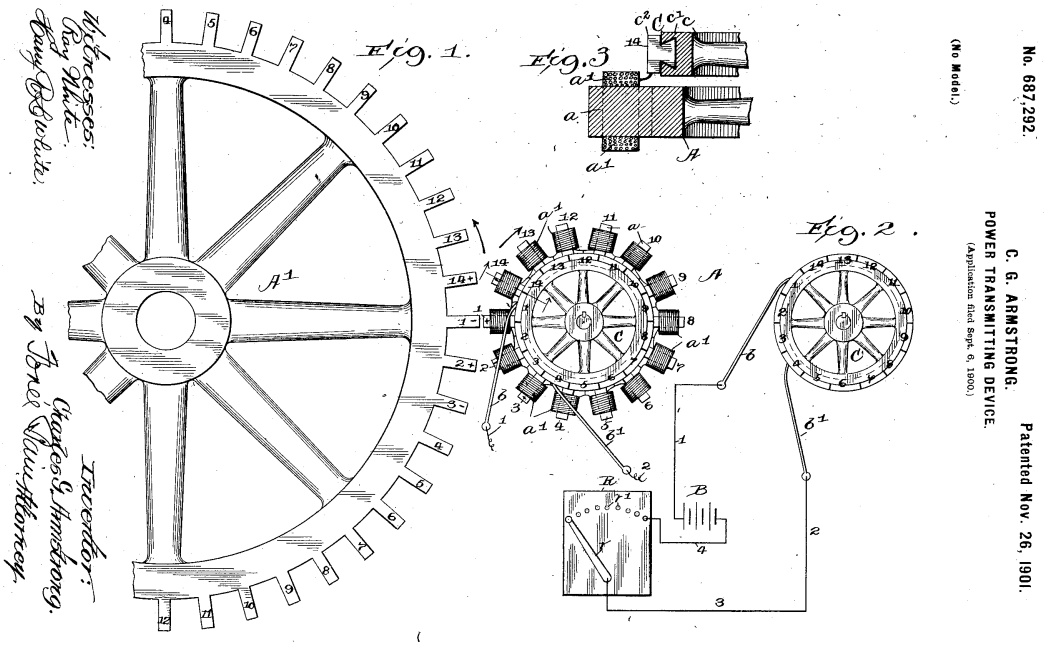

Fig. 1.1: Proposed electromagnetic spur gear in 1901 [13].

In 1941 a patent for several PM excited MGs with spur and worm type topology was filed, where the fundamental operating principle is based on the repulsive force of PM poles [14]. In the following decades other PM excited MG topologies have been reported, with an operating principle similar to that of mechanical gears, Fig. 1.2. Most of these early designs for MGs exhibit small torque densities compared to mechanical gears, hence indicating that simple analogy conversion would mostly lead to inferior designs compared to their mechanical counterparts. However, in the recent decades MGs have received renewed and increased interest due to the availability of high energy PMs, as well as the development of new topologies [8]. A disadvantage of most of the MG topologies in Fig. 1.2 is that only a part of the PMs engage actively at a given time in the torque transmission, which limits the torque densities that can be achieved compared to mechanical gears. With the exception of the planetary MG which may also exhibit torque densities of $\sim 100 kNm/m^3$, however, the high torque density capability would significantly dependent on the number of planets which require a complicated mechanical configuration [15]. Furthermore, several new topologies that may be capable of torque densities similar to those of mechanical gears have been developed in the recent decades, of which the

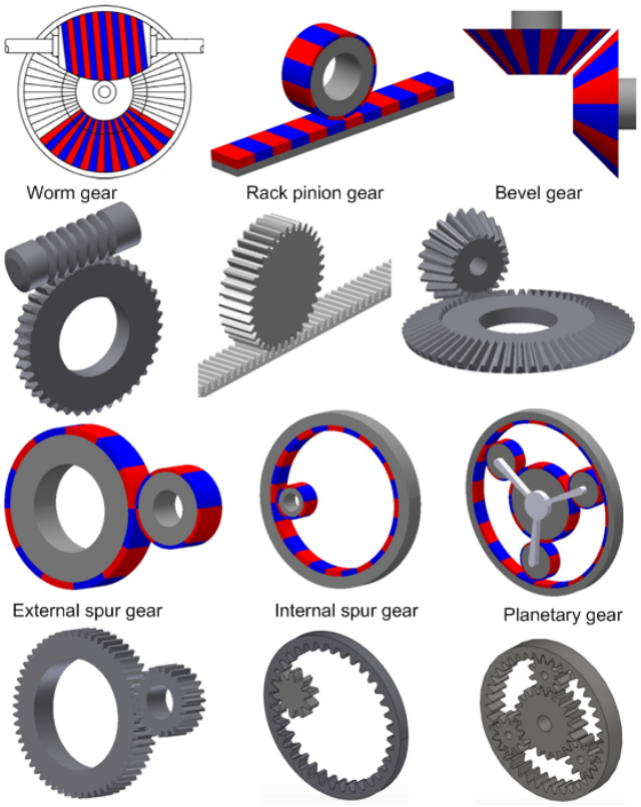

Fig. 1.2: Mechanical gears and their corresponding MG counter parts [8].

most significant are harmonic and concentric MGs.

A patent for a new type of mechanical gear called the strain wave gear has been filed in 1955 [17]. The topology is comprised of three basic components: a high-speed wave generator with an appropriate profile, a flexible low-speed rotor spline, and a fixed circular spline. The wave generator deforms the flexible spline through a sliding interface, such that the flexible spline assumes the profile of the wave generator while rotating at a different speed. The patent for an analogous topology for an MG called harmonic gear has been filed in 1994 [18], Fig. 1.3a). Similar to the mechanical gear the MG consists of a fixed stator equipped with PMs, a high-speed rotor with a profile, and an eccentric, Fig. 1.3a), or flexible, Fig. 1.3b) and c), low-speed rotor equipped with PMs. It is particularly suitable for applications where high gear ratios are demanded and has been shown to be ripple free. For this type of MG the modulation of the harmonics series produced by either rotor is achieved by the sinusoidal variation of the airgap length. Since all of the PMs are contributing simultaneously to the torque transmission, torque densities of up to

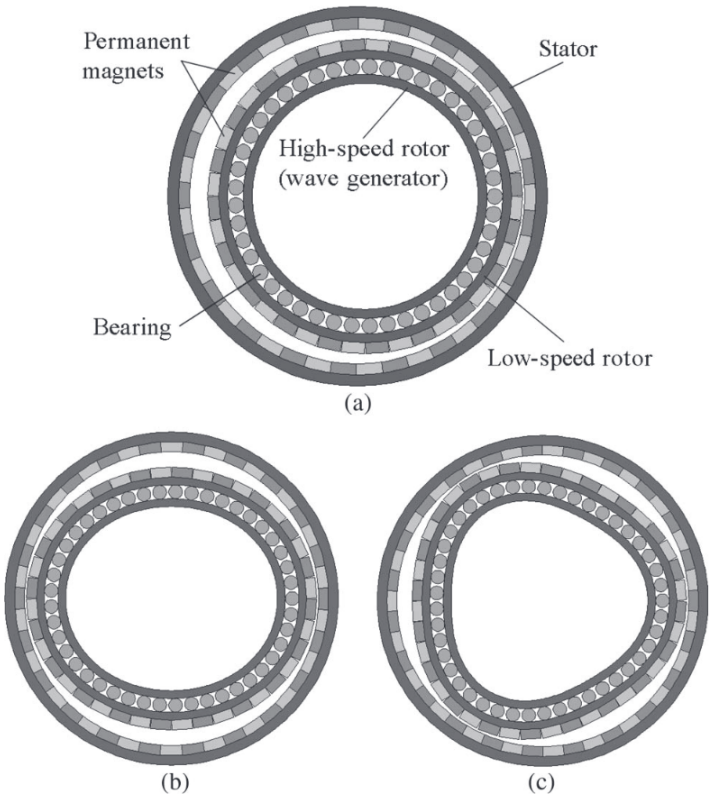

Fig. 1.3: Harmonic MGs with different numbers of sinusoidal cycles p_w: (a) $p_w = 1$, (b) $p_w = 2$, (c) $p_w = 3$ [16].

$150kNm/m^3$ and a gear ratio of 360:1 can be achieved when high energy PMs are employed. A disadvantage of this topology may be that the low-speed rotor may be mounted eccentrically or is flexible, and hence a mechanical system is required that connects the low-speed rotor to the external concentric low-speed shaft. However, this may be overcome by adding a second stage of harmonic gearing, in which the low-speed rotor interacts with a rotating concentric ring equipped with PMs and which then constitutes the low-speed output of the MG [16].

In 1993 a multi-layer axial MG based on the circumferential variation of the axial reluctance has been presented in [19]. It comprises of a set of stator and low-speed rotor disks which are alternately stacked, and a high-speed rotor equipped with PMs, Fig. 1.4. The sets of low-speed rotor and stator disks are comprised of ferromagnetic pole-pieces, however with different numbers of pole-pieces. The difference in the angle between the pole-pieces leads to a circumferential variation of the axial reluctance, which in turn leads to a modulation of the magnetic field produced by the PMs in such a manner that a magnetic gearing effect is enabled

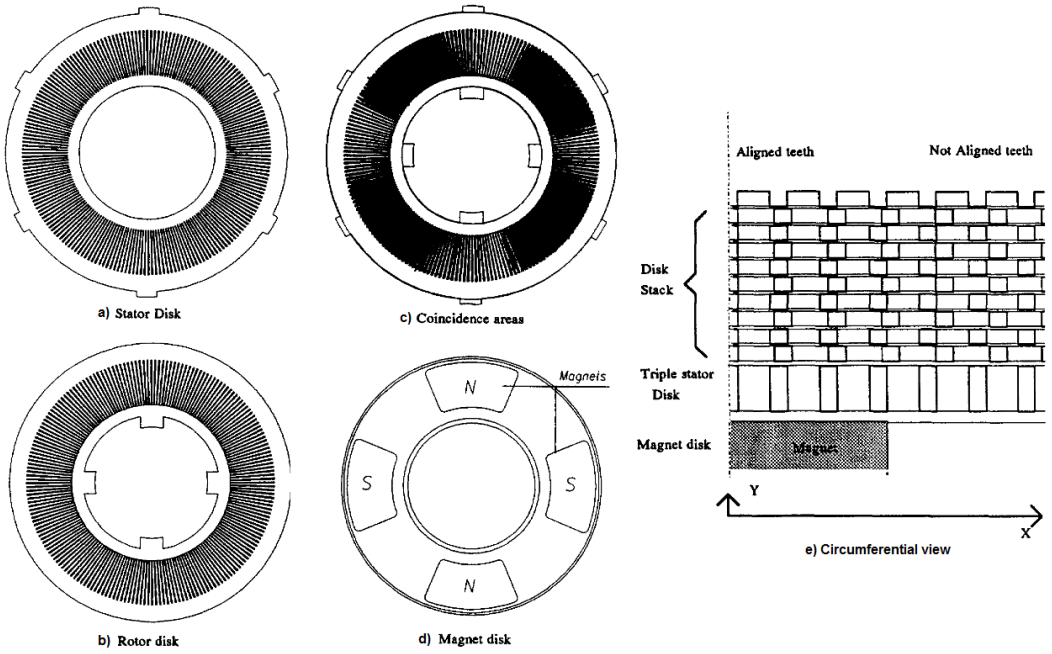

Fig. 1.4: MG based on the circumferential variation of the axial reluctance [19].

between the stator, the low-speed rotor and the high-speed rotor. The MG topology is capable of very high gear ratios, where the presented gear ratio was 50:1, however, it may suffer from high friction and limited controllability due to the mutual contact between the disks, as well as limitations in maximum shaft speeds.

Another approach that achieves the engagement of all PMs in the torque transmission is presented by the concentric MG, where the torque transmission is provided through modulation of the flux distributions by an electromagnetically active ring. A US patent from 1968 mentions such an MG topology employing two rotors with different numbers of PM pole pairs and a flux modulating ring of PPs [20], Fig. 1.5, however, no further explanation of the operational principle of the modulation is given. In general many designs for the modulating ring have been filed for this type of topology with various degrees of complexity of the shapes and arrangements [20, 21]. In 1995 a US patent was filed in which the required relationships between the number of poles of two PM excited rotors and the number of modulating PPs are given, and the effects of the PPs on the flux density distributions in the airgaps are presented [22]. Further work including a more detailed analysis of the effects of the PPs on the harmonic order of the flux density in the airgaps between the rotors

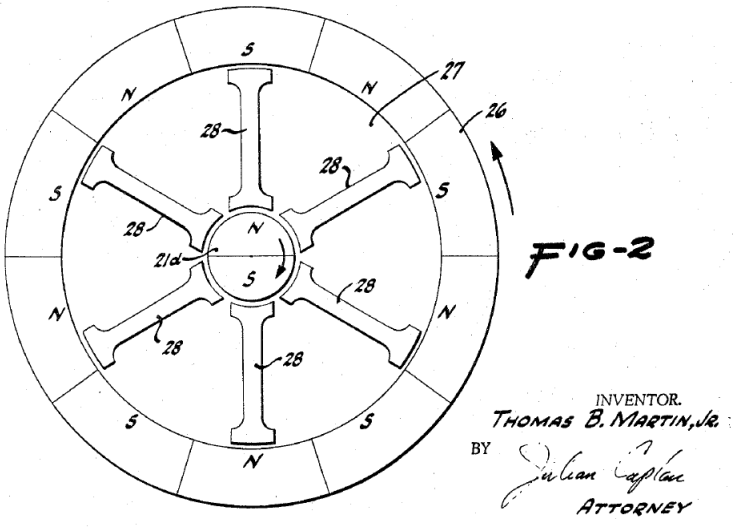

Fig. 1.5: MG topology employing a modulating ferromagnetic ring [20].

has been presented by [9], and it has been shown that torque densities in excess of $100 kNm/m^3$ at a gear ratio of 5.5:1 can be achieved with this type of topology when high energy PMs are employed. In comparison, direct drive machines may also achieve torque densities ~$80-120 kNm/m^3$ [23, 24]. Employing the same operation principle this type of MG topology can also be designed for linear and axial MGs, and high torque densities have also been claimed for these types of topologies [25, 26].

The advances in MG technology in the recent decades have lead to the development of a new type of electrical machine: the magnetically geared machine. In general a MG can be combined in series with an electrical machine by mechanically connecting the shafts. However, a MG can also be magnetically integrated with an electrical machine within the same volume, which allows for increased system torque densities compared to configurations where a gear is employed in series with an electrical machine. This has been envisaged first in [19] for the case of the multilayer axial MG shown in Fig. 1.4. Several topologies for an electrical machine with a magnetically and mechanically integrated concentric MG have been presented since [27, 12, 28, 29]. The designs in [27, 12] (Fig. 1.6a), require 3 airgaps and 3 rotors and the mechanical construction could be, therefore, challenging [8]. However, the design also allows for an operation as a continuously variable transmission

(CVT) device - a device which is extensively used in heavy duty and hybrid electric vehicles. For the CVT a fixed gear ratio operation is achieved by locking one of the rotors, typically either the PP rotor or the rotor having the larger PM pole-pair number. By allowing the fixed rotor to rotate a variable gear ratio operation is achieved, hence enabling a magnetic continuously variable transmission [30, 31]. The design in [29] (Fig. 1.6b) only requires 2 airgaps, however, the windings are fitted between the pole-pieces, which would require a more difficult winding structure and limit the amount of copper that can be installed by the dimensions of the PPs. The design in [28] (Fig. 1.6c) is called Pseudo Direct Drive (PDD). The brushless machine has a simple mechanical structure with the outer PMs being fixed to the stator, which is equipped with a 3-phase winding. In the topology the stator windings interact with the fundamental space harmonic of the flux density created by the PMs of the inner rotor to produce torque. The high-speed low-torque produced by the interaction is then transmitted as a low-speed high-torque output to the output shaft through the interaction of the stator PMs with the asynchronous space harmonic created from the modulation by the PPs with the HS rotor PMs. It has been shown that torque densities of more than $60kNm/m^3$ can be achieved with air-cooling at an average current density of less than $2A_{rms}/mm^2$ for a PDD with a rated torque of $\sim 100Nm$ [11]. Furthermore, due to the relatively low operating current densities the achieved efficiencies of a PDD are typically higher than that of electrical machines with similar torque/power ratings.

1.3 Wind turbine generators

Until the 1990s wind turbines were mostly built as constant-speed turbines employing a multi-stage gearbox in series with an asynchronous squirrel cage generator which is directly connected to the grid , Fig. 1.7a) [4]. Since then many manufacturers have changed to building variable speed wind-turbines, mainly due to improved flexibility in matching requirements such as energy yield, power quality and noise. Often a doubly-fed induction generator (DFIG) which requires a power con-

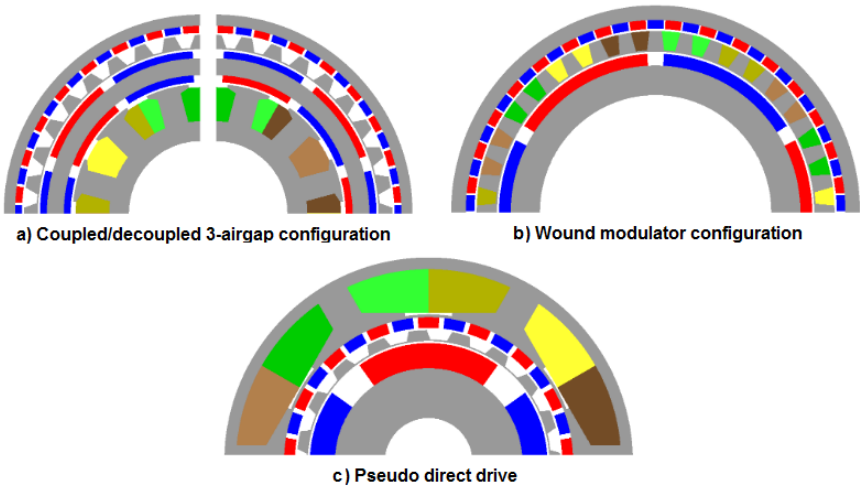

Fig. 1.6: Topologies for magnetically geared machines [8].

verter typically with a power rating 30% of that of the turbine has been employed in series with a multi-stage gearbox, Fig. 1.7b). Manufacturers also introduced gearless systems called direct drives, mainly due to reliability issues with gearboxes and reduced maintenance. These system, however, require a power converter with the full rated power for the grid connection, Fig. 1.7c). Direct drives can be constructed with electrical excitation or with PM excitation to operate as variable-speed synchronous generators. PM excited direct drives (PMDD) eliminate the need for brushes and have no excitation losses, and they could, therefore, offer improved efficiencies [4], however, the cost of PMs could be an issue. Recent developments of PMs with a high energy product, have also enabled the manufacture of large drive trains. Furthermore, the development of NdFeB grades which exhibit improved corrosion and temperature resistance further assists its employment in wind turbines. However, concerns about price volatility and future availability have been present, albeit prices seem to have stabilised and become more reasonable in recent years [32, 33]. With increasing size and power rating of the turbine, these direct drives may become increasingly large and expensive due to an over-proportional growth of the torque levels compared to the power rating. Therefore, combined systems of these types of generators in series with a gearbox have also been suggested in order to increase the efficiency and reduce the size and cost of the generator. However, this topology, called multibrid system, could combine disadvantages of the gearbox

system with those of a direct drive, such as increased maintenance, additional losses in the gearbox and the requirement for a fully rated converter [4].

With increasing size of the turbine the size and torques of the generator would increase even faster [6], making the direct drive generator solutions even heavier. However, a gearbox system may also follow similar scaling rules and would, therefore, also become increasingly heavy and costly. In order to overcome current mass and size limitations, and break through the barriers faced by the conventional topologies, various innovative and novel designs have been proposed for the application in large wind turbines [7]. Direct drives which employ superconductive coils for the DC excitation have been proposed [35, 36]. Due to the high currents that can be achieved at almost negligible resistance superconductive direct drives could operate at higher airgap flux densities and offer increased high-torque densities and efficiencies. However, a disadvantage remains the low temperatures at which the superconducting material has to be operated and the associated necessity for a complex cooling system and thermal insulation [7].

1.4 The PDD as a wind turbine drive train

More recently more interest has also been expressed to the application of MG integrated generators to the field wind turbines [37]. The proposed topology in [37] comprises a complex structure with 3 airgaps, Fig. 1.6a), and therefore would be more difficult to manufacture, especially for multi-MW power ratings. A more simpler design with only 2 airgaps has been introduced in [11] and has been described in Section 1.2. Magnetically geared systems could offer increased reliability compared to mechanical gearbox systems due to the overload protection due to the pullout torque. This could be an advantage in applications with increased reliability demand, such as for offshore wind turbines where the contribution of the operational expenditures may be in the order of 30% [7]. Furthermore, compared to conventional direct drives the PDD could also offer higher efficiencies as well as reduced volume and mass [7]. However, designs of PDDs presented so far would

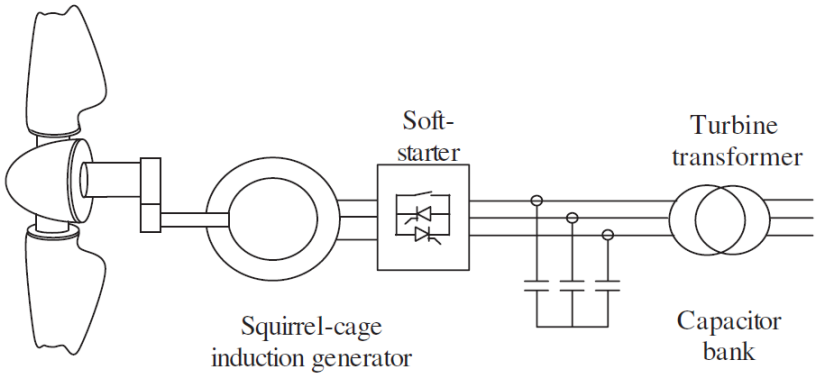

a) Constant-speed squirrel-cage induction wind turbine

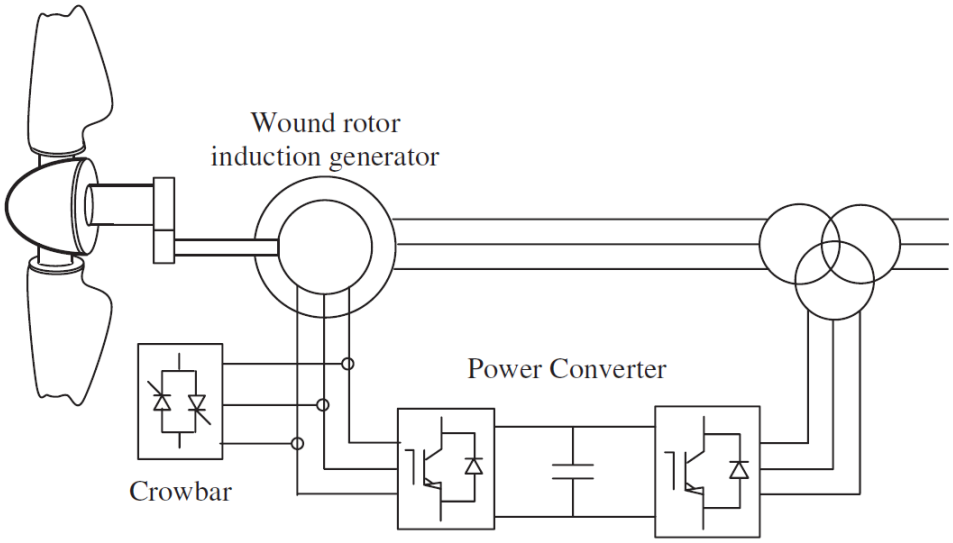

b) DFIG wind turbine

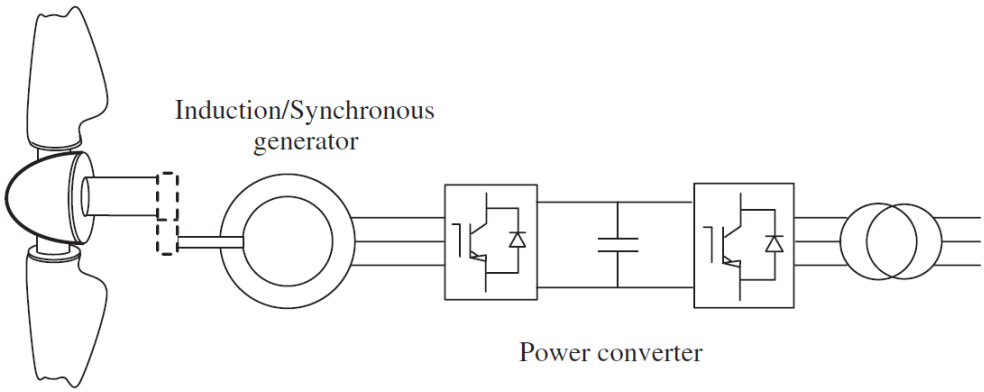

c) Variable-speed wind turbine with fully-rated converter

Fig. 1.7: Topologies for typical wind turbine generators [34].

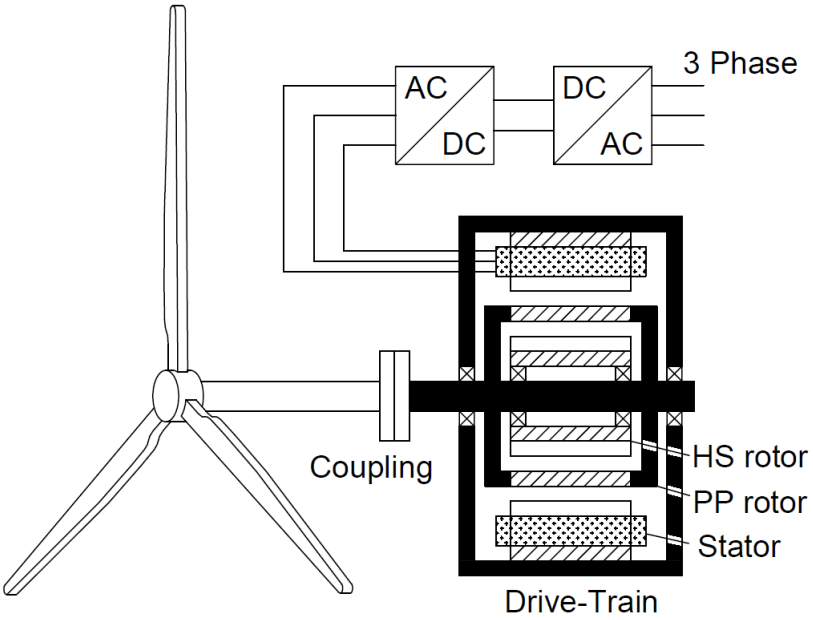

Fig. 1.8: Schematic for the integration of a PDD within a wind turbine.

also require increased PM mass for their realisation.

In the PPD topologies investigated in this thesis, the turbine rotor is directly connected to the pole-piece (PP) rotor of the PDD and the torque is magnetically transmitted to the high-speed (HS) rotor of the PDD which is also electromagnetically coupled to the stator windings to produce electrical power, Fig. 1.8. Typically these machines can be built with a high power factor, resulting in large short-circuit currents which could induce very large electromagnetic torque when a fault occurs. However, unlike other direct drive machines, where a high power factor and a winding short circuit would subject the drive train to an electromagnetic torque several times larger than the rated torque, in a PDD torque would be applied to the HS rotor, and the drivetrain would only be subjected to the pullout torque of the MG element of the PDD. Although subjecting the drive-train to cyclic torques during pole-slip could also be an issue, the effect on the fatigue life will depend on the number of pole-slips during the life time of the wind turbine.

The PDD has been considered as a drive train for wind turbines of the power class 10-20MW in the framework of the project INNWIND.EU, which is funded under European Union's Seventh Framework programme, grant agreement No.308974. INNWIND.EU started in 2012 as a successor of the project UPWIND, which was

funded by the European Union's 6th Framework Programme, and which investigated the feasibility of large wind turbines for the power class 8-10MW. The project, therefore, builds on the results gained by UPWIND, but attempts to go beyond the scope of UPWIND by investigating innovative designs which could allow for large wind turbines with a higher performance than conventional designs. Findings in this work may, therefore, also be found as results of the project INNWIND.EU, work package 3.

1.5 Modelling of magnetic gears and PDDs

The optimisation of the PDD is key to achieving a cost effective and light weight drive train solution. However, the optimisation may involve handling many variables and therefore large amounts of data. While finite element (FE) predictions may allow for an accurate analysis and is able to account for saturation and 3D effects it also could result in a significant computational effort. Generally in order to decrease the numerical effort and allow for reasonably simple solutions or solution processes, problems are often considered in two dimensions (2D) [38, 39] and geometric symmetries are exploited. However, concentric MGs often do not exhibit circumferential symmetry due the relations between the number of pole-pairs and the number of pole-pieces [8], which would also add to the requirement of computationally extensive FE studies.

Analytical and semi-analytical methods, such as reluctance network models, offer computationally faster approaches and several methods have been proposed for electromagnetic machines and MGs [39, 8]. In particular for an MG a reluctance network model approach has been employed in [40] and it has been shown to exhibit a high accuracy while also being capable of accounting for non-linear effects of the steel [41] and end effects [42], however, it still would require a large amount of discretisation of the geometry. On the other hand analytical models based on the formal solutions of Maxwell's equations for the entire geometry also offer a numerically fast, yet sufficiently accurate approach for optimisation purposes,

assuming that non linear effects of the steel are negligible. The PDD is a relatively new machine topology with a significantly more complex magnetic structure than conventional machines, and FE analysis has been so far the most common method used for the design and optimisation of PDDs. Furthermore, 1-dimensional and 2D analytical models have been proposed for the determination of the magnetic field distributions in the airgap and the PM regions of synchronous machines [43, 44, 45, 46, 47, 48, 49, 50]. However, the structure of MGs is significantly more complex and the analytical models which have been proposed for conventional machines are not applicable. Therefore analytical models for the determination of the magnetic field distributions in the airgaps and PM regions of MGs, assuming radial magnetisation [51, 52] distribution on the PMs, that surpass the numerical limitations faced by FE methods for MGs have only recently been proposed. However, analytical models for the design and analysis of PDDs are yet to be proposed.

1.6 Outline of this thesis

The work in each chapter of this thesis is as follows:

Chapter 2 - A 2D analytical model for the prediction of the flux density distribution in the airgaps and PMs of a MG is presented for arbitrary magnetisation distributions dependent only on the circumferential coordinate, and applied for radial and Halbach magnetisation. The model is employed to investigate the effect of scaling of the MG on various quantities, such as the shear stress.

Chapter 3 - The analytical models are employed for the study of large MGs in order to determine the effects of the leading design parameters of the MG on the main performance indicators (PI), such as the masses of the active components. The models are compared to 2D FE predictions and a selected study of the main design parameters is presented. Furthermore, numerical challenges for the models are investigated and solutions are provided.

Chapter 4 - The models are extended to account for the effects of stator windings in order to enable the analysis of PDDs. Furthermore, additional models are

developed for the prediction of the average flux density distribution in the stator core and the flux density distributions in the PPs.

Chapter 5 - The models are employed for the study and optimisation of a PDD for a 10MW wind turbine, and the presented design is employed for the comparison of the analytical model with 2D FE predictions. Furthermore, a selected study of the effects of the main design parameters on the PI is presented.

Chapter 6 - A PDD with HS rotor coil excitation is introduced. The analytical models for the PM excited PDD are adapted to the requirements of the coil excited PDD and compared with 2D FE predictions. Optimisation studies are undertaken on the effects of the leading design parameters on the PI, such as the active masses and the efficiency. Furthermore the control of the PDD, which may be significantly different to that one of a PM excited PDD, is discussed.

Chapter 7 - The analytical models for the PM excited and the coil excited PDDs are employed to study the effects of scaling of the turbine on the active masses and the electromagnetic efficiency.

Chapter 8 - The analytical models for the PDD are compared with experimental results obtained from the measurements on a 5kNm demonstrator PDD developed by Magnomatics Ltd.

Chapter 9 - The presented designs for PDDs with PM and coil excited HS rotors are compared to a 10MW PM direct drive, and a discussion on the core differences is given.

Chapter 2

Analytical model for the magnetic gear

A 2D analytical model for the prediction of the magnetic field distributions in the airgaps and PMs of radial-field MGs with arbitrary magnetisation distributions is presented. The model is employed to study the effect of scaling on the various quantities, such as the shear stress in the airgaps and the active masses.

The expressions of the model are further specified for particular magnetisation distributions. Although the expressions for a radial magnetisation are provided in [51], the model in this thesis further refines these expressions by accounting for airgaps in between the PMs. Furthermore, a Halbach magnetisation distribution is considered in this thesis. It provides several attractive features such as an inherently sinusoidal magnetic field which allows for small torque ripple, and a self-shielding magnetisation which reduces the required back-iron. Studies have also shown that a Halbach magnetisation can result in improved torque transmission capability and reduced cogging torque, albeit at an increased manufacturing cost [53, 54]. The analytical model developed is, therefore, also applied for the analysis of a Halbach magnetisation.

2.1 Principle of operation

An MG consists of two rotors equipped with multi-pole PMs which are separated by a third rotor having ferromagnetic PPs. The PPs modulate the magnetic fields produced by each rotor, resulting in an asynchronous harmonic having the same number of poles as the PMs of the other rotor and interacting with them to transmit torque. The number of pole-pairs of the space flux density harmonics produced by the HS rotor and LS rotor PMs is given by

$$p_{HS}^{*}(m,k) = |mp_{HS} + kQ| \tag{2.1}$$

and

$$p_{S}^{*}(m,k) = |mp_{S} + kQ| \tag{2.2}$$

respectively, where p_{HS} is the number of PM pole-pairs on the HS rotor, p_S is the number of pole-pairs on the LS rotor, Q is the number of PPs, $m \in \{1,3,..,\infty\}$ and $k \in \mathbb{Z}$ [5]. The largest space harmonic usually corresponds to $m = 1$ and $k = -1$ for which

$$Q = p_{HS} + p_S \tag{2.3}$$

The rotational speeds of the space harmonics produced by the HS rotor PMs and the LS rotor PMs are given by

$$\omega_{HS}^{*}(m,k) = \frac{mp_{HS}}{mp_{HS} + kQ}\omega_{HS} + \frac{kQ}{mp_{HS} + kQ}\omega_{PP} \tag{2.4}$$

and

$$\omega_{S}^{*}(m,k) = \frac{mp_{S}}{mp_{S} + kQ}\omega_{LS} + \frac{kQ}{mp_{S} + kQ}\omega_{PP} \tag{2.5}$$

respectively. ω_{HS}, ω_S and ω_{PP} are the rotational speeds of the HS , LS and PP rotor respectively. There are two different ways of achieving a fixed ratio MG. The first one is by fixing the speed of the PP rotor and taking input/output from the PM rotors resulting in a gear ratio

$$G = -\frac{p_S}{p_{HS}} \tag{2.6}$$

The second one is by fixing the LS rotor and taking the input/output from the HS rotor and the PP rotor, resulting in

$$G = \frac{Q}{p_{HS}} \tag{2.7}$$

In this thesis the LS rotor is fixed and is referred to in the following as the stator.

2.2 Flux density in the airgap and PM regions

The prediction of the magnetic field distribution in the airgaps of non-PM machines differs significantly to a structure with PMs. Due to the low recoil permeability of PMs a much larger effective airgap has to be taken into account and for a precise analysis a 1-dimensional approach might not suffice any longer [45]. In MGs the problem is magnified by the existence of two sets of PM regions and their adjacent airgaps, and the air spaces between the PPs. A two dimensional computational model capable of analysing the MG is introduced in [51] and is employed and refined to meet the characteristics of the adopted topologies. End effects are neglected in this model and the permeability of iron is assumed to be infinite. The problem is treated as magneto-static, and therefore the effects of eddy currents are neglected. Furthermore, due the size of the MG considered in this thesis, it may be constructed from magnetically identical sections, with each section satisfying the required relationship between the numbers of pole-pairs and the number of PPs. Fig. 2.1 shows the schematic of a MG section and its various regions employed for the development of the analytical model in section 2.2.

The analytical model provides the solutions for the flux density distribution in the airgaps and PM regions of a MG for arbitrary magnetisation distributions. Furthermore, the model is further developed by providing the solutions for PMs with radial, discrete Halbach and continuous Halbach magnetisations in Section 2.5.

For quasi-static conditions the Maxwell equations in PMs and air are

$$\nabla \vec{B} = 0 \tag{2.8}$$

$$\nabla \times \vec{H} = \vec{J} \tag{2.9}$$

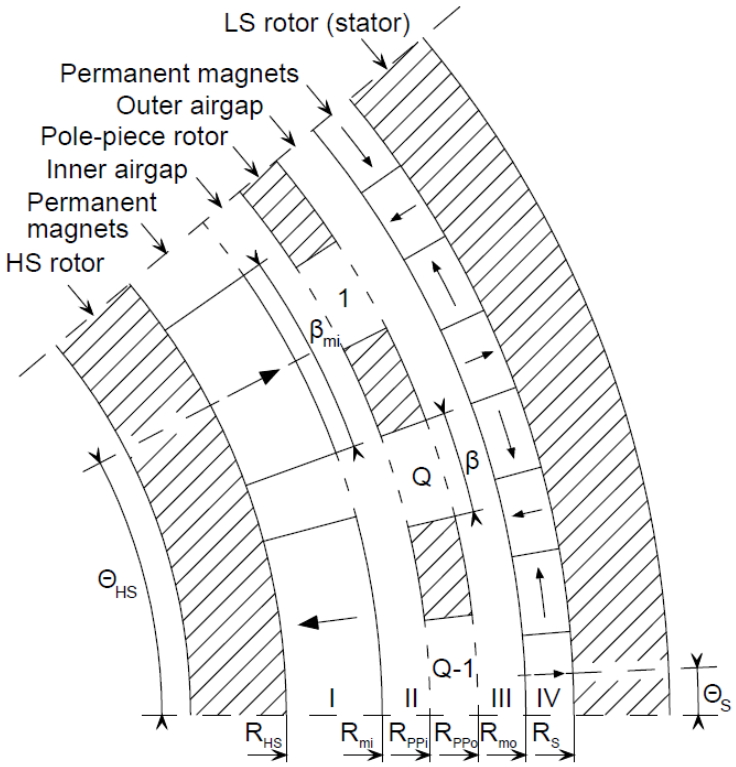

Fig. 2.1: Geometry for a MG section with a periodic symmetry of 40 degrees. PMs consist of radially magnetised PMs on the HS rotor and 4 Halbach-segments per pole-pair on the LS rotor (stator).

By introducing the vector potential $\vec{A}$

$$\vec{B} = \nabla \times \vec{A} \tag{2.10}$$

and using the identity $\nabla(\nabla \times \vec{A}) = 0$ in equation (2.8) it can be seen that the magnetic flux density is invariant under the transformation

$$\vec{A} \rightarrow \vec{A} + \nabla\Psi \tag{2.11}$$

where Ψ is a scalar. Ψ can be chosen such that $\nabla\vec{A} = 0$, and therefore

$$\nabla \times \vec{B} = \nabla \times (\nabla \times \vec{A}) = \nabla(\nabla\vec{A}) - \triangle\vec{A} = -\triangle\vec{A} \tag{2.12}$$

where $\triangle = \nabla^2$ is the Laplace operator. The magnetic flux density is related to the magnetic field strength via

$$\vec{B} = \mu_0\vec{H} \qquad \text{in air} \tag{2.13}$$

$$\vec{B} = \mu_0\mu_r\vec{H} + \mu_0\vec{M} \qquad \text{in PMs} \tag{2.14}$$

With equation (2.9) the Poisson equations for the vector potential are derived from

equation (2.12) as

$$\triangle\vec{A} = -\mu_0\mu_r\vec{J} \qquad \text{in air regions} \tag{2.15}$$

$$\triangle\vec{A} = -\mu_0\mu_r\vec{J} - \mu_0\nabla\times\vec{M} \qquad \text{in PM regions} \tag{2.16}$$

In the models developed in this thesis the iron is assumed to have infinite permeability. The problem is treated in two dimensions and end effects are therefore neglected. The magnetic flux density in z-direction is thus zero and $\vec{A}$ possesses only a non-zero z-component A. The equations for the magnetic flux density reduce to

$$B_{rad} = \frac{1}{r}\frac{\partial A}{\partial\theta} \tag{2.17}$$

$$B_\theta = -\frac{\partial A}{\partial r} \tag{2.18}$$

where B_{rad} and B_θ are the radial and circumferential components of the flux density, respectively. The relative permeability of the adjacent iron regions is assumed to be infinite. Therefore, the flux density lines will always be perpendicular to the iron surface. The Poisson equation is solved for the PP region, the airgap regions and the PM regions by [51]. However the solution was only provided for radially magnetised PMs on the HS and LS rotors. In this thesis a general approach for arbitrary magnetisations is proposed and applied for radial, continuous and discrete HM (section 2.5).

An arbitrary magnetisation in the PM region of the HS rotor can be written in terms of a Fourier series as

$$\vec{M}_I(\theta) = \frac{B_r}{\mu_0}\sum_{n=1}^{\infty}\begin{bmatrix} f_{c,I,n} & f_{s,I,n} \\ g_{c,I,n} & g_{s,I,n}\end{bmatrix}\begin{pmatrix}\cos(n\theta)\\ \sin(n\theta)\end{pmatrix} \tag{2.19}$$

and for the PM region on the stator as

$$\vec{M}_{IV}(\theta) = \frac{B_r}{\mu_0}\sum_{n=1}^{\infty}\begin{bmatrix} f_{c,IV,n} & f_{s,IV,n} \\ g_{c,IV,n} & g_{s,IV,n}\end{bmatrix}\begin{pmatrix}\cos(n\theta)\\ \sin(n\theta)\end{pmatrix} \tag{2.20}$$

The upper entries in the matrices correspond to the radial components and the lower entries to the circumferential components of the magnetisation. The boundary conditions at the interfaces between the PM regions (region I and II) and the steel

back-irons are

$$\frac{B_{\theta,I}(R_{HS},\theta)}{\mu_0\mu_r} - \frac{M_{\theta,I}(\theta)}{\mu_r} = H_{\theta,I}(R_{HS},\theta) = 0 \tag{2.21}$$

$$\frac{B_{\theta,IV}(R_S,\theta)}{\mu_0\mu_r} - \frac{M_{\theta,IV}(\theta)}{\mu_r} = H_{\theta,IV}(R_S,\theta) = 0 \tag{2.22}$$

The boundary conditions at the interface between the PM regions and the adjacent airgap regions (regions II and regions III)

$$\frac{B_{\theta,I}(R_{mi},\theta)}{\mu_0\mu_r} - \frac{M_{\theta,I}(\theta)}{\mu_r} = H_{\theta,I}(R_{mi},\theta) = H_{\theta,II}(R_{mi},\theta) = \frac{B_{\theta,II}(R_{mi},\theta)}{\mu_0} \tag{2.23}$$

$$B_{rad,I}(R_{mi},\theta) = B_{rad,II}(R_{mi},\theta) \tag{2.24}$$

$$\frac{B_{\theta,IV}(R_{mo},\theta)}{\mu_0\mu_r} - \frac{M_{\theta,IV}(\theta)}{\mu_r} = H_{\theta,IV}(R_{mo},\theta) = H_{\theta,III}(R_{mo},\theta) = \frac{B_{\theta,III}(R_{mo},\theta)}{\mu_0} \tag{2.25}$$

$$B_{rad,IV}(R_{mo},\theta) = B_{rad,III}(R_{mo},\theta) \tag{2.26}$$

At the boundary between the airgap regions and PP rotor air regions the flux density is continuous.

The Poisson equation (2.16) is solved with consideration of the boundary conditions at the adjacent interfaces to the back-iron and the airgap regions, and the solutions in the PM regions I and IV take the form

$$A_I(r,\theta) = A_{G,I}(r,\theta) + A_{P,I}(r,\theta) \tag{2.27}$$

$$A_{IV}(r,\theta) = A_{G,IV}(r,\theta) + A_{P,IV}(r,\theta) \tag{2.28}$$

where $A_{G,I}$ and $A_{G,IV}$ are the general solutions in regions I and IV respectively, and $A_{P,I}$ and $A_{P,IV}$ are the particular solutions in regions I and IV respectively. As can be seen in appendix A.1 the solution for the vector potential in region I can be expressed as

$$A_{G,I}(r,\theta) = \sum_{n=1}^{\infty} \frac{R_{mi}}{n} \frac{P_n(r,R_{HS})}{P_n(R_{mi},R_{HS})} \begin{pmatrix} A_{I,n} \\ C_{I,n} \end{pmatrix} \cdot \begin{pmatrix} \cos(n\theta) \\ \sin(n\theta) \end{pmatrix} \tag{2.29}$$

$$A_{P,I}(r,\theta) = B_r \sum_{n=1}^{\infty} \begin{pmatrix} X_{A,I,n}(r) \\ X_{C,I,n}(r) \end{pmatrix} \cdot \begin{pmatrix} \cos(n\theta) \\ \sin(n\theta) \end{pmatrix} \tag{2.30}$$

and the solution for the vector potential in region IV as

$$A_{G,IV}(r,\theta) = \sum_{n=1}^{\infty} \frac{R_{mo}}{n} \frac{P_n(r,R_S)}{P_n(R_{mo},R_S)} \begin{pmatrix} A_{IV,n} \\ C_{IV,n} \end{pmatrix} \cdot \begin{pmatrix} \cos(n\theta) \\ \sin(n\theta) \end{pmatrix} \tag{2.31}$$

$$A_{P,IV}(r,\theta) = B_r \sum_{n=1}^{\infty} \begin{pmatrix} X_{A,IV,n}(r) \\ X_{C,IV,n}(r) \end{pmatrix} \cdot \begin{pmatrix} \cos(n\theta) \\ \sin(n\theta) \end{pmatrix} \tag{2.32}$$

where

$$P_n(r,v) = \left(\frac{r}{v}\right)^n + \left(\frac{r}{v}\right)^{-n} \tag{2.33}$$

$$E_n(r,v) = \left(\frac{r}{v}\right)^n - \left(\frac{r}{v}\right)^{-n} \tag{2.34}$$

For arbitrary circumferential magnetisations as in (2.19) and (2.20), $X_{A,I,n}(r)$, $X_{C,I,n}(r)$, $X_{A,IV,n}(r)$ and $X_{C,IV,n}(r)$ are derived in appendix A.1 and are given by

$$\begin{pmatrix} X_{A,I,n}(r) \\ X_{C,I,n}(r) \end{pmatrix} = \left(\tfrac{r}{R_{HS}}\right)^{-n} \begin{pmatrix} G_{I,n} \\ H_{I,n} \end{pmatrix} + f_n(r) \begin{pmatrix} nf_{s,I,n} - g_{c,I,n} \\ -nf_{c,I,n} - g_{s,I,n} \end{pmatrix} \tag{2.35}$$
$$-\tfrac{P_n(r,R_{HS})}{P_n(R_{mi},R_{HS})} \left[\left(\tfrac{R_{mi}}{R_{HS}}\right)^{-n} \begin{pmatrix} G_{I,n} \\ H_{I,n} \end{pmatrix} + f_n(R_{mi}) \begin{pmatrix} nf_{s,I,n} - g_{c,I,n} \\ -nf_{c,I,n} - g_{s,I,n} \end{pmatrix} \right]$$

$$\begin{pmatrix} X_{A,IV,n}(r) \\ X_{C,IV,n}(r) \end{pmatrix} = \left(\tfrac{r}{R_S}\right)^{n} \begin{pmatrix} G_{IV,n} \\ H_{IV,n} \end{pmatrix} + f_n(r) \begin{pmatrix} nf_{s,IV,n} - g_{c,IV,n} \\ -nf_{c,IV,n} - g_{s,IV,n} \end{pmatrix} \tag{2.36}$$
$$-\tfrac{P_n(r,R_S)}{P_n(R_{mo},R_S)} \left[\left(\tfrac{R_{mo}}{R_S}\right)^{n} \begin{pmatrix} G_{IV,n} \\ H_{IV,n} \end{pmatrix} + f_n(R_{mo}) \begin{pmatrix} nf_{s,IV,n} - g_{c,IV,n} \\ -nf_{c,IV,n} - g_{s,IV,n} \end{pmatrix} \right]$$

where

$$\begin{pmatrix} G_{I,n} \\ H_{I,n} \end{pmatrix} = \frac{R_{HS}}{n} \left[\begin{pmatrix} g_{c,I,n} \\ g_{s,I,n} \end{pmatrix} + f_n'(R_{HS}) \begin{pmatrix} nf_{s,I,n} - g_{c,I,n} \\ -nf_{c,I,n} - g_{s,I,n} \end{pmatrix} \right] \tag{2.37}$$

$$\begin{pmatrix} G_{IV,n} \\ H_{IV,n} \end{pmatrix} = -\frac{R_S}{n} \left[\begin{pmatrix} g_{c,IV,n} \\ g_{s,IV,n} \end{pmatrix} + f_n'(R_{LS}) \begin{pmatrix} nf_{s,IV,n,s} - g_{c,IV,n} \\ -nf_{c,IV,n} - g_{s,IV,n} \end{pmatrix} \right] \tag{2.38}$$

and $f_n^{'}(r)$ is the derivative of the function

$$f_n(r) = \begin{cases} r\frac{1}{1-n^2} & n > 1 \\ \frac{1}{2} r \ln r & n = 1 \end{cases} \tag{2.39}$$

The solutions in the airgaps (region II+III) and the airspaces between the PPs (region $i\varepsilon\{1,..,Q\}$) can be expressed as [51]:

$$A_{II}(r,\theta) = A_{II,0} + \sum_{n=1}^{\infty} \left\{ \begin{pmatrix} A_{II,n} \\ C_{II,n} \end{pmatrix} \frac{R_{mi}}{n} \frac{P_n(r,R_{PPi})}{E_n(R_{mi},R_{PPi})} \right. \tag{2.40}$$
$$\left. + \begin{pmatrix} B_{II,n} \\ D_{II,n} \end{pmatrix} \frac{R_{PPi}}{n} \frac{P_n(r,R_{mi})}{E_n(R_{PPi},R_{mi})} \right\} \cdot \begin{pmatrix} \cos(n\theta) \\ \sin(n\theta) \end{pmatrix}$$

$$A_{III}(r,\theta) = A_{III,0} + \sum_{n=1}^{\infty} \left\{ \begin{pmatrix} A_{III,n} \\ C_{III,n} \end{pmatrix} \frac{R_{PPo}}{n} \frac{P_n(r,R_{mo})}{E_n(R_{PPo},R_{mo})} + \begin{pmatrix} B_{III,n} \\ D_{III,n} \end{pmatrix} \frac{R_{mo}}{n} \frac{P_n(r,R_{PPo})}{E_n(R_{mo},R_{PPo})} \right\} \cdot \begin{pmatrix} \cos(n\theta) \\ \sin(n\theta) \end{pmatrix} \tag{2.41}$$

$$A_i(r,\theta) = R_{PPi}(A_{i,0} + B_{i,0} \ln \frac{r}{R_{PPi}}) + \sum_{n=1}^{\infty} R_{PPi} \left\{ A_{i,n} \frac{E_{n\pi/\beta}(r,R_{PPo})}{E_{n\pi/\beta}(R_{PPi},R_{PPo})} + B_{i,n} \frac{E_{n\pi/\beta}(r,R_{PPi})}{E_{n\pi/\beta}(R_{PPi},R_{PPo})} \right\} \cdot \cos\left(\frac{n\pi}{\beta}(\theta - \theta_i) \right) \tag{2.42}$$

The boundary conditions at the interfaces between the PM regions and airgap regions, and the boundary conditions at the interfaces between the air regions lead to a set of relations between coefficients. The boundary conditions at the interface between the HS rotor PM region and the inner airgap region (equations (2.23)-(2.24)) lead to

$$\begin{pmatrix} A_{I,n} \\ C_{I,n} \end{pmatrix} = \begin{pmatrix} A_{II,n} \\ C_{II,n} \end{pmatrix} \frac{P_n(R_{mi},R_{PPi})}{E_n(R_{mi},R_{PPi})} + \begin{pmatrix} B_{II,n} \\ D_{II,n} \end{pmatrix} \frac{R_{PPi}}{R_{mi}} \frac{2}{E_n(R_{PPi},R_{mi})} \tag{2.43}$$

$$\mu_r \begin{pmatrix} A_{II,n} \\ C_{II,n} \end{pmatrix} = B_r \begin{pmatrix} g_{c,I,n} + X'_{A,I,n}(R_{mi}) \\ g_{s,I,n} + X'_{C,I,n}(R_{mi}) \end{pmatrix} + \begin{pmatrix} A_{I,n} \\ C_{I,n} \end{pmatrix} \frac{E_n(R_{mi},R_{HS})}{P_n(R_{mi},R_{HS})} \tag{2.44}$$

where $X'_{A,I,n}(r)$ and $X'_{C,I,n}$ are the the derivatives of $X_{A,I,n}(r)$ and $X_{C,I,n}(r)$ respectively. The boundary conditions at the interface between the stator PM region and the outer airgap region (equations (2.25)-(2.26)) lead to

$$\begin{pmatrix} A_{IV,n} \\ C_{IV,n} \end{pmatrix} = \begin{pmatrix} B_{III,n} \\ D_{III,n} \end{pmatrix} \frac{P_n(R_{mo},R_{PPo})}{E_n(R_{mo},R_{PPo})} + \begin{pmatrix} A_{III,n} \\ C_{III,n} \end{pmatrix} \frac{R_{PPo}}{R_{mo}} \frac{2}{E_n(R_{PPo},R_{mo})} \tag{2.45}$$

$$\mu_r \begin{pmatrix} B_{III,n} \\ D_{III,n} \end{pmatrix} = B_r \begin{pmatrix} g_{c,IV,n} + X'_{A,IV,n}(R_{mo}) \\ g_{s,IV,n} + X'_{C,IV,n}(R_{mo}) \end{pmatrix} + \begin{pmatrix} A_{IV,n} \\ C_{IV,n} \end{pmatrix} \frac{E_n(R_{mo},R_S)}{P_n(R_{mo},R_S)} \tag{2.46}$$

where $X'_{A,IV,n}(r)$ and $X'_{C,IV,n}$ are the the derivatives of $X_{A,IV,n}(r)$ and $X_{C,IV,n}(r)$ respectively. The relations between coefficients gained by the boundary conditions at

the interfaces between the airgap and PP air regions [51] lead to

$$\begin{pmatrix} B_{II,n} \\ D_{II,n} \end{pmatrix} = \sum_{i=1}^{Q} \left\{ \frac{B_{i,0}}{\pi} \begin{pmatrix} r(n,i) \\ s(n,i) \end{pmatrix} + \sum_{k=1}^{\infty} \frac{k}{\beta} \left[A_{i,k} \frac{P_{k\pi/\beta}(R_{PPi}, R_{PPo})}{E_{k\pi/\beta}(R_{PPi}, R_{PPo})} - B_{i,k} \frac{2}{E_{k\pi/\beta}(R_{PPi}, R_{PPo})} \right] \begin{pmatrix} f(k,n,i) \\ g(k,n,i) \end{pmatrix} \right\} \quad (2.47)$$

$$\begin{pmatrix} A_{III,n} \\ C_{III,n} \end{pmatrix} = \sum_{i=1}^{Q} \left\{ \frac{B_{i,0}}{\pi} \begin{pmatrix} r(n,i) \\ s(n,i) \end{pmatrix} + \sum_{k=1}^{\infty} \frac{k}{\beta} \left[A_{i,k} \frac{2}{E_{k\pi/\beta}(R_{PPi}, R_{PPo})} - B_{i,k} \frac{P_{k\pi/\beta}(R_{PPo}, R_{PPi})}{E_{k\pi/\beta}(R_{PPi}, R_{PPo})} \right] \begin{pmatrix} f(k,n,i) \\ g(k,n,i) \end{pmatrix} \right\} \quad (2.48)$$

$$A_{i,k} = \sum_{n=1}^{\infty} \frac{2}{n\beta} \left(\begin{pmatrix} A_{II,n} \\ C_{II,n} \end{pmatrix} \frac{R_{mi}}{R_{PPi}} \frac{2}{E_n(R_{mi}, R_{PPi})} - \begin{pmatrix} B_{II,n} \\ D_{II,n} \end{pmatrix} \frac{P_n(R_{mi}, R_{PPi})}{E_n(R_{mi}, R_{PPi})} \right) \cdot \begin{pmatrix} f(k,n,i) \\ g(k,n,i) \end{pmatrix} \quad (2.49)$$

$$B_{i,k} = \sum_{n=1}^{\infty} \frac{2}{n\beta} \left(\begin{pmatrix} A_{III,n} \\ C_{III,n} \end{pmatrix} \frac{R_{PPo}}{R_{PPi}} \frac{P_n(R_{PPo}, R_{mo})}{E_n(R_{PPo}, R_{mo})} - \begin{pmatrix} B_{III,n} \\ D_{III,n} \end{pmatrix} \frac{R_{mo}}{R_{PPi}} \frac{2}{E_n(R_{PPo}, R_{mo})} \right) \cdot \begin{pmatrix} f(k,n,i) \\ g(k,n,i) \end{pmatrix} \quad (2.50)$$

$$A_{i,0} = A_{II,0} + \sum_{n=1}^{\infty} \frac{2}{n\beta} \left(\begin{pmatrix} A_{II,n} \\ C_{II,n} \end{pmatrix} \frac{R_{mi}}{R_{PPi}} \frac{2}{E_n(R_{mi}, R_{PPi})} - \begin{pmatrix} B_{II,n} \\ D_{II,n} \end{pmatrix} \frac{P_n(R_{mi}, R_{PPi})}{E_n(R_{mi}, R_{PPi})} \right) \cdot \begin{pmatrix} r(n,i) \\ s(n,i) \end{pmatrix} \quad (2.51)$$

$$A_{i,0} + B_{i,0} \ln \frac{R_{PPo}}{R_{PPi}} = A_{III,0} + \sum_{n=1}^{\infty} \frac{2}{n\beta} \left(\begin{pmatrix} A_{III,n} \\ C_{III,n} \end{pmatrix} \frac{R_{PPo}}{R_{PPi}} \frac{P_n(R_{PPo}, R_{mo})}{E_n(R_{PPo}, R_{mo})} - \begin{pmatrix} B_{III,n} \\ D_{III,n} \end{pmatrix} \frac{R_{mo}}{R_{PPi}} \frac{2}{E_n(R_{PPo}, R_{mo})} \right) \cdot \begin{pmatrix} r(n,i) \\ s(n,i) \end{pmatrix} \quad (2.52)$$

where $r(n,i)$, $s(n,i)$, $f(k,n,i)$ and $g(k,n,i)$ are functions independent from r and are given by [51]:

$$r(n,i) = \frac{1}{n} [\sin(n(\beta + \theta_i)) - \sin(n\theta_i)] \quad (2.53)$$

$$s(n,i) = -\frac{1}{n} [\cos(n(\beta + \theta_i)) - \cos(n\theta_i)] \quad (2.54)$$

For $k\pi \neq n\beta$

$$f(k,n,i) = \frac{-n\beta^2}{k^2\pi^2 - n^2\beta^2}\left[(-1)^k \sin(n(\beta+\theta_i)) - \sin(n\theta_i)\right] \quad (2.55)$$

$$g(k,n,i) = \frac{n\beta^2}{k^2\pi^2 - n^2\beta^2}\left[(-1)^k \cos(n(\beta+\theta_i)) - \cos(n\theta_i)\right] \quad (2.56)$$

and for $k\pi = n\beta$

$$f(k,n,i) = \frac{\beta}{2}\cos(n\theta_i) + \frac{\beta}{4k\pi}\left[\sin(n(2\beta+\theta_i)) - \sin(n\theta_i)\right] \quad (2.57)$$

$$g(k,n,i) = \frac{\beta}{2}\sin(n\theta_i) - \frac{\beta}{4k\pi}\left[\cos(n(2\beta+\theta_i)) - \cos(n\theta_i)\right] \quad (2.58)$$

2.3 Torque and shear stress in the airgaps

The electromagnetic torque in the airgap regions is acquired by using the Maxwell stress tensor and integrating over a circle at a radius r within the airgap regions: The torque in the inner airgap is given by

$$T_i = \frac{l_a R_i^2}{\mu_0}\int_0^{2\pi} B_{rad,II}(R_i,\theta)B_{\theta,II}(R_i,\theta)d\theta \quad (2.59)$$

$$= \frac{\pi l_a R_i^2}{\mu_0}\sum_{n=1}^{\infty}(W_{II,1,n}W_{II,2,n} + W_{II,3,n}W_{II,4,n})$$

where R_i is a radius in the inner airgap, and

$$W_{II,1,n} = -A_{II,n}\frac{R_{mi}}{R_i}\frac{P_n(R_i,R_{PPi})}{E_n(R_{mi},R_{PPi})} - B_{II,n}\frac{R_{PPi}}{R_i}\frac{P_n(R_i,R_{mi})}{E_n(R_{PPi},R_{mi})} \quad (2.60)$$

$$W_{II,2,n} = -C_{II,n}\frac{R_{mi}}{R_i}\frac{E_n(R_i,R_{PPi})}{E_n(R_{mi},R_{PPi})} - D_{II,n}\frac{R_{PPi}}{R_i}\frac{E_n(R_i,R_{mi})}{E_n(R_{PPi},R_{mi})} \quad (2.61)$$

$$W_{II,3,n} = C_{II,n}\frac{R_{mi}}{R_i}\frac{P_n(R_i,R_{PPi})}{E_n(R_{mi},R_{PPi})} + D_{II,n}\frac{R_{PPi}}{R_i}\frac{P_n(R_i,R_{mi})}{E_n(R_{PPi},R_{mi})} \quad (2.62)$$

$$W_{II,4,n} = -A_{II,n}\frac{R_{mi}}{R_i}\frac{E_n(r,R_{PPi})}{E_n(R_{mi},R_{PPi})} - B_{II,n}\frac{R_{PPi}}{R_i}\frac{E_n(R_i,R_{mi})}{E_n(R_{PPi},R_{mi})} \quad (2.63)$$

A similar set of expressions can be derived for the electromagnetic torque in the outer airgap

$$T_o = \frac{l_a R_o^2}{\mu_0}\int_0^{2\pi} B_{rad,III}(R_o,\theta)B_{\theta,III}(R_o,\theta)d\theta \quad (2.64)$$

where R_o is a radius in the outer airgap. The torques in the inner and outer arigaps are generated by the shear stress in the inner airgap σ_i and the shear stress in the

outer airgap σ_o, respectively. Furthermore, these are related by

$$\sigma_i = \frac{2}{\pi l_a (D - 2(w_{PP} + \frac{1}{2}l_{gi} + \frac{1}{2}l_{go}))^2} T_i \tag{2.65}$$

$$\sigma_o = \frac{2}{\pi l_a D^2} T_o \tag{2.66}$$

where w_{PP} is the Radial thickness of the PPs, l_{gi} is the length of inner airgap, and l_{go} is the length of the outer airgap. Using equation (2.59) these can be expressed as

$$\sigma_i = \frac{1}{2\pi\mu_0} \int_0^{2\pi} B_{rad,II}(R_i, \theta) B_{\theta,II}(R_i, \theta) d\theta \tag{2.67}$$

$$\sigma_o = \frac{1}{2\pi\mu_0} \int_0^{2\pi} B_{rad,III}(R_o, \theta) B_{\theta,III}(R_o, \theta) d\theta \tag{2.68}$$

For a fixed LS rotor the torque on the PP rotor is given by

$$T_{PP} = T_i + T_o \tag{2.69}$$

Furthermore, T_{PP} can also be given by

$$T_{PP} = \frac{1}{2}\pi D^2 l_a \sigma \tag{2.70}$$

where σ is the equivalent shear stress. In this work large MGs with large numbers of PPs are considered, hence $(w_{PP} + \frac{1}{2}l_{gi} + \frac{1}{2}l_{go}) \ll D$. For example, for the MG in Table 3.1 the ratio of radial PP width to airgap diameter is only $w_{PP}/D = 0.005$. For the designs investigated in this thesis the equivalent shear stress can, therefore, be approximated by

$$\sigma \approx \sigma_o + \sigma_i \tag{2.71}$$

with no significant loss of accuracy. In addition, due to the gearing effect, the torques are related by

$$T_{PP} = GT_i = \frac{G}{G-1} T_o \tag{2.72}$$

and σ is, therefore, also given by

$$\sigma = G\sigma_i = \frac{G}{G-1} \sigma_o \tag{2.73}$$

2.4 Scaling invariance

In theory a MG can be constructed with an arbitrary airgap length. However, physical and practical limitations may impose a limit on the minimum airgap length that can be achieved. Therefore, and in order to simplify the analysis, in this thesis the airgap length has been selected to be 0.1% of the airgap diameter. In this section the analytical model is employed to show, that if end effects are neglected, the flux density and hence the shear stress in the MG is independent of the airgap diameter. Furthermore, since the shear stress is linked to the overall volume of the MG, this invariance also allows for a simplified analysis of the masses of the active components.

The equations (2.43)-(2.52) can be rewritten in matrix form as

$$M\overrightarrow{x} = \overrightarrow{v} \tag{2.74}$$

where $\overrightarrow{x}$ consists of the unknown coefficients and the only non-zero elements of $\overrightarrow{v}$ are given by equations (2.44) and (2.46). It can be seen that both $\overrightarrow{v}$ and M are independent when scaled by a factor s:

$$r \rightarrow sr \tag{2.75}$$

As can be seen from equation (2.74) also the coefficients are invariant with this transformation. Furthermore, and as can be seen from equations (2.29)-(2.32) and (2.40)-(2.42) the vector potentials scale as

$$A(r,\theta) \longrightarrow sA(sr,\theta) \tag{2.76}$$

and the magnetic flux density scales as

$$\overrightarrow{B}(r,\theta) \longrightarrow \overrightarrow{B}(sr,\theta) \tag{2.77}$$

From equation (2.67) and (2.68) it can be seen that also the shear stress remains constant.

Furthermore, if the active length is scaled as

$$l_a \rightarrow s^{-2} l_a \tag{2.78}$$

the Torque, the PM mass and the PP rotor laminated steel mass is also constant. Since it is undesirable to operate laminated steel at flux densities higher than $\approx 1.7T$ as saturation effects would effectively decrease the torque, the back-iron is designed such that the maximum operating flux density is aimed to not exceed $B_{lim} = 1.5T$. This is realised by estimating the required HS rotor and stator back-iron widths with consideration of the p_{HS}-th and p_S-th harmonics of the flux density present at the interfaces between PMs and the back-irons. The HS rotor laminated steel mass is therefore estimated by

$$M_{L,HS} = m_L l_a (R_{HS}^2 - (R_{HS} - w_{HS,L})^2)\pi \tag{2.79}$$

where

$$\begin{aligned} w_{HS,L} &= \frac{1}{2}\frac{R_{HS}}{B_{lim}} \int_0^{\pi/p_{HS}} B_{rad,p_{HS}}(R_{HS}) \sin(p_{HS}\theta) d\theta \\ &\quad + \frac{1}{2}\frac{R_{HS}}{B_{lim}} \int_0^{\pi/p_S} B_{rad,p_S}(R_{HS}) \sin(p_S\theta) d\theta \\ &= \frac{R_{HS}}{p_{HS}}\frac{B_{rad,p_{HS}}(R_{HS})}{B_{lim}} + \frac{R_{HS}}{p_S}\frac{B_{rad,p_S}(R_{HS})}{B_{lim}} \end{aligned} \tag{2.80}$$

is the estimated required radial HS rotor back iron thickness. m_L is the mass density of laminated steel, and $B_{rad,p_{HS}}(r)$ and $B_{rad,p_S}(r)$ are the radial peak flux density values of the p_{HS}-th and p_S-th harmonic at a radius r. The stator laminated steel mass is estimated by

$$M_{L,S} = m_L l_a ((R_S + w_{HS,L})^2 - R_S^2)\pi \tag{2.81}$$

where

$$\begin{aligned} w_{S,L} &= \frac{1}{2}\frac{R_S}{B_{lim}} \int_0^{\pi/p_{HS}} B_{rad,p_{HS}}(R_S) \sin(p_{HS}\theta) d\theta \\ &\quad + \frac{1}{2}\frac{R_S}{B_{lim}} \int_0^{\pi/p_S} B_{rad,p_{LS}}(R_S) \sin(p_S\theta) d\theta \\ &= \frac{R_S}{p_{HS}}\frac{B_{rad,p_{HS}}(R_S)}{B_{lim}} + \frac{R_S}{p_S}\frac{B_{rad,p_S}(R_S)}{B_{lim}} \end{aligned} \tag{2.82}$$

is the estimated required radial stator back iron thickness. From equations (2.79)-

(2.82) it can be seen that if the axial length is scaled as in (2.78) also the HS rotor and stator laminated steel mass would remain constant.

2.5 Particular magnetisations

The expressions in Section 2.2 are further specified for three types of magnetisation distributions. These are radial magnetisation (RM), discrete Halbach magnetisation, and continuous Halbach magnetisation.

2.5.1 Radial magnetisation

For a radial magnetisation with a pole-pitch to pole-arc ratio $a_{HS} < 1$ the spaces in between the PMs have normally the same permeability as air, however, a solution can only be found if the permeability is uniform in region I. Therefore, for the analytical model the spaces between the PMs are assumed to be occupied by non-magnetised PM material with the same permeability as the PMs. Although single PMs would normally be uniformly magnetised a radial magnetisation would give a sufficiently well enough approximation for MGs where a large number of poles are present. Furthermore, if the MG is equipped with a low number of poles, each pole would normally be segmented due to ease of manufacturing and in order to reduce eddy current losses and the poles could, therefore, also be approximated by a radial magnetisation.

The residual magnetisation of radially magnetised PMs on the HS rotor can then be expressed in terms of a Fourier series as

$$\overrightarrow{M}_I(\theta) = \frac{B_r}{\mu_0} \sum_{n=1}^{\infty} \begin{bmatrix} c_n + c_{-n} & j(c_n - c_{-n}) \\ 0 & 0 \end{bmatrix} \begin{pmatrix} cos(n\theta) \\ sin(n\theta) \end{pmatrix} \tag{2.83}$$

where j is the imaginary unit and

$$\begin{aligned} c_n &= \sum_{q=1}^{2p_{HS}} \frac{1}{2\pi} \int_{q\pi/p_{HS} - \frac{1}{2}\beta_{mi} + \Theta_{HS}}^{q\pi/p_{HS} + \frac{1}{2}\beta_{mi} + \Theta_{HS}} (-1)^q e^{-jn\theta} d\theta \qquad (2.84) \\ &= k_{I,n} e^{-jn\Theta_{HS}} \\ k_{I,n} &= \frac{2sin(\frac{1}{2}n\beta_{mi})}{n\pi} (1 - \varepsilon_{n,2p_{HS}}) p_{HS} \varepsilon_{n,p_{HS}} \qquad (2.85) \end{aligned}$$

Θ_{HS} is the angular offset of the HS rotor PMs and β_{mi} is the pole arc.

$$\varepsilon_{t,s} = \begin{cases} 1 & t \bmod s = 0 \\ 0 & t \bmod s \neq 0 \end{cases} \tag{2.86}$$

is a function of two integer values t and s, and $t \bmod s$ is the modulo operation. The function $\varepsilon_{t,s}$ is derived in App. A.3. The residual magnetisation may also be expressed in the more familiar form [55]:

$$M_{rad,I}(\theta) = \frac{B_r}{\mu_0} \sum_{n=1,3,5,..}^{\infty} \frac{4sin(\frac{1}{2}np\beta_{mi})}{n\pi} \begin{pmatrix} \cos(np\Theta_{HS}) \\ -\sin(np\Theta_{HS}) \end{pmatrix} \cdot \begin{pmatrix} \cos(np\theta) \\ \sin(np\theta) \end{pmatrix} \tag{2.87}$$

$$M_{\theta,I}(\theta) = 0 \tag{2.88}$$

where $M_{rad,I}$ and $M_{\theta,I}(\theta)$ are the radial and circumferential residual magnetisations, respectively. For region I the expressions for $X_{A,I,n}(r)$ and $X_{C,I,n}(r)$ are given by

$$\begin{pmatrix} X_{A,I,n}(r) \\ X_{C,I,n}(r) \end{pmatrix} = X_{RM,I,n}(r) \begin{pmatrix} \sin(n\Theta_{HS}) \\ -\cos(n\Theta_{HS}) \end{pmatrix} \tag{2.89}$$

where

$$X_{RM,I,n}(r) = 2k_{I,n} \left(Y_{I,n}(r) - \frac{P_n(r,R_{HS})}{P_n(R_{mi},R_{HS})} Y_{I,n}(R_{mi}) \right) \tag{2.90}$$

$$Y_{I,n} = \left(\frac{r}{R_{HS}} \right)^{-n} R_{HS} f_n^{'}(R_{HS}) + n f_n(r) \tag{2.91}$$

The relation between the coefficients of regions I and II, given in equations (2.43)-(2.44) are then given by

$$\begin{pmatrix} A_{I,n} \\ C_{I,n} \end{pmatrix} = \begin{pmatrix} A_{II,n} \\ C_{II,n} \end{pmatrix} \frac{P_n(R_{mi},R_{PPi})}{E_n(R_{mi},R_{PPi})} + \begin{pmatrix} B_{II,n} \\ D_{II,n} \end{pmatrix} \frac{2}{E_n(R_{PPi},R_{mi})} \tag{2.92}$$

$$\mu_r \begin{pmatrix} A_{II,n} \\ C_{II,n} \end{pmatrix} = \begin{pmatrix} A_{I,n} \\ C_{I,n} \end{pmatrix} \frac{E_n(R_{mi},R_{HS})}{P_n(R_{mi},R_{HS})} + B_r X_{RM,I,n}^{'}(R_{mi}) \begin{pmatrix} \sin(n\Theta_{HS}) \\ -\cos(n\Theta_{HS}) \end{pmatrix} \tag{2.93}$$

where $X_{RM,I,n}^{'}$ is the derivative of $X_{RM,I,n}$.

2.5.2 Discrete Halbach magnetisation

A HM distribution provides several attractive features such as an inherently sinusoidal magnetic field, which allows for small torque ripple and a self-shielding magnetisation that reduces the required back-iron and may result in a significantly higher airgap field than equivalent radially magnetized PMs. In practice, however,

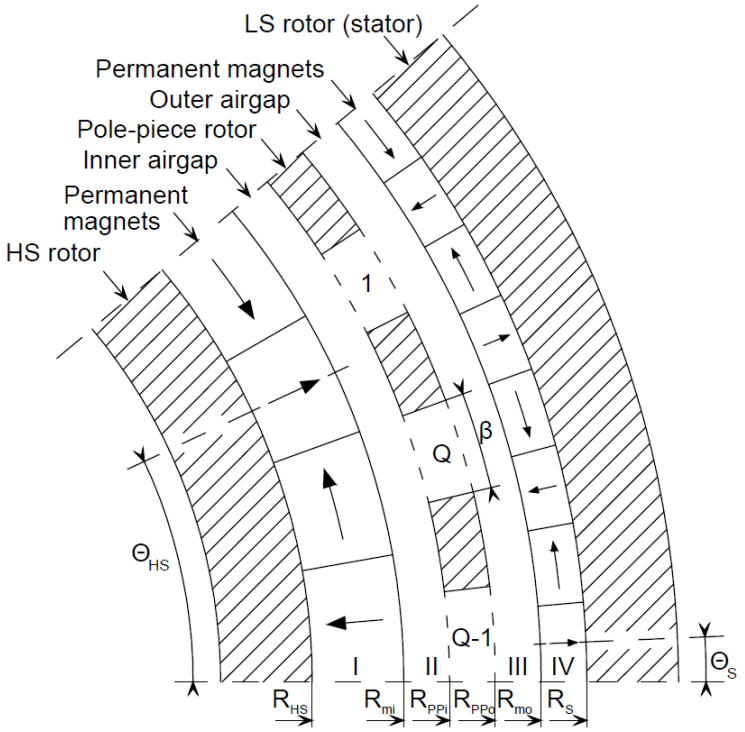

Fig. 2.2: Geometry for a MG section with a periodic symmetry of 40 degrees. PMs consist of 4 Halbach-segments per pole-pair on the HS rotor and the LS rotor (stator).

HM distribution is approximated by employing a discrete number of segments per pole-pair. Furthermore, due to the large size of the MG and therefore the small pole pitch of the PMs, a uniform magnetisation in Cartesian coordinates may be sufficiently well represented by a uniform magnetisation in radial coordinates. Given a segmentation of m pieces per pole-pair, the magnetic field within the k-th segment of a pole-pair is then given in radial coordinates by

$$\vec{M}_k = \frac{B_r}{\mu_0} \begin{pmatrix} \cos(2\pi\frac{k}{m}) \\ \pm\sin(2\pi\frac{k}{m}) \end{pmatrix} \tag{2.94}$$

where the upper sign $(+)$ corresponds to an internal field, normally applied to the stator, and the lower sign $(-)$ corresponds to an external field, normally applied to the HS rotor. The magnetisation for one particular segment can be extended outside the segment by introducing the function

$$f_{k,q}(\theta) = \begin{cases} 1 & -\frac{1}{2m}\frac{2\pi}{p} \leq \theta - \theta_{k,q} \leq \frac{1}{2m}\frac{2\pi}{p}; \\ 0 & else \end{cases} \tag{2.95}$$

where $\theta_{k,q}$ is the angular position at the center of of the k-th segment of the q-th pole-pair given by

$$\theta_{q,k} = \frac{2\pi}{p}(q + \frac{k}{m}) - \Theta_0$$

where Θ_0 is the position of the rotor. $f_{k,q}(\theta)$ can be expressed as a Fourier series as

$$f_{k,q}(\theta) = \sum_{n=-\infty}^{\infty} c_{n,k,q} e^{jn(\theta-\Theta_0)} \tag{2.96}$$

where the coefficients are given by (see App.A.2)

$$c_{n,k,q} = \frac{\sin(n\pi/mp)}{n\pi} \exp\left[-jn\frac{2\pi}{p}(q + \frac{k}{m})\right] \tag{2.97}$$

The residual magnetisation including all segments is then given by (see App.A.2)

$$\begin{aligned} \overrightarrow{M}(\theta) &= \sum_{k=0}^{m-1} \vec{M}_k \sum_{q=0}^{p-1} f_{k,q}(\theta) && (2.98) \\ &= \frac{B_r}{\mu_0} \sum_{n=1}^{\infty} h_{n,m,p} \begin{bmatrix} \varepsilon^+_{n,m,p}\cos(n\Theta_0) & \varepsilon^+_{n,m,p}\sin(n\Theta_0) \\ -\varepsilon^-_{n,m,p}\sin(n\Theta_0) & \varepsilon^-_{n,m,p}\cos(n\Theta_0) \end{bmatrix} \begin{pmatrix} \cos(n\theta) \\ \sin(n\theta) \end{pmatrix} \end{aligned}$$

where

$$\varepsilon^+_{n,m,p} = \varepsilon_{mp,n\mp p} + \varepsilon_{mp,n\pm p} \tag{2.99}$$

$$\varepsilon^-_{n,m,p} = \varepsilon_{mp,n\mp p} - \varepsilon_{mp,n\pm p} \tag{2.100}$$

$$h_{n,m,p} = mp\frac{\sin(n\pi/mp)}{n\pi}\varepsilon_{n,p} \tag{2.101}$$

The expressions for $X_{A,I,n}(r)$ and $X_{C,I,n}(r)$ are given by

$$\begin{pmatrix} X_{A,I,n}(r) \\ X_{C,I,n}(r) \end{pmatrix} = X_{dHM,I,n}(r) \begin{pmatrix} \sin(n\Theta_{HS}) \\ -\cos(n\Theta_{HS}) \end{pmatrix} \tag{2.102}$$

where

$$X_{dHM,I,n}(r) = h_{n,m_{HS},p_{HS}} \left(Y_{I,n}(r) - \frac{P_n(r,R_{HS})}{P_n(R_{mi},R_{HS})} Y_{I,n}(R_{mi})\right) \tag{2.103}$$

$$Y_{I,n}(r) = \frac{R_{HS}}{n}\left(\frac{r}{R_{HS}}\right)^{-n} G_{I,n} + f_n(r)(n\varepsilon^+_{n,m_{HS},p_{HS}} + \varepsilon^-_{n,m_{HS},p_{HS}}) \tag{2.104}$$

$$G_{I,n} = \left[f_n'(R_{HS})(n\varepsilon^+_{n,m_{HS},p_{HS}} + \varepsilon^-_{n,m_{HS},p_{HS}}) - \varepsilon^-_{n,m_{HS},p_{HS}}\right] \tag{2.105}$$

The function $f_n(r)$ is given in equation (2.39), and $f_n'(r)$ is its derivative. The relation between the coefficients of regions I and II, given in equations (2.43)-(2.44)

are then given by

$$\begin{pmatrix} A_{I,n} \\ C_{I,n} \end{pmatrix} = \begin{pmatrix} A_{II,n} \\ C_{II,n} \end{pmatrix} \frac{P_n(R_{mi}, R_{PPi})}{E_n(R_{mi}, R_{PPi})} + \begin{pmatrix} B_{II,n} \\ D_{II,n} \end{pmatrix} \frac{2}{E_n(R_{PPi}, R_{mi})} \quad (2.106)$$

$$\mu_r \begin{pmatrix} A_{II,n} \\ C_{II,n} \end{pmatrix} = \begin{pmatrix} A_{I,n} \\ C_{I,n} \end{pmatrix} \frac{E_n(R_{mi}, R_{HS})}{P_n(R_{mi}, R_{HS})} \quad (2.107)$$

$$+B_r \left[X'_{dHM,I,n}(R_{mi}) - h_{n,m_{HS},p_{HS}} \varepsilon^-_{n,m_{HS},p_{HS}} \right] \begin{pmatrix} \sin(n\Theta_{HS}) \\ -\cos(n\Theta_{HS}) \end{pmatrix}$$

where $X'_{dHM,I,n}$ is the derivative of $X_{dHM,I,n}$. The expressions for $X_{A,IV,n}(r)$ and $X_{C,IV,n}(r)$ are given by

$$\begin{pmatrix} X_{A,IV,n}(r) \\ X_{C,IV,n}(r) \end{pmatrix} = X_{dHM,IV,n}(r) \begin{pmatrix} \sin(n\Theta_S) \\ -\cos(n\Theta_S) \end{pmatrix} \quad (2.108)$$

where

$$X_{dHM,IV,n}(r) = h_{n,m_S,p_S} \left(Y_{IV,n}(r) - \frac{P_n(r, R_S)}{P_n(R_{mo}, R_S)} Y_{IV,n}(R_{mo}) \right) \quad (2.109)$$

$$Y_{IV,n}(r) = \frac{R_S}{n} \left(\frac{r}{R_S} \right)^n G_{IV,n}(R_S) + f_n(r)(n\varepsilon^+_{n,m_S,p_S} + \varepsilon^-_{n,m_S,p_S}) \quad (2.110)$$

$$G_{IV,n}(w) = -\left[f'_n(R_S)(n\varepsilon^+_{n,m_S,p_S} + \varepsilon^-_{n,m_S,p_S}) - \varepsilon^-_{n,m_S,p_S} \right] \quad (2.111)$$

The relations between the coefficients of regions III and IV, given in equations (2.45)-(2.46) are then given by

$$\begin{pmatrix} A_{IV,n} \\ C_{IV,n} \end{pmatrix} = \begin{pmatrix} B_{III,n} \\ D_{III,n} \end{pmatrix} \frac{P_n(R_{mo}, R_{PPo})}{E_n(R_{mo}, R_{PPo})} + \begin{pmatrix} A_{III,n} \\ C_{III,n} \end{pmatrix} \frac{2}{E_n(R_{PPo}, R_{mo})} \quad (2.112)$$

$$\mu_r \begin{pmatrix} B_{III,n} \\ D_{III,n} \end{pmatrix} = \begin{pmatrix} A_{IV,n} \\ C_{IV,n} \end{pmatrix} \frac{E_n(R_{mo}, R_S)}{P_n(R_{mo}, R_S)} \quad (2.113)$$

$$+B_r \left[X'_{dHM,IV,n}(R_{mo}) - h_{n,m_S,p_S} \varepsilon^-_{n,m_S,p_S} \right] \begin{pmatrix} \sin(n\Theta_S) \\ -\cos(n\Theta_S) \end{pmatrix}$$

where $X'_{dHM,IV,n}$ is the derivative of $X_{dHM,IV,n}$.

2.5.3 Continuous Halbach magnetisation

A continuous Halbach magnetised ring of PM material is considered and the solutions are obtained by applying the limit $m \to \infty$, and $\varepsilon^{+}_{n,m,p}$, $\varepsilon^{-}_{n,m,p}$ and $h_{n,m,p}$ become

$$\varepsilon^{+}_{n,m\to\infty,p} = \delta_{n,p} \tag{2.114}$$

$$\varepsilon^{-}_{n,m\to\infty,p} = \pm\delta_{n,p} \tag{2.115}$$

$$h_{n,m\to\infty,p} = \delta_{n,p} \tag{2.116}$$

For a continuous external HM on the HS rotor the residual magnetisation given in (2.98) becomes

$$\vec{M}_I(\theta) = \frac{B_r}{\mu_0}\begin{bmatrix} \cos(p_{HS}\Theta_{HS}) & \sin(p_{HS}\Theta_{HS}) \\ \sin(p_{HS}\Theta_{HS}) & -\cos(p_{HS}\Theta_{HS}) \end{bmatrix}\begin{pmatrix} \cos(p_{HS}\theta) \\ \sin(p_{HS}\theta) \end{pmatrix} \tag{2.117}$$

and for a continuous internal HM on the LS rotor the residual magnetisation becomes

$$\vec{M}_{IV}(\theta) = \frac{B_r}{\mu_0}\begin{bmatrix} \cos(p_S\Theta_S) & \sin(p_S\Theta_S) \\ -\sin(p_S\Theta_S) & \cos(p_S\Theta_S) \end{bmatrix}\begin{pmatrix} \cos(p_S\theta) \\ \sin(p_S\theta) \end{pmatrix} \tag{2.118}$$

The expressions for $X_{A,I,n}(r)$ and $X_{C,I,n}(r)$ are given by

$$\begin{pmatrix} X_{A,I,n}(r) \\ X_{C,I,n}(r) \end{pmatrix} = \delta_{n,p_{HS}} X_{cHM,I}(r)\begin{pmatrix} \sin(p_{HS}\Theta_{HS}) \\ -\cos(p_{HS}\Theta_{HS}) \end{pmatrix} \tag{2.119}$$

where

$$X_{cHM,I}(r) = \left(Y_I(r) - \frac{P_n(r,R_{HS})}{P_n(R_{mi},R_{HS})}Y_I(R_{mi})\right) \tag{2.120}$$

$$Y_I(r) = \frac{R_{HS}}{p_{HS}}\left(\frac{r}{R_{HS}}\right)^{-p_{HS}}\left[f'_{p_{HS}}(R_{HS})(p_{HS}-1)+1\right]+f_n(r)(p_{HS}-1) \tag{2.121}$$

The relations between the coefficients of regions I and II, given in equations (2.43)-(2.44) are then given by

$$\begin{pmatrix} A_{I,n} \\ C_{I,n} \end{pmatrix} = \begin{pmatrix} A_{II,n} \\ C_{II,n} \end{pmatrix}\frac{P_n(R_{mi},R_{PPi})}{E_n(R_{mi},R_{PPi})} + \begin{pmatrix} B_{II,n} \\ D_{II,n} \end{pmatrix}\frac{2}{E_n(R_{PPi},R_{mi})} \tag{2.122}$$

$$\mu_r\begin{pmatrix} A_{II,n} \\ C_{II,n} \end{pmatrix} = \begin{pmatrix} A_{I,n} \\ C_{I,n} \end{pmatrix}\frac{E_n(R_{mi},R_{HS})}{P_n(R_{mi},R_{HS})} + \delta_{n,p_{HS}}B_r\left[X'_{cHM,I}(R_{mi})+1\right]\begin{pmatrix} \sin(p_{HS}\Theta_{HS}) \\ -\cos(p_{HS}\Theta_{HS}) \end{pmatrix} \tag{2.123}$$

where $X'_{cHM,I,n}$ is the derivative of $X_{cHM,I,n}$. The expressions for $X_{A,IV,n}(r)$ and

$X_{C,IV,n}(r)$ are given by

$$\begin{pmatrix} X_{A,IV,n}(r) \\ X_{C,IV,n}(r) \end{pmatrix} = \delta_{n,p_S} X_{cHM,IV}(r) \begin{pmatrix} \sin(p_S\Theta_S) \\ -\cos(p_S\Theta_S) \end{pmatrix} \tag{2.124}$$

where

$$X_{cHM,IV}(r) = \left(Y_{IV}(r) - \frac{P_n(r,R_S)}{P_n(R_{mo},R_S)} Y_{IV}(R_{mo}) \right) \tag{2.125}$$

$$Y_{IV}(r) = -\frac{R_S}{p_S}\left(\frac{r}{R_S}\right)^{p_S}\left[f'_{p_S}(R_S)(p_S+1)-1\right] + f_n(r)(p_S+1) \tag{2.126}$$

The relations between the coefficients of regions III and IV, given in equations (2.45)-(2.46) are then given by

$$\begin{pmatrix} A_{IV,n} \\ C_{IV,n} \end{pmatrix} = \begin{pmatrix} B_{III,n} \\ D_{III,n} \end{pmatrix} \frac{P_n(R_{mo},R_{PPo})}{E_n(R_{mo},R_{PPo})} + \begin{pmatrix} A_{III,n} \\ C_{III,n} \end{pmatrix} \frac{2}{E_n(R_{PPo},R_{mo})} \tag{2.127}$$

$$\begin{aligned} \mu_r \begin{pmatrix} B_{III,n} \\ D_{III,n} \end{pmatrix} &= \begin{pmatrix} A_{IV,n} \\ C_{IV,n} \end{pmatrix} \frac{E_n(R_{mo},R_S)}{P_n(R_{mo},R_S)} \\ &\quad + \delta_{n,p_S} B_r \left[X'_{cHM,IV}(R_{mo}) - 1\right] \begin{pmatrix} \sin(p_S\Theta_S) \\ -\cos(p_S\Theta_S) \end{pmatrix} \end{aligned} \tag{2.128}$$

where $X'_{cHM,IV,n}$ is the derivative of $X_{cHM,IV,n}$.

2.6 Conclusions

A 2D analytical model for the prediction of the magnetic field distributions in the airgaps and PMs of radial-field MGs is presented for arbitrary magnetisation distributions dependent only on the circumferential coordinate. The coefficients of the solutions for the various regions are determined by applying the boundary condition at the interfaces. End effects are neglected and the iron is assumed to be infinitely permeable. Using the analytical solutions several quantities can be derived, e.g. shear stress and torque. The developed model is employed to show that the flux density distributions in the air and PM regions, and the shear stresses remain constant when the radial dimensions, including the airgaps, of the MG gear are scaled. It is also shown that the active masses are independent of the aspect ratio of the MG. Finally the model is applied for radial, discrete Halbach and continuous Halbach magnetisation distributions.

Chapter 3

Large magnetic gears

MGs may be employed in applications where high torques are required, such as multi-MW wind turbines. Due to the size and speed of these MGs they may be constructed with a large number of poles. Therefore, the MGs may be constructed from several magnetically identical sections, with each section satisfying the required relationship between the numbers of pole pairs and the number of PPs. In this chapter the analytical model developed in Chapter 2 is compared with FE for an MG with a pullout torque of a 11.9MNm which has been selected following an optimisation process. Furthermore, since for MGs with a high pole number the analytical solution may become numerically challenging, these issues are also addressed. Finally, the effects of leading design parameters on the key PI of an MG, such as the shear stress and the active masses, are presented.

3.1 Optimisation process

The analytical model developed in Chapter 2 is employed for the optimisation of a large MG for a wind turbine application. Several performance indicators (PIs) have been identified for the determination of the goodness of a MG design, and the the optimised design has been selected such that for all of these PIs a good result is achieved. Since the cost of the MG would to a large extend depend on the masses of the active components, the PM mass and the laminated steel mass have

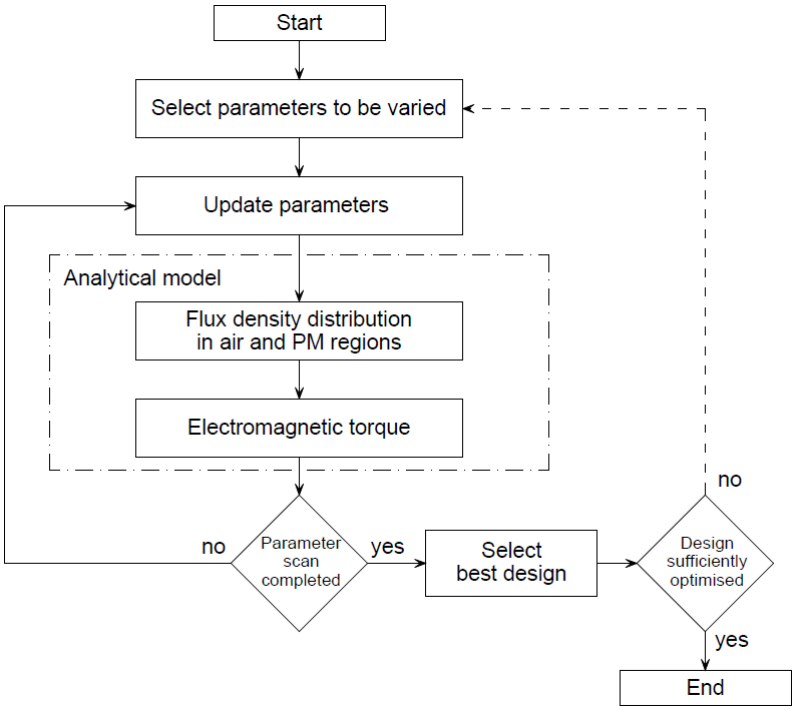

Fig. 3.1: Flowchart for the optimisation procedure.

been selected as PIs. Furthermore, in order to achieve a light weight and compact design also the volume and, therefore, the shear stress of the MG have also been identified as PI. Although the MG can realistically not be operated at the pullout torque, the equivalent shear stress at pullout torque σ_{pull} still provides a good PI for the compactness of the MG. Further secondary PI, such as the aspect ratio of the MG and the gear ratio, have also been considered in order to determine the best design. In summary, the parameters that have been varied in the optimisation analysis are: the PM thickness, the PP thickness, the airgap diameter and hence the aspect ratio, the magnetisation distribution, the PM arc, the number of identical sections, and the gear ratio.

Fig. 3.1 shows the flowchart for the optimisation procedure that has been employed. After selection of an initial MG design, parameters suitable for the investigation of one or more design parameters is selected. After completion of the parameter scan the best design is identified. If the design requires further improvement a new selection of parameters is investigated. Table 3.1 gives the parameters for a large MG with a pullout torque of $11.9MNm$ that is optimised through this

iterative process, and where a radial magnetisation and a discrete Halbach magnetisation with 4 segments per pole-pair has been employed on the HS rotor and the stator, respectively, see Fig. 3.2. The MG is optimised to achieve the required torque with the main goals of minimising the PM mass and the total active mass, while achieving a sufficiently high shear stress.

	Quantity	Value
T_{Pull}	Analytical pullout torque	11.9 MNm
p_{HS}	Pole-pairs on HS rotor	40
p_S	Pole-pairs on stator	260
m_S	Halbach segments per pole-pair on stator	4
Q	Pole pieces	300
K	Number of magnetically identical sections	20
a_{mi}	Ratio of pole arc to pole pitch for the HS rotor PMs	0.8
G	Gear ratio	7.5
D	Inner airgap diameter	6.0 m
	Radial thickness of HS rotor PMs	39.8 mm
	Radial thickness of stator PMs	25.2 mm
	Radial thickness of PP segments	31.4 mm
	Airgap lengths	6.0 mm
l_a	Active axial length	1.66 m
β	PP slot opening angle	$\pi/300$ rad
B_r	Remanence of PMs	1.25 T
μ_r	Relative recoil permeability	1.05
	PM mass	13.5 $tons$
	Mass of laminated steel	21.5 $tons$
	Mass of structural steel	70 $tons^{\#}$

[#] For a 6m airgap diameter MG the structural mass is assumed to be twice the active mass.

Table 3.1: Parameters of the MG component.

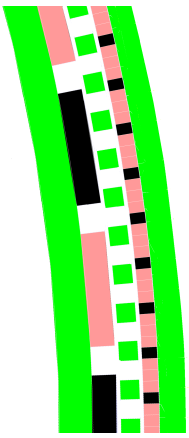

Fig. 3.2: Cross section of the MG.

3.2 Comparison with finite element

The analytical model from Chapter 2 is compared with 2D-FE studies for the MG in Table 3.1. Figs. (3.3)-(3.6) show the radial and circumferential components of the flux density in the inner and outer airgap. It can be seen a good agreement exists between analytical and FE predictions.

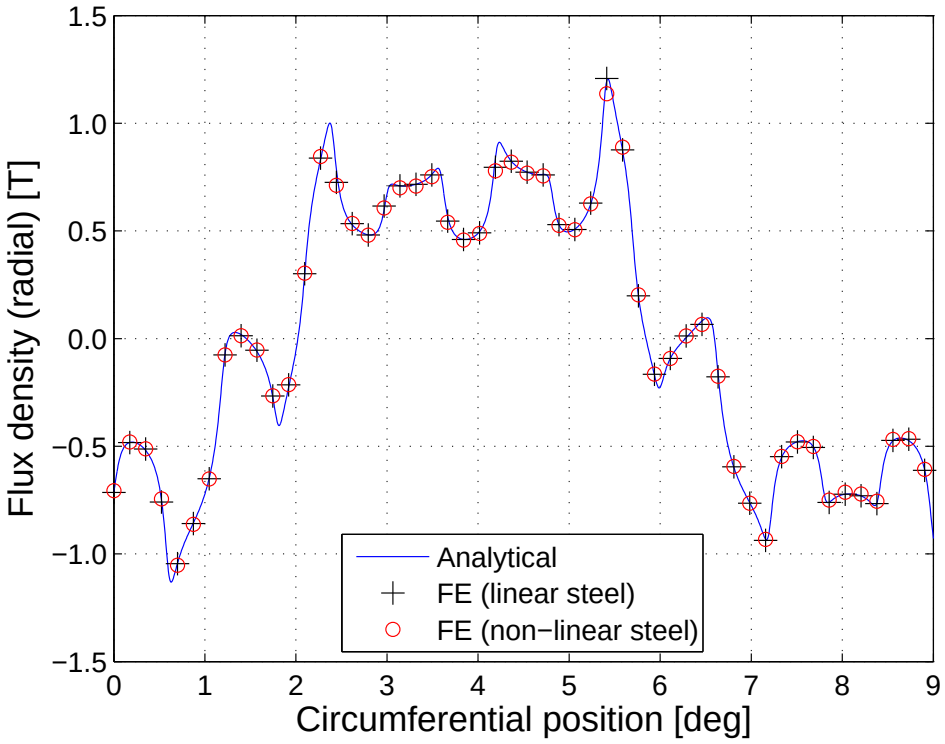

Fig. 3.3: Variation of the radial component of the magnetic flux density in the inner airgap with the circumferential position.

Figs. 3.7-3.8 show the variation of the electromagnetic torque on the PP and HS rotor. It can be seen that a good agreement exists between analytical model and FE if steel with linear characteristics is assumed, and that the effect of the nonlinear characteristics of the steel is not significant.

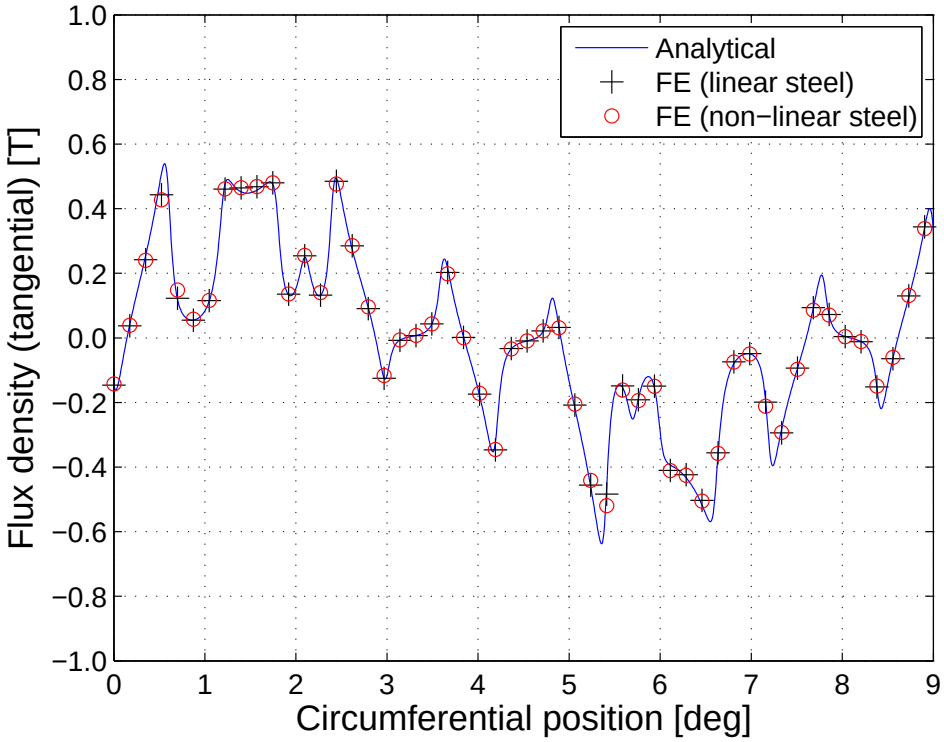

Fig. 3.4: Variation of the angular component of the magnetic flux density in the inner airgap with the circumferential position.

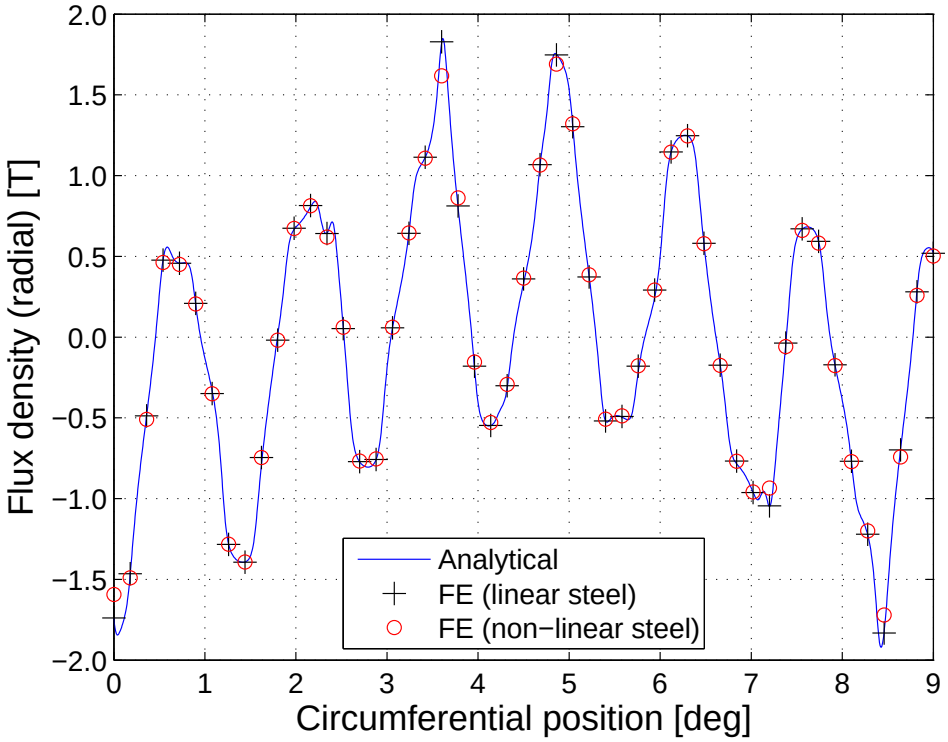

Fig. 3.5: Variation of the radial component of the magnetic flux density in the outer airgap with the circumferential position.

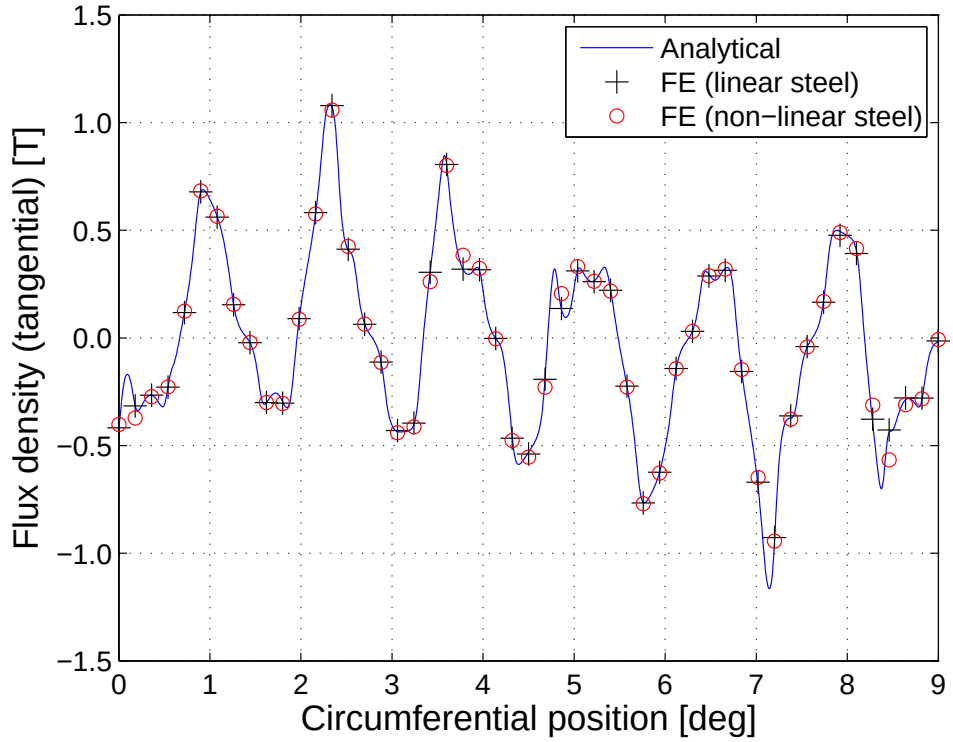

Fig. 3.6: Variation of the angular component of the magnetic flux density in the outer airgap with the circumferential position.

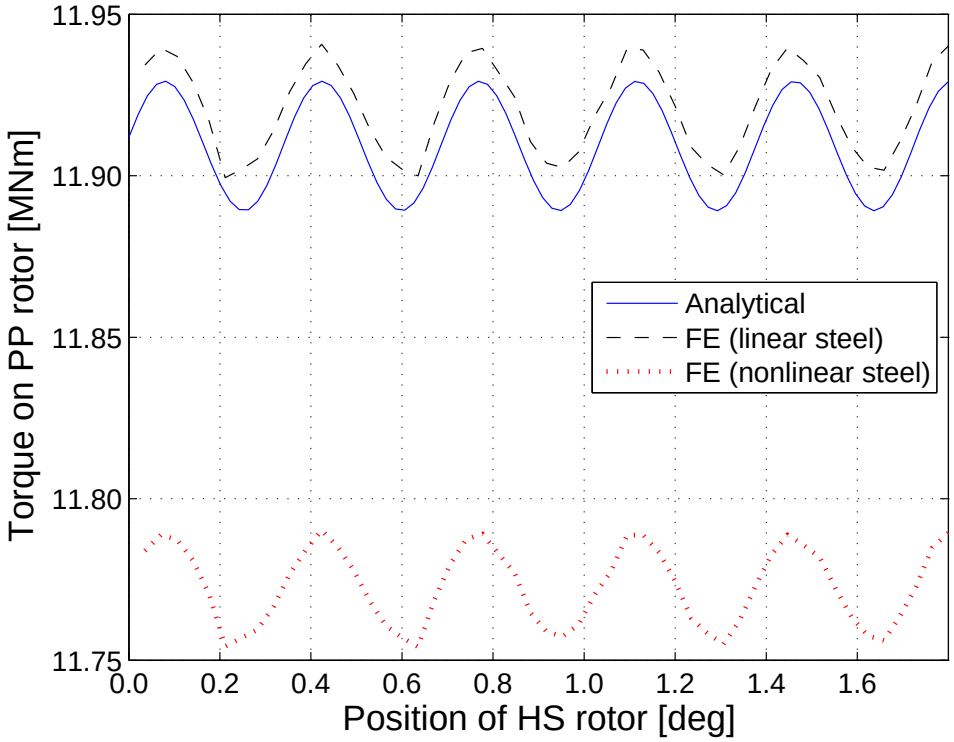

Fig. 3.7: Variation of the torque on the PP rotor with the position of the HS rotor.

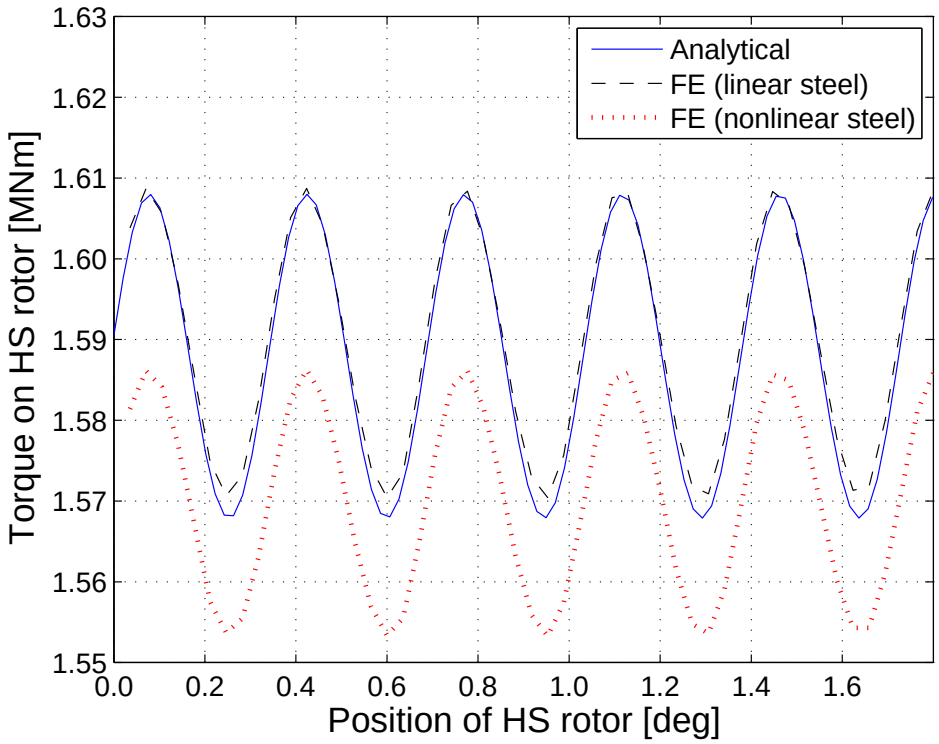

Fig. 3.8: Variation of the torque on the HS rotor with the position of the HS rotor.

3.3 Numerical challenges

The analytical solutions in the airgap and PM regions are computed with a finite number of Fourier series components. In general for machines equipped with a large number of poles, the harmonic order required in order to achieve an adequate accuracy has to be larger than the number of poles. For the MG the problem is magnified by the existence of two sets of PMs and associated airgaps, and more importantly the existence of air spaces between the PPs. More specifically the total size of the matrix to be inverted to attain the solutions for the vector potentials is $N_{total} \times N_{total}$, where $N_{total} = 12N + (2Q+2)N_Q$, where N is the highest order harmonic considered in regions I, II, III and IV, and N_Q is the highest order harmonic considered in the PP rotor air regions. This may require an amount of numerical operations in the order of N_{total}^2 or more. Furthermore, during the solving process large exponents may have to be handled, which could lead to numerical issues, with values exceeding the set limits. Several methods of handling these issues are proposed.

3.3.1 Periodicity

Due their size large MGs are likely to be constructed from K magnetically identical sections, with each section satisfying the required relationship between the numbers of pole-pairs and the number of PPs $Q = p_{HS} + p_S$, see Fig. 2.1. Therefore, the analytical solution should take into account the circumferential symmetry. Any function with a periodicity of $2\pi/K$ and of the form

$$f_n(\theta) = \sum_{n=1}^{N} R_n(r)\left(a_n \cos n\theta + b_n \sin n\theta\right) \tag{3.1}$$

where $R_n(r)$ is a function of r, and a_n and b_n are coefficients, can be reduced to

$$f_n(\theta) = \sum_{j=K}^{N_{eff}} R_j(r)\left(a_j \cos j\theta + b_j \sin j\theta\right) \tag{3.2}$$

where N_{eff} is the next lower integer to N/K and j are multiples of K, and where the wavelength of the fundamental $j = 1$ is equal to the angular span of a magnetically

identical section. In addition the number of boundary conditions related to the Q PP rotor air regions reduce by a factor of K since the vector potential in the PP air regions would be periodic, i.e. $A_i = A_{i+Q/K}$. Therefore, the total number of Fourier components is reduced by a factor of K, while the matrix to be inverted for a solution is reduced by K^2.

3.3.2 Approximation for large exponents

As can be seen from equation (2.43)-(2.52) for large Fourier series values with exponents of very large order may have to be evaluated in order to solve the problem. However, while some of the exponents on their own might exceed certain limits, leading to numerical issues, a combination of several of the exponents might converge to a constant value for large exponents. The terms that enable such an approximation are in particular

$$\frac{1}{E_n(R_{in}, R_{out})} \approx -\left(\frac{R_{out}}{R_{in}}\right)^{-n} \tag{3.3}$$

$$\frac{1}{P_n(R_{in}, R_{out})} \approx \left(\frac{R_{out}}{R_{in}}\right)^{-n} \tag{3.4}$$

$$\frac{E_n(R_{in}, R_{out})}{P_n(R_{in}, R_{out})} = -\frac{E_n(R_{out}, R_{in})}{P_n(R_{out}, R_{in})} \approx -1 \tag{3.5}$$

where R_{in} and R_{out} are the inner and outer radius, respectively. In addition to circumventing the numerical limits that would be faced with large exponents, this simplification may also lead to significant reductions in computational effort, because large exponents in (3.3)-(3.5) can be replaced by their approximate values.

3.3.3 Order of the Fourier series

The solutions in the airgap and PM regions are computed with a finite number of Fourier series components. For the air regions II and III, and the PM regions I and IV the highest considered harmonic order N_{eff} may be required to be many times larger than the number of PM pole-pairs. Figs. 3.9 and 3.10 show the variations of the radial component of the flux density in the airgaps adjacent to the HS rotor and

stator PMs, respectively, with the circumferential position. It can be seen that when a large harmonic order ($N_{eff} = 300$) is considered a very good agreement exists between FE and analytical model. However, it can also be seen that an acceptable agreement can also exist for a much lower harmonic order $N_{eff} = (p_S + Q)/K = 28$. Furthermore, Figs. 3.11 and 3.12 show the harmonic spectra of the radial flux density in the airgaps adjacent to the HS rotor and stator PMs, respectively. It can be seen that the lower harmonics are already accurately predicted for $N_{eff} = (p_S + Q)/K = 28$.

Fig 3.13 shows the variation of the torque on the PP rotor with the position of the HS rotor. It can be seen that a good agreement exists between FE and analytical prediction for $N_{eff} = 300$, including the torque ripple. However, it can also be seen that a good agreement for the average torque exists for a much lower N_{eff}.

The circumferential span of a single PP and its adjacent air region is smaller than the pole pitch of the HS rotor and LS rotor PM pole pairs, and therefore a much smaller highest order of the Fourier series in the PP air regions N_Q may be sufficient, to achieve the required accuracy. Fig. 3.14 shows the variation of the average torque on the PP rotor with the highest order of harmonics considered in the PP air regions. It can be seen that the average torque converges quickly towards a constant value.

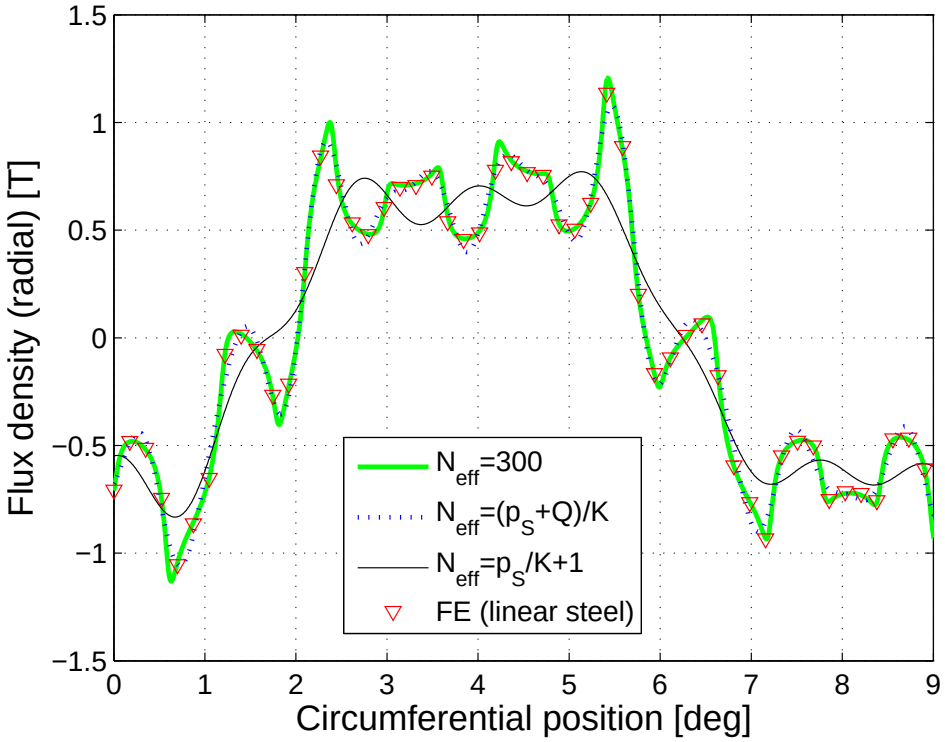

Fig. 3.9: Variation of radial flux density in the airgap adjacent to the HS rotor PMs for FE and analytical model. The number of Fourier series components for the PP air regions is set to $N_Q = 40$.

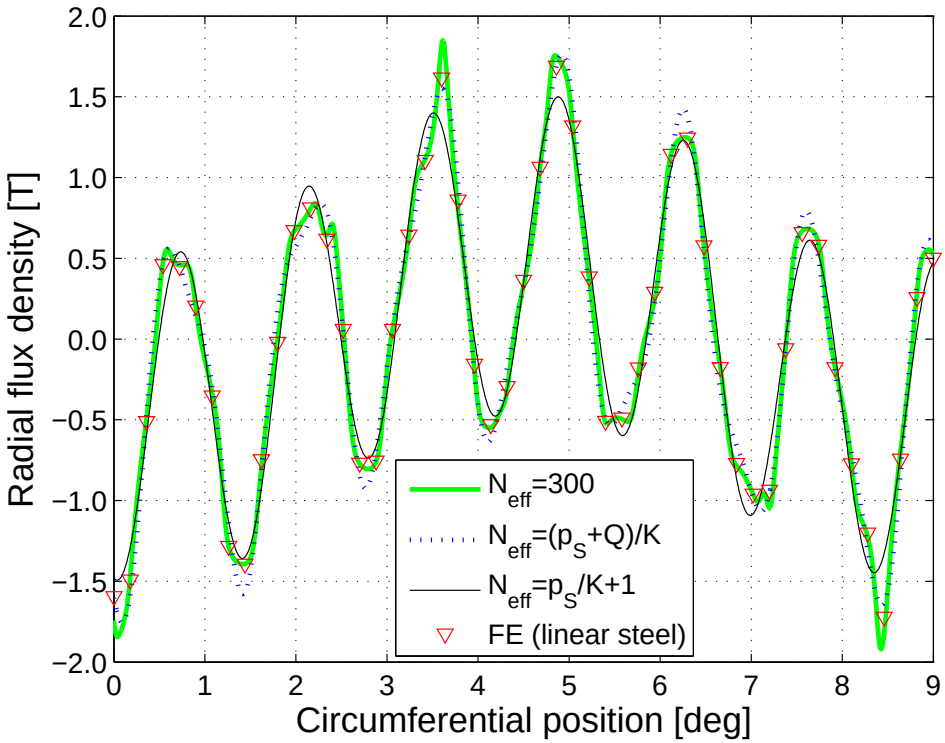

Fig. 3.10: Variation of radial flux density in the airgap adjacent to the stator PMs for FE and analytical model. The number of Fourier series components for the PP air regions is set to $N_Q = 40$.

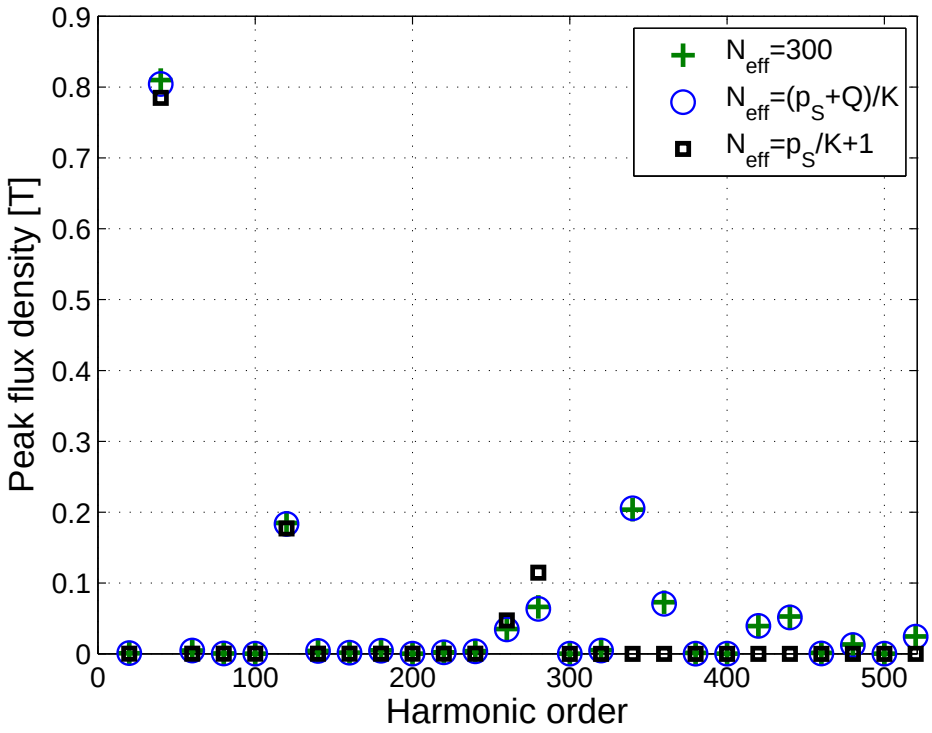

Fig. 3.11: Harmonic spectra of the radial flux density in the airgap adjacent to the HS rotor PMs for the analytical model. (The number of Fourier series components for the PP air regions is set to $N_Q = 40$.)

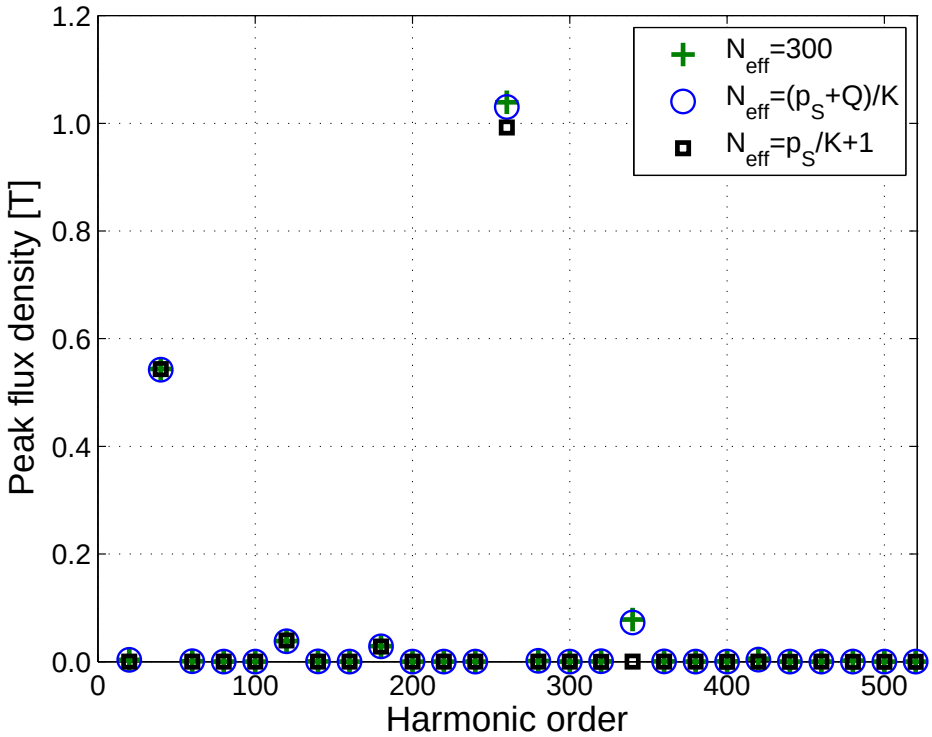

Fig. 3.12: Harmonic spectra of the radial flux density in the airgap adjacent to the stator PMs for the analytical model. (The number of Fourier series components for the PP air regions is set to $N_Q = 40$.)

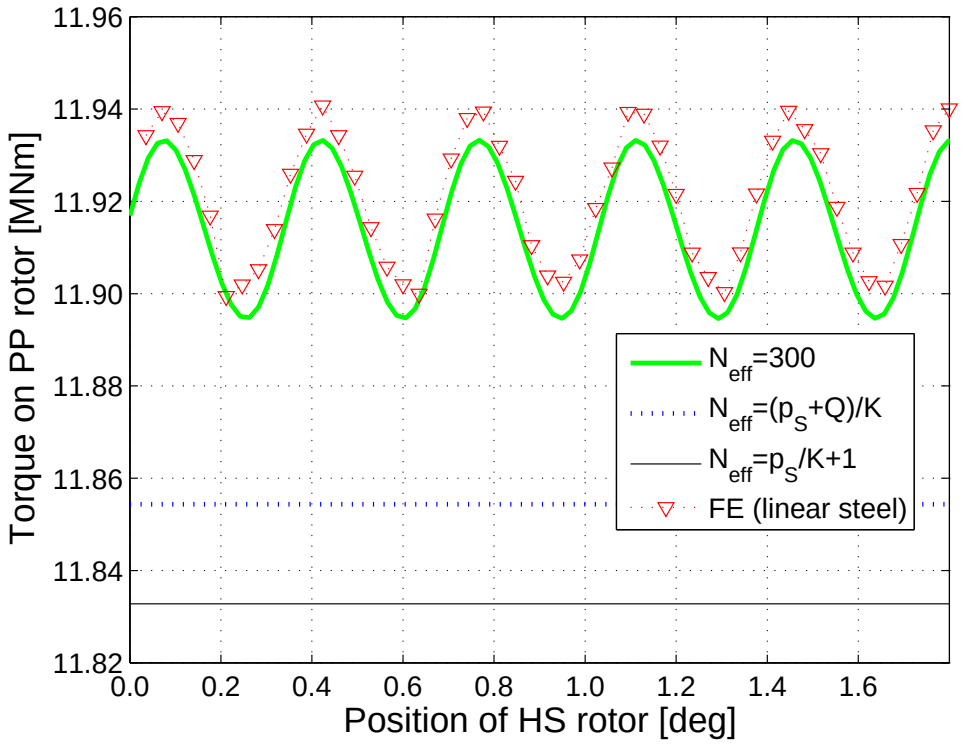

Fig. 3.13: Variation of torque on the PP rotor with the angular position of the HS rotor for FE and analytical model. The highest order harmonic considered in the PP air regions is $N_Q = 40$.

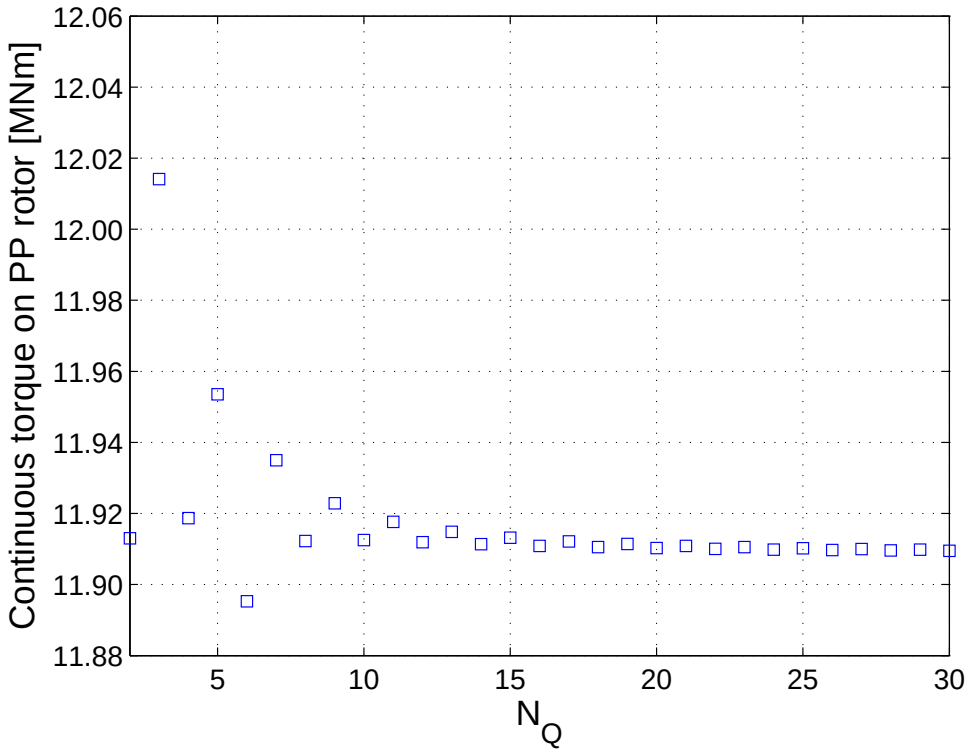

Fig. 3.14: Variation of average torque on the PP rotor with the highest order harmonic N_Q considered in the PP air regions. The highest order harmonic considered in the air and PM regions is set to $N_{eff} = 100$.

3.4 Effects of leading design parameters

In this section MGs with the same pullout torque as the MG in Table 3.1 are studied. The MG in Table 3.1 is thereby employed as a benchmark for the forthcoming simulation studies.

3.4.1 Effects of the airgap diameter and the aspect ratio

The torque capability of a MG may in general be affected by the selected airgap diameter. Fig. 3.15 shows the variation of the equivalent shear stress at pullout torque σ_{pull} with the diameter, when the dimensions of the PMs and PPs are scaled linearly with the airgap diameter. It can be seen that σ_{pull} increases significantly with the airgap diameter if the the airgap length is fixed. However, this may be mechanically be difficult to achieve and, therefore, in this work the airgap length is linearly scaled (0.1% of the airgap diameter). It can also be seen, as has been explained in section 2.4, if the airgap is scaled linearly σ_{pull} remains constant if

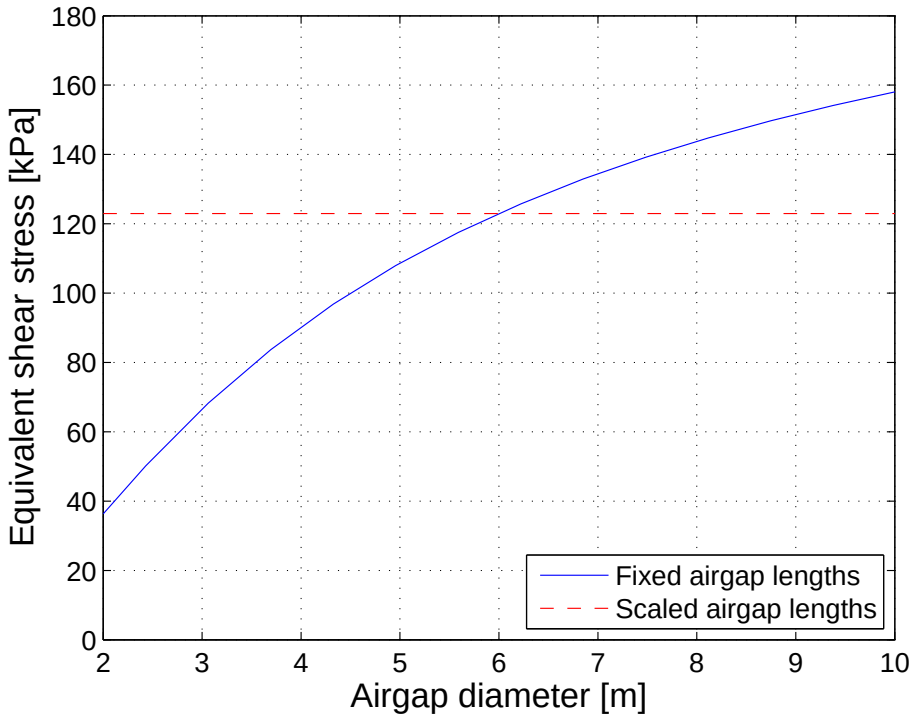

Fig. 3.15: Variation of σ_{pull} with the airgap diameter. Scaled airgap lengths have been selected to be 0.1% of the airgap diameter.

end effects are neglected. Furthermore, if the axial length is adjusted such that the MG produces the same torque, the PM mass and the laminated steel mass are also constant, see Section 2.4.

Although the shear stress would remain constant if only 2D effects are considered, end effects could considerably reduce the achievable torque in the MGs and PDDs. While similarly to other electrical machines *leakage* and *fringing* would contribute to the end effects, MG topologies would also be subject to an effect called *escaping* in which opposing magnetic poles would tend to force flux into the axial direction in the end regions. The impact of the end effects on the shear stress would, therefore, significantly depend on the aspect ratio

$$a = \frac{l_a}{D} \tag{3.6}$$

of the MG component. Intuitively the ratio of the pole-pitch of the HS rotor PMs to the active axial length

$$a_{pitch,l} = \frac{\left(\frac{\pi D}{2p_{HS}}\right)}{l_a} \tag{3.7}$$

would, therefore, also have an impact on the shear stress. For example, the MG in Table 3.1 $a_{pitch,l}$ is very small, less than 15%, while for other published work this may not be the case, where the ratio is closer to 100% [5, 56].

In order to illustrate the impact of the end effects on the pullout torque Fig. 3.16 shows the variation of σ_{pull} with the aspect ratio and where the radial dimensions are kept the same, while the axial length is varied. It can be seen that above an aspect ratio of about $a = 0.05$ the 3D FE calculated value of σ_{pull} is more than 85% of the analytically calculated value, and that for the aspect ratio of the MG in Table 3.1 the discrepancy is only about 5%. Furthermore, the introduction of flux barriers at specific axial locations along the PPs can further decrease the end effects.

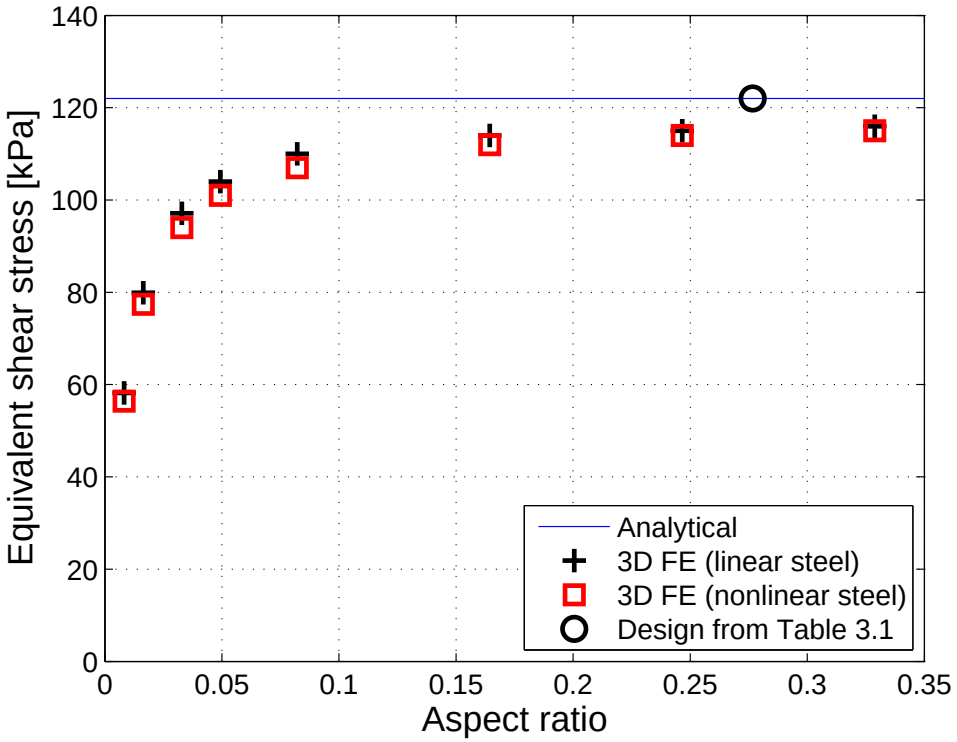

Fig. 3.16: Variation of σ_{pull} with the aspect ratio, where the FE analysis has been performed in 3D to account for end-effects.

3.4.2 Effects of the magnetisation distribution

Dependent on the application the MG may be required to achieve a certain torque density (shear stress) and/or active mass. In addition, the overall size of the MG also influences the structural costs of the MG. Fig. 3.18, therefore, shows the variation of the PM mass with the achievable σ_{pull} for a MG with the same airgap diameter, and the same number of pole-pairs on the HS rotor and stator as the MG in Table 3.1, and when the axial length is adjusted to match the pullout torque. Curves are shown for radial magnetisation (RM) with pole-arc to pole pitch ratios $a_m = 1$, and a discrete HM with 4 segments per pole-pair (dHM) on the HS rotor and the LS rotor/stator, see Fig. 3.17. Furthermore, a continuous HM (cHM) on both rotors, which may be approximated by selecting a high number of segments per pole-pair, has also been considered. It can be seen that a cHM on both rotors results in the highest σ_{pull}, however, in practice the realization of a cHM is difficult, albeit it could be approximated by employing a discrete HM with a large number of segments per

pole-pair. From Fig. 3.18 it can also be seen that replacing the RM on the stator by a dHM would also considerably increase the achievable σ_{pull}. Replacing the RM on the HS rotor by a dHM also results in designs with higher σ_{pull}, albeit this would only be apparent at a higher PM mass (more than 18 tons). It can also be seen that the design from Table 3.1 exhibits a smaller PM and total active mass, which is due to the lower pole-arc to pole pitch ratio of the PMs on the HS rotor. Finally it can be seen that a minimum PM mass can be achieved at about 13tons.

Fig. 3.19 shows the variation of the laminated steel mass with σ_{pull}. It can be seen that due to the self-shielding effect of the HM for most shear stresses a much smaller back-iron mass may be required for those designs that employ a HM. It can also be seen that in this particular case, replacing the dHM on HS rotor and stator by a cHM did not further decrease the amount of required laminated steel.

Fig. 3.20 shows the variation of the total active mass with σ_{pull}. It can be seen that the total active mass is significantly reduced for the designs, employing a HM.

From Fig. 3.18 it can also be seen that for a large range of σ_{pull} a RM on the HS rotor might achieve a similar torque transmission as a dHM, whilst significantly reducing the PM mass. This type of design has, therefore, been taken forward to be studied in more detail. Since the PM material near the interface of two pole-pairs may not contribute significantly towards the produced torque the PM material at these locations may be replaced by non-magnetic material leading to a reduced HS rotor pole-arc to pole-pitch ratio a_{HS}. Fig. 3.21 shows the variation of the PM mass with σ_{pull} for several HS rotor pole-arc to pole-pitch ratios, where a RM on the HS rotor and a dHM on the stator is employed. It can be seen that for most σ_{pull} a value of about $a_{HS} \approx 0.8$ achieves the lowest PM mass.

For $a_{HS} = 0.8$ Fig. 3.22 shows the variations of the laminated steel mass with σ_{pull} for the various rotors. It can be seen that the stator, HS rotor, and PP rotor laminated steel mass decrease with increasing shear stress.

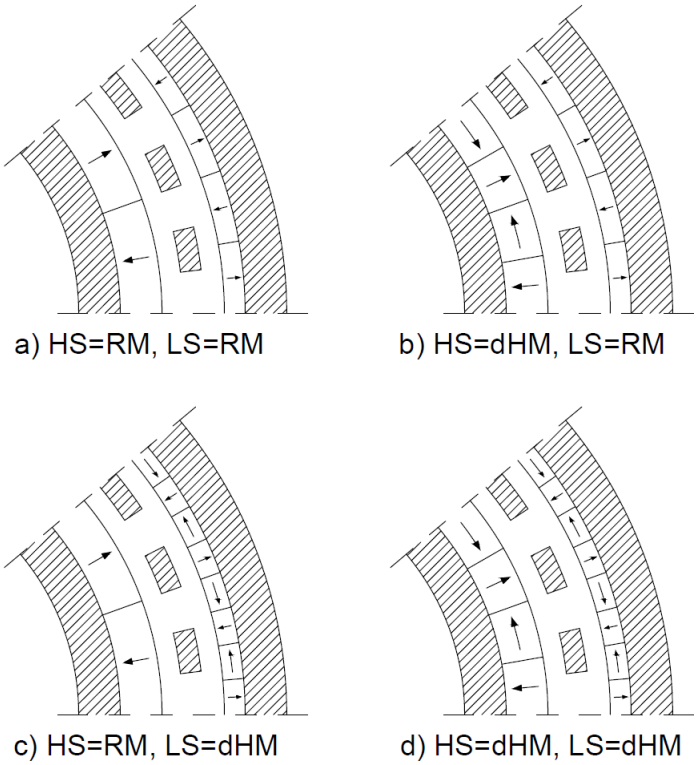

Fig. 3.17: Cross sections for MGs with a RM and a dHM on the HS rotor and the LS rotor/stator.

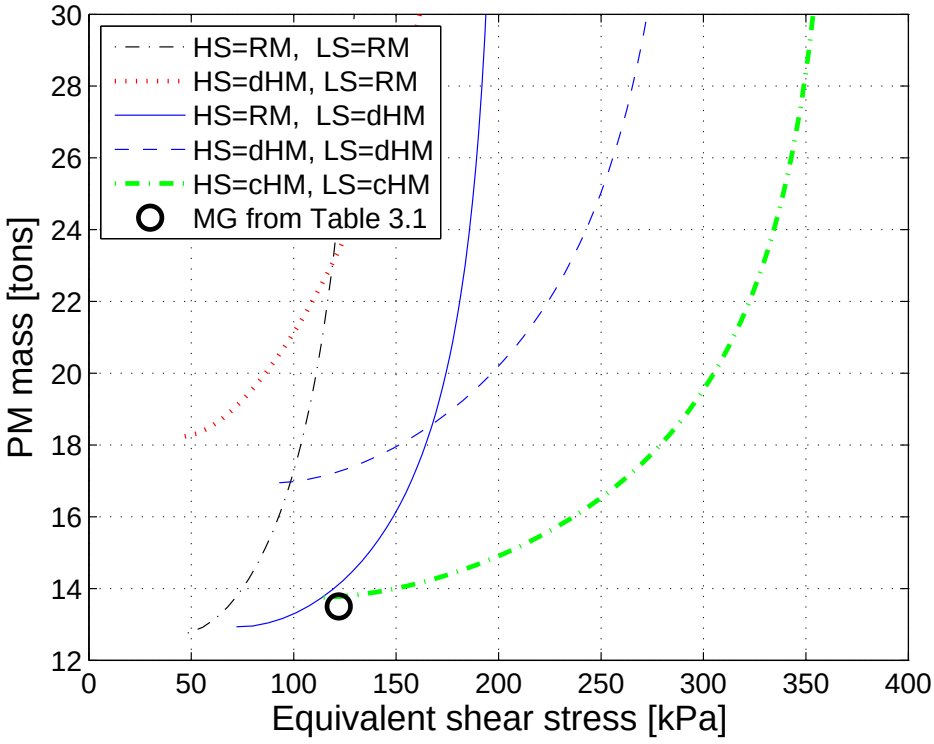

Fig. 3.18: Variation of PM mass with σ_{pull}.

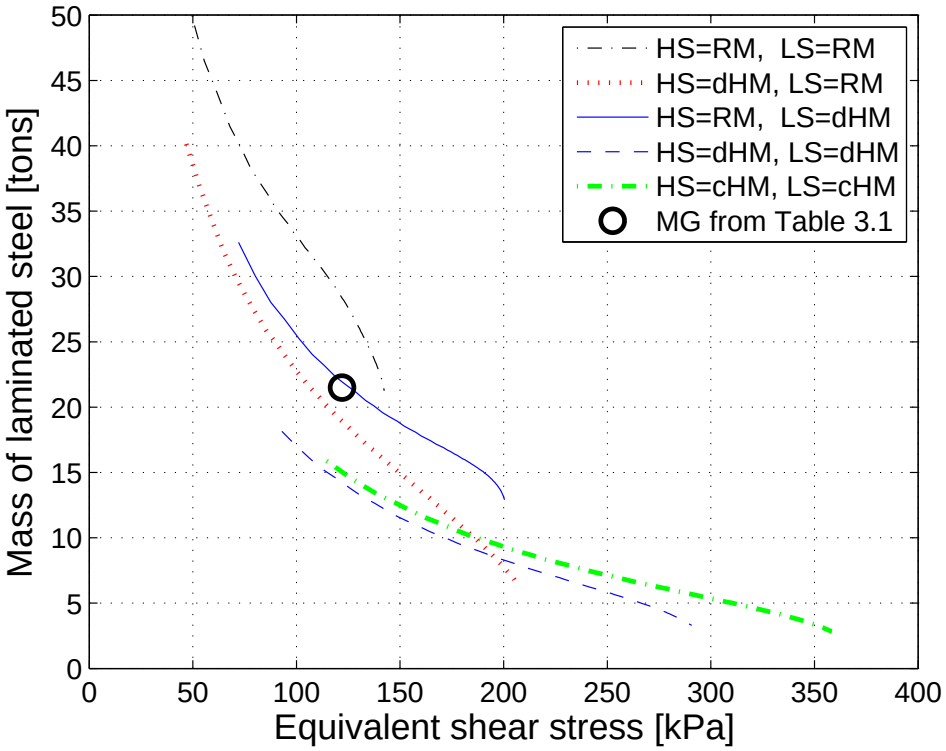

Fig. 3.19: Variation of laminated steel mass with σ_{pull}.

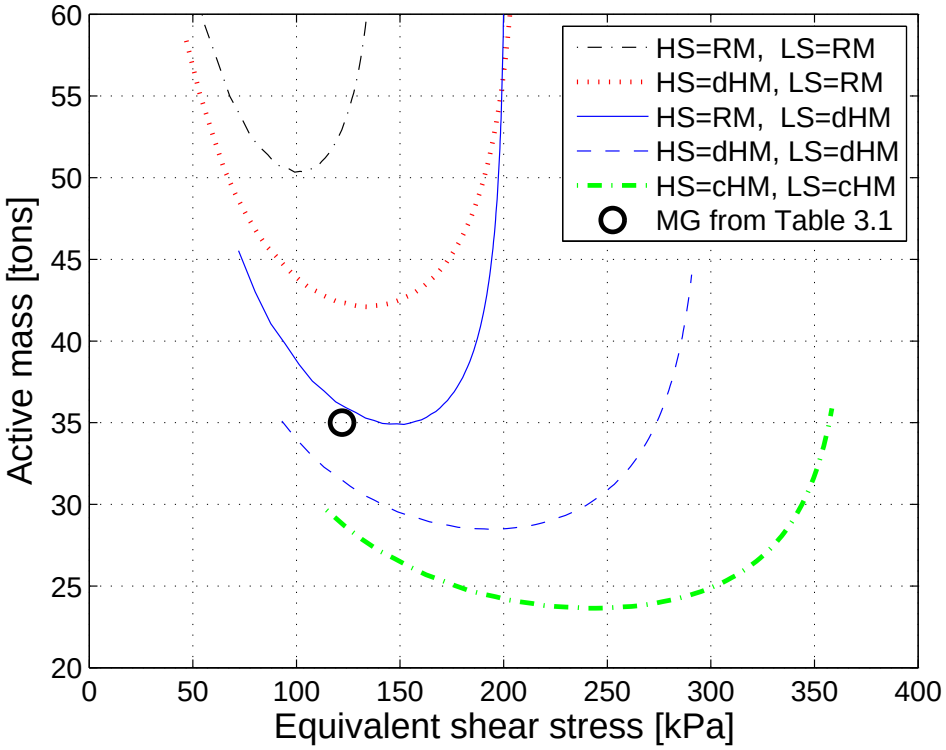

Fig. 3.20: Variation of total active mass with σ_{pull}.

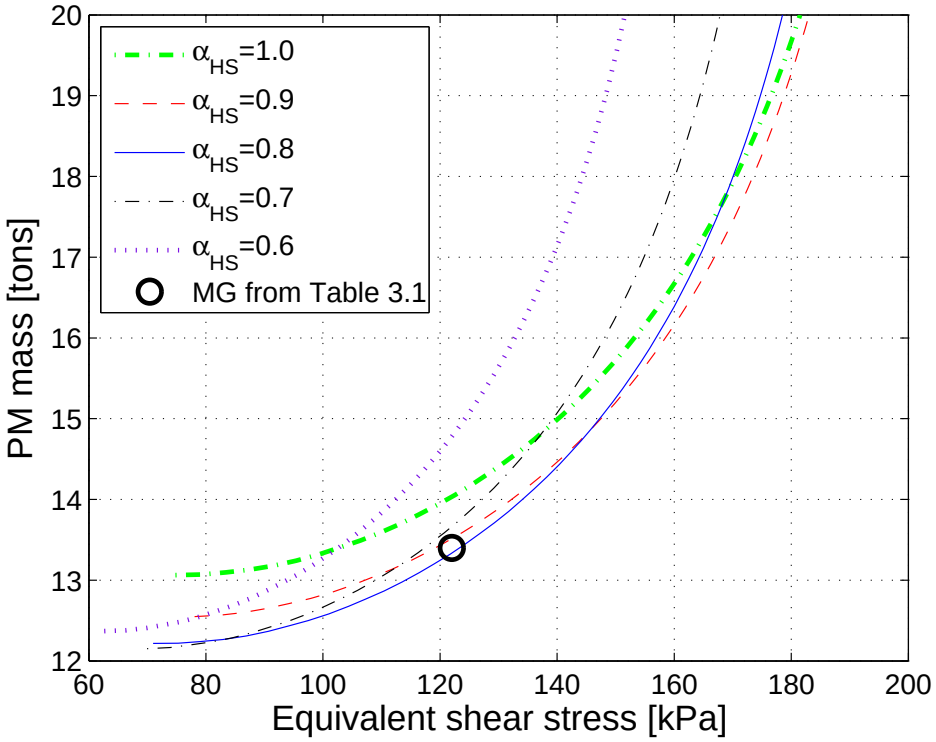

Fig. 3.21: Variation of PM mass with σ_{pull} for several HS rotor pole-arc to pole-pitch ratios a_{HS}.

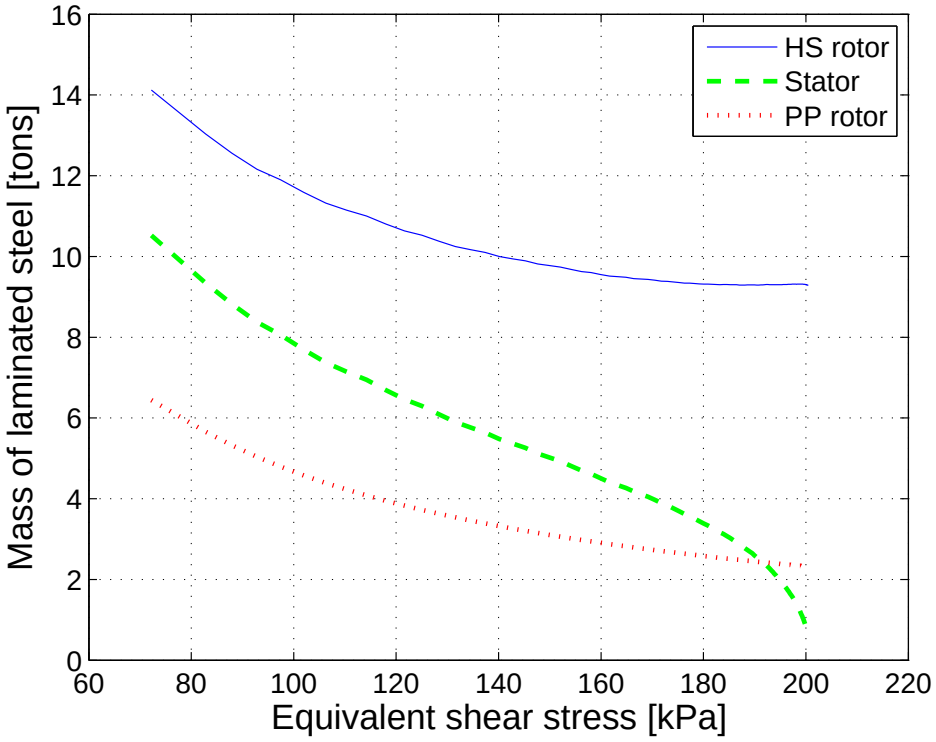

Fig. 3.22: Variations of the laminated steel mass for the various rotors with σ_{pull}.

3.4.3 Effects of the pole-piece dimensions

Fig. 3.23 shows the variation of σ_{pull} with the radial PP thickness w_{PP}. It can be seen that a maximum exists and that the shear stress drops significantly towards small values of w_{PP}. Furthermore, as can be seen by comparing the analysis for steel with linear and nonlinear characteristics saturation effects would also significantly reduce the torque transmission capability for small values of w_{PP}.

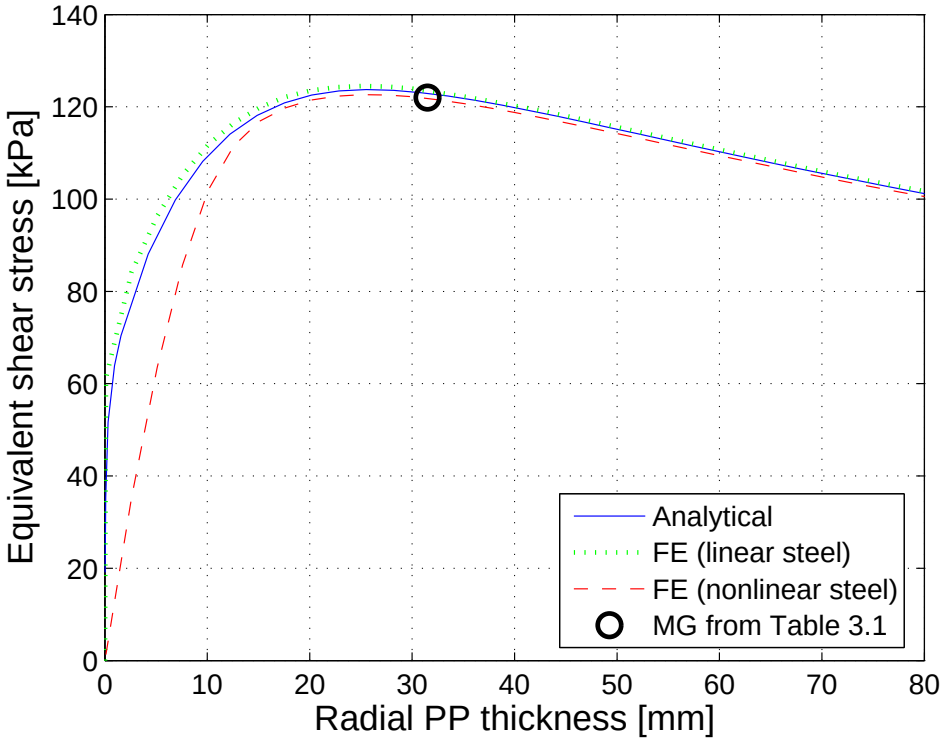

Fig. 3.23: Variation of σ_{pull} with the radial PP thickness w_{PP} for the analytical model and for FE.

3.4.4 Effects of the number of identical sections

As has been mentioned in section 3.3 large MGs may be constructed from several magnetically identical sections. For the forthcoming analysis the gear ratio, the air-gap lengths, the outer airgap diameter and the aspect ratio of the PP is kept constant and the radial PP thickness is selected as

$$w_{PP} = \frac{\pi R_{PPi}}{Q} \tag{3.8}$$

Fig. 3.24 shows the variation of σ_{pull} with the number of magnetically identical setions K, where the radial dimensions of the HS rotor and stator PMs are fixed. It can be seen that an optimum number of sections (pole pairs) exists, for which σ_{pull} is maximum and that for small numbers of sections the shear stress increases almost linearly.

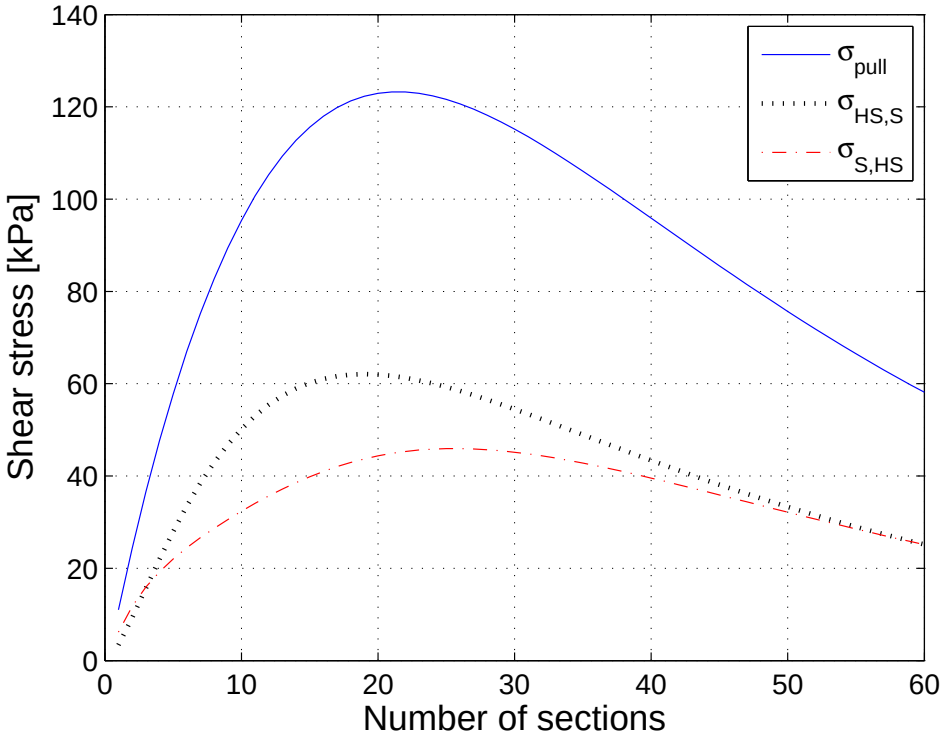

Fig. 3.24: Variation of shear stress with the number of magnetically identical sections K.

In order to analyse the effect further, it is useful to separate the flux density in the outer airgap into the flux density produced by the HS rotor PMs and the stator PMs. In particular, the radial component of the flux density in the outer airgap at the radius R_o can be expressed as a superposition of the radial component flux density due to the HS rotor PMs $B_{rad,III,HS}$ and the radial component flux density due to the stator PMs $B_{rad,III,S}$ as

$$B_{rad,III}(R_o,\theta) = B_{rad,III,HS}(R_o,\theta) + B_{rad,III,S}(R_o,\theta) \tag{3.9}$$

Similarly the circumferential component can be expressed as

$$B_{\theta,III}(R_o,\theta) = B_{\theta,III,HS}(R_o,\theta) + B_{\theta,III,S}(R_o,\theta) \tag{3.10}$$

where $B_{\theta,III,HS}$ and $B_{\theta,III,S}$ are the circumferential components of the flux density due to the HS rotor PMs and the stator PMs, respectively. The torque in the outer airgap (2.64) can, therefore, be expressed as

$$\begin{aligned} T_o &= \frac{l_a R_o^2}{\mu_0}\int_0^{2\pi} B_{rad,III,HS}(R_o,\theta)B_{\theta,III,HS}(R_o,\theta)d\theta \\ &+\frac{l_a R_o^2}{\mu_0}\int_0^{2\pi} B_{rad,III,S}(R_o,\theta)B_{\theta,III,S}(R_o,\theta)d\theta \\ &+\frac{l_a R_o^2}{\mu_0}\int_0^{2\pi} B_{rad,III,HS}(R_o,\theta)B_{\theta,III,S}(R_o,\theta)d\theta \\ &+\frac{l_a R_o^2}{\mu_0}\int_0^{2\pi} B_{rad,III,S}(R_o,\theta)B_{\theta,III,HS}(R_o,\theta)d\theta \end{aligned} \tag{3.11}$$

Since torque from the interactions from the radial and circumferential components of flux density from the same source is zero the first and second term in (3.11) are zero. The shear stress in the outer airgap can, therefore, be expressed as

$$\sigma_o = \sigma_{HS,S} + \sigma_{S,HS} \tag{3.12}$$

where

$$\sigma_{HS,S} = \frac{1}{2\pi\mu_0}\int_0^{2\pi} B_{rad,III,HS}(R_o,\theta)B_{\theta,III,S}(R_o,\theta)d\theta \tag{3.13}$$

$$\sigma_{S,HS} = \frac{1}{2\pi\mu_0}\int_0^{2\pi} B_{rad,III,S}(R_o,\theta)B_{\theta,III,HS}(R_o,\theta)d\theta \tag{3.14}$$

Using (3.12) and (2.73) the equivalent shear stress may also be expressed as

$$\sigma = \frac{G}{G-1}(\sigma_{HS,S} + \sigma_{S,HS}) \tag{3.15}$$

From Fig. 3.24 it can be seen that $\sigma_{HS,S}$ and $\sigma_{S,HS}$ also exhibit maxima, albeit at different numbers of sections (pole pairs).

Since the shear stress components $\sigma_{HS,S}$ and $\sigma_{S,HS}$ are mainly produced by the p_S-th harmonics, Fig. 3.25 shows the variation of the peak flux densities of the p_S-th harmonics of the flux density components in the outer airgap with K. It can be seen that both circumferential components of the flux density increase almost linearly from zero, while the radial components of the flux density converge towards

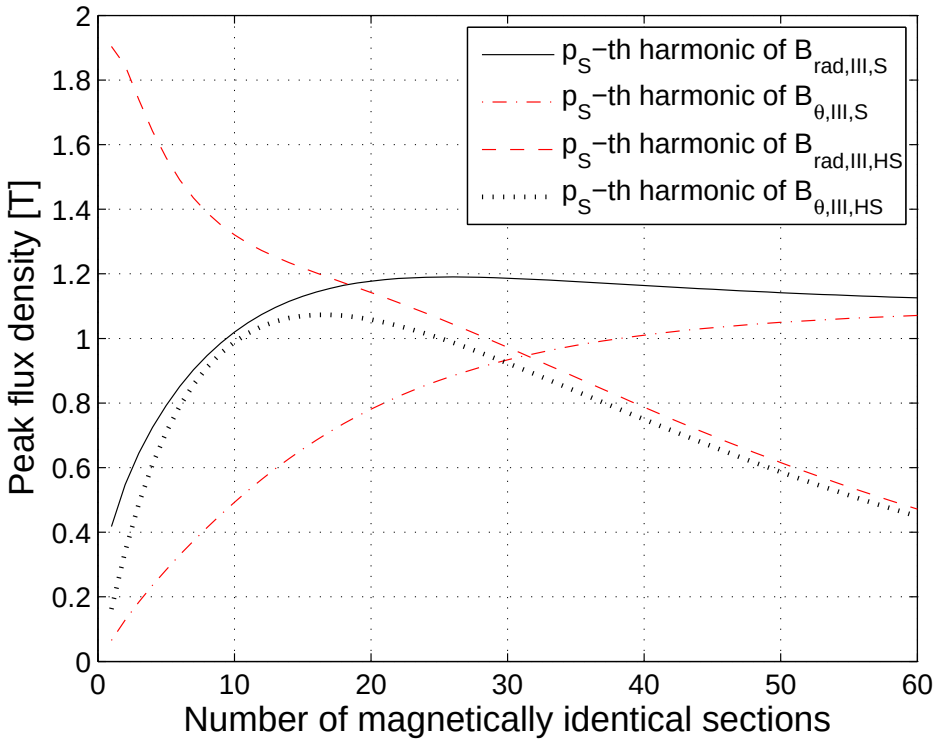

Fig. 3.25: Variation of peak flux density with the number of magnetically identical sections K.

a constant value towards small values of K. Hence, the initial increase in shear stress could be largely determined by the linear increase of the circumferential component of the flux density. It can also be seen that for large values of K the p_S-th harmonic of the flux density due to the interaction of the HS rotor PMs with the PPs can decrease significantly.

Fig. 3.26 shows the variation of the PM mass with the maximum achievable σ_{pull} and K. It can be seen that for a given PM mass a number of sections exists, for which the σ_{pull} is maximum.

Fig 3.27 shows the variation of the total active mass, which is the PM mass and the mass of laminated steel, with the maximum achievable σ_{pull} and with the number of sections K. Similarly to Fig. 3.26 a maximum shear stress exists for a given total active mass, albeit at a different K.

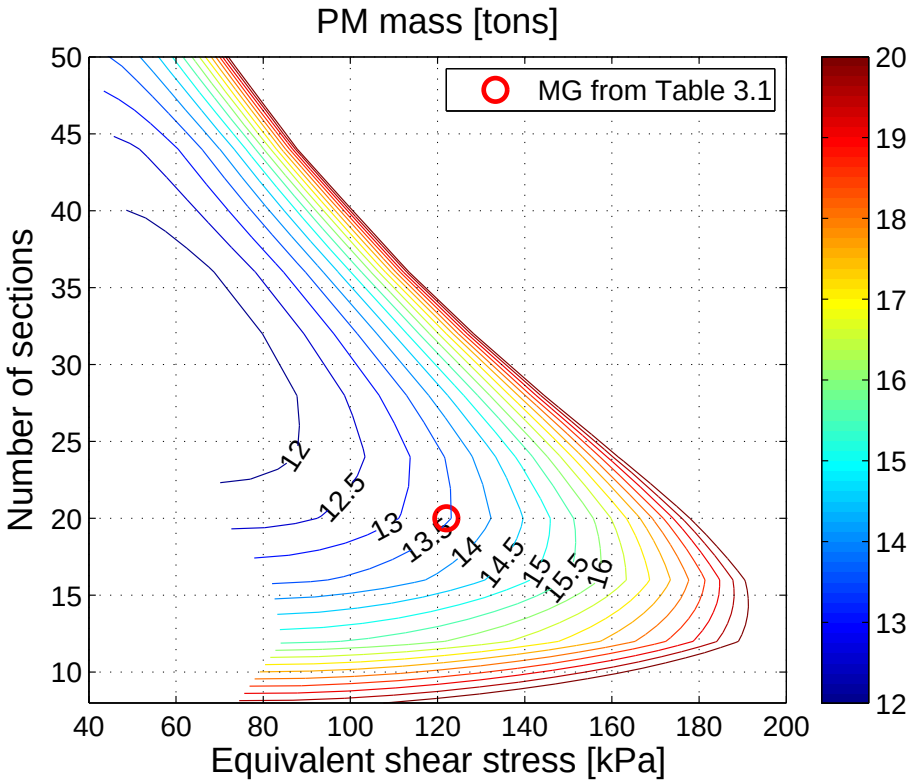

Fig. 3.26: Variation of PM mass with the maximum achievable σ_{pull} and the number of sections K.

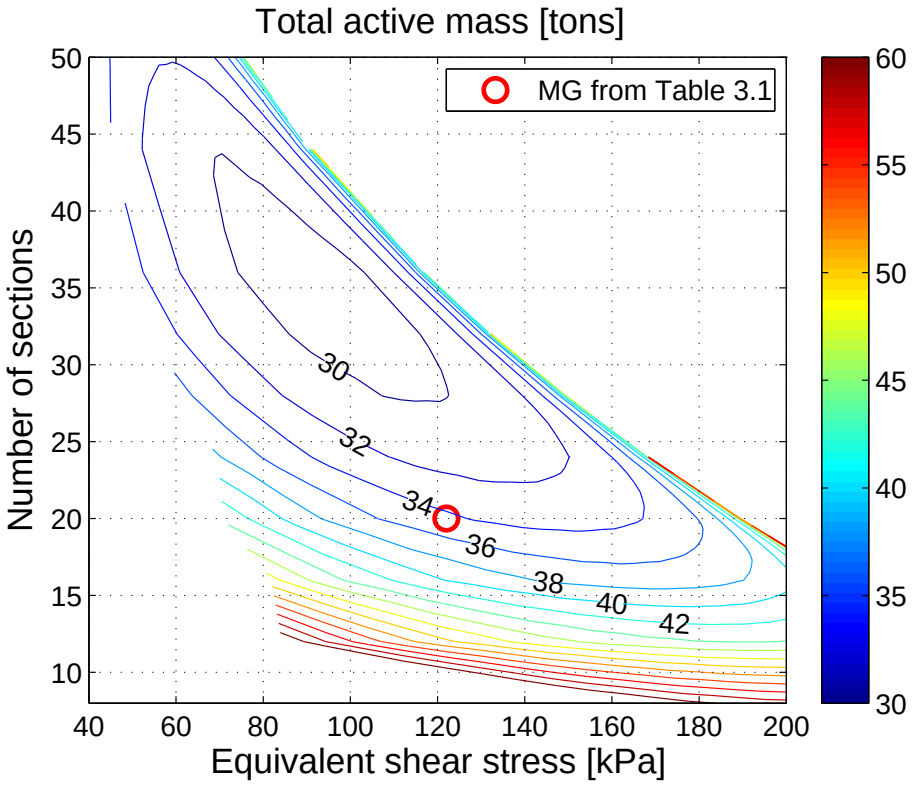

Fig. 3.27: Variation of the total active mass with the the maximum achievable σ_{pull} and the number of sections K.

3.4.5 Effects of the gear ratio

In general the choice of the gear ratio G has a significant impact on the overall performance of the system into which the MG is incorporated. While a MG with a higher gear ratio has the potential to reduce the masses of the generator that the MG is coupled to, it also might require increased active masses compared to MGs with a lower gear ratio. Fig. 3.28 shows the variation of the minimum PM mass with the maximum achievable σ_{pull} if all number of sections are considered. It can be seen that a higher gear ratio may require a higher PM mass to achieve a similar σ_{pull}.

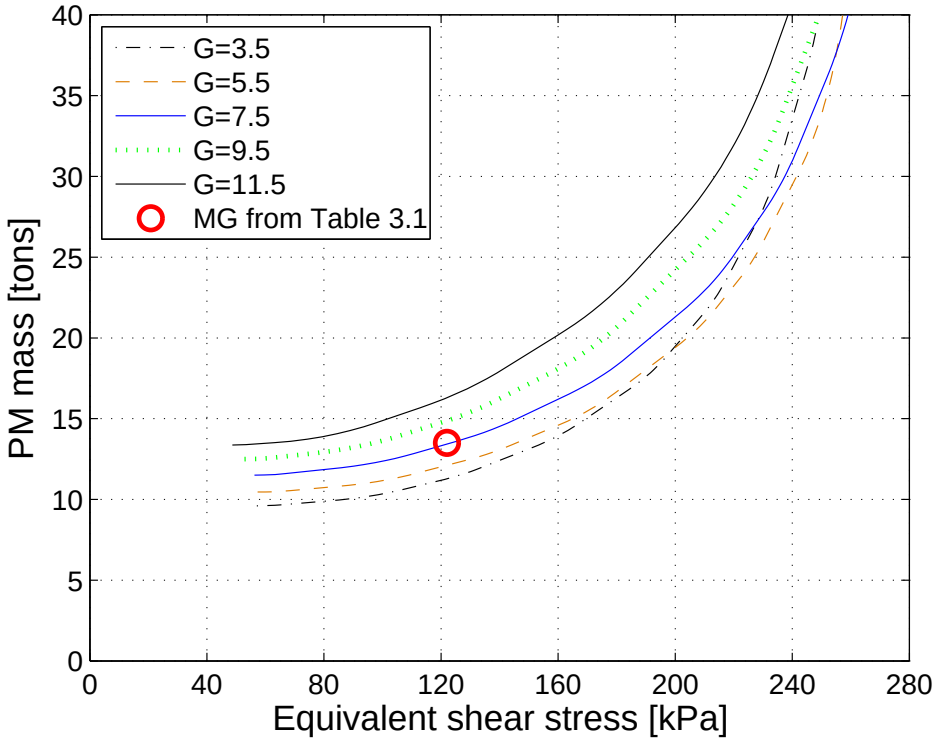

Fig. 3.28: Variation of the minimum PM mass with the the maximum achievable σ_{pull} if all numbers of sections are considered, for several gear ratios G.

Fig. 3.29 shows the variation of the active mass with the maximum achievable σ_{pull} for the designs shown in Fig. 3.28. Again it can be seen that higher gear ratios may require a larger amount of active mass to achieve a similar σ_{pull}.

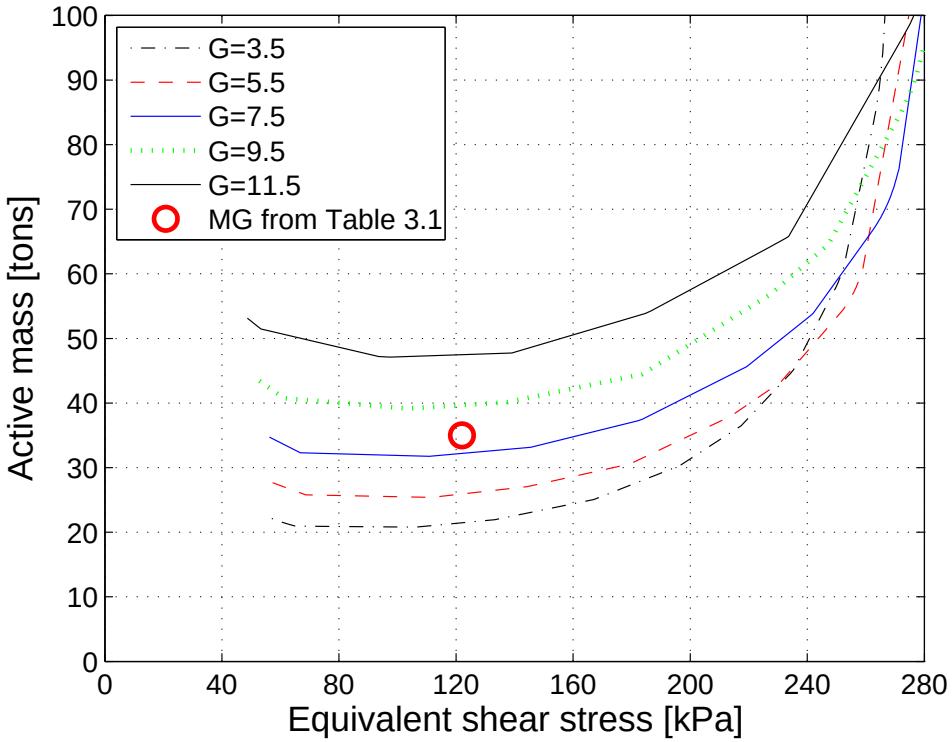

Fig. 3.29: Variation of the active mass with the the maximum achievable σ_{pull} if all numbers of sections are considered, for several gear ratios G.

3.5 Conclusions

The analytical model developed in Chapter 2 has been employed for the optimisation of a large MG with a pullout torque of $11.9MNm$. The MG has been optimised to achieve a sufficiently high shear stress and gear ratio, whilst minimizing the required PM mass and total active mass. The optimised design has a PM mass of $13.5tons$ and a total active mass of $35tons$. The MG is employed for the comparison of the analytical model with 2D FE studies and a good agreement is found for the flux density distributions and the torques including the torque ripple. It is shown that since large MGs are likely to be constructed using a set of circumferentially identical sections, applying symmetry conditions can result in significant computational simplifications. Furthermore, although a high order of harmonics may be required in order to represent the torque ripple and the flux density distribution sufficiently well, the average torque can be accurately predicted with a significantly

lower harmonic order. The analytical model is also employed to discuss the effects of the leading design parameters on the main performance indicators, such as PM and laminated steel mass, etc. It is shown that the equivalent shear stress remains constant when scaling the radii of the MG when end effects are neglected, and that end effects only reduce the equivalent shear stress considerably for small aspect ratios. Furthermore, adopting a discrete HM distribution, in particular on the stator, results in significant improvements in torque transmission capability without significantly increasing the required PM mass. It is also shown that the equivalent shear stress, the number of circumferential sections, and the gear ratio may have a significant impact on the active masses of the MG.

Chapter 4

Analytical model for the Pseudo Direct Drive

The 2D analytical models developed in Chapter 2 are extended to account for the effects of stator windings in order to enable the analysis of PDDs. Since the iron loss calculation requires the accurate prediction of the flux density distributions in the iron regions, analytical models are also developed for the prediction of the average flux density distributions in the stator core and the flux density distributions in the PPs. Furthermore, the calculation of the losses in the PDD is given in detail.

4.1 Principal of operation

The PDD introduced in [11] is a magnetically and mechanically integrated brushless PM machine with an MG. The PPs in an MG modulate the field produced by the HS rotor, resulting in a synchronous space harmonic having the same number of poles as the HS rotor, and asynchronous harmonics. In an MG the latter interacts with the PMs on the LS rotor/stator to produce torque, while the synchronous harmonic mainly produces losses. However, in the PDD, a winding having the same number of poles as the synchronous harmonic/HS rotor is introduced on the stator to produce torque on the HS rotor, which is then transmitted to the PP rotor through the interaction between the asynchronous harmonic and the PMs on the stator. This

results in a highly efficient utilisation of the HS rotor PM field and enables significantly higher torque densities through the gearing effect.

The PDD is operated at a torque T_E equal or lower than $\frac{T_{pull}}{G}$. In a brushless AC mode operation the electromagnetic torque produced by the interaction of stator winding and the HS rotor is given by [11]

$$T_E = \frac{2\pi}{\sqrt{2}} k_w R_S^2 l_a Q_{rms} B_{p_{HS},S} \tag{4.1}$$

where k_w is the winding factor, $B_{p_{HS},S}$ is the peak value of the p_{HS}-th harmonic of the radial flux density produced by the HS rotor PMs at the stator bore radius R_S.

$$Q_{rms} = \frac{3 p_{HS} I_{rms}}{2\pi R_S} \tag{4.2}$$

is the current loading, where I_{rms} is the rms current in a coil. A concentrated winding is selected, for which the winding factor is $k_w = \frac{\sqrt{3}}{2}$. For a continuous speed operation the average torque on the HS rotor has to be zero, i.e. the average torque produced by the interaction between HS rotor and stator PMs and the average torque produced by the interaction between HS rotor PMs and the field produced by the stator windings has to cancel. In order to match T_E with the torque on the HS rotor produced by the interaction with the stator rotor PMs, the PP rotor position is shifted from the maximum torque position by the angle

$$\Theta_{\Delta PP} = \frac{1}{Q} \arccos\left(\frac{T_E G}{T_{pull}}\right) = \frac{1}{Q} \arccos\left(\frac{T_{PP,R}}{T_{pull}} \frac{I_{rms}}{I_{rms,R}}\right) \tag{4.3}$$

where Q is the number of PPs, $T_{PP,R}$ is the rated torque on the PP rotor, and $I_{rms,R}$ is the rated current in a coil. Furthermore, T_E is related to the power by

$$P_E = T_E \omega_{PP} G \tag{4.4}$$

where ω_{PP} is the rotational speed of the PP rotor. Using (4.4) in (4.1) the rms electric loading is given by

$$Q_{rms} = \frac{\sqrt{2}}{2\pi} \frac{1}{k_w R_S^2 l_a B_{p_{HS},S}} \frac{P_E}{\omega_{PP} G} = \frac{\sqrt{2}}{2\pi} \frac{1}{k_w R_S^2 l_a B_{p_{HS},S}} T_E \tag{4.5}$$

For completeness and in order to allow for a more detailed comparison with a coil excited PDD in Chapter 6 the equations which govern the motion of the HS rotor,

the PP rotor, and the turbine are given. They are in particular

$$J_{HS}\frac{d^2\Theta_{HS}}{dt^2} = \frac{p_{HS}}{Q}T_{pull}\sin(Q\Theta_{PP} - p_{HS}\Theta_{HS}) - T_E(I_{rms}) \quad (4.6)$$

$$J_{PP}\frac{d^2\Theta_{PP}}{dt^2} = k_T(\Theta_T - \Theta_{PP}) - T_{pull}\sin(Q\Theta_{PP} - p_{HS}\Theta_{HS}) \quad (4.7)$$

$$J_T\frac{d^2\Theta_T}{dt^2} = T_W - k_T(\Theta_T - \Theta_{PP}) \quad (4.8)$$

where J_{HS} is the inertia of the HS rotor, J_{PP} is the inertia of the PP rotor, and J_T is the inertia of the turbine shaft and the components connected to it, such as the turbine. Θ_{PP} is the PP rotor angle, Θ_{HS} is the HS rotor angle, Θ_T is the angle of the turbine shaft, T_W is the load torque, and k_T is the stiffness of the shaft connecting the turbine to the PP rotor. Fig. 4.1 shows the torsional model of a wind turbine drive train employing a PM excited PDD. It can be seen that the MG element of the PDD can be replaced by two ideal gears and a 1-to-1 magnetic coupling, having a stiffness k_G given by

$$k_G = \frac{T_{pull}}{Q}\cos(Q\Theta_{PP} - p_{HS}\Theta_{HS}) = \frac{T_{pull}}{Q}\cos(\Theta_E) \quad (4.9)$$

where Θ_E is referred to as the load angle.

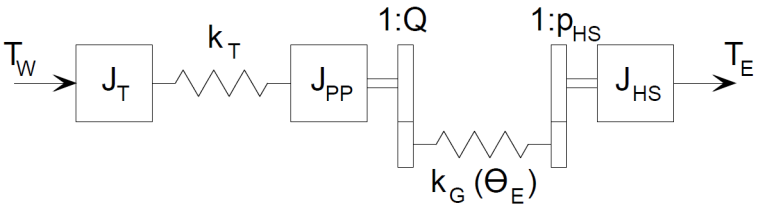

Fig. 4.1: Fig. 3. 3-inertia torsional model of the PDD.

4.2 Flux density in the airgap and PM regions

Fig. 4.2 shows the schematic of a PDD and its various regions employed for the development of the analytical models. In addition to the models described in chapter 2 the models are extended to take into account of the effects of the stator windings on the magnetic field distributions in the air and PM regions. The windings are represented by a current sheet at the stator iron bore radius R_S [44, 45]. Furthermore, since the iron loss prediction requires the accurate prediction of the flux density dis-

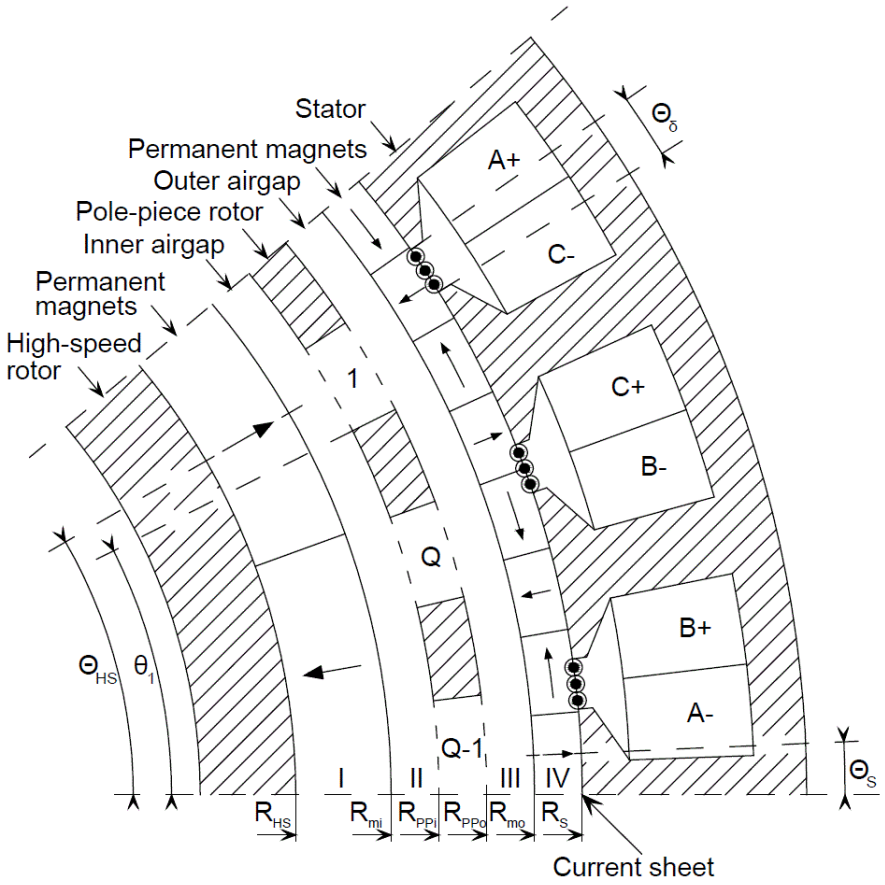

Fig. 4.2: Geometry for a PDD section with a periodic symmetry of 40 degrees. A current sheet is introduced at the stator bore radius R_S.

tributions in the iron regions, analytical models are also developed for the prediction of the flux density distribution in the stator core and the PPs.

At the stator bore radius R_S, the circumferential component of the magnetic field equals the current sheet, thus

$$H_{\theta,IV}(R_S,\theta) = \frac{B_{\theta,IV}(R_S,\theta)}{\mu_0\mu_r} - \frac{M_{\theta,IV}(\theta)}{\mu_r} = -j_S(\theta) \tag{4.10}$$

where $H_{\theta,IV}$ is the circumferential component of the magnetic field, and j_S is the current sheet representing the stator windings. The current sheet is expressed in terms of a Fourier series by

$$j_S(\theta) = \sum_{n=1}^{\infty} \begin{pmatrix} j_{A,n} \\ j_{C,n} \end{pmatrix} \cdot \begin{pmatrix} \cos(n\theta) \\ \sin(n\theta) \end{pmatrix} \tag{4.11}$$

The solution in region IV (2.28) is extended by a term $A_{C,IV}$ which takes into account of the current sheet:

$$A_{IV}(\theta,r) = A_{G,IV}(r,\theta) + A_{P,IV}(r,\theta) + A_{C,IV}(r,\theta) \tag{4.12}$$

Furthermore $A_{C,IV}$ is given by

$$A_{C,IV}(r,\theta) = \mu_0\mu_r \sum_{n=1}^{\infty} \frac{R_S}{n} \frac{E_n(r,R_{mo})}{P_n(R_S,R_{mo})} \begin{pmatrix} j_{A,n} \\ j_{C,n} \end{pmatrix} \cdot \begin{pmatrix} \cos(n\theta) \\ \sin(n\theta) \end{pmatrix} \tag{4.13}$$

The form of the solutions in regions I, II, III and the PP air regions i,..,Q are the same as in Section (2.2), however the coefficients are different due to the addition of the current sheet. The relations between the coefficients of regions III and IV, given in equations (2.45) and (2.46) are then given by

$$\mu_r \begin{pmatrix} B_{III,n} \\ D_{III,n} \end{pmatrix} = \begin{pmatrix} A_{IV,n} \\ C_{IV,n} \end{pmatrix} \frac{E_n(R_{mo},R_S)}{P_n(R_{mo},R_S)} + B_r \begin{pmatrix} g_{c,IV,n} + X'_{A,IV,n}(R_{mo}) \\ g_{s,IV,n} + X'_{C,IV,n}(R_{mo}) \end{pmatrix} + \mu_0\mu_r \frac{R_S}{R_{mo}} \frac{2}{P_n(R_{mo},R_S)} \begin{pmatrix} j_{A,n} \\ j_{C,n} \end{pmatrix} \tag{4.14}$$

$$\begin{pmatrix} A_{IV,n} \\ C_{IV,n} \end{pmatrix} = \begin{pmatrix} B_{III,n} \\ D_{III,n} \end{pmatrix} \frac{P_n(R_{mo},R_{PPo})}{E_n(R_{mo},R_{PPo})} + \begin{pmatrix} A_{III,n} \\ C_{III,n} \end{pmatrix} \frac{2}{E_n(R_{PPo},R_{mo})} \tag{4.15}$$

4.3 Flux density waveforms in the stator iron

The solution for the flux density distribution at the stator bore radius R_S, obtained from the analysis in section 4.2, is employed to predict the average flux densities in the stator regions, viz. tooth tip, tooth body and back-iron, as shown in Fig 4.3. The average flux density in each of the segments shown in Fig 4.3 is assumed by adding the flux entering/exciting the segment and dividing by the maximum cross section of the segment perpendicular to the flux paths. Since the value of the average flux density varies along the radial direction of a tooth, especially on load, each tooth is split into N layers of radial thickness Δh. For the flux across the slot and the slot opening equivalent magnetic circuits are assumed in regions R_1, R_2 and for each layer of region R_3, where the permeability of iron is assumed to be infinite. For example for a layer in region $R_3$the magnetomotive force according to Ampere's

law is equal to the current in the surrounded region, hence

$$I_{Sl,m}(h) = \oint Hdl = H_{R3}(h)w_2 \tag{4.16}$$

where h is the radial width of the surrounded coil material at that particular layer, $I_{Sl,m}(h)$ is the current going through the surrounded coil material, w_2 is the average slot width and $H_{R3}(h)$ is the circumferential magnetic field strength in the slot at h. The flux through each layer in region R_3 is then given by

$$\Phi_{R3,m}(h) = \mu_0 \frac{I_{Sl,m}}{w_2} \frac{h}{d_3} \Delta h l_a \tag{4.17}$$

where $I_{Sl,m}$ is the total current in the m–th slot, and d_3 is the radial width of the slot.

The magnetic field strength in region R_2 is approximated by averaging the magnetic field in region R_1 and the magnetic field calculated at the bottom of the coil slot. The flux across region R_2 is then given by

$$\Phi_{R2,m} = \mu_0 \frac{I_{Sl,m}}{w_1} \frac{1}{2} \left(1 + \frac{w_1}{w_2}\right) d_2 l_a \tag{4.18}$$

where w_1 is the slot opening, and d_2 is the radial width of the shoe slope, Fig 4.3. The flux across R_1 is given by

$$\Phi_{R1,m} = \mu_0 \frac{I_{Sl,m}}{w_1} d_1 l_a \tag{4.19}$$

where d_1 is the radial width of the shoe tip, Fig 4.3. The flux in the back-iron is given by [57]

$$\Phi_{B,m} = \frac{1}{M} \begin{cases} -\sum_{k=1}^{M-1} (N-k)\Phi_{1+k} & m = 1 \\ \sum_{k=1}^{M-1} (M-k)\Phi_{N-k+1} & m = M \\ \sum_{k=1}^{m-1} (m-k)\Phi_{m-k+1} - \sum_{k=1}^{M-m} (M-m-k+1)\Phi_{m+k} & \text{else} \end{cases} \tag{4.20}$$

where Φ_m is the flux at the end of the m–th tooth, $\Phi_{B,m}$ is the flux in the back-iron adjacent to the m–th tooth, and M is the total number of teeth for one section.

4.4 Flux density waveforms in the pole-pieces

Due to the complexity of the flux density distribution in the PPs a representation through average values in radial or circumferential directions may not be accurate.

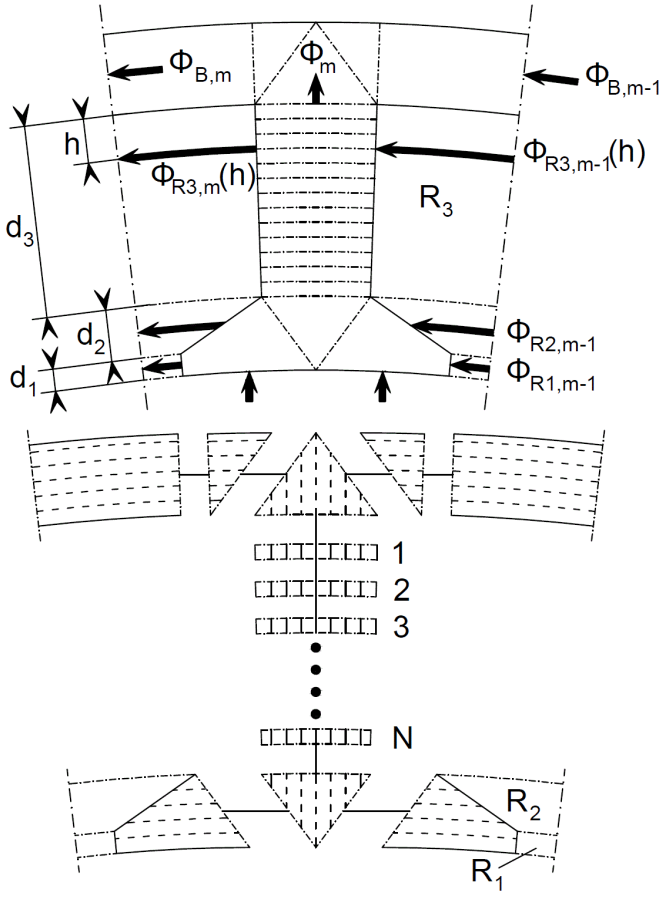

Fig. 4.3: Division of one stator tooth and back-iron into segments. Assumed flux paths are shown as arrows for entering/exciting flux paths to the segment (above figure). The flux paths assumed within the segments are indicated as dashed lines within the laminations (bottom figure).

Therefore, an analytical model for the prediction of the flux density distribution in the PPs is developed. Since large PDDs are likely to have a large number of poles the radial and circumferential dimensions of the PPs are very small compared to the airgap diameters. Therefore, for simplicity a Cartesian coordinate system is employed. x and y are the local Cartesian coordinates in one PP as is shown in Fig. 4.4, with

$$x = (\theta - \theta_i) R_{PPm} \tag{4.21}$$

$$y = r - R_{PPi} \tag{4.22}$$

where

$$R_{PPm} = \frac{1}{2}(R_{PPi} + R_{PPo}) \tag{4.23}$$

is the mean radius of the PPs. The average circumferential dimension of a PP is given by

$$L = \theta_{PP} R_{PPm} \tag{4.24}$$

where θ_{PP} is the angular dimension of a PP. It is assumed the PPs have a constant relative permeability $\mu_{iron} \gg \mu_{air}$, and the vector potential in the i-th PP $\vec{A}_{PP,i}$ satisfies the Laplace equation

$$\Delta \vec{A}_{PP,i} = 0 \tag{4.25}$$

The problem is treated in two dimensions and only the z-component of the vec-

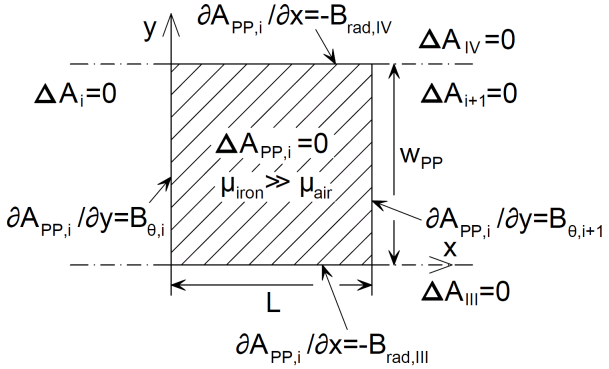

Fig. 4.4: i-th PP domain with its boundary conditions.

tor potential $A_{PP,i}$ is considered. The solutions can be determined by applying the boundary conditions and utilising the values for the flux density in the air regions, that are found by evaluating the model in section 4.2. Since the radial coordinate system is approximated by a Cartesian coordinate system the following relationships are assumed for the boundary conditions:

$$\partial A_{PP,i}(0,y)/\partial y = B_\theta(R_{PPi}+y, \theta_i) \tag{4.26}$$

$$\partial A_{PP,i}(L,y)/\partial y = B_\theta(R_{PPi}+y, \theta_i+\theta_{PP}) \tag{4.27}$$

$$\partial A_{PP,i}(x,0)/\partial x = -B_{rad}(R_{PPi}, \theta_i + x/R_{PPm}) \tag{4.28}$$

$$\partial A_{PP,i}(x,w_{PP})/\partial x = -B_{rad}(R_{PPo}, \theta_i + x/R_{PPm}) \tag{4.29}$$

For a given PP the solution of the Laplace equation (4.25) can be expressed as a super position

$$A_{PP,i}(x,y) = A_{x=0}(x,y) + A_{x=L}(x,y) + A_{y=0}(x,y) + A_{y=w_{PP}}(x,y) + A_0(x,y) \quad (4.30)$$

of the functions

$$A_{x=0}(x,y) = \sum_{n=1}^{\infty} a_{x,0,n} \sinh(n\pi[L-x]/w_{PP}) \sin(n\pi y/w_{PP}) \quad (4.31)$$

$$A_{x=L}(x,y) = \sum_{n=1}^{\infty} a_{x,L,n} \sinh(n\pi x/w_{PP}) \sin(n\pi y/w_{PP}) \quad (4.32)$$

$$A_{y=0}(x,y) = \sum_{n=1}^{\infty} a_{y,0,n} \sin(n\pi x/L) \sinh(n\pi[w_{PP}-y]/L) \quad (4.33)$$

$$A_{y=w_{PP}}(x,y) = \sum_{n=1}^{\infty} a_{y,w_{PP},n} \sin(n\pi x/L) \sinh(n\pi y/L) \quad (4.34)$$

$$A_0(x,y) = a_x x + a_y y + a_{xy} xy \quad (4.35)$$

The tangential derivatives of the functions $A_{x=0}(x,y)$, $A_{x=L}(x,y)$, $A_{y=0}(x,y)$ and $A_{y=w_{PP}}(x,y)$ at the boundaries are zero for three sides of the PP, Fig. 4.5, while for the remaining side their values are given by

$$\partial A_{x=0}(0,y)/\partial y = B_{\theta,i}(R_{PPi}+y,\theta_i) - \bar{B}_{\theta,i}(\theta_i) \quad (4.36)$$

$$\partial A_{x=L}(L,y)/\partial y = B_{\theta,i}(R_{PPi}+y,\theta_i+\theta_{PP}) - \bar{B}_{\theta,i}(\theta_i+\theta_{PP}) \quad (4.37)$$

$$\partial A_{y=0}(x,0)/\partial x = -B_{rad}(R_{PPi},\theta_i+x/R_{PPm}) + \bar{B}_{rad}(R_{PPi}) \quad (4.38)$$

$$\partial A_{y=w_{PP}}(x,w_{w_{PP}})/\partial x = -B_{rad}(R_{PPo},\theta_i+x/R_{PPm}) + \bar{B}_{rad}(R_{PPo}) \quad (4.39)$$

where $\bar{B}_{\theta,i}(\theta_i)$, $\bar{B}_{\theta,i}(\theta_i+\theta_{PP})$, $\bar{B}_{rad}(R_{PPi})$ and $\bar{B}_{rad}(R_{PPo})$ are the average flux density values at the respective side. Furthermore, the derivatives of the function $A_0(x,y)$ at each side of the PP are equal to the average value at that side, Fig. 4.5.

The coefficients of the functions are then determined by applying the boundary

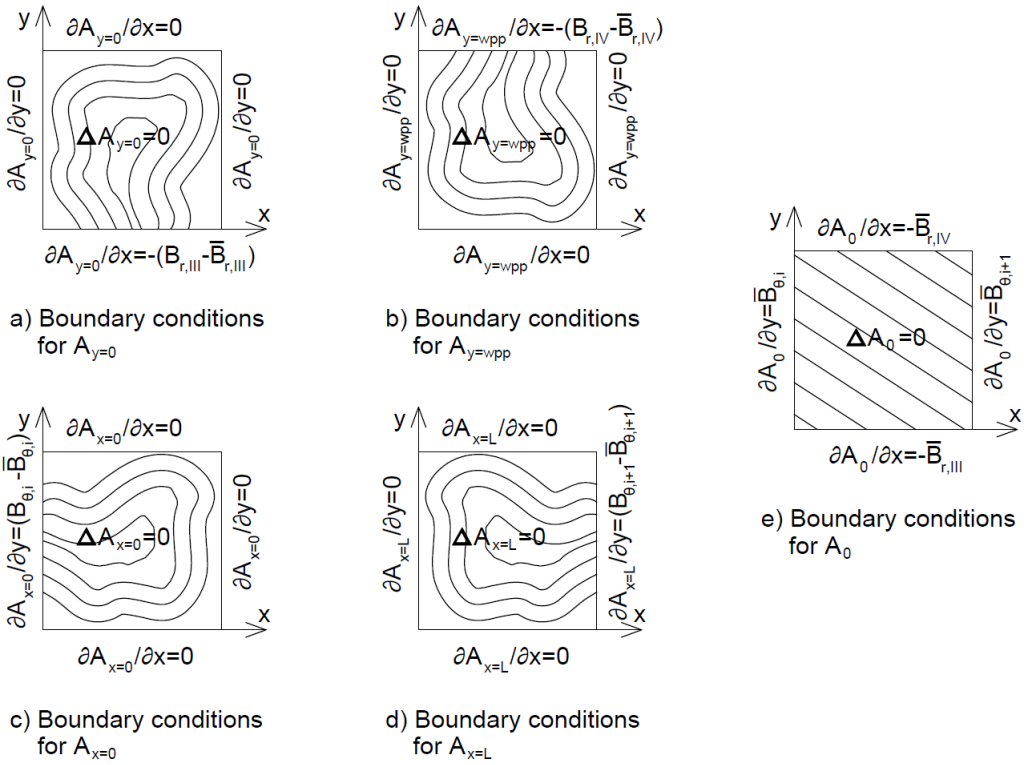

Fig. 4.5: Boundary conditions for the functions $A_{x=0}(x,y)$, $A_{x=L}(x,y)$, $A_{y=0}(x,y)$, $A_{y=w_{PP}}(x,y)$ and $A_0(x,y)$ for a given PP. The equivalent flux paths for each function are schematically indicated.

conditions at the interfaces between iron and air regions and they are given by:

$$a_{x,0,n} = \frac{1}{n\pi}\int_0^{w_{PP}} \frac{\cos(n\pi y/w_{PP})}{\sinh(n\pi L/w_{PP})}\frac{\partial A_{PP,i}(0,y)}{\partial y}dy \tag{4.40}$$

$$a_{x,L,n} = \frac{1}{n\pi}\int_0^{w_{PP}} \frac{\cos(n\pi y/w_{PP})}{\sinh(n\pi L/w_{PP})}\frac{\partial A_{PP,i}(L,y)}{\partial y}dy \tag{4.41}$$

$$a_{y,0,n} = \frac{1}{n\pi}\int_0^{L} \frac{\cos(n\pi x/L)}{\sinh(n\pi w_{PP}/L)}\frac{\partial A_{PP,i}(x,0)}{\partial x}dx \tag{4.42}$$

$$a_{y,w_{PP},n} = \frac{1}{n\pi}\int_0^{L} \frac{\cos(n\pi x/L)}{\sinh(n\pi w_{PP}/L)}\frac{\partial A_{PP,i}(x,w_{PP})}{\partial x}dx \tag{4.43}$$

$$a_x = \frac{1}{L}\int_0^{L} \frac{\partial A_{PP,i}(x,0)}{\partial x}dx \tag{4.44}$$

$$a_y = \frac{1}{w_{PP}}\int_0^{w_{PP}} \frac{\partial A_{PP,i}(0,y)}{\partial y}dy \tag{4.45}$$

$$a_{xy} = \frac{1}{Lw_{PP}}\int_0^{w_{PP}} \left[\frac{\partial A_{PP,i}(L,y)}{\partial y} - \frac{\partial A_{PP,i}(0,y)}{\partial y}\right]dy \tag{4.46}$$

4.5 Losses and efficiency

Two sources of losses are considered, namely the iron loss and the copper loss. Stator PMs and to a lesser extent HS rotor PMs will exhibit time variations in the operating points. Therefore, eddy currents will be induced, however, their magnitude and associated losses will depend on the level of axial, radial and circumferential segmentation, which is usually a compromise between the tolerated losses and the manufacturing limitations [58]. Hence, this loss component is neglected in the analysis. Furthermore, AC losses in the windings are also not considered.

4.5.1 Copper loss

The copper loss in the stator windings is given by the sum of DC copper losses, which are calculated by considering only the rms current in the winding, and AC copper losses, which are due to skin effects and to a lesser extend proximity effects [59]. Due to the range of the considered electrical frequencies, the skin depths are of similar magnitude as the coil slot dimension, e.g. at an electrical frequency $f = 50Hz$ the skin depth is about $\delta = 0.01m$. Furthermore, the magnitudes of the eddy currents depend significantly on the selected wire diameters and the number of parallel strands. The losses due to skin effects can, therefore, be minimized by optimising the number of conductor strands while considering constraints such as the available coil slot area and the desired packing factor. The copper loss in the stator windings is, therefore, approximated by the DC loss component which is given by

$$P_{Cu,S} = 3R_S^* I_{rms}^2 = \rho_{Cu}(l_a + l_{e,S}) i_{rms} 2\pi R_S Q_{rms} \tag{4.47}$$

where i_{rms} is the rms current density in the coils, I_{rms} is the rms value of the current in the coils, and R_S^* is the resistance of the coils for one phase calculated at the operating temperature of $T = 120^o C$. The resistivity of copper is temperature dependent and it is given by [60]

$$\rho_{Cu} = \rho_{20}(1 + \alpha_{Cu}(T - 20°C))$$

where $\rho_{20} = 1.724e-8\Omega m$ and $\alpha_{Cu} = 0.00393^{o}C^{-1}$ are the resistivity coefficient and the temperature coefficient at $20°C$, respectively. The length of the end windings is given by

$$l_{e,S} = \frac{2\pi R_S}{3p_{HS}}\left[(1-\alpha_{c,S}) + \frac{\pi}{2}\alpha_{c,S}\right] \tag{4.48}$$

where

$$\alpha_{c,S} = p_{HS}\beta_{c,S} \tag{4.49}$$

and $\beta_{c,S}$ is the coil pitch for one phase. The mass of copper on the stator is given by

$$M_{Cu,S} = m_{Cu}\frac{2\pi R_S Q_{rms}}{i_{rms}}(l_a + l_{e,S}) \tag{4.50}$$

Combining (4.50) in (4.47) gives the following expression for the copper loss:

$$P_{Cu} \quad = \quad \rho_{Cu} i_{rms}^2 \frac{M_{Cu,S}}{m_{Cu}} \tag{4.51}$$

4.5.2 Iron losses

The analysis of the iron losses is a highly non-linear problem due to the hysteresis property and domain structures, and a thorough analysis is required to give an accurate prediction. A commonly used approach is to separate the loss per unit volume p_{iron} into three loss mechanisms [61, 62]:

$$p_{iron} = p_{hyst} + p_{class} + p_{exc} \tag{4.52}$$

where p_{hyst} is the hysteresis loss, p_{class} the classical eddy current loss, and p_{exc} the excess eddy current loss. Each of the loss components is a function of the frequency and the flux density multiplied by a coefficient. Although the separation of the iron loss provides a calculation method that is practical and easy to implement it remains an approximation and further studies have shown that the loss coefficients of the various loss components could depend noticeably on the frequency and the flux density [61]. However, in order to include the variability of the coefficients,

further knowledge about the magnetic behaviour of the laminated steel would be required, which often is not available. Therefore, and similar to common practice, the coefficients in this analysis are assumed to be constant and independent of the frequency and the flux density. Furthermore, their values are given in Table 5.2.

Hysteresis loss

Hysteresis losses are due to localised and nearly instantaneous irreversible changes in the domain structure. Hence, the loss per magnetic cycle is fairly independent of the magnetising frequency and the hysteresis loss per unit mass is therefore given by the area enclosed by the hysteresis loop:

$$p_{hyst} = \frac{1}{m_L} f \oint H \mathrm{d}B \tag{4.53}$$

where f is the frequency of the excitation. The evaluation of this integral is not trivial and empirical methods by fitting experimental data are often preferred. The following empirical expression provides a good approximation [62]:

$$p_{hyst} = k_{hyst} f B_m^{\alpha_{hyst}} \tag{4.54}$$

where

$$\alpha_{hyst} = a_{hyst} + b_{hyst} B_m \tag{4.55}$$

and k_{hyst}, a_{hyst} and b_{hyst} are fitting coefficients which depend on the material property and have to be determined by experimental data, and

$$B_m = \frac{B_{max} - B_{min}}{2} \tag{4.56}$$

where B_{max} and B_{min} are the maximum and minimum peak flux densities reached during the excursion of the loop. The latter choice for B_m is given by the assumption that an offset of the hysteresis loop does not have any effect on the hysteresis loss. This simplification is particularly significant for the PDD, where the stator PMs may result in an unbalanced flux density offset in the stator iron. If N_{ml} minor hysteresis loops are caused, a correction can be applied [63]:

$$p_{hyst} = k_{hyst} f B_m^{\alpha_{hyst}} \left(1 + \frac{0.65}{B_m} \sum_{i=1}^{N_{ml}} \Delta B_i \right) \tag{4.57}$$

where ΔB_i is the change in flux density during the excursion of the minor loop.

Classical eddy current loss

Eddy currents are induced when the magnetic flux density is varied in the laminations. In materials with no structural/magnetic inhomogeneities these losses are equal to the classical eddy current losses which are given by [62]:

$$p_{class} = \frac{\sigma_L d_L^2}{12 m_L} f \int_{1/f} \left(\frac{\partial B}{\partial t} \right)^2 \mathrm{d}t \tag{4.58}$$

where σ_L is the electrical conductivity, and d_L the lamination thickness.

Excess eddy current loss

In addition to the classical eddy current losses, excess eddy current losses can contribute significantly to the iron loss. The excess eddy current loss is given by

$$p_{exc} = k_{exc} f \int_{1/f} \left| \frac{\partial B}{\partial t} \right|^{1.5} \mathrm{d}t \tag{4.59}$$

where k_{exc} is the excess coefficient that has to be determined experimentally [62]. Furthermore, in [61] it is shown that the coefficient may vary more than 50% with the magnetic induction, however accounting for a variability of k_{exc} would also require further knowledge about the magnetic behaviour of the material in question. However, since additionally required data has not been available for this work k_{exc} is assumed to be constant.

4.6 Conclusions

The analytical models for the prediction of the magnetic field distributions in the airgaps and PMs of radial-field MGs presented in Chapter 2 are extended to account for the effects of stator windings. In order to predict accurately the iron losses analytical models for the flux density distributions in the PPs and the average flux density distributions in the stator core at no-load and on-load conditions are presented. Finally, for completeness the electromagnetic loss prediction techniques adopted in this thesis are described.

Chapter 5

PDDs for a 10MW wind turbine

The analytical models in Chapter 4 are employed for the study and optimisation of a PDD for a 10MW wind turbine. The operation of the turbine is outlined and an optimised design of the PDD suitable for the application is presented. The presented design is employed for the comparison of the analytical models with 2D FE predictions on no-load and on-load conditions. Furthermore, the effects of the leading design parameters on the main PIs of the PDD, such as the electromagnetic efficiency, and the masses of the active components, i.e. PM, laminated steel and copper, is presented.

5.1 Operation as a wind turbine generator

The available shaft power of a wind turbine is given by [23]

$$P_W = \frac{1}{2} m_{air} c_p(\lambda, \theta_{pitch}) \pi R_{blade}^2 v_w^3 \tag{5.1}$$

where v_w is the wind speed, m_{air} is the mass density of air, R_{blade} is the turbine rotor radius, and $c_p(\lambda, \theta_{pitch})$ is the power coefficient of the aerodynamic efficiency, which is a function of the tip speed ratio λ and the pitch angle θ_{pitch}. At wind speeds above the rated wind speed $v_{w,R}$ the blades are pitched to reduce aerodynamic efficiency and thus limit the power to the rated power

$$P_R = \frac{1}{2} m_{air} c_{p,R} \pi R_{blade}^2 v_{w,R}^3 \tag{5.2}$$

Therefore, the torque on the PP rotor can then be expressed in terms of the power by

$$T_W = R_{blade} v_w^{-1} P_W = \left[\frac{1}{2} \rho_{air} c_p(\lambda, \theta_{pitch}) \pi R_{blade}^5 \right]^{1/3} P_W^{2/3} \tag{5.3}$$

Both the variation of the capacity factor and the rotational speed of the turbine have been determined by the project INNWIND.EU for a 10MW reference turbine with a turbine radius of $R_{blade} = 89.166m$ [64]. The turbine is designed to have a cut-in wind speed of $v_{w,min} = 4m/s$, a rated wind speed of $v_{w,R} = 12m/s$, and a cut-out wind speed of $v_{w,max} = 25m/s$. At wind speeds below $v_{w,min}$ the power supplied by the wind is employed to accelerate the rotor for the start-up. Between the wind speeds $v_{w,1} = 7m/s$ and $v_{w,2} = 11m/s$ the turbine is controlled as to maximize the power capture. At wind speeds above $v_{w,R}$ the turbine is controlled such that the power remains constant. At wind speeds between $v_{w,min}$ and $v_{w,1}$ the rotational speed is kept constant in order to limit the wind turbines operational speed range [65]. Furthermore, in the analysis in this work the mechanical input power is assumed to be 10.0MW compared to 10.6MW of the reference turbine and the capacity factor is, therefore, also reduced at wind speeds between $v_{w,2}$and $v_{w,R}$ to limit the the maximum input power of the turbine to 10.0MW. Fig. 5.1 shows the variations of the capacity factor c_p and the rotational speed of the turbine with the wind speed that has been employed for the PDD.

Fig. 5.2 shows the variation of the turbine shaft power and the torque on the PP rotor with wind speed. It can be seen that for this particular turbine the rated torque is reached at a lower wind speed than the rated power.

The speed curve in Fig.5.1 and the torque and power curve 5.2 are utilised to investigate the efficiency performance of PDDs at partial load and full-load for a PDD with PM excited HS rotor in Sections 5.3, and for PDDs with coil excited HS rotor in Sections 6.4. These values can be further utilised to assess the overall annual energy efficiency of the PDD. In order to calculate the annual energy efficiency a Weibull probability distribution for the wind speed frequency is adopted [66]:

$$p(v_w) = \frac{k}{A} \left(\frac{v_w}{A} \right)^{k-1} \exp \left[- \left(\frac{v_w}{A} \right)^k \right] \tag{5.4}$$

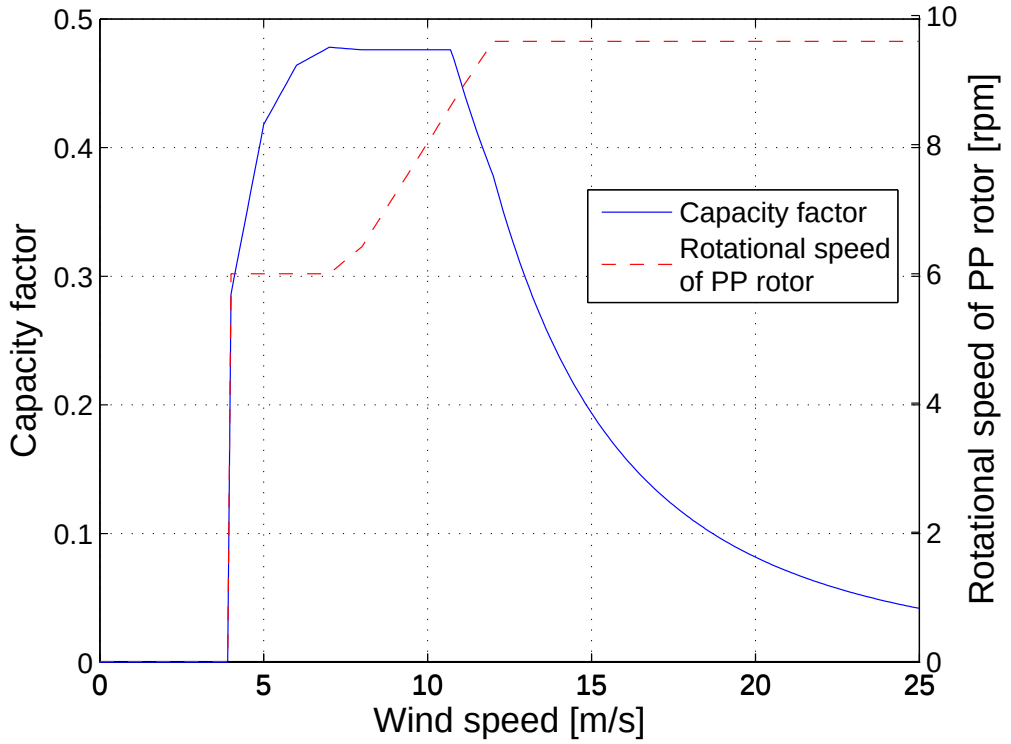

Fig. 5.1: Variation of the capacity factor and the rotational speed of the PP rotor for a 10MW wind turbine with the wind speed.

where $k = 2.35$ is the shape parameter and $A = 12.01$m/s is the scale parameter, which are selected to fit a measured wind profile at a height of 110m at the FINO3 offshore research platform in the north sea [67], as can be seen in Fig 5.3.

Fig. 5.4 shows the variation of the cumulative annual energy of the turbine

$$E_c = \int_{v_{w,min}}^{v_{w,c}} P_W(v_w) p(v_w) dv_w \tag{5.5}$$

with the maximum considered wind speed $v_{w,c}$. It can be seen that wind speeds above the rated wind speed contribute to more than 60% of the total annual energy, and that E_c decreases rapidly with decreasing $v_{w,c}$. In order to reduce the numerical effort of the analysis for the forthcoming optimisation studies the rated efficiency is, therefore, employed as an indicator for the efficiency performance of the investigated PDD designs.

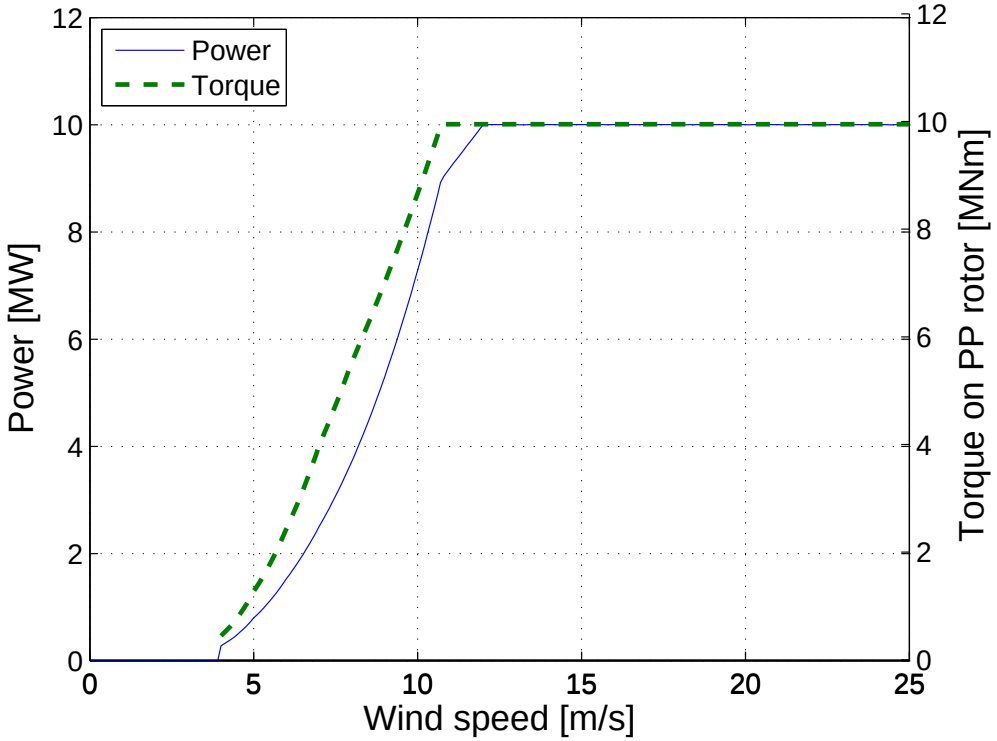

Fig. 5.2: Variation of the capacity factor and the rotational speed of the PP rotor for a 10MW wind turbine with the wind speed.

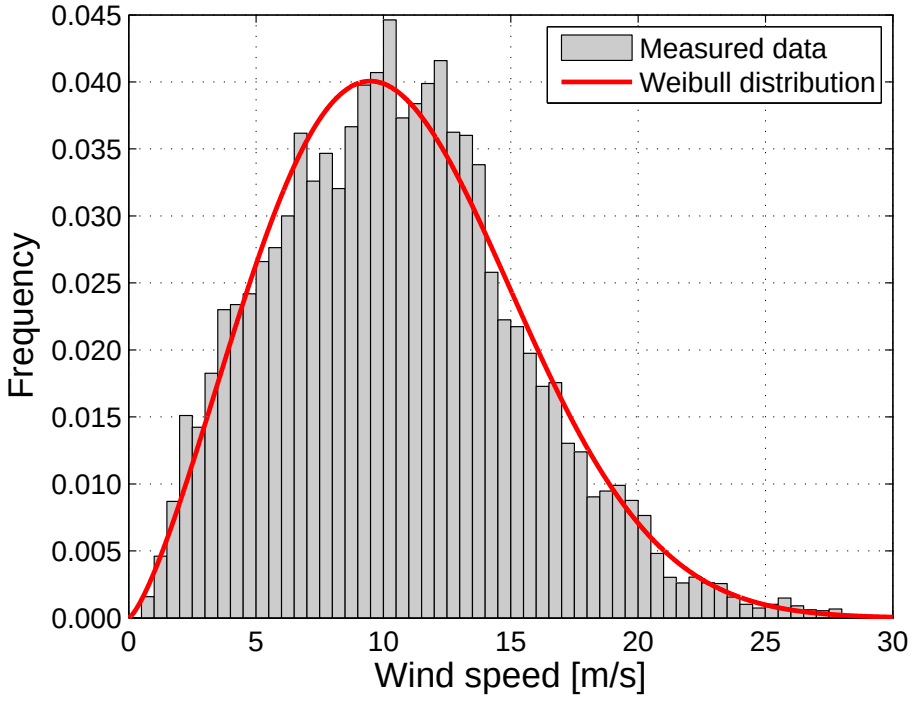

Fig. 5.3: Frequency of the wind speeds at the research platform FINO3 at 110m height for the year 2011 [67]. The Weibull distribution is fitted to the measured data.

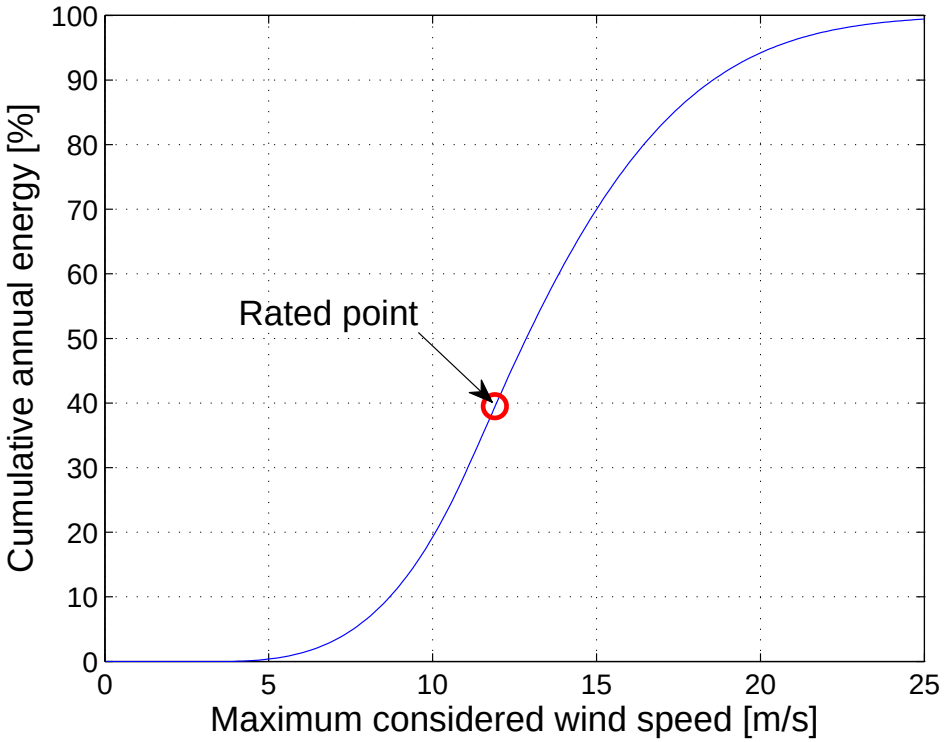

Fig. 5.4: Cumulative annual energy E_c in percent of the total annual energy of the turbine with the maximum considered wind speed $v_{w,c}$.

5.2 Optimisation process

The analytical models developed in Chapters 2 and 4 are employed for the optimisation of a PDD. Similarly to Section 3.1 several PIs have been identified for the determination of the goodness of a PDD design. In addition to the PIs from Section 3.1 also the mass of the copper and the electromagnetic efficiency are included as PI. Fig. 5.5 shows the flowchart for the optimisation procedure that has been employed. After selection of an initial PDD design, a set of parameters is selected which are varied to investigate the designs. After completion of the parameter scan the design with the best improvements is identified. If the design requires further improvement a new set of parameters is investigated. Table 5.1 gives the parameters for a PDD which is designed to meet the requirements of a 10MW wind turbine, and where the parameters of the MG component are given in Table 3.1. The turbine is assumed to be directly connected to the PP rotor and the pullout torque is required to achieve 11.9 *MNm* which is 20% higher than the rated torque. The HS rotor is magnetically

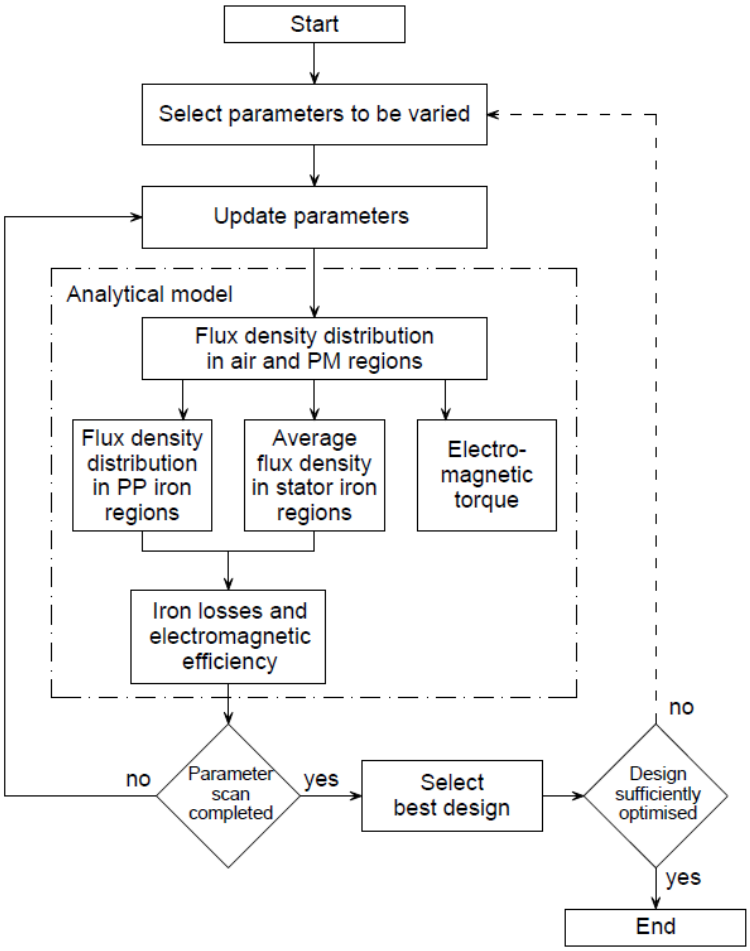

Fig. 5.5: Flowchart for the optimisation procedure.

coupled to the stator windings. The PDD is optimised including its MG component to achieve the required torque with the primary goals of minimising the PM mass, the copper mass and the total active mass, while achieving a high electromagnetic efficiency and a sufficiently high shear stress. In summary, the parameters that have been varied in the optimisation analysis are: the PM thickness, the airgap diameter and hence the aspect ratio, the current density, the number of identical sections, and the gear ratio.

It can be seen, that a PDD can be achieved with a rated efficiency of ~98.7%, a PM mass of 13.5$tons$, a copper mass of 7$tons$ and a total active mass of 50$tons$. The structural mass has been assumed to be twice the active mass, hence the total mass of the PDD would be 150$tons$. In comparison, instead of constructing a PDD, the MG component in Table 3.1 could also be coupled in line with a PM direct drive,

where the latter would have a torque rating of $1.33 MNm$. [4] presented a PM direct drive for a torque rating of $1.9 MNm$. Although the values for the PM direct drive overestimate the required masses for the generator it may give a good indication of the required active masses. The design exhibits a PM mass of $1.7 tons$, a copper mass of $4.3 tons$ and a total active mass of $24.1 tons$, with a rated electromagnetic efficiency of ~95.7%. If the structural mass is assumed to scale linearly with the diameter [68], the estimated structural mass would be $10 tons$. Hence, the coupled system of MG and PM direct drive could exhibit a similar total mass of ~$140 tons$, however the electromagnetic efficiency could be significantly lower.

	Quantity	Value
P_R	Rated shaft power	10 MW
$T_{PP,R}$	Rated torque on PP rotor	9.9 MNm
$\omega_{PP,R}$	Rated rotational speed of PP rotor	9.6 rpm
$f_{out,R}$	Rated supply frequency	48 Hz
	Slot packing factor	0.5
	Rated current density in the stator windings	2.1 A_{rms}/mm^2
	Rated electromagnetic efficiency	98.7 %
	Annual energy efficiency	98.5 %
	Mass of PMs	13.5 $tons$
	Mass of copper	7 $tons$
	Mass of HS rotor and PP rotor laminated steel	14 $tons$
	Mass of stator laminated steel	15.5 $tons$
	Mass of structural steel	100 $tons^{\#}$

$^{\#}$ For a 6m airgap diameter MG the structural mass is assumed to be twice the active mass.

Table 5.1: Parameters of the PDD where the MG in table 3.1 is integrated into the PDD.

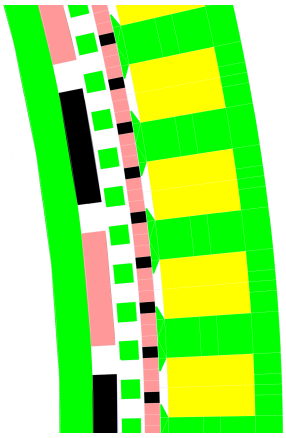

Fig. 5.6: Cross section of the PDD.

5.3 Comparison with finite element

The analytical models from Chapter 4 are compared with 2D-FE studies for the PDD in Table 5.1. Figs. 5.7-5.10 show the radial and circumferential components of the flux density in the inner and outer airgap at on-load conditions. It can be seen a good agreement exists between analytical and FE predictions.

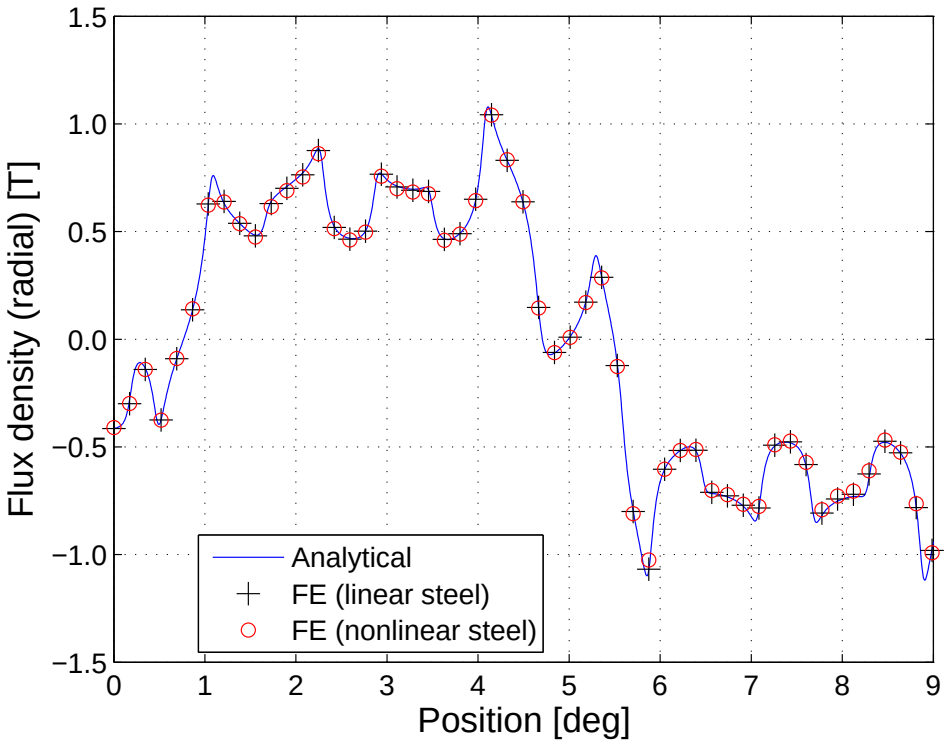

Fig. 5.7: Variation of the radial component of the magnetic flux density in the inner airgap with the circumferential position at on-load conditions.

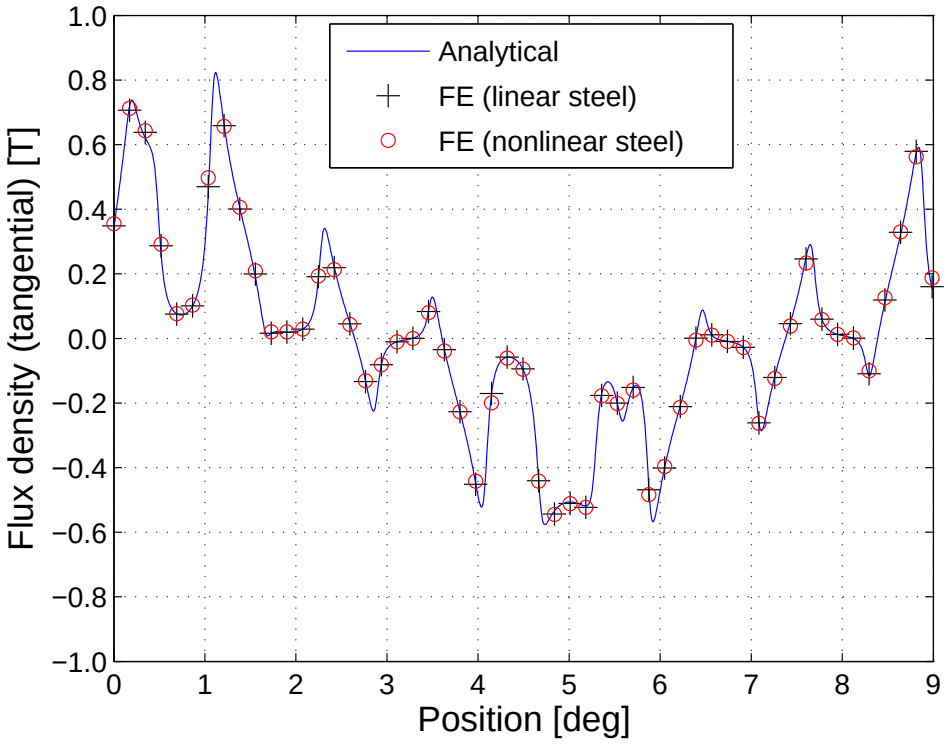

Fig. 5.8: Variation of the circumferential component of the magnetic flux density in the inner airgap with the circumferential position at on-load conditions.

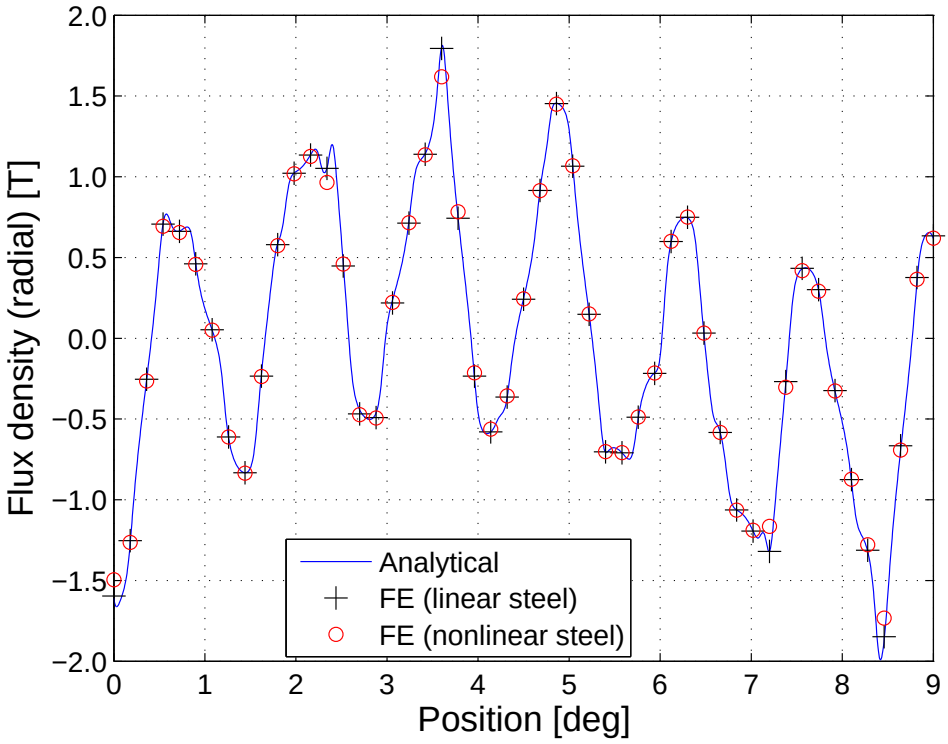

Fig. 5.9: Variation of the radial component of the magnetic flux density in the outer airgap with the circumferential position at on-load conditions.

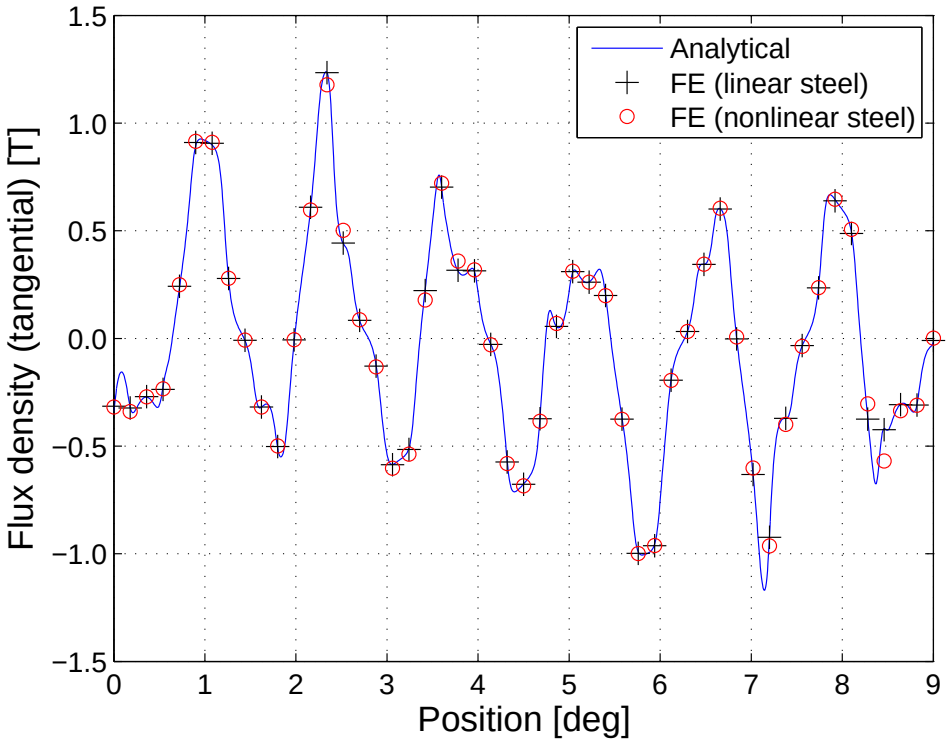

Fig. 5.10: Variation of the circumferential component of the magnetic flux density in the outer airgap with the circumferential position at on-load conditions.

Figs. 5.11-5.12 show the variation of the electromagnetic torque on the PP rotor and HS rotor at the rated speed. It can be seen that a good agreement exists between analytical model and FE if steel with linear characteristics is assumed and that the difference between analytical model and FE if steel with nonlinear characteristics is employed is less than 2%.

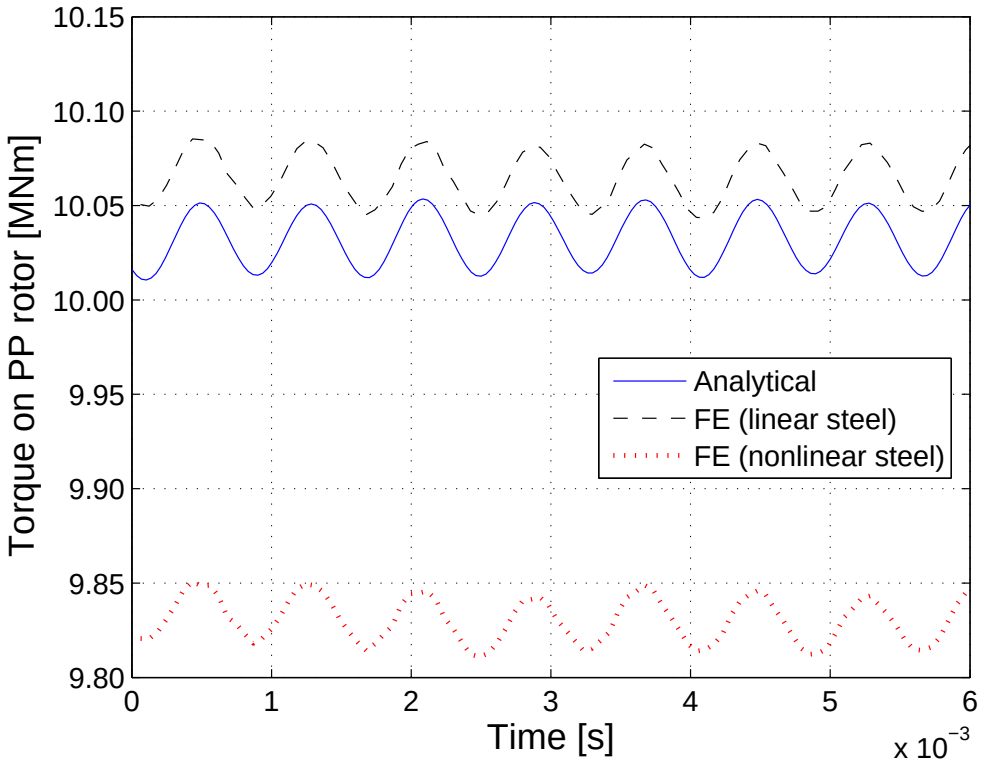

Fig. 5.11: Variation of the torque on the PP rotor with time at rated speed and at full load.

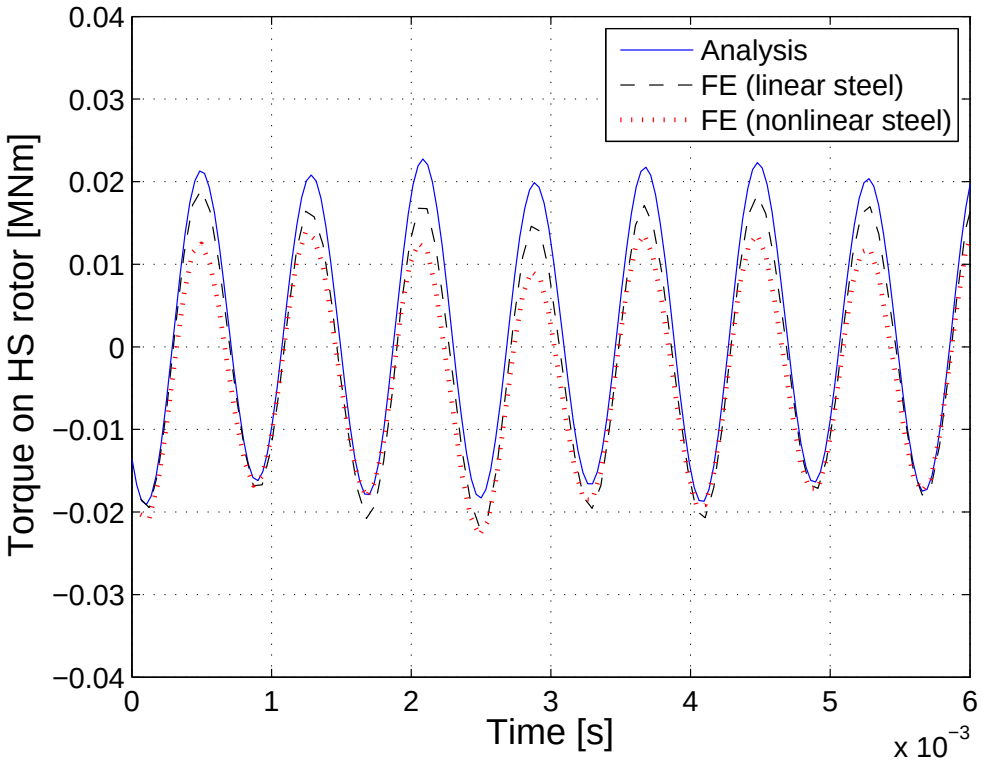

Fig. 5.12: Variation of the torque on the HS rotor with time at rated speed and at full load.

Fig. 5.13 shows the variation of the torque on the PP rotor with the stator current. It can be seen that the FE predicted torque agrees well with the analytical model, both for linear and non-linear steel.

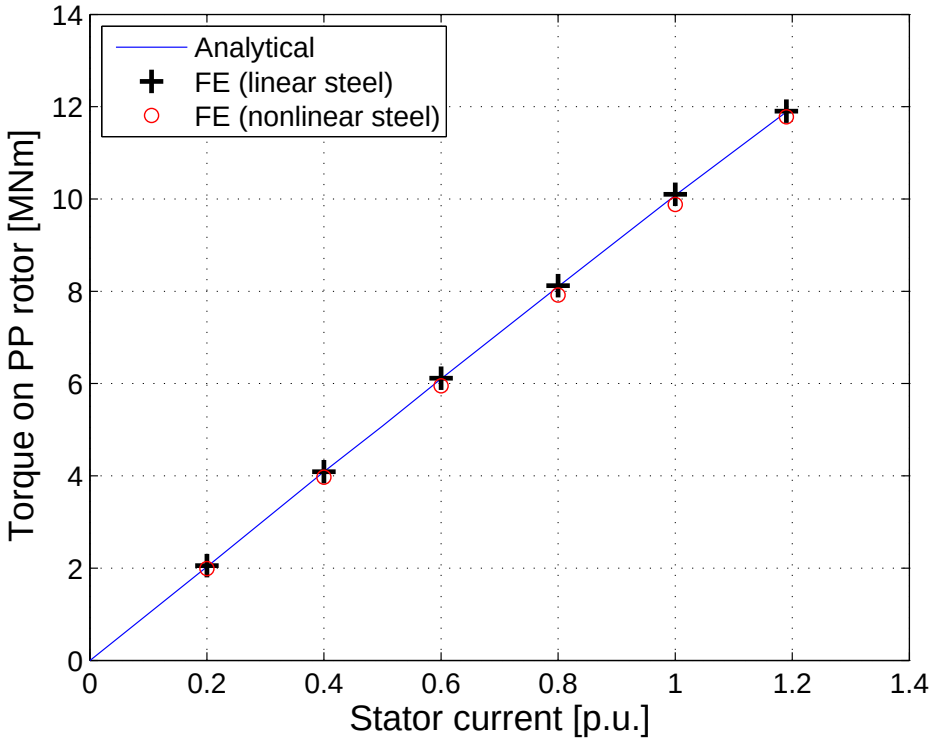

Fig. 5.13: Variation of average torque on the PP rotor with stator current. (per unit of the rated stator current)

Figs. 5.14-5.15 show the the variation of the radial and circumferential components of the flux density in a PP with the relative circumferential position on a PP. In addition, at the relative circumferential position $\theta_{PP}/2$ in a PP Figs. 5.16-5.17 show the variation of the radial and circumferential components of the flux density in a PP with the relative radial position on the PP. Again good agreement exists between FE and analytical predictions. However, although the introduction of the nonlinear steel characteristic results in increased local discrepancies between the analytical model and the FE analysis, this has minimal impact on the prediction of the iron losses in the PPs as will be seen in Fig. 5.25.

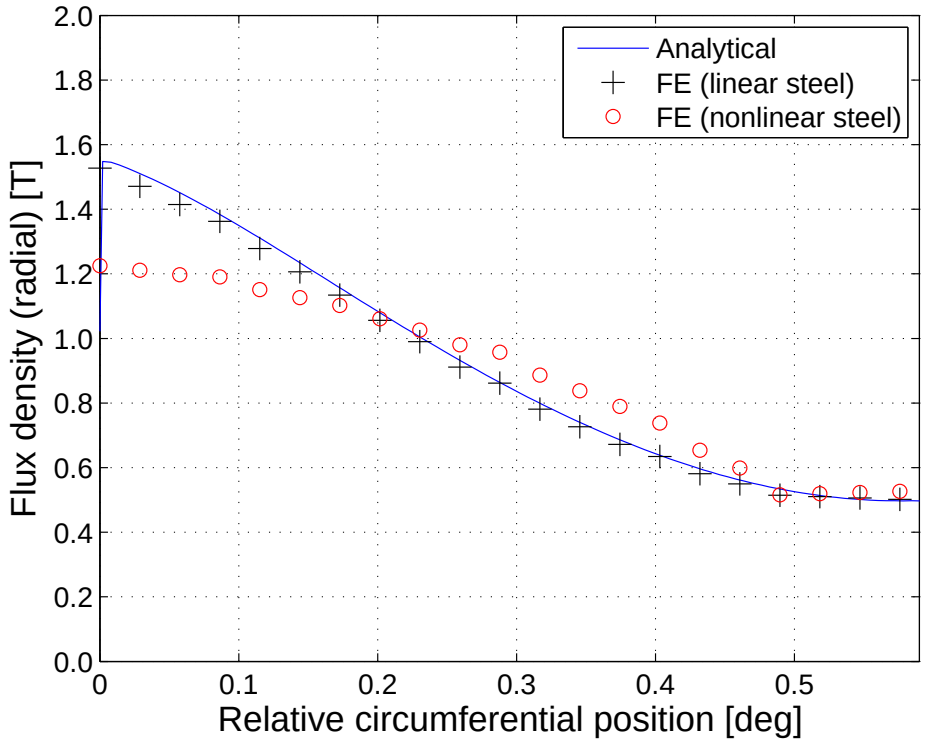

Fig. 5.14: Variation of the radial component of the magnetic flux density in one PP with the relative circumferential position at the mean radial position of the PP.

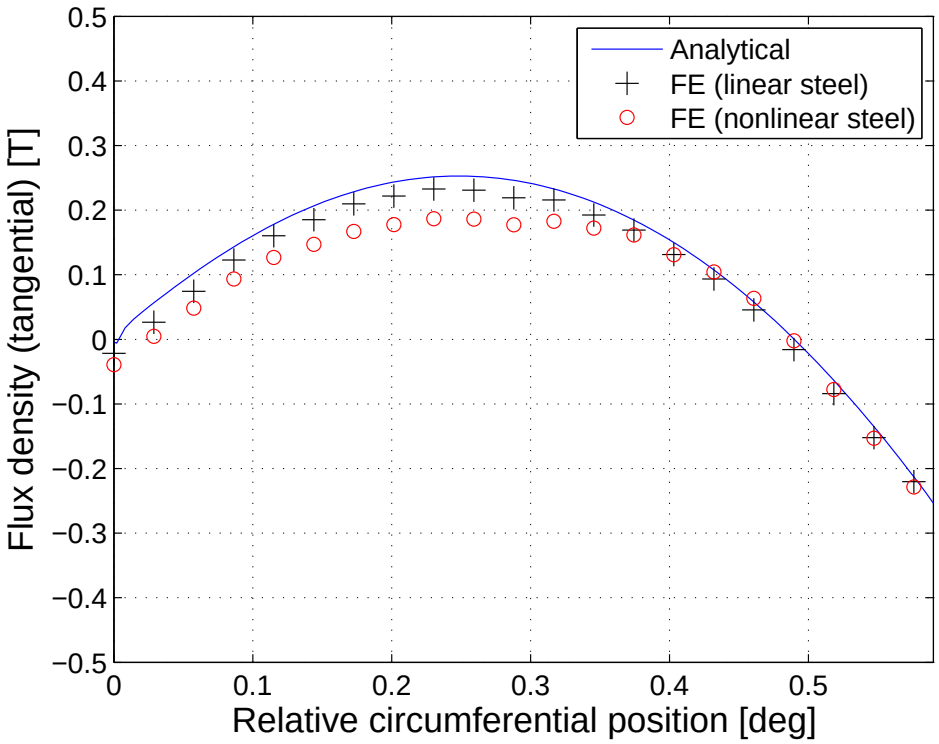

Fig. 5.15: Variation of the circumferential component of the magnetic flux density in one PP with the relative circumferential position at the mean radial position of the PP.

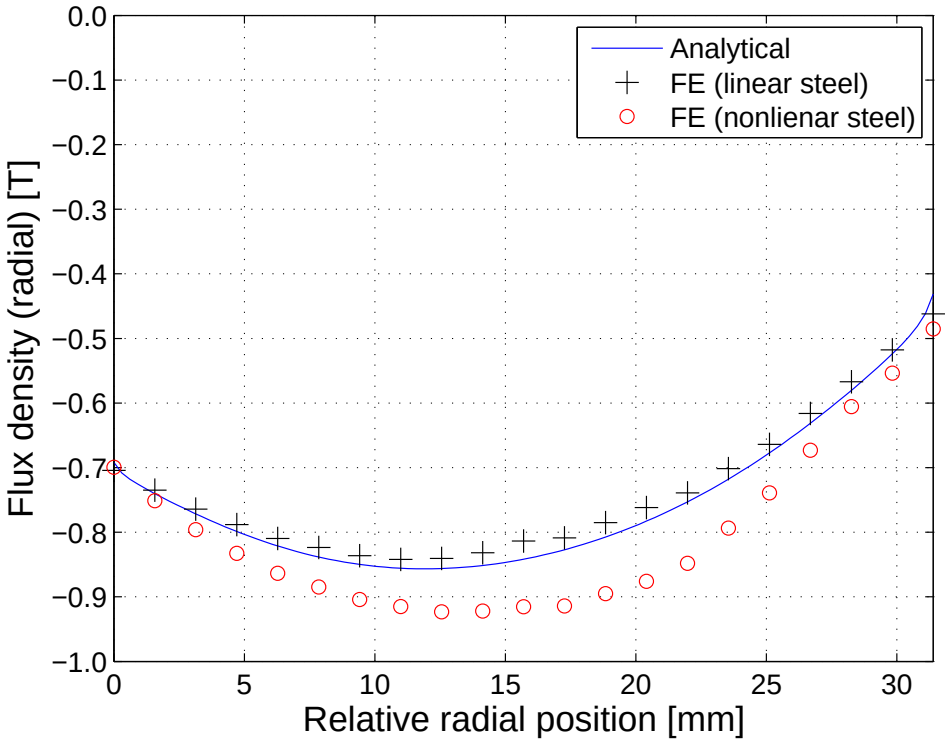

Fig. 5.16: Variation of the radial component of the magnetic flux density in one PP with the relative radial position at the relative circumferential position θ_{PP}.

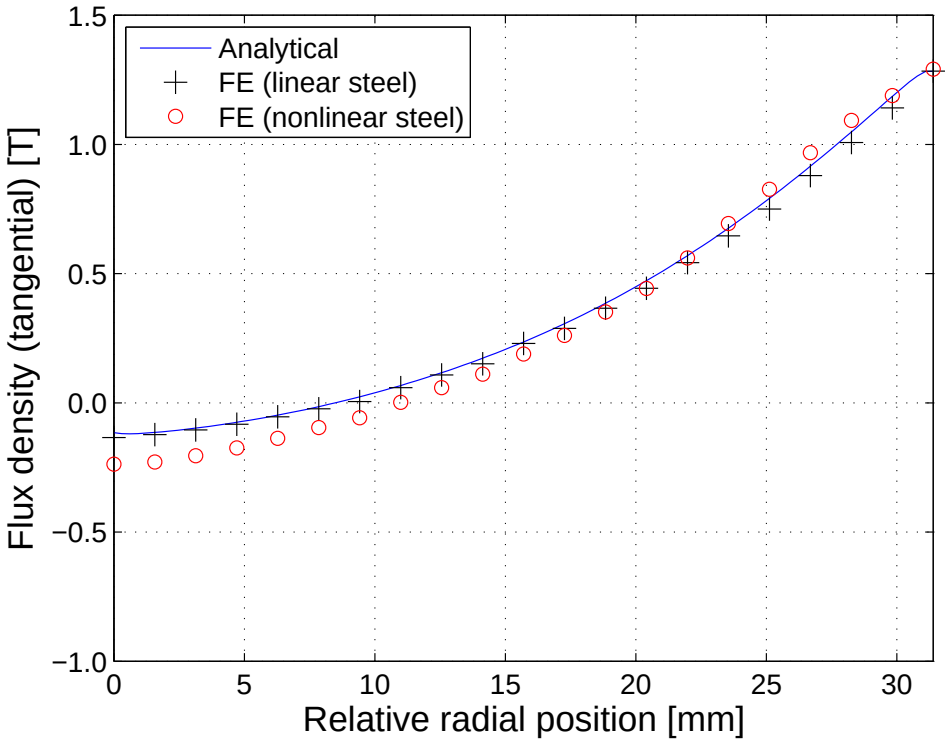

Fig. 5.17: Variation of the circumferential component of the magnetic flux density in one PP with the relative radial position at the relative circumferential position θ_{PP}.

Figs. 5.18-5.20 show the variation of the radial and circumferential components of flux density in the centre of a PP, with time at rated speed. It can be seen that at the centre of a PP there is good agreement between the analytical and FE predictions. The loss calculation for the PPs has been performed by considering the loss due to the circumferential and radial flux density separate. However, as can be seen from Fig. 5.20, the iron loss in the PPs could be dominated by rotational loss. Nevertheless, separating the iron loss components into circumferential and radial components may give a good indication on the loss in the PPs. Furthermore, it may be worth mentioning that the fundamental electrical frequency of the flux density waveforms on the PPs is different from the stator and it is given by

$$f_{PP,el} = \frac{G-1}{G} f_{out} \tag{5.6}$$

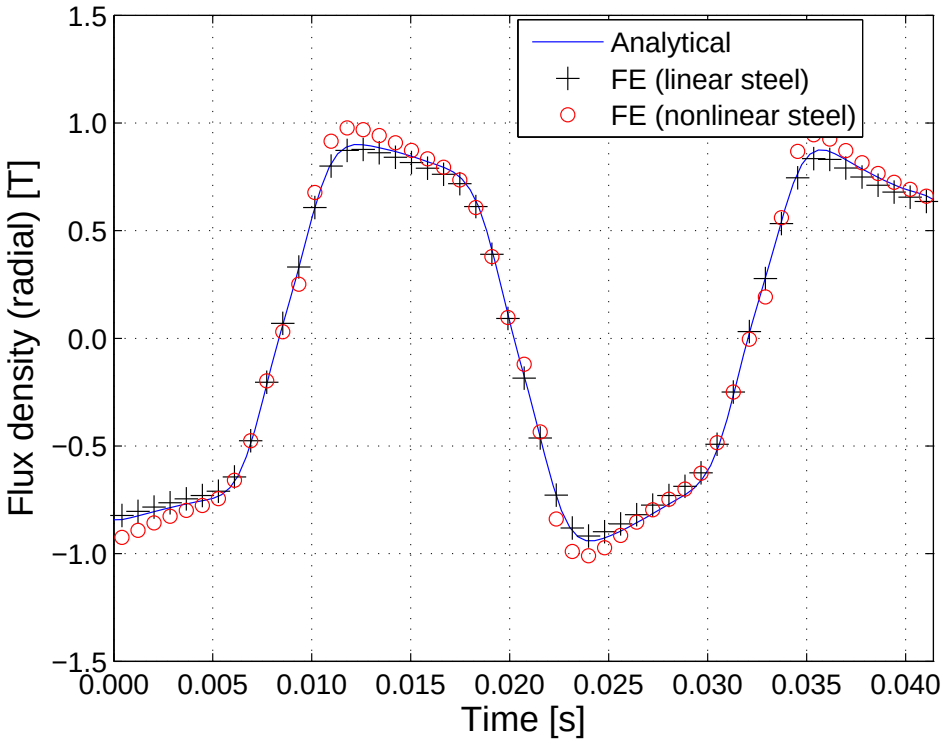

Fig. 5.18: Variation of the radial component of the magnetic flux density at the center of one PP with time at rated speed.

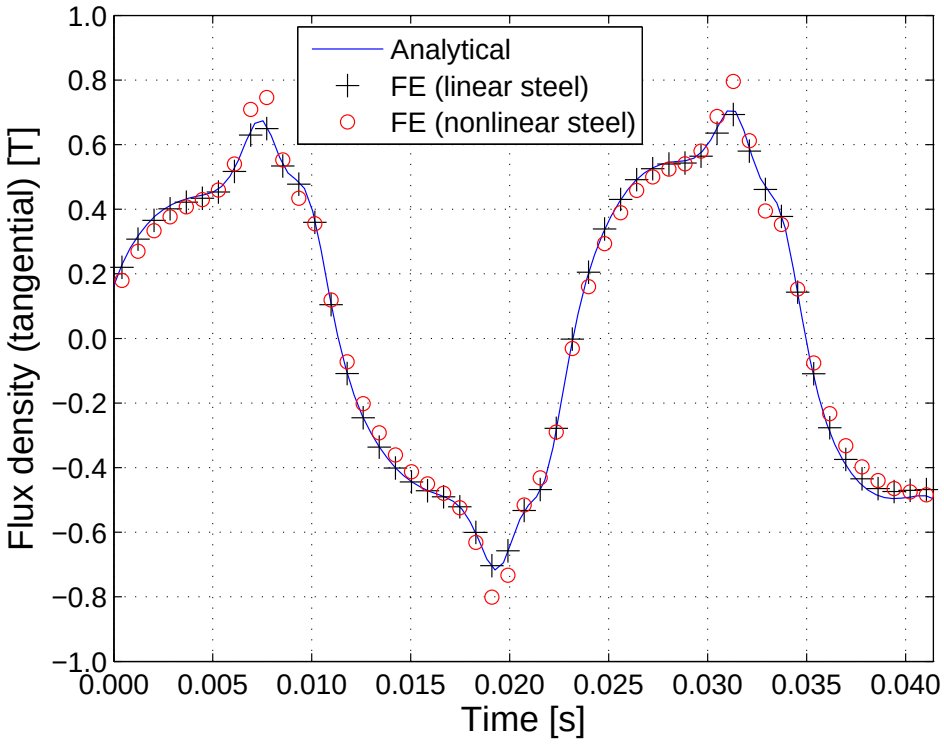

Fig. 5.19: Variation of the circumferential component of the magnetic flux density at the centre of one PP with time at rated speed.

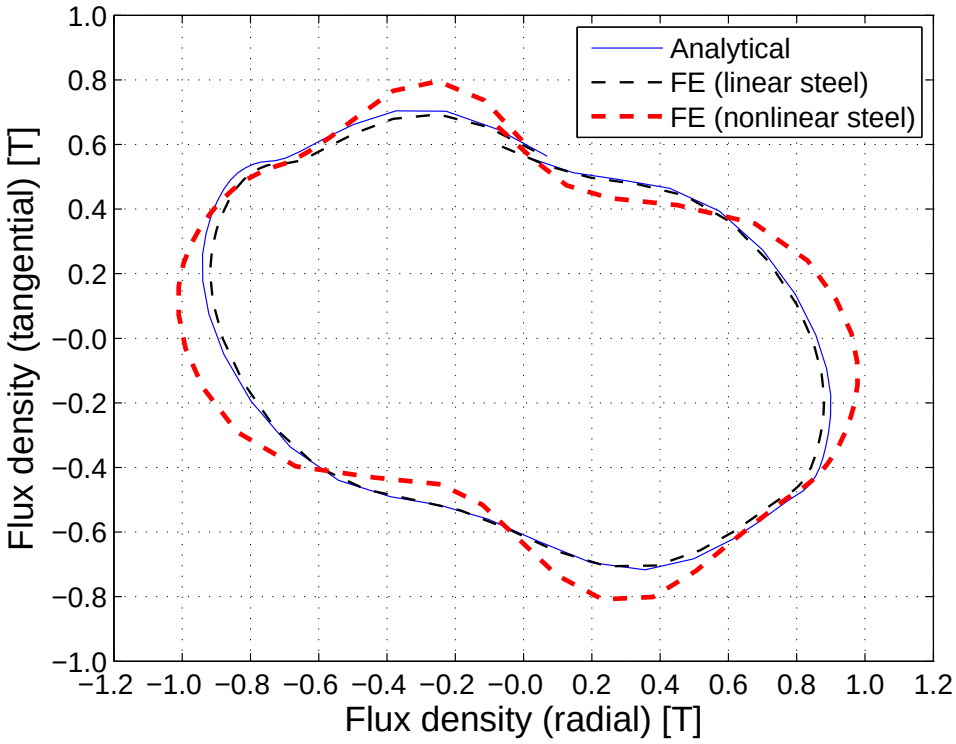

Fig. 5.20: Variation of circumferential magnetic flux density against radial flux density for one PP electric cycle.

5.21-5.24 show the average flux density waveforms in the stator teeth and the back-iron respectively at full-load and no-load conditions. It can be seen that a good agreement between the analytical and FE models exists. It can also be seen that the load condition has a noticeable effect on the flux density waveforms, particularly in the teeth.

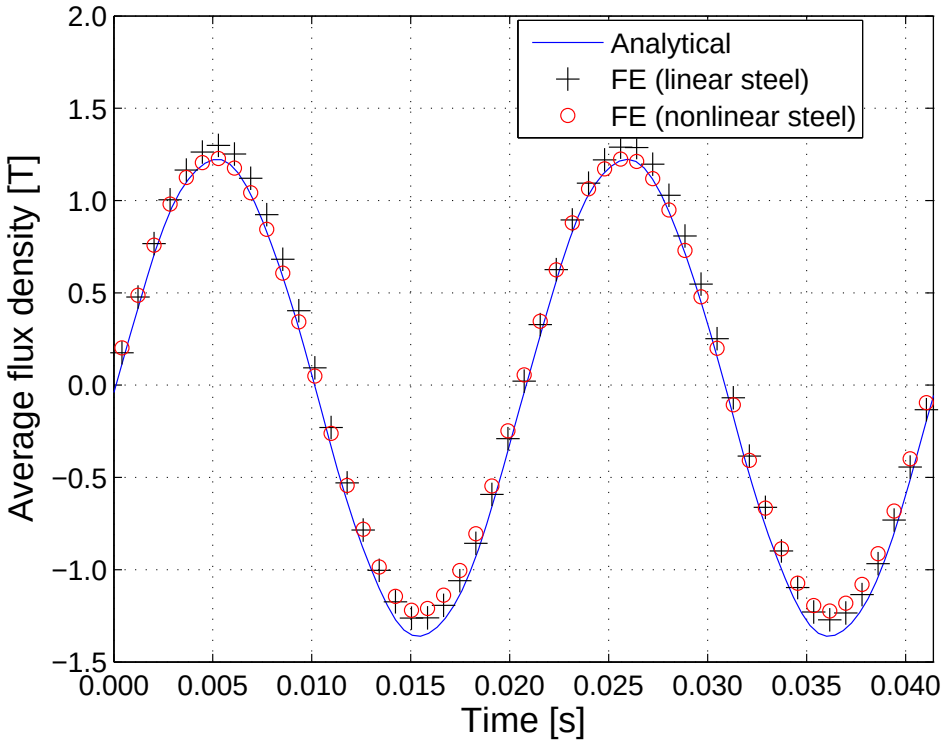

Fig. 5.21: Variation of average magnetic flux density at the back of one stator tooth with time at rated power at rated speed at full-load conditions.

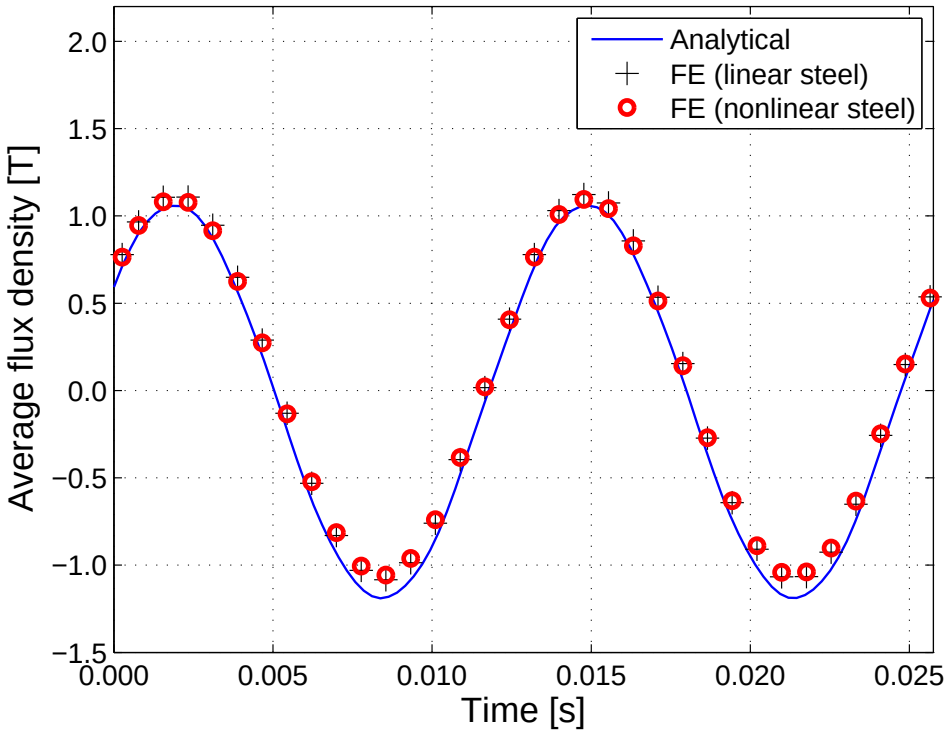

Fig. 5.22: Variation of average magnetic flux density at the back of one stator tooth with time at rated power at rated speed at no-load conditions.

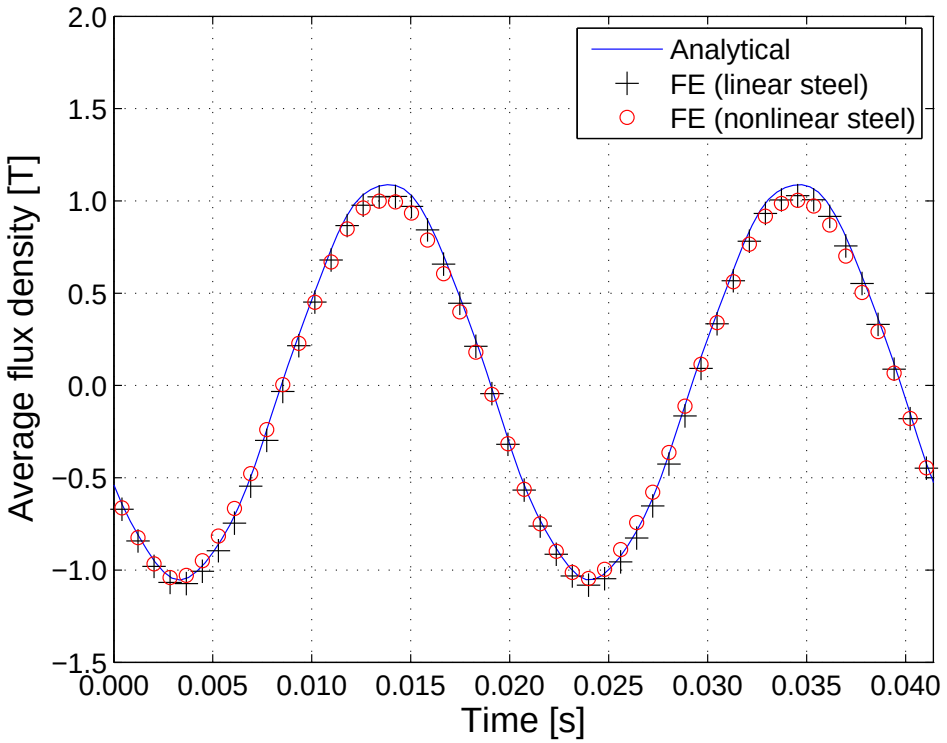

Fig. 5.23: Variation of average magnetic flux density in the back iron with time at rated power at rated speed at full-load conditions.

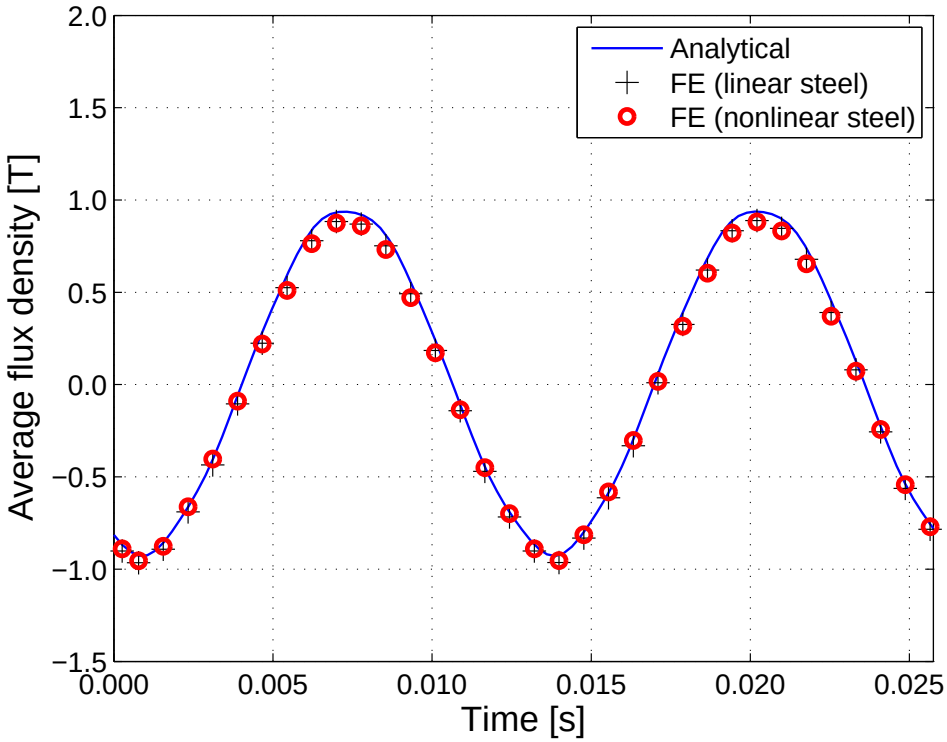

Fig. 5.24: Variation of average magnetic flux density in the back iron with time at rated power at rated speed at no-load conditions.

Fig. 5.25 shows the variation of the losses with the output power. The loss coefficients for the silicon iron employed for the manufacture of the stator and the PPs are given in Table 5.2. It can be seen that good agreement exists between analytical predictions and FE for the flux density. It can also be seen that for this particular design, the iron loss in the PPs accounts for about 15% of the total iron loss. Fig. 5.26 shows the variation of the efficiency with the output power. Efficiencies in excess of 98.5% can be achieved, albeit, the mechanical losses, eddy current losses in the PMs, and the AC losses in the windings are neglected in the analysis. Finally the annual energy efficiency is calculated using the wind distribution in Section 5.1 and it is given in Table 5.1.

	Quantity	Value
k_{hyst}	Hysteresis loss coefficient	$17.9 \times 10^{-3}\ WsT^{-2}kg^{-1}$
a_{hyst}	Hysteresis loss exponent	2.0
b_{hyst}	Hysteresis loss exponent	0
k_{exc}	Excess loss coefficient	$2.0 \times 10^{-4}\ Ws^{1.5}T^{-1.5}kg^{-1}$
m_L	Mass density of laminations	$7.61\ tons/m^3$
d_L	Lamination thickness	$0.35\ mm$
σ_L	Conductivity of laminations	$2.22 \times 10^6\ \Omega^{-1}m^{-1}$

Table 5.2: Parameters for the iron loss calculation.

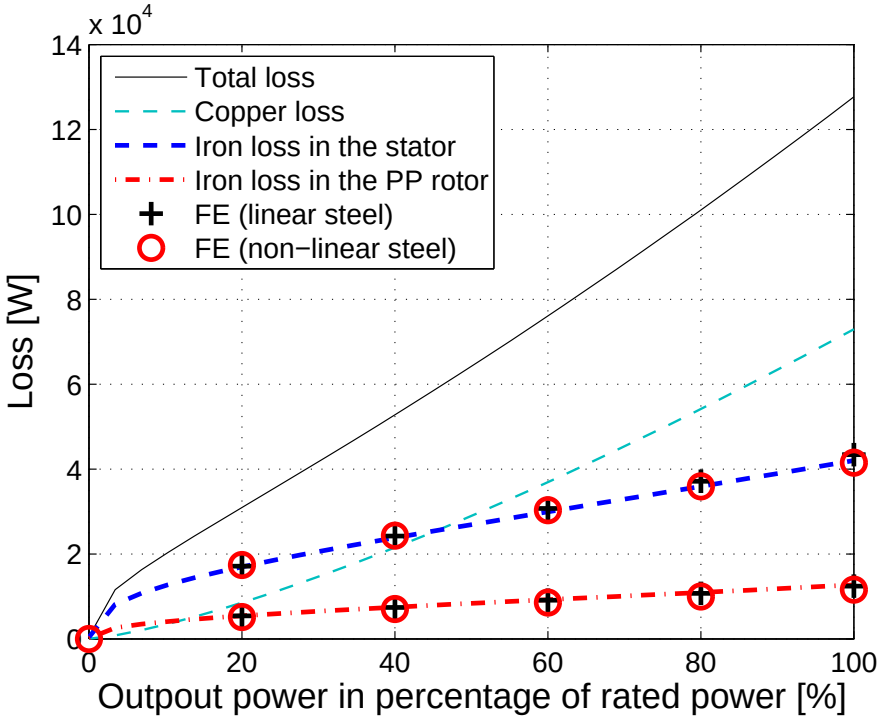

Fig. 5.25: Variation of the losses with the output power.

5.3.1 Interaction of stator PMs with the stator windings

Fig. 5.27 shows the variation of the electromagnetic torque on the PP rotor at the rated speed. For the analysis with the stator currents off, i.e. when the PDD is operated as an MG, the same HS rotor and PP rotor positions are assumed as when the stator currents are on. It can be seen that the torque on the PP rotor is decreased by ~1.5% when the stator coils are turned off. In the following it is shown that the difference in torque can be explained by the existence of the EMF produced by the interaction of the stator PMs and the PPs, and that the magnitude of this torque depends on the relative positions of the PPs and the stator PMs.

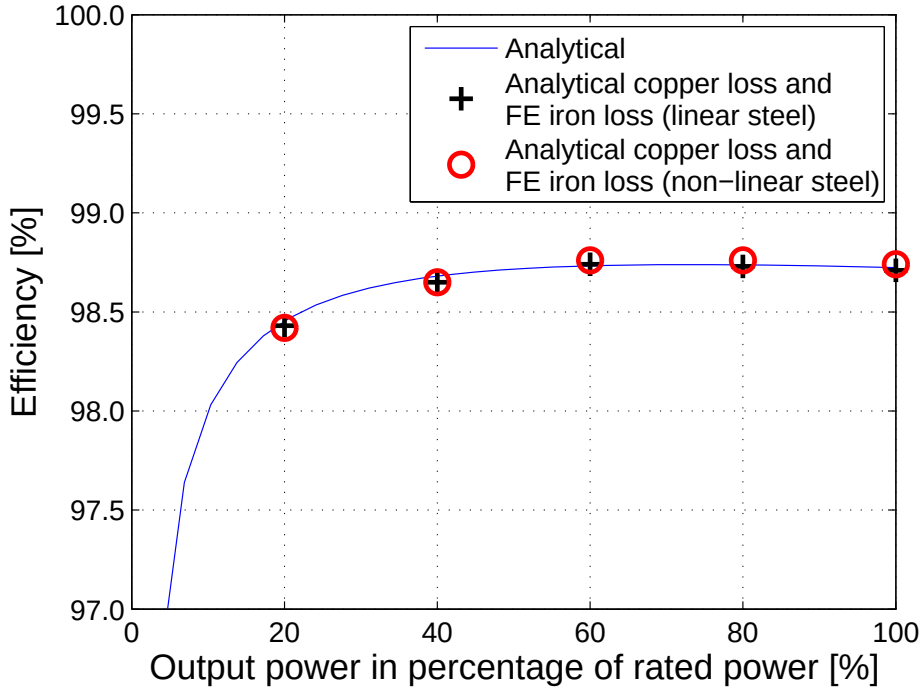

Fig. 5.26: Variation of the efficiency with the output power.

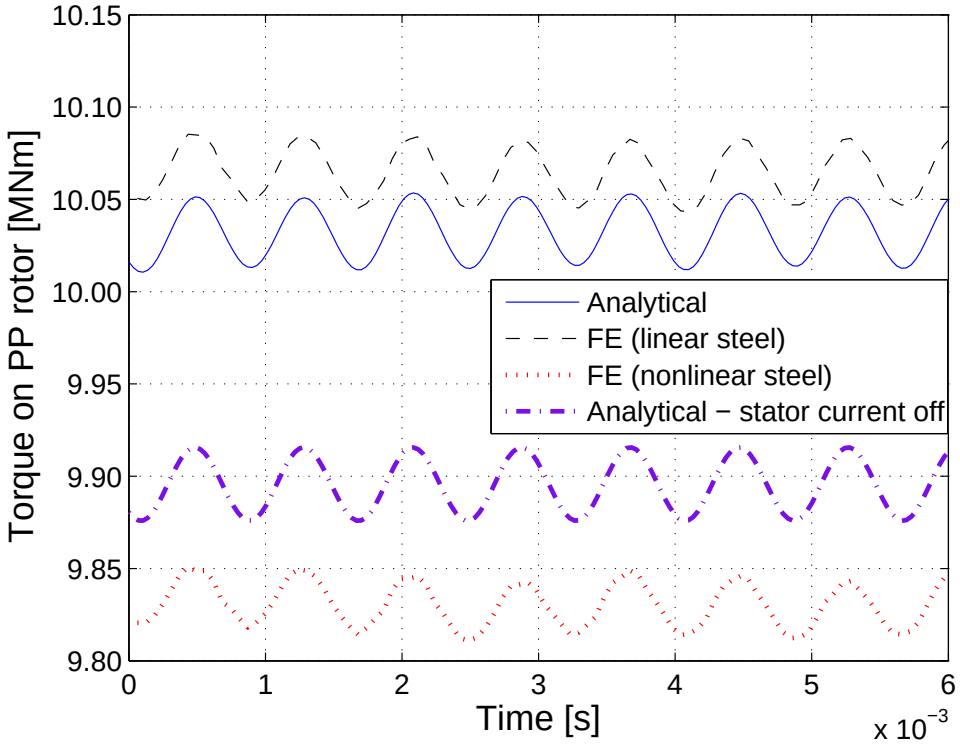

Fig. 5.27: Variation of the torque on the PP rotor with time at rated speed and at full load.

In the analytical and FE models the stator currents are controlled such that they are aligned with the EMF produced by the HS rotor PMs in order to produce max-

imum torque between HS rotor and stator coils. However, the interaction of the stator PMs with the PPs introduces an additional EMF component, and its relative position to the EMF produced by the HS rotor PMs depends on the relative positions of the stator PMs, the HS rotor PMs and the PP rotor. If the rotor positions are selected according to (4.3) the electrical angle between the EMF component due to the stator PMs and the EMF component due to the HS rotor PMs is given by

$$\Theta_{S,EMF} = \frac{\pi}{2} - p_{HS} G \Theta_{\Delta PP} \tag{5.7}$$

where $\Theta_{\Delta PP}$ is given by (4.3), see Fig. 5.28.

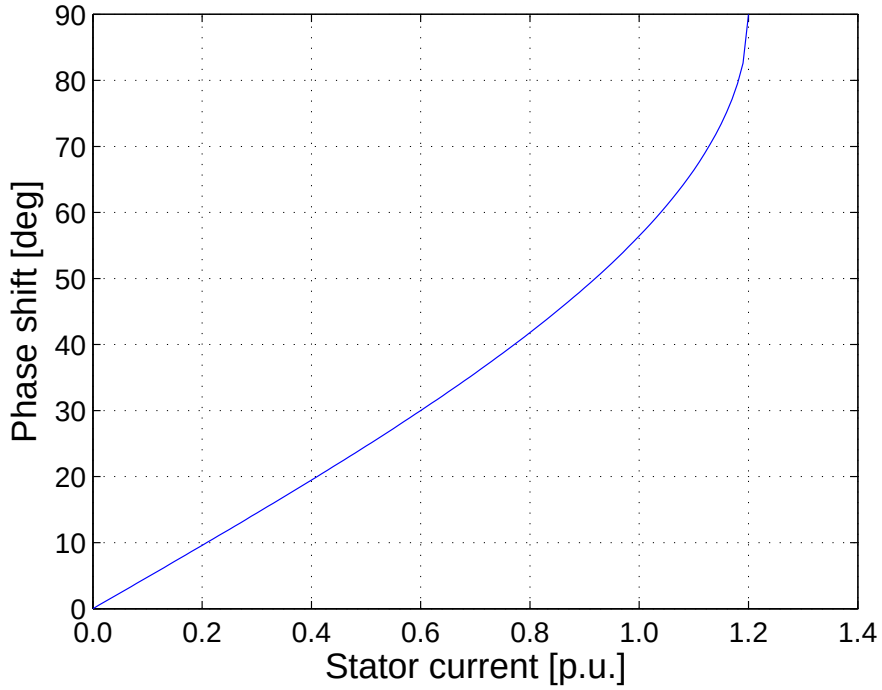

Fig. 5.28: Variation of the electrical angle between the EMF produced by the HS rotor PMs and the EMF produced by the stator PMs with the stator current.

In order to illustrate the effect Fig. 5.29 shows the variation of the torque on the PP rotor with the applied current when the HS rotor PMs are off, while the rotors have the same relative positions as if the HS rotor PMs are turned on. The torque on the PP rotor is then given by

$$T_{PP}^{*} = k_{PP} \sin(Q \Theta_{\Delta PP}) I_{rms} \tag{5.8}$$

where k_{PP} is a constant which is determined by calculating the torque at one particular current and when the HS rotor PMs are off. Since T_{PP}^{*} is much smaller than

T_{PP} (less than 1.5%), the effects of this interaction are neglected in the forthcoming analysis.

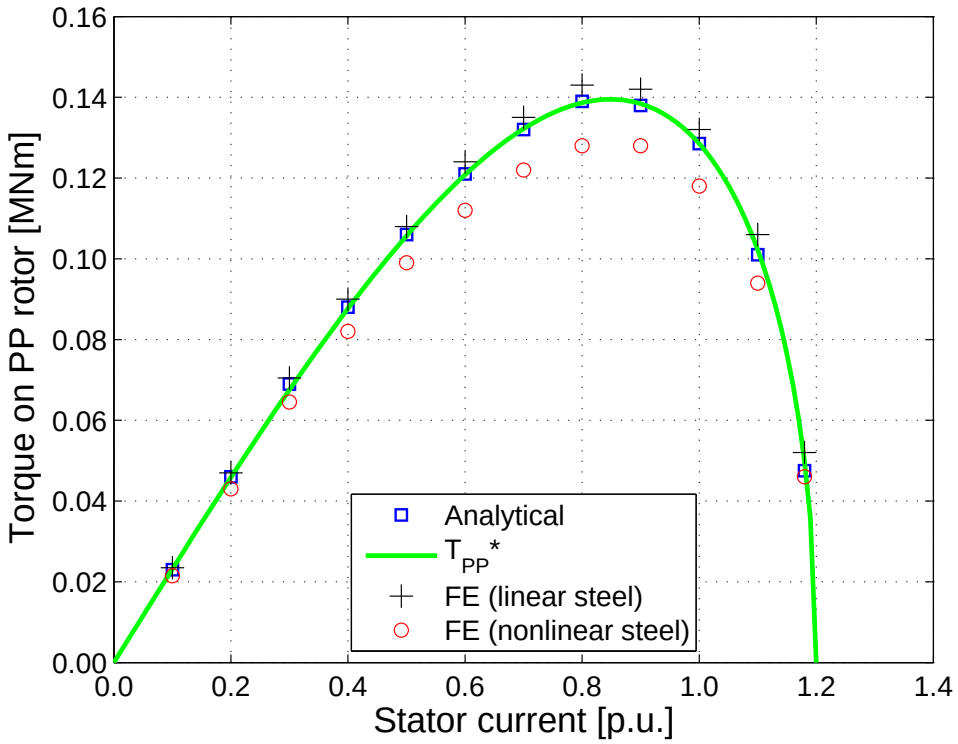

Fig. 5.29: Variation of the torque on the PP rotor with the stator current (per unit of the rated stator current), when the HS rotor PMs are turned off and torque is only produced between stator PMs and the stator coils.

5.4 Effects of leading design parameters

In this section PDDs with the same pullout torque and the same power rating as the PDD in Table 5.1 are studied. The PDD in Table 5.1 is, therefore, employed as a benchmark for the forthcoming simulation studies.

5.4.1 Effects of the rated current density and the airgap diameter

Since analytically the flux density distribution in the airgaps is only dependent on the current in the slot and the equivalent current sheet (see section 4.2) a variation of the current density at rated power and hence the amount of copper have no effect

on the flux density distribution in the MG component and the torque transmission. Furthermore, it is shown in section 2.4 that the flux density and the shearstress due to the flux density produced by the PMs remain constant when scaling by a factor s. For continuous operation the average torque on the HS rotor produced by the interaction of the HS rotor and stator PMs has to be cancelled by T_E. Hence, from (4.5) it can be seen that also Q_{rms} and, therefore, the coefficients of the current sheet remain constant when the radial dimensions of the MG component are scaled. Similarly to section 2.4 equations (2.43)-(2.52) and (4.14) can be written in matrix form as

$$M\overrightarrow{x} = \overrightarrow{v} \tag{5.9}$$

where $\overrightarrow{x}$ consists of the unknown coefficients and the only non-zero elements of $\overrightarrow{v}$ are given by (2.44) and (4.14). Therefore, both $\overrightarrow{v}$ and M are constant and independent of s. If the axial length is adjusted by a factor s^{-2} also the torque, the PM mass and the PP rotor and HS rotor laminated steel mass remain constant, and are, therefore, independent from the aspect ratio of the MG component, and their values for this design are given in Table 5.1.

Figs. 5.30 and 5.31 show the variations of the copper mass and the stator laminated steel mass with the airgap diameter and the current density at rated power, respectively. A packing factor of $p = 0.5$ has been assumed in the slot area, see Table 5.1. The dimensions of the stator teeth and the back-iron are selected, such that the average flux densities remain below 1.5T. It can be seen that for a given current density, increasing the diameter decreases the copper and lamination steel mass. However, an increase in airgap diameter could lead to an increase in the mass of structural components [68] and therefore could also lead to an increase of the total cost of the PDD. Furthermore, an increase of the diameter would also increase the impact of the end effects on the transmitted torque.

Fig. 5.32 shows the variation of the efficiency with the airgap diameter and the current density at rated power. It can be seen that for a given efficiency an airgap diameter exists, below which a particular efficiency cannot be achieved.

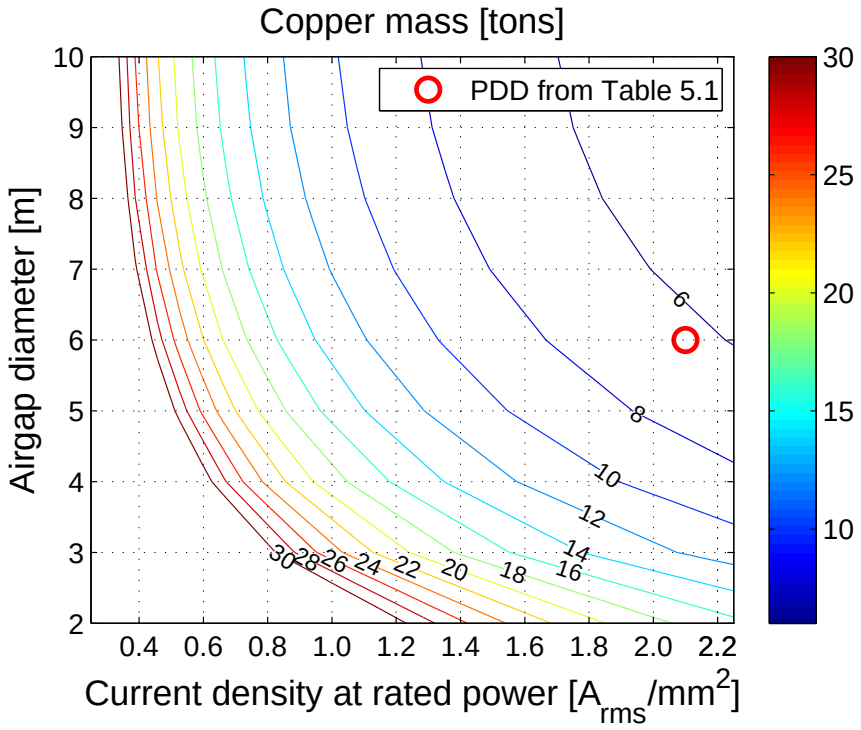

Fig. 5.30: Variation of copper mass with the airgap diameter and current density at rated power.

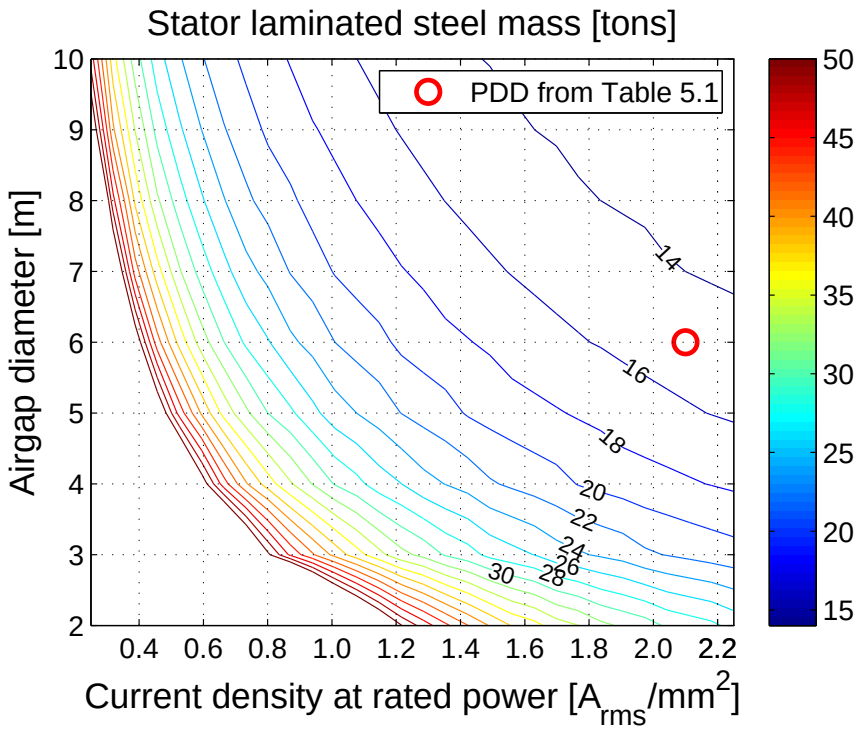

Fig. 5.31: Variation of stator laminated steel mass with the airgap diameter and current density at rated power.

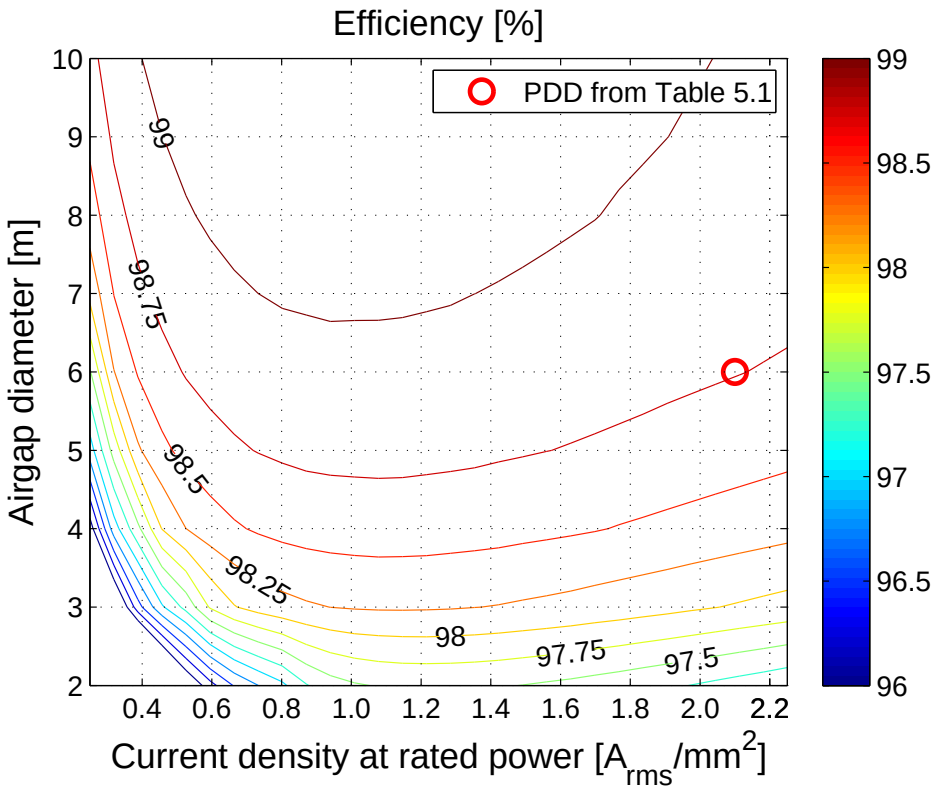

Fig. 5.32: Variation of efficiency at rated power with the airgap diameter and current density at rated power.

Fig. 5.33 shows the variation of the efficiency with the total active mass. It can be seen that a maximum exists for a given airgap diameter at about $1.0A_{rms}/mm^2$. However, it can also be seen that the efficiency does not reduce significantly when the current density is increased to $2.0A_{rms}/mm^2$, while the active mass is reduced significantly. For example, at the airgap diameter of $6m$ an efficiency of ~99.0% can be achieved with a total active mass of less than 60tons for a current density of $1.0Arms/mm^2$, however, if the current density is increased to $2.0Arms/mm^2$ an efficiency larger than 98.5% can be achieved with a total active mass of only ~45 tons.

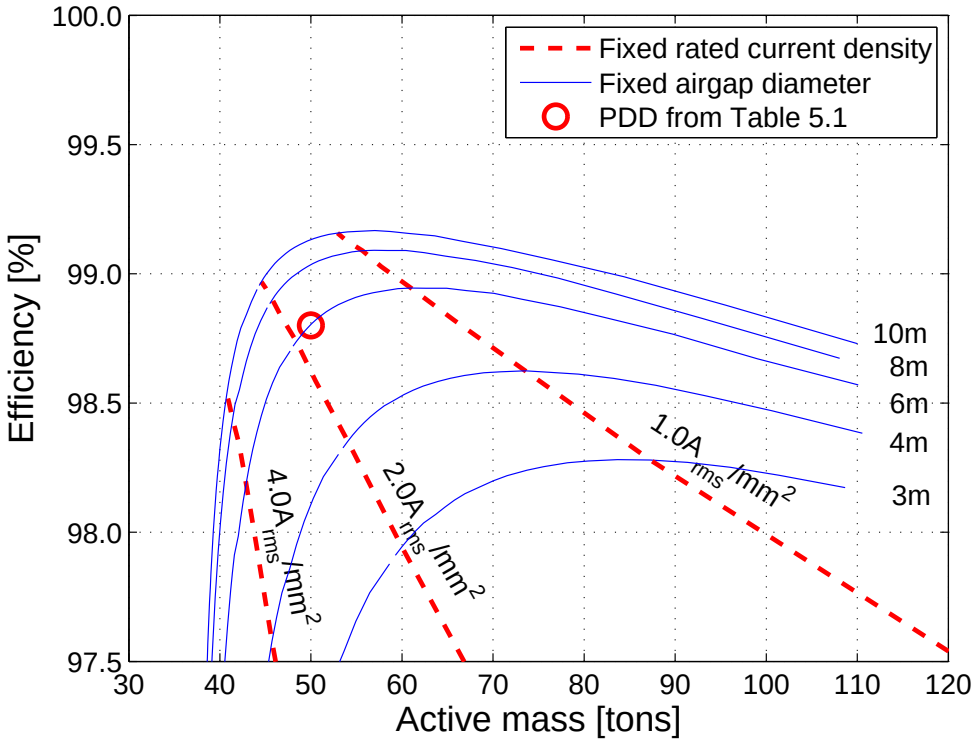

Fig. 5.33: Variation of efficiency at rated power with the total active mass.

5.4.2 Effects of the electrical output frequency

In general a wide range of rated output frequencies may be considered for the PDD, where the output frequency is related to the number of sections by

$$f_{out,R} = G\omega_{PP}Kp^*_{HS} \tag{5.10}$$

Figs. 5.34-5.36 show the variations of the PM mass, the active mass and the efficiency at rated power with the rated electrical output frequency and the achievable σ_{pull} in the MG element of the PDD. The airgap diameter is fixed to 6.0m and the current density is $2.0A_{rms}/mm^2$ at rated power. It can be seen that for this particular airgap diameter and gear ratio, and for a rated frequency of $f_{out,R} \approx 50Hz$ and $\sigma_{pull} = 120kPa$, an efficiency in excess of 98.7% can be achieved with a total active mass of less than 50tons and a total PM mass of less than 13.5 tons. It can also be seen that for a given PM mass σ_{pull} of the MG element varies significantly and an optimum electrical output frequency (number of poles on the HS rotor) exists for which the achievable σ_{pull} is maximum, Fig. 5.34.

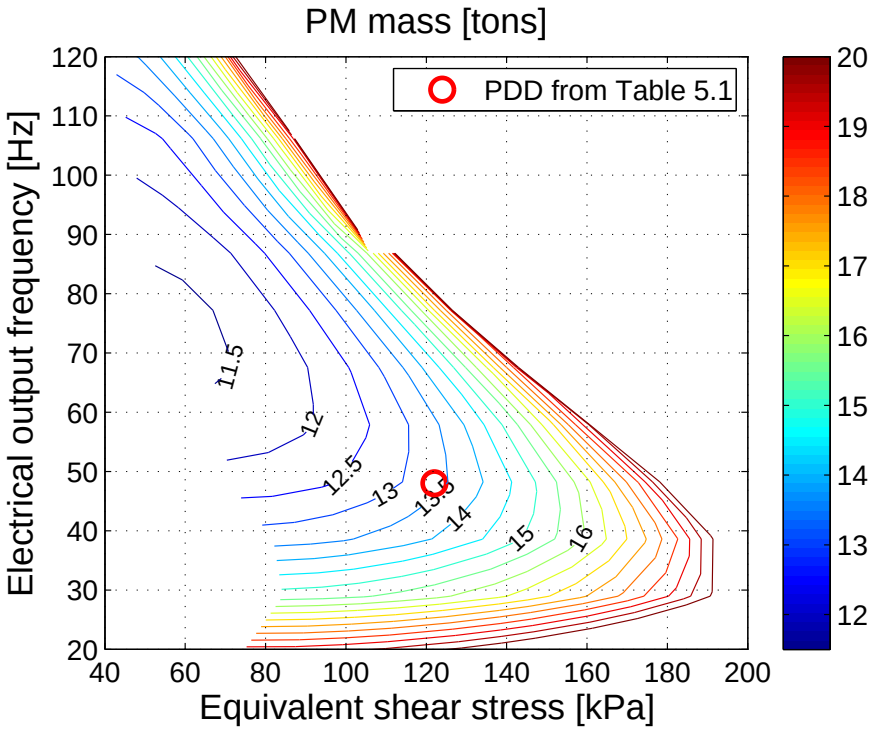

Fig. 5.34: Variation of PM mass with the rated electrical output frequency and σ_{pull}.

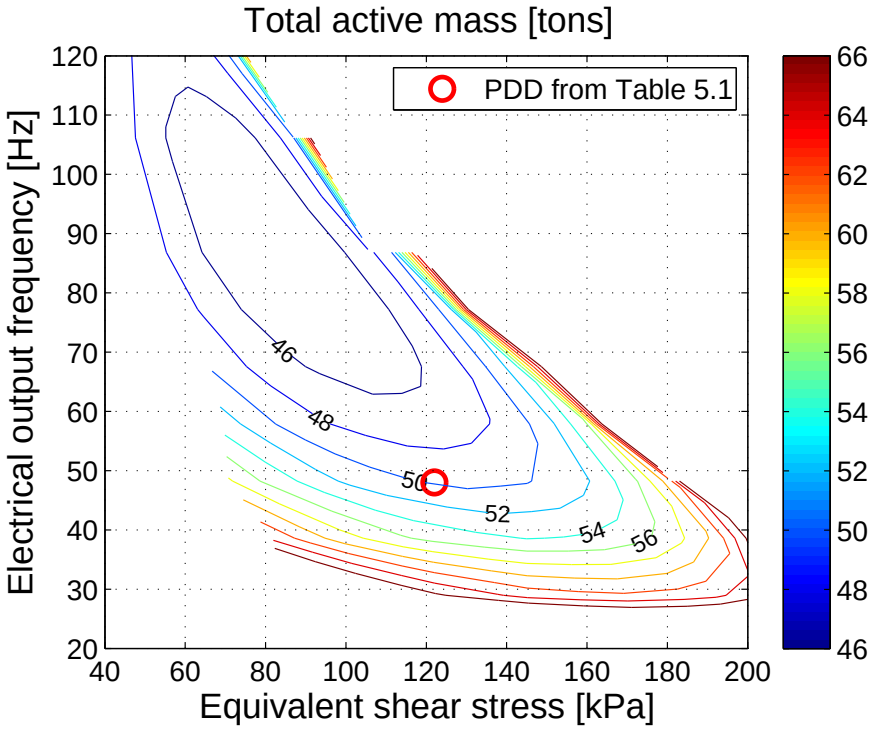

Fig. 5.35: Variation of total active mass with the rated electrical output frequency and σ_{pull}.

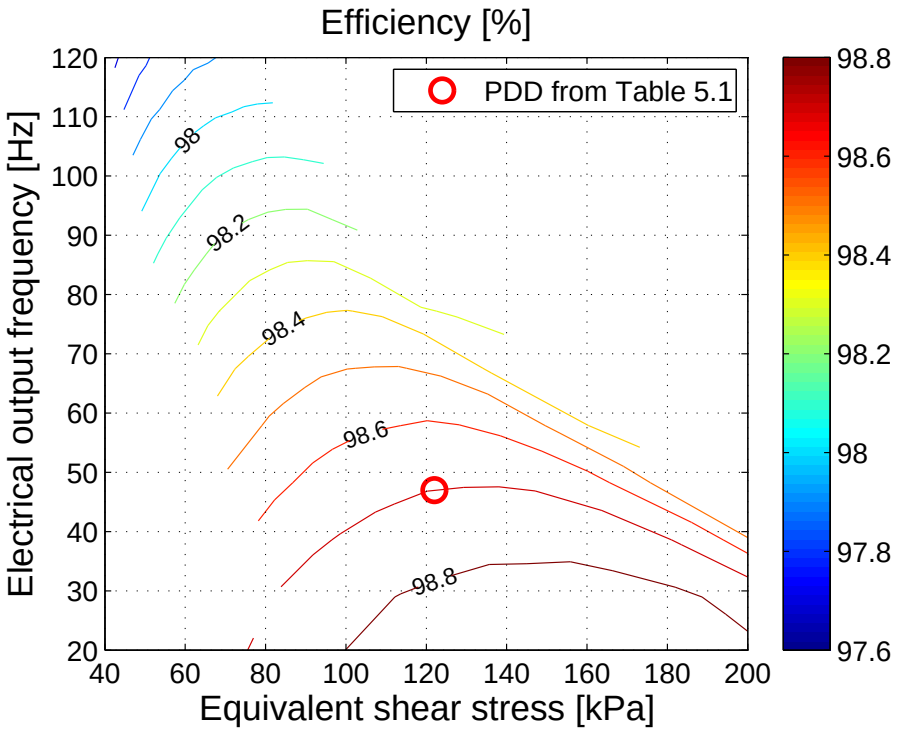

Fig. 5.36: Variation of rated efficiency with the rated electrical output frequency and σ_{pull}.

5.4.3 Effects of the gear ratio

Figs. 5.37-5.38 show the variations of the PM mass and active mass of the PDD with the maximum achievable σ_{pull} in the MG element of the PDD, when the rated current density is $1.0A_{rms}/mm^2$. The designs have the same electrical output frequency $f_{out,R} \approx 50Hz$ at the rated speed. It can be seen that for a given gear ratio a minimum active mass exists, however, for different gear ratios the minimum may be at different σ_{pull}. Similar to the analysis in section 3.4.5 it can also be seen that for higher gear ratios the required PM mass may be increased.

For a 6m airgap diameter and when the designs highlighted in Fig. 5.37 are selected, Figs. 5.39-5.40 show the variations for the active mass and the efficiency of the PDD, respectively, with the current density. It can be seen and as expected, the active mass of the PDD is decreased when the current density is increased. Furthermore and similar to the results of the analysis in section 5.4.1, an optimum current density for which the efficiency is maximum exists at ~$1.0A_{rms}/mm^2$ for the investigated gear ratios.

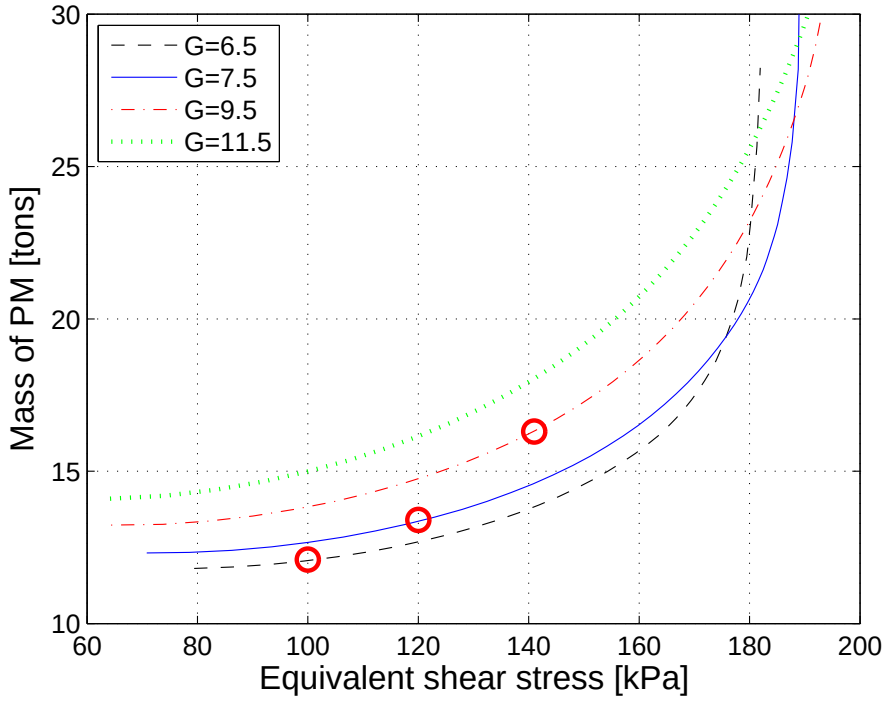

Fig. 5.37: Variation of PM mass with maximum achievable σ_{pull} and with a rated electrical output frequency of about $f_{out,R} \approx 50Hz$ for several gear ratios G. Three designs are selected for further investigation of the PDD (highlighted in red).

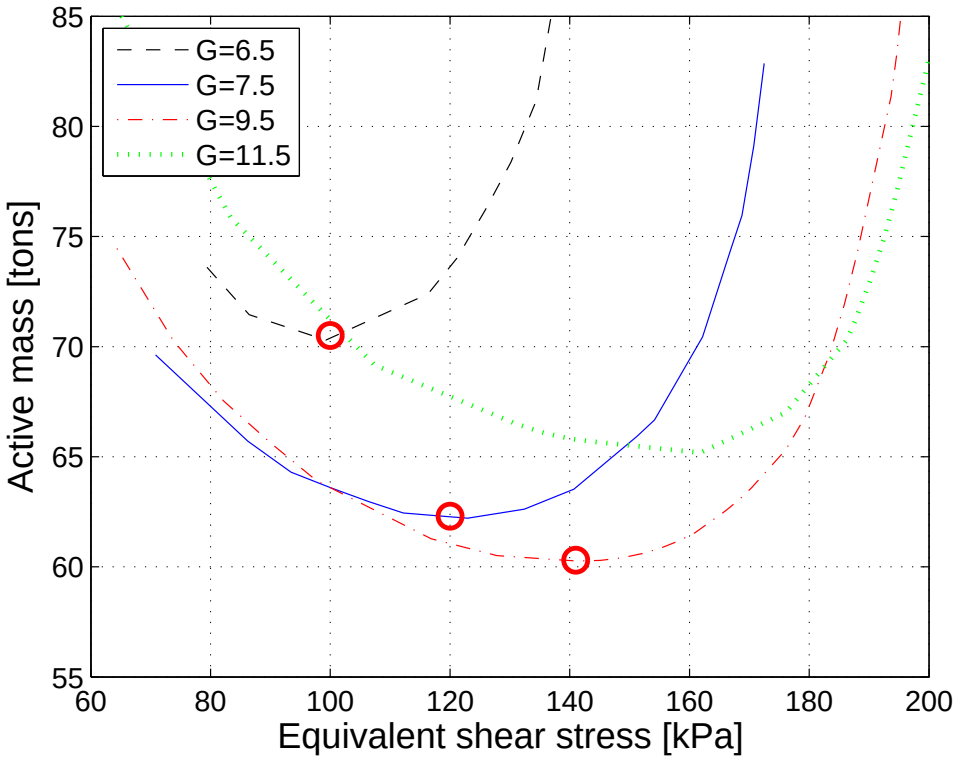

Fig. 5.38: Variation of total active mass with maximum achievable σ_{pull} and with a rated electrical output frequency of about $f_{out,R} \approx 50Hz$ for several gear ratios G. Three designs are selected for further investigation of the PDD (highlighted in red).

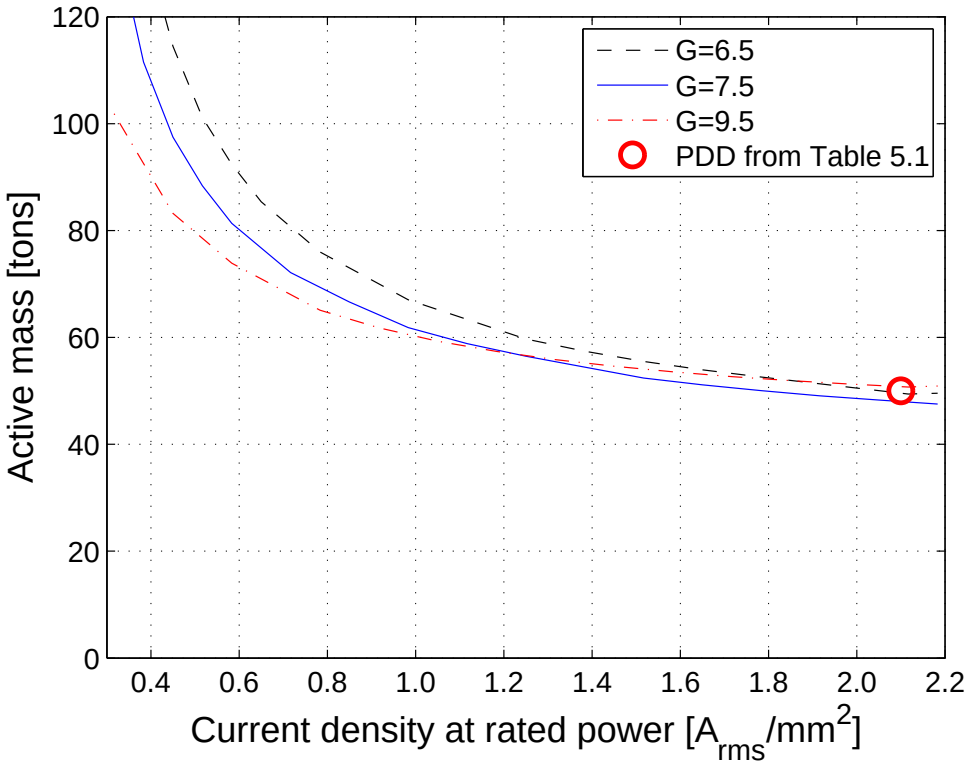

Fig. 5.39: Variation of active mass with the selected current density for several gear ratios G.

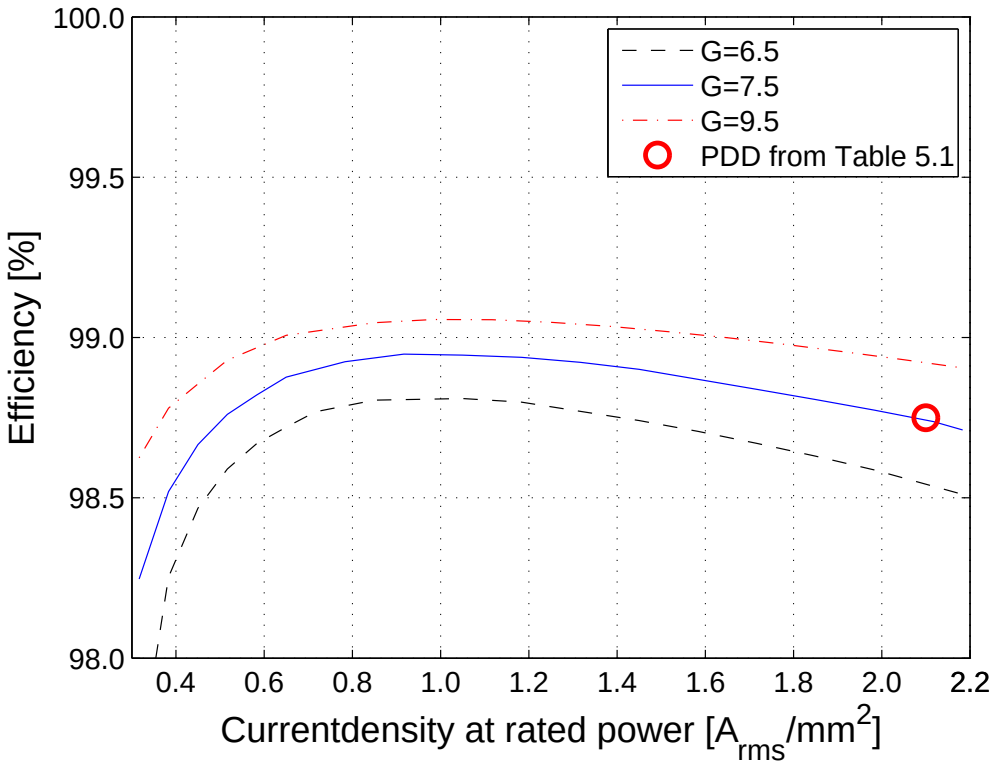

Fig. 5.40: Variation of active mass with the selected current density for several gear ratios G.

5.5 Conclusions

The application of a PDD generator for a 10MW wind turbine is investigated. The developed analytical models in Chapter 4 are utilised for the optimisation of a PDD and it is shown that a rated efficiency of ~98.7% can be achieved. The selected design has a PM mass of 13.5$tons$, a copper mass of 7$tons$ and a total active mass of 50$tons$. Furthermore, the total mass of the generator could exhibit a similar mass as a system, where the MG component is coupled to a PM direct drive, however the efficiency could be improved. The optimised PDD is employed for the comparison of the predictions of the analytical models with those from 2D FE studies, and it is shown that a good agreement with 2D FE analysis exists for the flux density waveforms, the transmitted torque, the torque ripple and the iron loss. Furthermore, the models are further employed to discuss the effects of the leading design parameters on the main PIs. It is shown that although increasing the airgap diameter could result in significant reductions of the active masses and an improved efficiency, this may only be achieved at the expense of increased cost of the structural components. It is also shown that the number of circumferential sections, and the gear ratios could have a significant effect on the active masses and the electromagnetic efficiency of the PDD.

Chapter 6

PDDs with coil excited magnetic gear

Despite the many advantages, a drawback of PDDs remains the large volume of PM required for their realisation. Therefore, in this chapter it is proposed that in order to reduce the PM mass and introduce an extra degree of controllability, the HS rotor is excited using coils supplied with a DC current, Fig. 6.1. Analytical techniques similar to those of PM excited PDDs are developed in order to investigate the effects of the key design parameters on the PI of the PDD, such as the active masses and the electromagnetic efficiency. However, similarly to the PM excited PDD, a design is selected for a more detailed analysis using FE methods to take into account of effects such as non-linearity of the steel.

6.1 Principle of operation

Similarly to the PM excited PDD the windings on the HS rotor interact with the windings on the stator to produce electromagnetic torque, which is transferred to the PP rotor by the interaction of the windings on the HS rotor and the PMs on the stator. Fig. 6.2 shows the harmonic spectra of the flux density waveforms in the airgaps adjacent to the stator and the HS rotor, due to the windings on the HS rotor and the PMs on the stator, respectively.

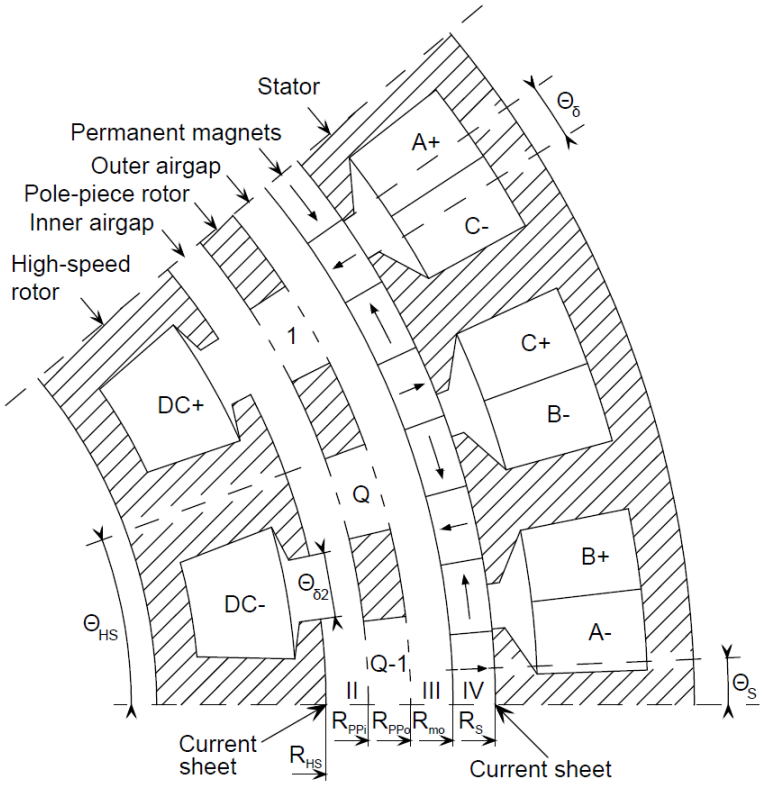

Fig. 6.1: Geometry for a coil excited PDD section with a periodic symmetry of 40 degrees. Permanent magnets consist of 4 Halbach segments on the stator.

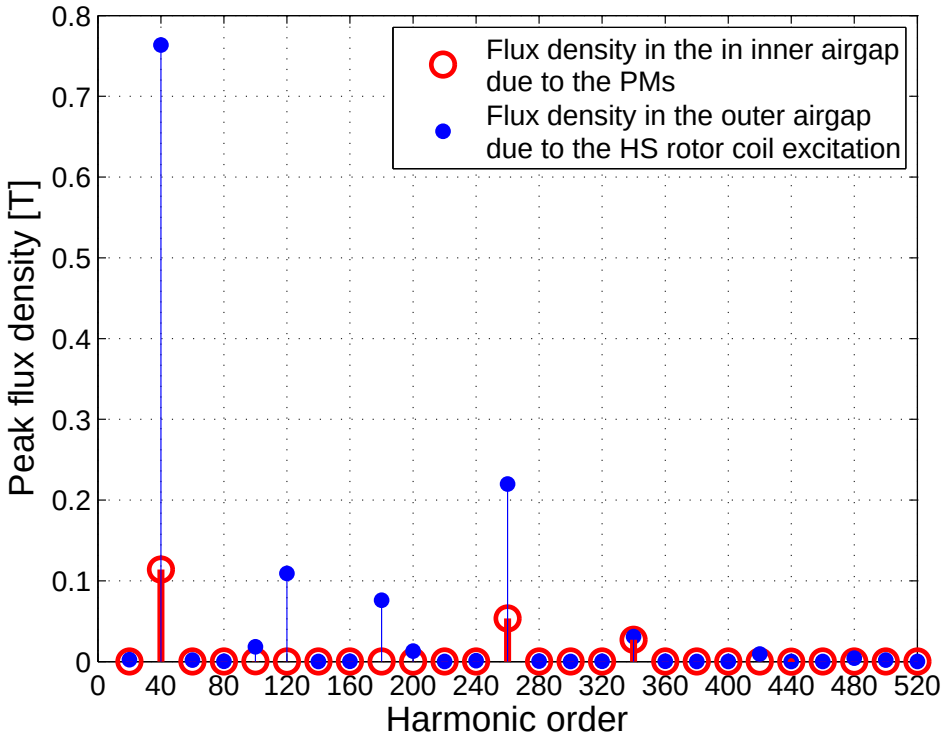

Fig. 6.2: Harmonic spectra of the flux density waveforms in the inner and outer airgap due to the HS rotor coil excitation and the PMs respectively.

The equations (4.6)-(4.7) which govern the motion of the HS and PP rotors are now in addition to the current of the stator windings I_{rms} also dependent on the dc current in the HS rotor I_{HS}:

$$J_{HS}\frac{d^2\Theta_{HS}}{dt^2} = \frac{p_{HS}}{Q}T_{pull}(I_{HS})\sin(Q\Theta_{PP} - p_{HS}\Theta_{HS}) - T_E(I_{HS}, I_{rms}) \quad (6.1)$$

$$J_{PP}\frac{d^2\Theta_{PP}}{dt^2} = k_T(\Theta_T - \Theta_{PP}) - T_{pull}(I_{HS})\sin(Q\Theta_{PP} - p_{HS}\Theta_{HS}) \quad (6.2)$$

$$J_T\frac{d^2\Theta_T}{dt^2} = T_W - k_T(\Theta_T - \Theta_{PP}) \quad (6.3)$$

Fig. (6.3) shows the torsional model of a wind turbine drive train employing a coil excited PDD. Similar to the PM excited PDD the MG element of the PDD can be replaced by two ideal gears and a 1-to-1 magnetic coupling with the stiffness

$$k_G = \frac{T_{pull}(I_{HS})}{Q}\cos(Q\Theta_{PP} - p_{HS}\Theta_{HS}) = \frac{T_{pull}(I_{HS})}{Q}\cos(\Theta_E) \quad (6.4)$$

It can be seen that in addition to the the load angle Θ_E the stiffness is now also dependent on the current I_{HS}. Furthermore, and similar to a wound rotor synchronous machine the back EMF of the PDD is controlled by the current I_{HS}. However, in addition the pullout torque of the PDD is also dependent on the magnitude of I_{HS}. This should be taken into consideration, when controlling such a PDD.

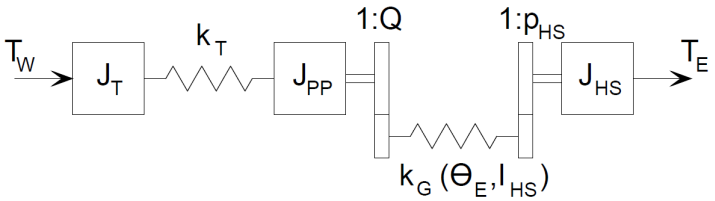

Fig. 6.3: Fig. 3. 3-inertia torsional model of the coil excited PDD.

6.2 Analytical model, optimisation procedure and comparison with finite element

6.2.1 Analytical model

The analytical techniques which are developed for the prediction for the flux density distribution in the airgaps of the MGs and PDDs with PM excitation in chapters 2

and 4 are extended to accommodate the HS rotor winding similarly to section 4.2, by replacing the PMs on the HS rotor by current sheets on the surface of the HS rotor. At the stator bore radius R_S, the circumferential component of the magnetic field equals the current sheet, thus

$$H_{\theta,II}(R_{HS},\theta) = \frac{B_{\theta,IV}(R_{HS},\theta)}{\mu_0} = -j_{HS}(\theta) \tag{6.5}$$

where $H_{\theta,II}$ is the circumferential component of the magnetic field, and j_{HS} is the current sheet representing the HS rotor windings. The current sheet is expressed in terms of a Fourier series by

$$j_{HS}(\theta) = \sum_{n=1}^{\infty} \begin{pmatrix} j_{A,n} \\ j_{C,n} \end{pmatrix} \cdot \begin{pmatrix} \cos(n\theta) \\ \sin(n\theta) \end{pmatrix} \tag{6.6}$$

The coefficients $A_{II,n}$and $B_{II,n}$ in equation (2.40) are then given by

$$\begin{pmatrix} A_{II,n} \\ C_{II,n} \end{pmatrix} = \mu_0 \begin{pmatrix} j_{A,n} \\ j_{C,n} \end{pmatrix} \tag{6.7}$$

6.2.2 Optimisation process

The same optimisation process as in Section 5.2 has been employed for the PDD with coil excited HS rotor, however, for the HS rotor only the copper losses are considered in the optimisation process. Furthermore, since saturation effects in the HS rotor iron would also affect the torque transmission, the optimised design has been refined using 2D FE in order to take into account the saturation effects. Table 6.1 gives the parameters of the optimised PDD for a 10MW wind turbine. In summary, the parameters that have been varied in the optimisation analysis are: the PM thickness, the HS rotor slot opening, the airgap diameter, the current density, the number of identical sections, and the gear ratio.

	Quantity	Value
P_R	Rated shaft power	10 MW
$T_{PP,R}$	Rated torque	9.9 MNm
T_{Pull}	Analytical pullout torque	11.9 MNm
$\omega_{PP,R}$	Rated rotational speed of PP rotor	9.6 rpm
$f_{out,R}$	Rated supply frequency	48 Hz
p_{HS}	Pole-pairs on HS rotor	40
p_S	Pole-pairs on stator	260
m_S	Halbach segments per pole-pair on stator	4
Q	Pole pieces	300
K	Number of identical sections	20
G	Gear ratio	7.5
D	Inner airgap diameter	8.0 m
	Radial thickness of the stator PMs	19.5 mm
	Radial thickness of PP segments	41.9 mm
	airgap lengths	8.0 mm
l_a	Active axial length	1.22 m
β	PP slot opening angle	$\pi/300$ rad
B_r	Remanence of PMs	1.25 T
μ_r	Relative recoil permeability	1.05
	Slot packing factor on the stator	0.5
	Slot packing factor on the HS rotor	0.6
	Rated current density in the stator windings	3.1 A_{rms}/mm^2
	Rated current density in the HS rotor windings	3.1 A/mm^2
	Rated electromagnetic efficiency	95 %
	Annual energy efficiency*	94 %
	Mass of PMs	4.5 $tons$
	Mass of copper	20 $tons$
	Mass of laminated steel	59 $tons$
	Mass of structural steel	222 $tons^{\#}$

The structural masses is calculated assuming a linear relation to the airgap diameter and the active mass. For a 6m airgap diameter PDD the structural mass is assumed to be twice the active mass.
*Annual energy efficiency calculated with a minimum EMF equal to the minimum EMF of the PM excited PDD in Table 5.1.

Table 6.1: Parameters of the coil excited PDD

6.2.3 Comparison with finite element

The analytical model is compared with 2D-FE studies for the PDD in Table 6.1. Figs. 6.4 and 6.5 show the radial and circumferential flux density components in

the inner airgap on-load, respectively. Figs. 6.6 and 6.7 show the radial and circumferential flux density in the outer airgap on-load, respectively. It can be seen that a good agreement exists between FE and analytical model. However minor differences can be observed at the inner airgap due to the effects of the slot openings.

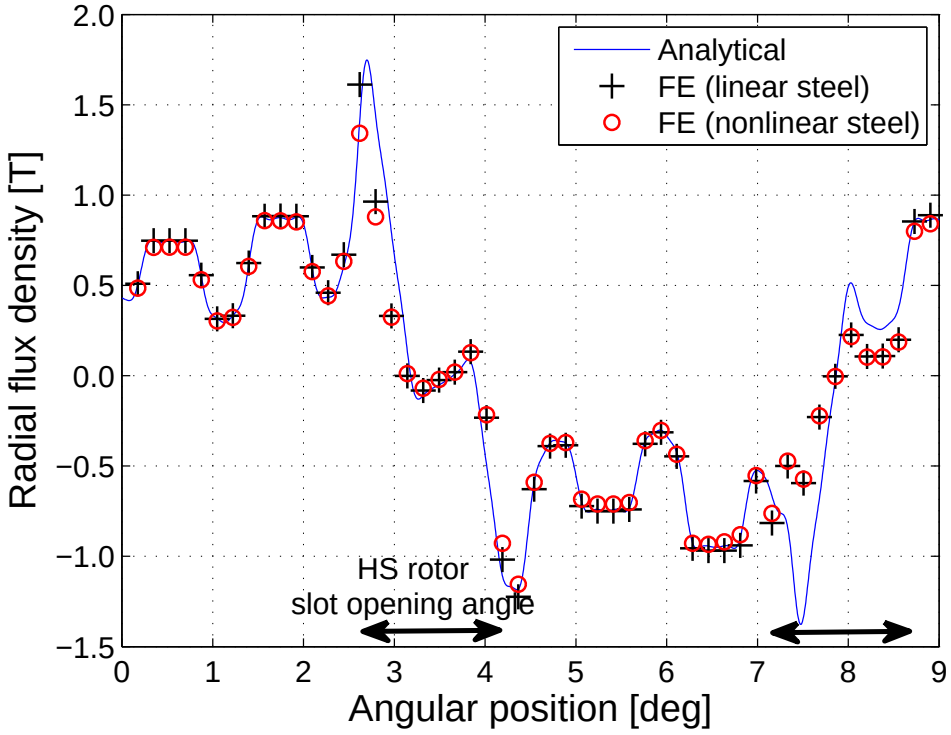

Fig. 6.4: Variation of the radial component of the magnetic flux density in the inner airgap with the circumferential position.

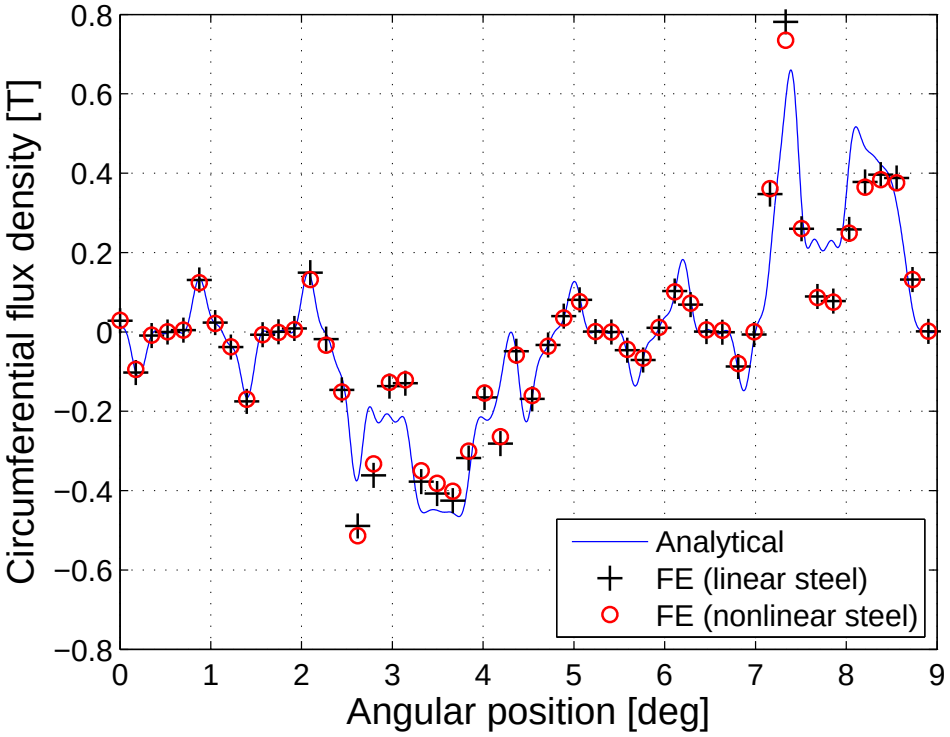

Fig. 6.5: Variation of the circumferential component of the magnetic flux density in the inner airgap with the circumferential position.

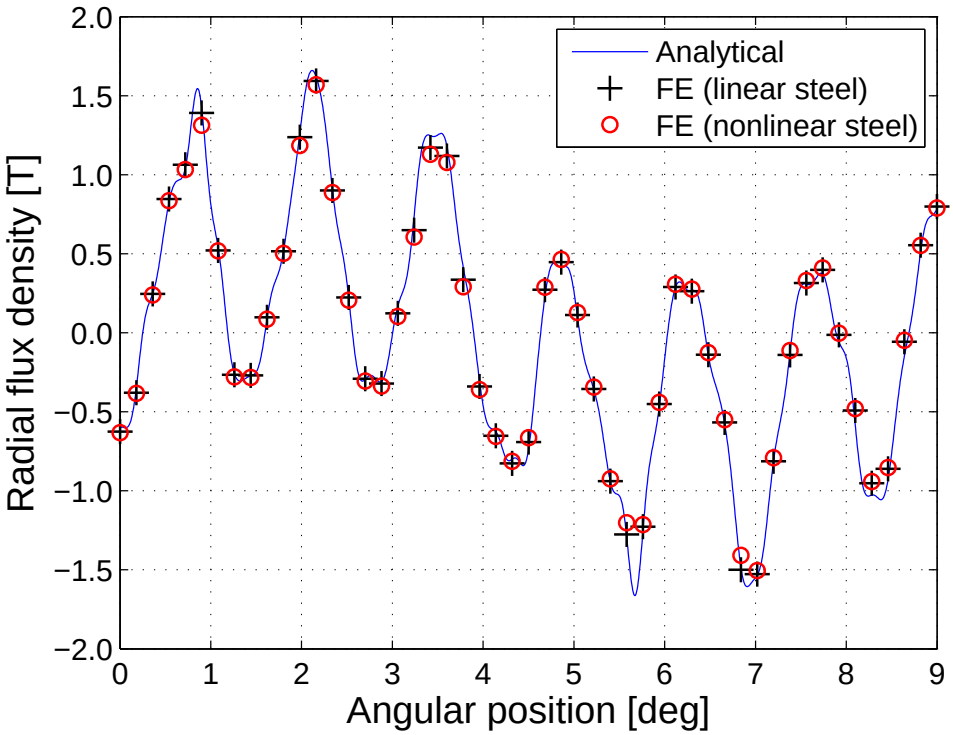

Fig. 6.6: Variation of the radial component of the magnetic flux density in the outer airgap with the circumferential position.

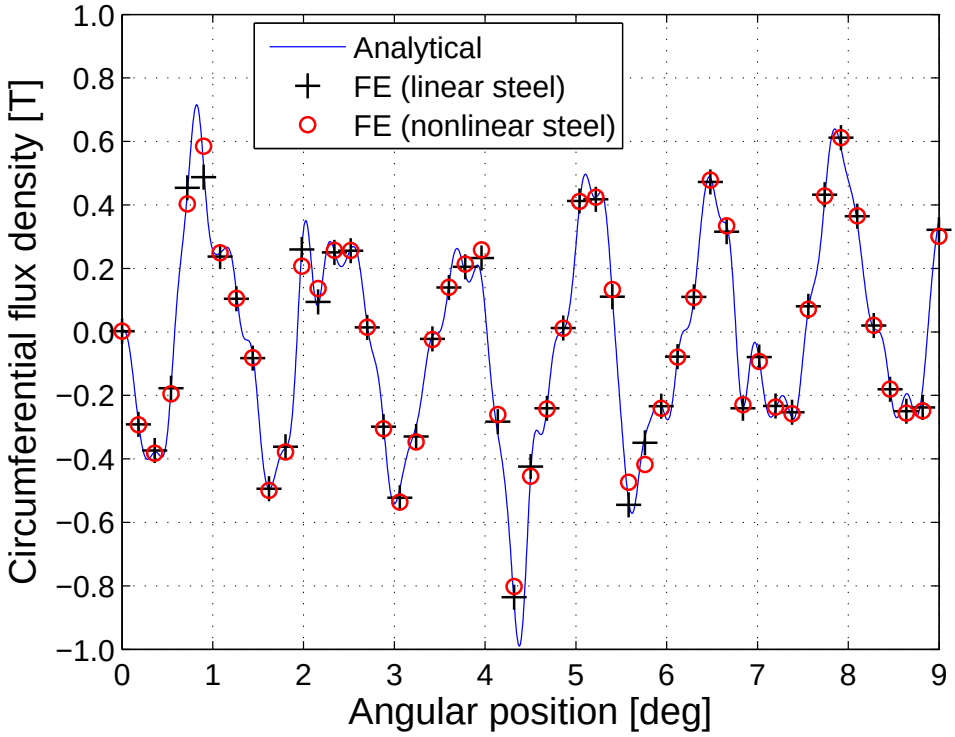

Fig. 6.7: Variation of the circumferential component of the magnetic flux density in the outer airgap with the circumferential position.

With the stator currents turned-off and the PDD being operated as a MG, Fig. 6.8 and Fig. 6.9 show the electromagnetic torque on the PP rotor and the HS rotor at pullout torque, respectively. It can be seen that the average torque calculated by FE is slightly lower, particularly for steel with non-linear characteristics, however the difference is only about 5%.

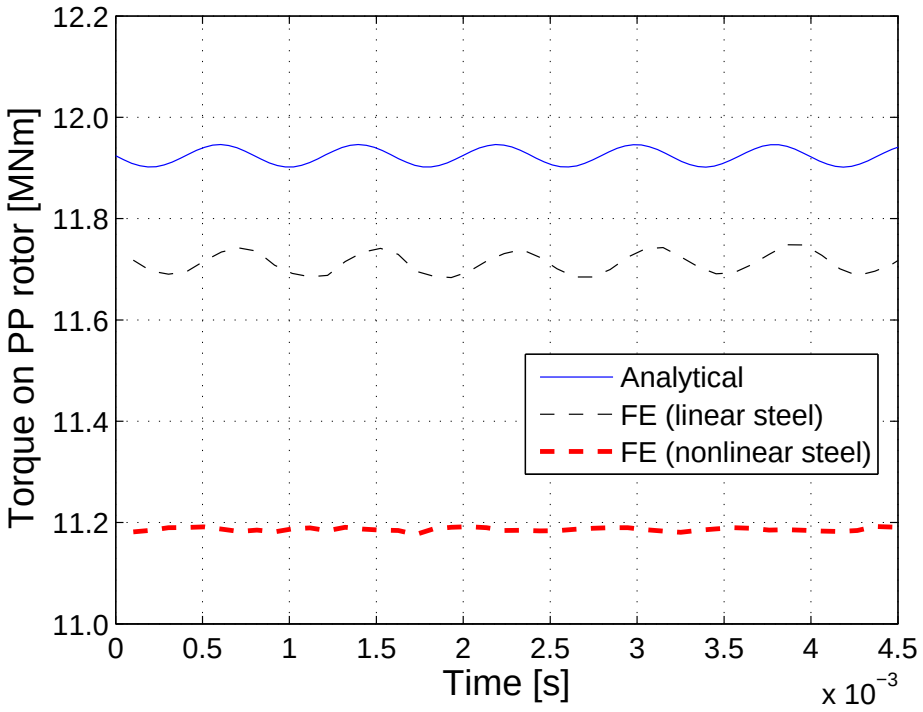

Fig. 6.8: Variation of the torque on the PP rotor with the MG in pullout torque position and with the stator current turned off.

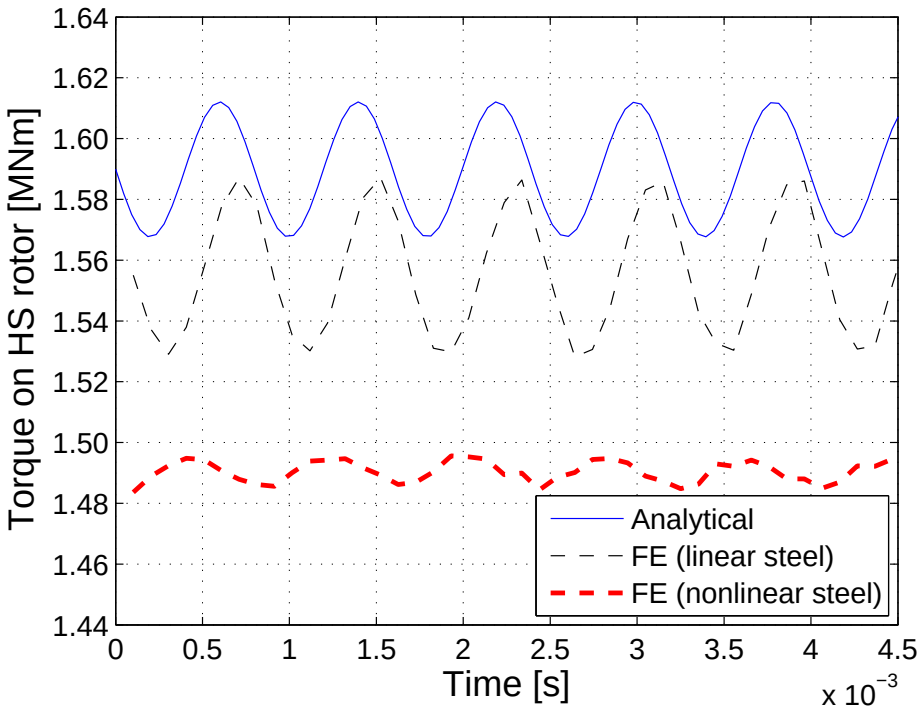

Fig. 6.9: Variation of the torque on the HS rotor with the MG in pullout torque position and with the stator current turned off.

Fig. 6.10 and Fig. 6.11 show the variations of the pullout torque and the fun-

damental component of the EMF with the current I_{HS}, respectively. It can be seen that the pullout torque and the EMF would initially vary linearly with I_{HS}, however, saturation in the HS rotor poles introduces a degree of non-linearity as I_{HS} is increased, particularly beyond the rated value. It may be worth noting that the EMF does not start at zero, due to the EMF induced by the interactions of the PMs on the stator with the PPs.

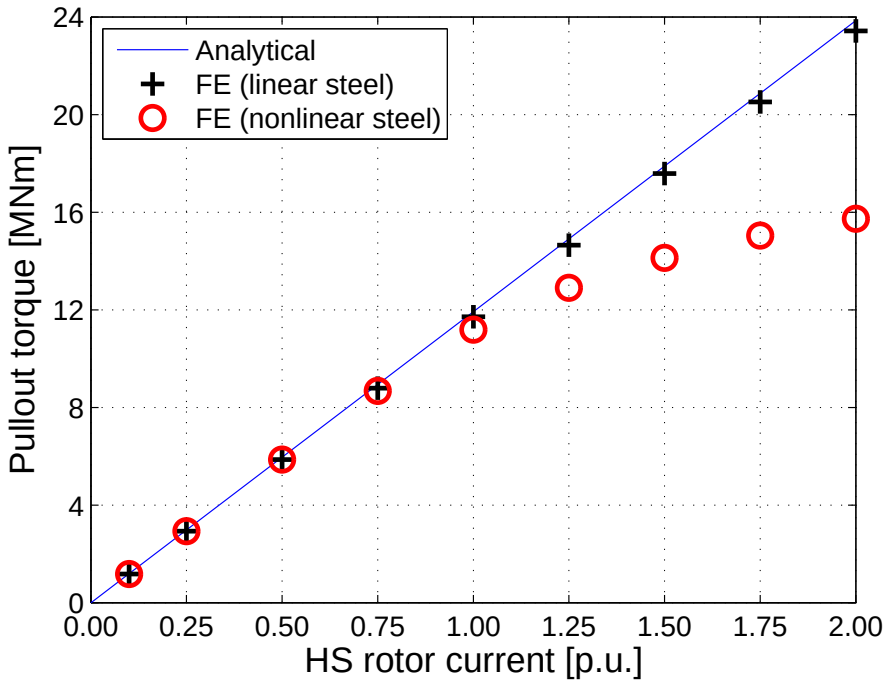

Fig. 6.10: Variation of the pullout torque with the HS rotor excitation current. (HS rotor current per unit of rated HS rotor current)

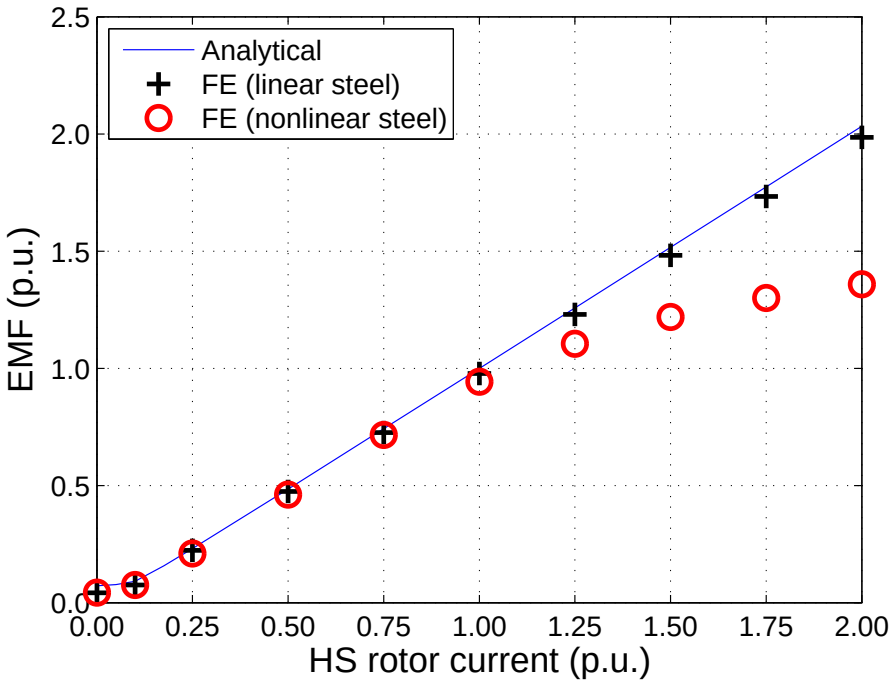

Fig. 6.11: Variation of the EMF with the HS rotor excitation current. (EMF per unit of the rated EMF and HS rotor current per unit of rated current)

6.3 Effects of leading design parameters

In this section coil excited PDDs with the same pullout torque and the same power rating as the PDD in Table 6.1 have been optimised. The analytical techniques developed in Section 6.2 have been thereby employed to undertake a study of the effects of the leading design parameters on the masses of the active components and the efficiency of the PDDs for a 10MW wind turbine. The PDD in Table 6.1 is employed as a benchmark for the forthcoming simulation studies. However, it should be noted that since the PDD with coil excited HS rotor exhibits increased issues with saturation effects than a PDD with PM excited HS rotor the optimised design has been refined in order to take into account of saturation effects and the analytical values in this section may be, therefore, lower than the values given in Table 6.1. Nevertheless, the analysis in this section will give an important insight into the effects of the leading design parameters on the main PIs of the PDD.

6.3.1 Effects of the HS rotor slot opening angle

Intuitively decreasing the HS rotor slot opening angle $\Theta_{\delta 2}$ and, therefore, the ratio of the slot opening angle to the HS rotor pole-pitch $a_{c,HS}$ would increase the leakage flux on the HS rotor due to the shorter airgap paths across the slot opening. This effect is magnified by the presence of the PPs, which could contribute to reducing the reluctance for the leakage paths for which the flux would cross the inner airgap without interacting with the PMs or the stator windings. For example Fig. shows the flux paths in a coil excited PDD, where $a_{c,HS} = 0.17$. It can be seen that a large amount of leakage flux is returning through the PPs positioned between the HS rotor poles.

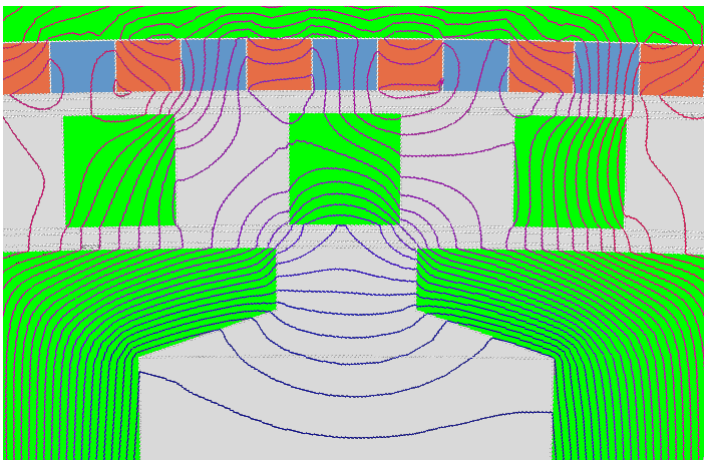

Fig. 6.12: Flux paths in a coil excited MG when $a_{c,HS} = 0.17$6.3.1

An increase in leakage flux would also increase the total flux in the HS rotor pole. However, since the pole width may be limited, saturation effects in the HS rotor poles would have an impact on the torque production of the PDD. Fig. 6.13 shows the variation of the pullout torque with $a_{c,HS}$. It may be worth noting that for this particular design the HS rotor slot opening angle is also limited due to the width of the HS rotor poles at about $a_{c,HS} = 0.47$. It can be seen that for the analytical model and for the analysis with FE with steel with linear characteristics, the pullout torque is increased when $a_{c,HS}$ is decreased. However, as can be seen from the analysis with steel with nonlinear characteristics saturation effects could significantly decrease the achievable torque.

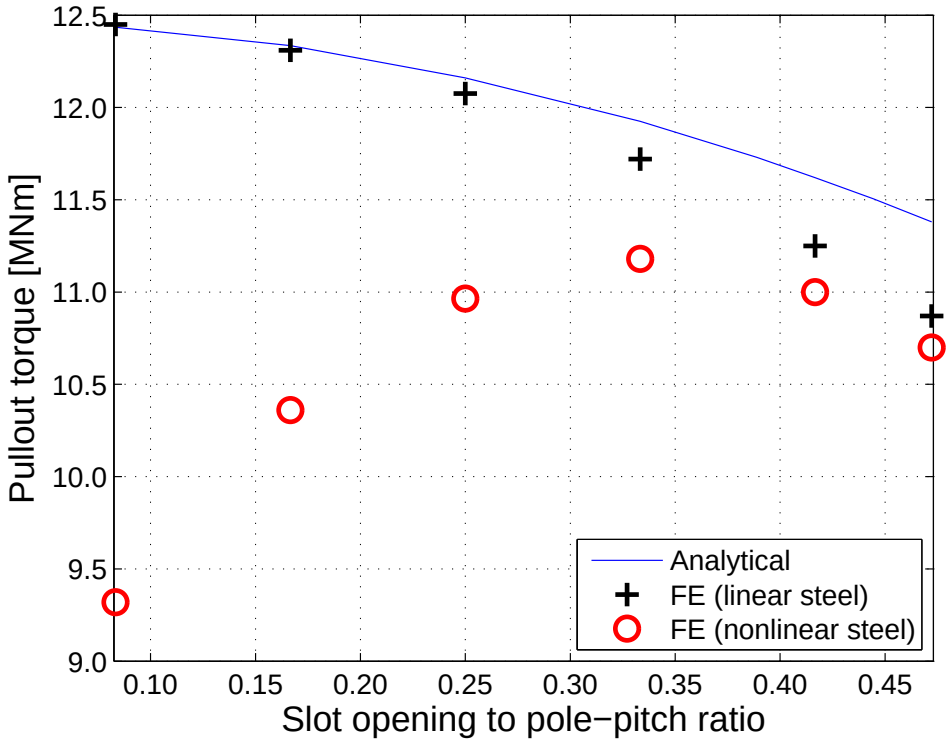

Fig. 6.13: Variation of the pullout torque with the ratio of the slot opening angle to the HS rotor pole-pitch $a_{c,HS}$.

6.3.2 Effects of the selected current densities

Although for a given PM mass the current loadings on the HS rotor and the stator are fixed, the design can still be further optimised to minimise the required copper mass when the copper loss is required not to exceed a certain limit. Therefore, in this section expressions for the selected current densities in the HS rotor and stator windings are provided, for which the copper mass is minimised while the current loadings and the total copper loss are fixed. Furthermore, for the investigated PDDs the copper loss is the main loss component and, therefore, the iron loss is not considered.

The total copper loss in a coil excited PDD is given by

$$P_{Cu} = P_{Cu,HS} + P_{Cu,S} \tag{6.8}$$

where the stator copper loss $P_{Cu,S}$ is given by (4.47) and the HS rotor copper loss $P_{Cu,HS}$ is given by (6.19). The HS rotor and stator current densities are related by

(6.8) and their relationship is given by

$$i_{rms} = \frac{P_{Cu}}{2\pi\rho_{Cu}} - \frac{(l_a + l_{e,HS})R_{HS}Q_{HS}}{(l_a + l_{e,S})R_S Q_{rms}} i_{HS} \tag{6.9}$$

Furthermore, the total copper mass is given by

$$M_{Cu} = M_{Cu,HS} + M_{Cu,S} \tag{6.10}$$

where the stator copper mass is given by (4.50), and the HS rotor copper mass is given by

$$M_{Cu,HS} = m_{Cu}\frac{2\pi R_{HS}Q_{HS}}{i_{HS}}(l_a + l_{e,HS}) \tag{6.11}$$

If the total copper loss is required not to exceed a given maximum copper loss $P_{Cu,max}$, the rated HS rotor current density $i_{HS,R}$ and the rated stator current density $i_{rms,R}$ can be selected such that the total copper mass is minimum. In order to find the minimum total copper mass the copper mass is differentiated by one of the rated current densities, i.e.

$$\frac{dM_{Cu}}{di_{HS,R}} = 0 \tag{6.12}$$

This leads to the following expression for the rated current densities which will result in a minimum copper mass for a given total copper loss (see Appendix A.5)

$$i_{HS,R} = i_{rms,R} = \frac{P_{Cu,max}}{2\pi\rho_{Cu}}\left[Q_{HS,R}R_{HS}(l_a + l_{e,HS}) + Q_{rms,R}R_S(l_a + l_{e,S})\right]^{-1} \tag{6.13}$$

It can be seen that a minimum copper mass is achieved, when both current densities are selected the same. For example for a coil excited PDD with the same current loadings and airgap dimensions as the PDD in Table 6.1, Figs. 6.14 and 6.15 show the variations of $i_{rms,R}$ and the copper masses with $i_{HS,R}$, respectively. It can be seen that a minimum total copper mass is achieved at about $i_{HS,R} = 2.9A/mm^2$ and $i_{rms,R} = 2.9A_{rms}/mm^2$.

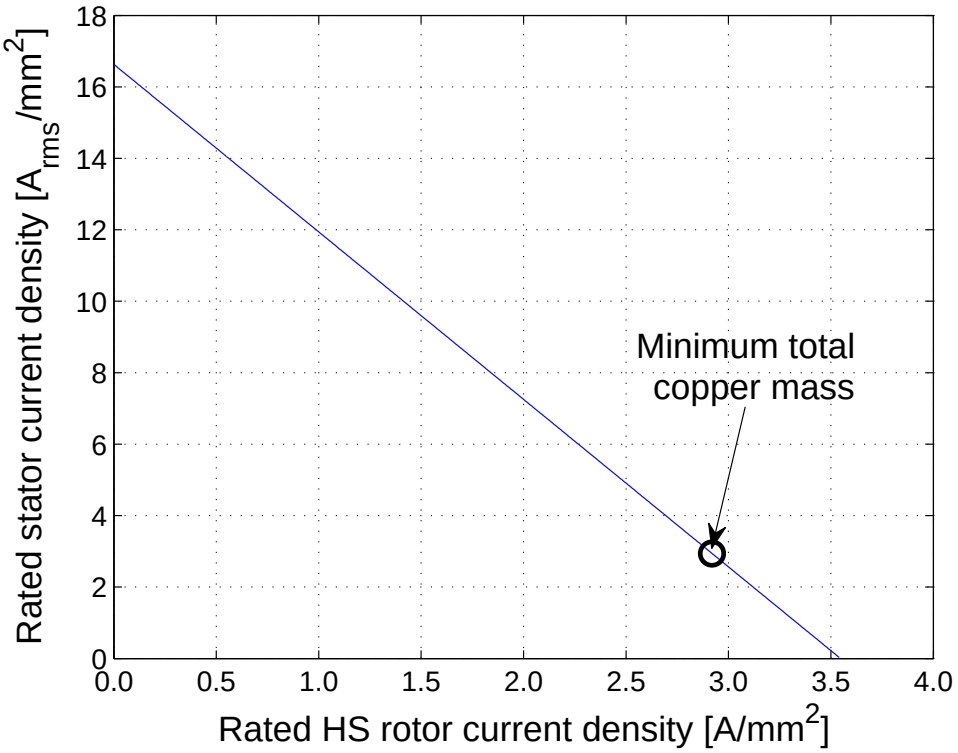

Fig. 6.14: Variation of stator current density with the HS rotor current density for fixed total copper loss.

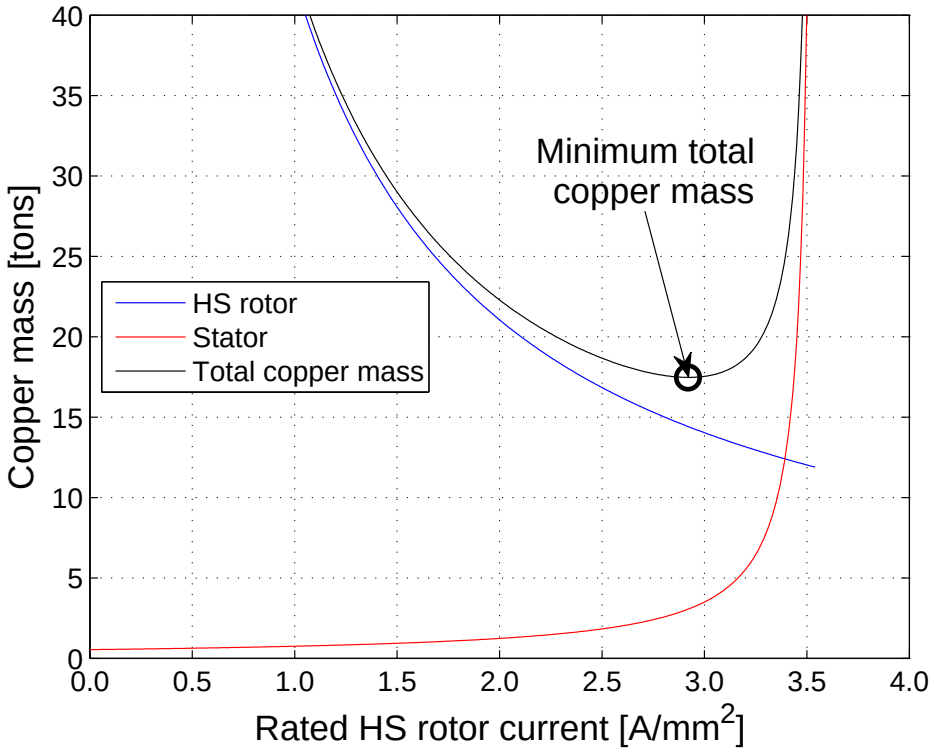

Fig. 6.15: Variation of copper masses with the HS rotor current density for fixed total copper loss.

6.3.3 Effects of the selected copper loss

For a PDD with the same airgap dimensions as the PDD given in Table 6.1, Fig. 6.16 and Fig. 6.17 show the variations of the copper mass and the active mass, which includes the PM mass, the copper mass, and the laminated steel mass, with the PM mass and the loss in the copper windings, respectively. The iron loss is neglected in this analysis, since for most of the considered designs it is the smaller loss component, with a contribution of about 1.0% of rated power. Only designs for which the flux density in the HS rotor iron poles can be kept below 1.5T are considered and, therefore, a maximum $Q_{HS,R}$ and consequently a minimum PM mass can achieved. It can be seen that if the copper loss is decreased the minimum achievable PM mass and as expected the copper mass increases. It can also be seen that for a given copper mass the copper loss may increase with increasing PM mass. Since an increase of PM mass would also increase the effective airgap length, this could lead to an increase of the required HS rotor current and therefore to increased copper losses. On the other hand, also the magnitude of the flux density due to the PMs would increase, which would decrease the current loading of the HS rotor required to achieve the pullout torque. However, this would decrease the EMF, which in turn would lead to an increase of the stator current and, therefore, also to increased copper losses. Finally it can be seen that for a given copper mass a minimum copper loss can be achieved at about 6tons of PM material, while for a given total active mass a minimum copper loss can be achieved at about 8tons of PM material.

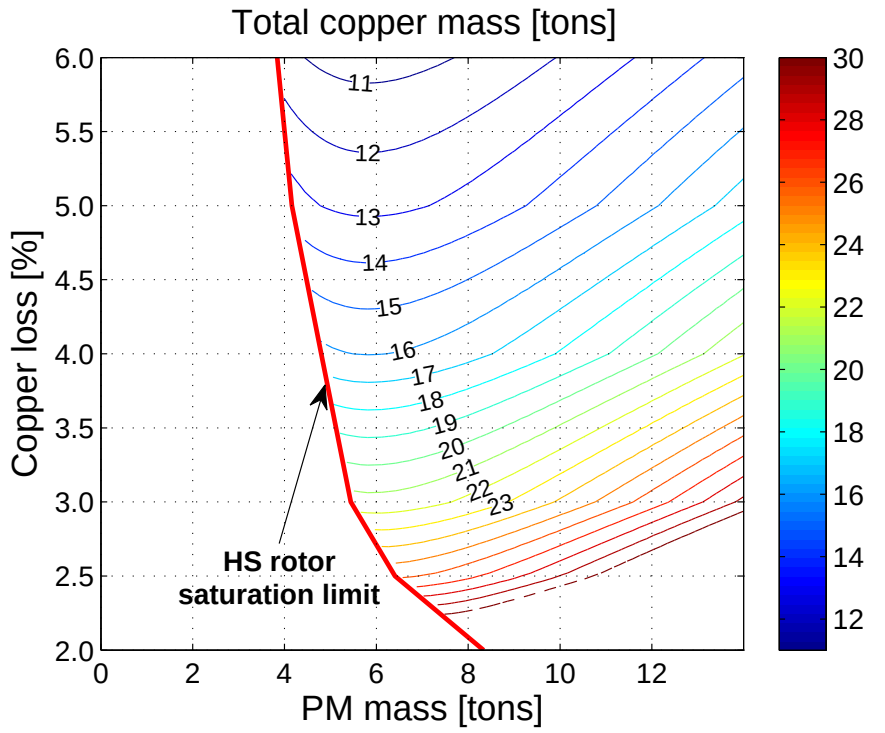

Fig. 6.16: Variation of copper mass with the PM mass and the total copper loss in percent of the rated power.

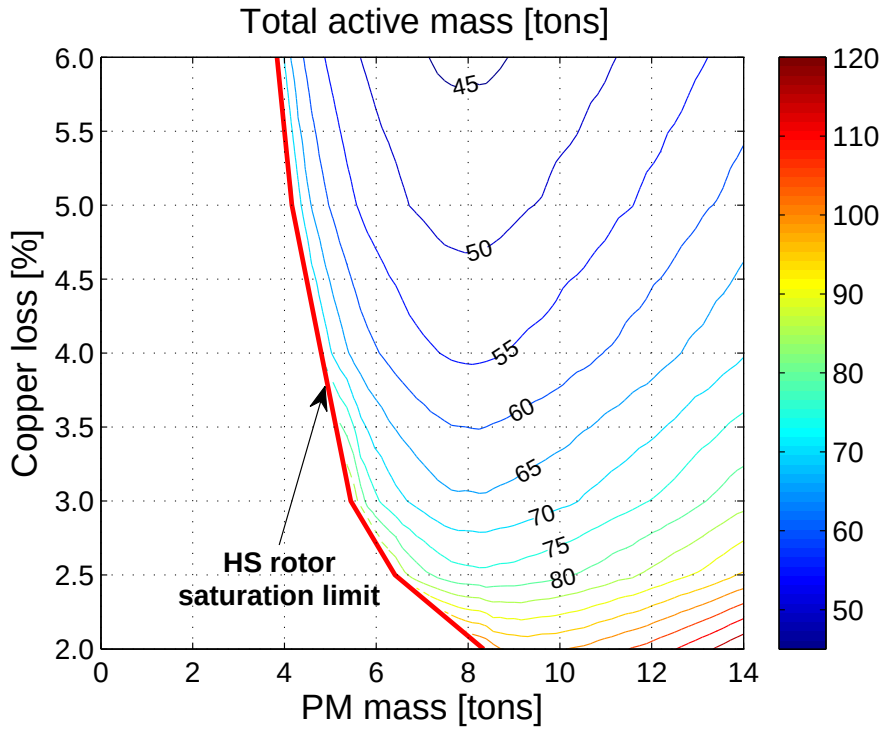

Fig. 6.17: Variation of total active mass with the PM mass and total copper loss in percent of the rated power.

6.3.4 Effects of the selected shear stress

In the analysis it is assumed that the airgap diameter is fixed to 8m, and the copper loss is kept at 4.0% of the rated power. For a gear ratio of 7.5 and the same number of circumferentially symmetrical sections as the PDDs in Table 6.1, Fig. 6.18 and Fig. 6.19 show the variations of the copper mass and the active mass with the PM mass and the σ_{pull}. Similar to Section 6.3.3 for a given equivalent shear stress an increase of PM mass decreases the required HS rotor current loading and increases the required stator current loading, which would also affect the associated copper masses. While for small PM masses the reduction in HS rotor copper mass could decrease the total copper mass, at larger PM masses the copper on the stator could be the larger mass component and its increase would also increase the total copper mass. It can, therefore, be seen that designs with minimum copper mass or total active mass can be achieved, however the PM mass may not be minimum. Furthermore, a minimum PM mass of about 3.5tons can be achieved, however at the expense of increased copper and total active mass.

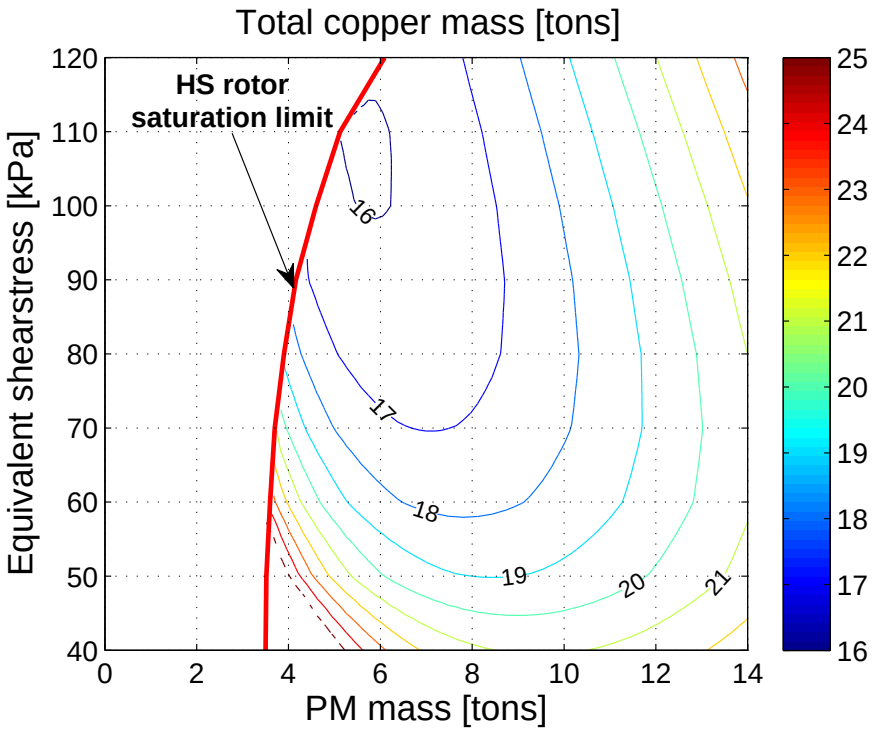

Fig. 6.18: Variation of the copper mass with the PM mass and σ_{pull}, when the copper loss is fixed to 4.0%.

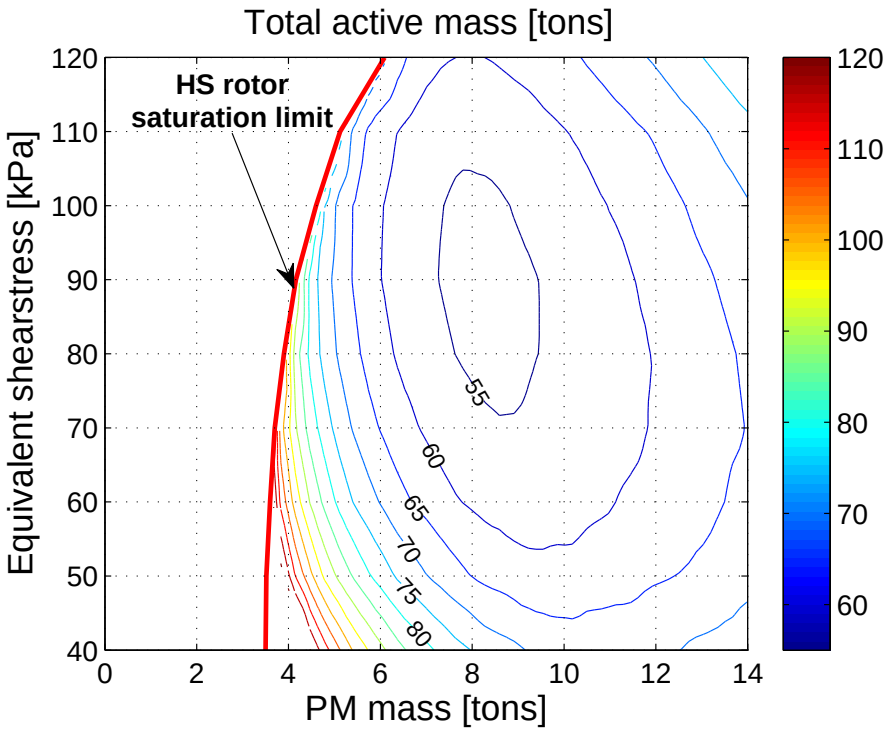

Fig. 6.19: Variation of the total active mass with the PM mass and the σ_{pull}, when the copper loss is fixed to 4.0%.

6.3.5 Effects of the number of sections

Due to the large size of the investigated PDDs, and similarly to the PM excited PDD, they are likely to be constructed from several circumferentially symmetrical sections. Fig. 6.20 and Fig. 6.21 show, therefore, the variations of the copper mass and the active mass, with the PM mass and the number of sections, where $\sigma_{pull} = 100kPa$ and the gear ratio is 7.5. It can be seen that a minimum copper mass or total active mass can be achieved, however the PM mass may not be minimum simultaneously. If only designs with a minimum PM mass are considered, a minimum active mass can be achieved for a number of sections of about 22. It can also be seen that when the number of sections is decreased the total active mass considerably increases, which is mainly due to the increased back iron mass.

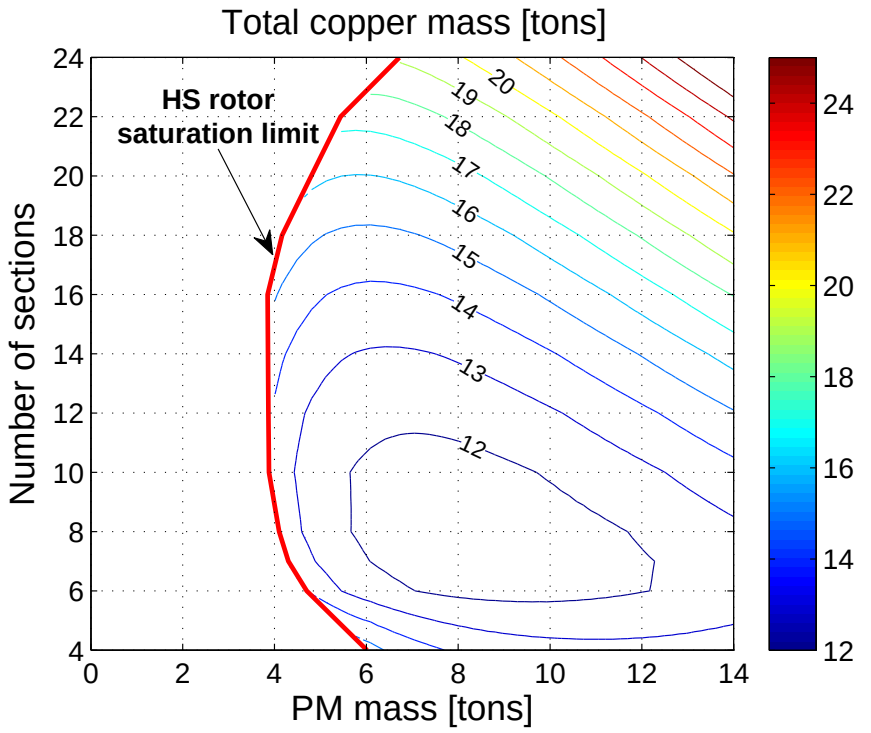

Fig. 6.20: Variation of the copper mass with the PM mass and the number of sections, when the copper loss is fixed to 4.0%.

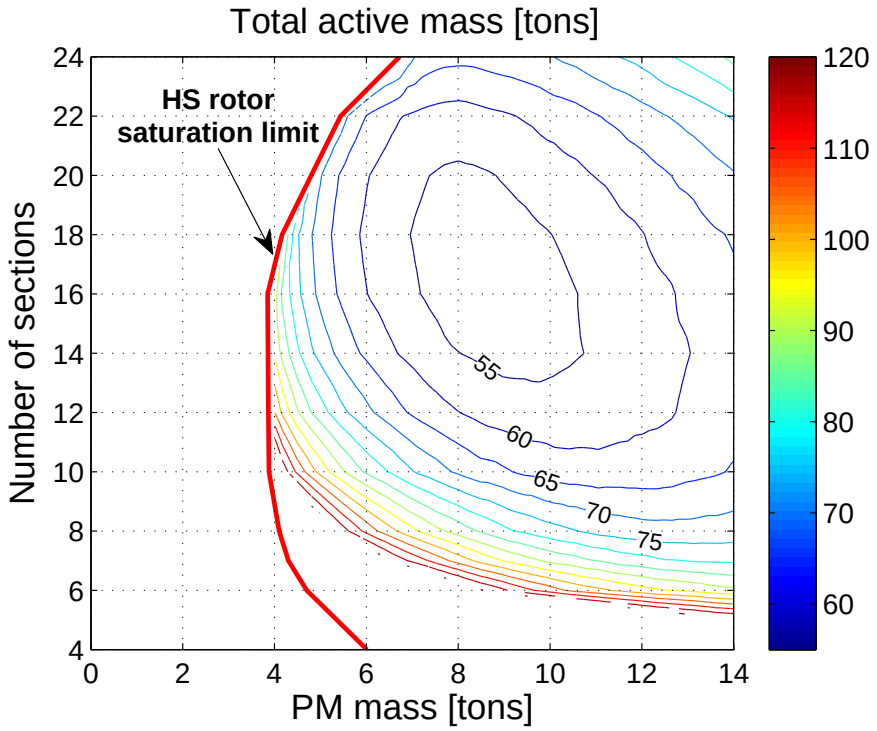

Fig. 6.21: Variation of the total active mass with the PM mass and the number of sections, when the copper loss is fixed to 4.0%.

6.3.6 Effects of the gear ratio

Fig. 6.22 and Fig. 6.23 show the variations of the copper and total active mass with the PM mass and the gear ratio, where the $\sigma_{pull} = 100kPa$ and the designs have the same number of sections as the PDDs in Table 6.1. It can be seen that the minimum PM mass does not vary significantly for the range of gear ratios from 5.5 to 8.5, and that also the total active mass and copper mass do not vary significantly over this range for these designs.

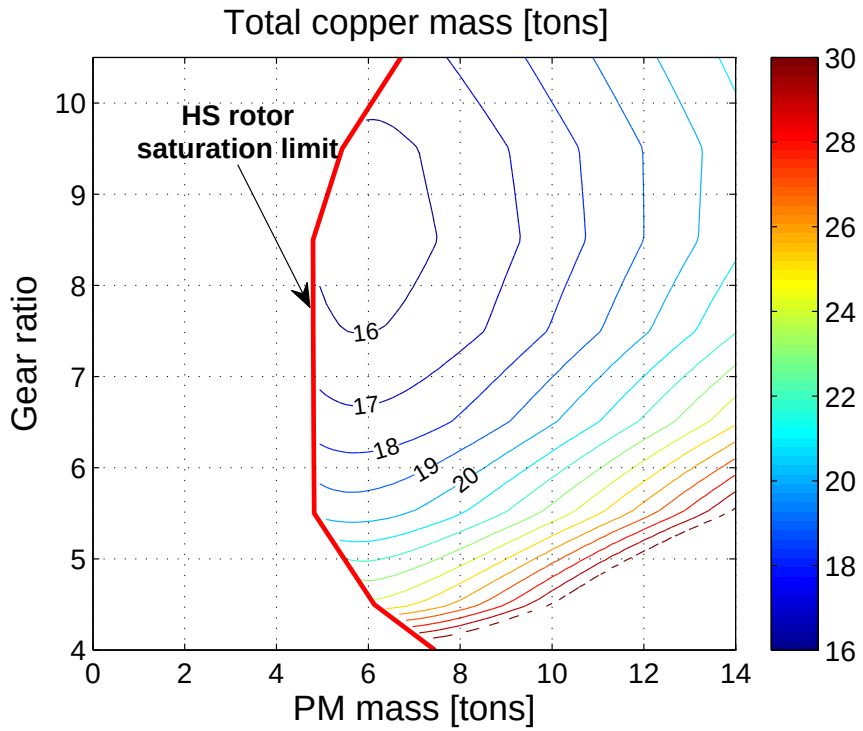

Fig. 6.22: Variation of the copper mass with the PM mass and the gear ratio, when the copper loss is fixed to 4.0%.

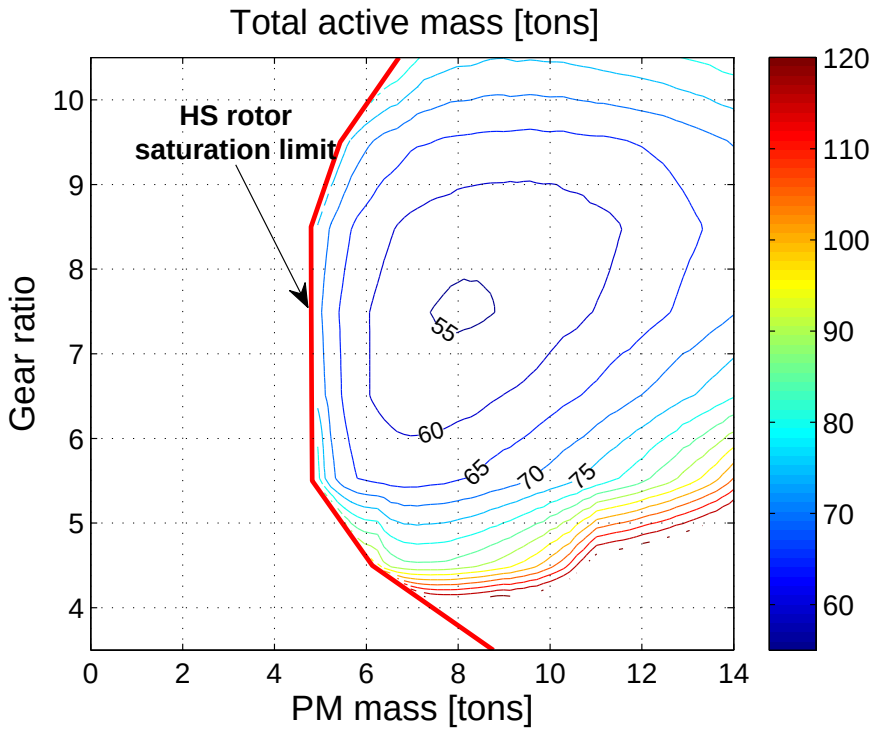

Fig. 6.23: Variation of the total active mass with the PM mass and the gear ratio, when the copper loss is fixed to 4.0%.

6.3.7 Effects of the airgap diameter

Fig. 6.24 shows the variations of the active masses in 6m and 8m airgap diameter PDDs with the PM mass, when the equivalent $\sigma_{pull} = 100kPa$, and the gear ratio is 7.5. It can be seen that for a given PM mass a PDD may be realised at an airgap diameter of less than 8m, however this can only be achieved at the expense of increased copper and laminated steel mass. Furthermore, similarly to Section 5.4.1, selecting a larger diameter could increase the structural cost of the PDD and increase the impact of the end effects on the transmitted torque.

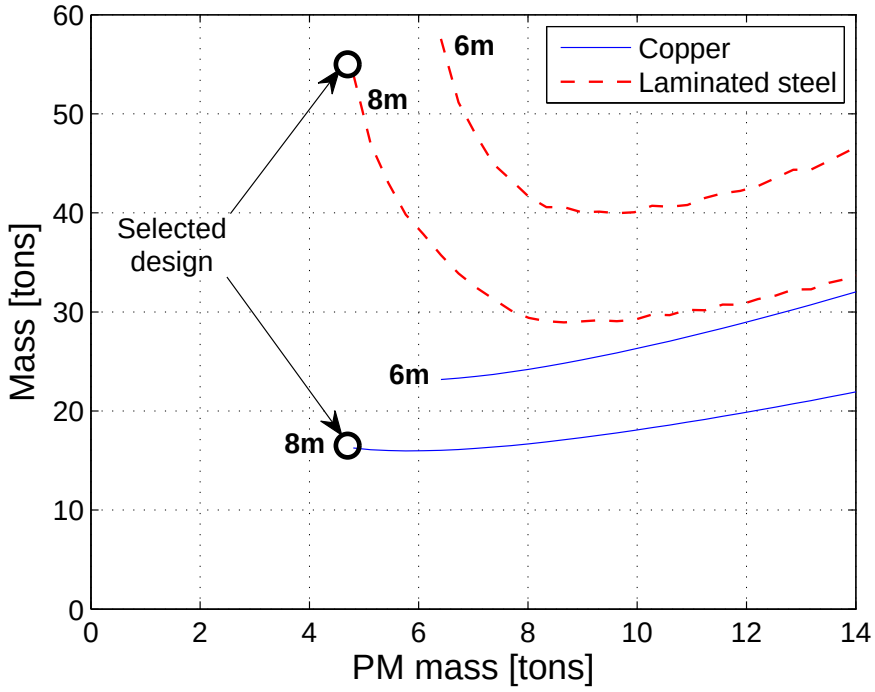

Fig. 6.24: Variation of the copper and laminated steel masses with the PM mass, for several airgap diameters. The copper loss is fixed to 4.0%,

6.4 Control of the coil-excited PDD

The generator may be connected to the grid employing a power electronic converter equipped with an active rectifier dc link and a grid inverter, as it would be the case for a conventional PM generator. However, since the excitation of the rotor can be actively controlled the active rectifier may be replaced by a passive diode rectifier, resulting in less costly, simpler and more reliable power electronics. The PDD can be controlled such that either the HS rotor current, the stator current or both can be adjusted to achieve a given electromagnetic torque. In any case the generator should be controlled to maximize efficiency, while satisfying the operational requirements/constraints as follows:

$$T_{pull} \geq 1.2 \cdot T_{PP} \tag{6.14}$$

$$EMF \geq EMF_{min} \tag{6.15}$$

$$I_{HS} \leq I_{HS,R} \tag{6.16}$$

$$I_{rms} \leq I_{rms,R} \tag{6.17}$$

where EMF_{min} is the minimum EMF. A limitation of the voltage range and hence a minimum EMF could be required due to limitations in acceptable voltage levels and losses for the converter that is employed and the components in series, such as a transformer that could be necessary to step-up the voltage level [69].

The electromagnetic loss in the coil excited PDD is given by

$$P_{loss} = P_{Cu,HS} + P_{Cu,S} + P_{iron} \tag{6.18}$$

where P_{iron} is the iron loss in the laminations, $P_{Cu,S}$ is the copper loss in the stator windings given by (4.47), and $P_{Cu,HS}$ is the copper loss in the HS rotor windings given by

$$P_{Cu,HS} = \rho_{Cu}(l_a + l_{e,HS})i_{HS}2\pi R_{HS}Q_{HS} = R^*_{HS}I^2_{HS} \tag{6.19}$$

where R^*_{HS} is the resistance of the HS rotor coils calculated at the operating temperature of 120^oC. Since the flux density distribution in the HS rotor laminated steel would be analytically difficult to model FE methods are selected to determine the iron losses in the laminated steel. However, in order to simplify the analysis and minimize the losses without the need for extensive and time consuming FE analysis, the iron loss components (4.57), (4.58) and (4.59) are assumed to be given by the following analytical expression of I_{HS}, I_{rms} and ω_{PP}:

$$p_{hyst} = \omega_{PP}(c_{h,HS}I^2_{HS} + c_{h,S}I^2_{rms}) \tag{6.20}$$

$$p_{class} = \omega^2_{PP}(c_{c,HS}I^2_{HS} + c_{c,S}I^2_{rms}) \tag{6.21}$$

$$p_{exc} = \omega^{1.5}_{PP}(c_{e,HS}I^2_{HS} + c_{e,S}I^2_{rms})^{0.75} \tag{6.22}$$

where $c_{h,HS}$, $c_{h,S}$, $c_{c,HS}$, $c_{c,S}$, $c_{e,HS}$, and $c_{e,S}$ are coefficients, determined from a selected number of iron loss predictions using FE analysis. The coefficients $c_{h,HS}$, $c_{c,HS}$ and $c_{e,HS}$ are determined by a single iron loss prediction on no-load condition, i.e. $I_{rms} = 0$, while $c_{h,S}$, $c_{c,S}$ and $c_{e,S}$, are subsequently determined when the machine is fully loaded.

The same variation of the capacitor factor and rotational speeds with the wind speed are employed as in section 5.1. As an example Fig. 6.25 shows the variation of the EMF of the PDDs with coil excited and PM excited HS rotors with the wind

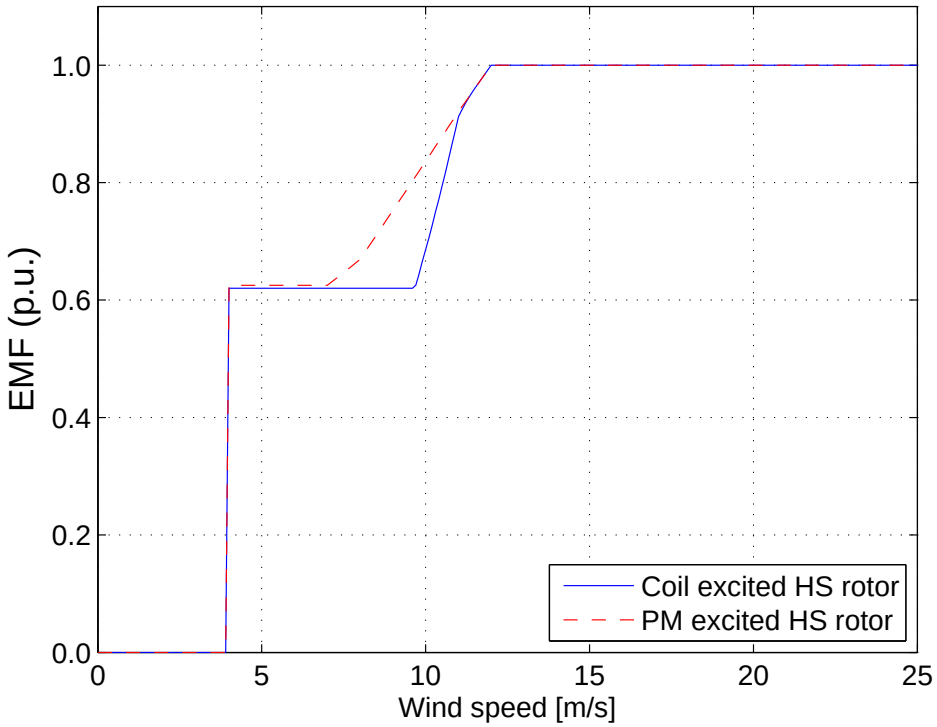

Fig. 6.25: Variation of the EMF with the wind speed for a PDD with HS rotor coil excitation and for a PDD with PM excited HS rotor. (EMF per unit of the rated EMF)

speed, where the minimum EMF for the coil excited PDD is kept the same as for the PM excited PDD in order to allow a more accurate comparison between the PDDs without reconsideration of the acceptability of the voltage levels for the converter. It can be seen that in order to minimise the electromagnetic losses the EMF in the coil excited PDD may have to be reduced faster than the rotational speed.

Fig. 6.26 shows the variation of the resulting copper and iron losses with the wind speed. It can be seen that in this case the stator current will remain constant until the minimum EMF is reached. In general in a PDD the stator losses are inherently lower compared to direct drive and other PM machines. Therefore, although the HS rotor losses are relatively high to the stator losses in this machine, they are not very high in absolute terms. Nevertheless due to their location on the rotor special forced air cooling should be considered.

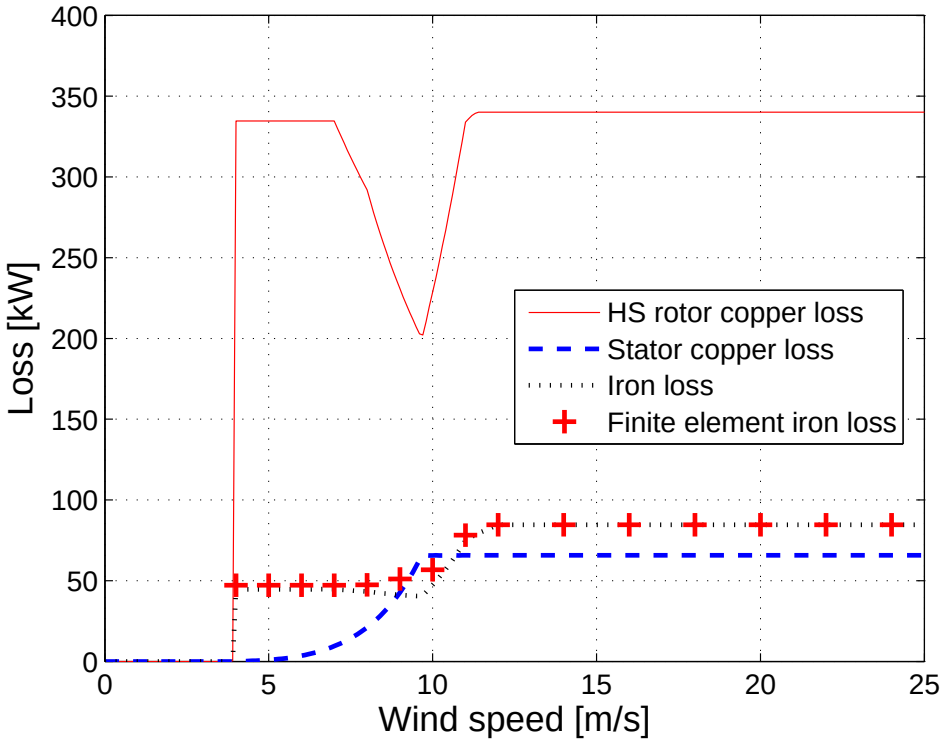

Fig. 6.26: Variation of the losses with the wind speed.

Fig. 6.27 shows the variation of the efficiency with the wind speed. It can be seen that the efficiency remains fairly constant until the excitation current is increased to ensure the EMF remains above the minimum value. It can also be seen that efficiency improvements can be realized, if the constraint in (6.14) is relaxed and the PDD is allowed to operate closer to the pullout torque. This is possible, because of the extra degree of controllability enabled by the coil excitation.

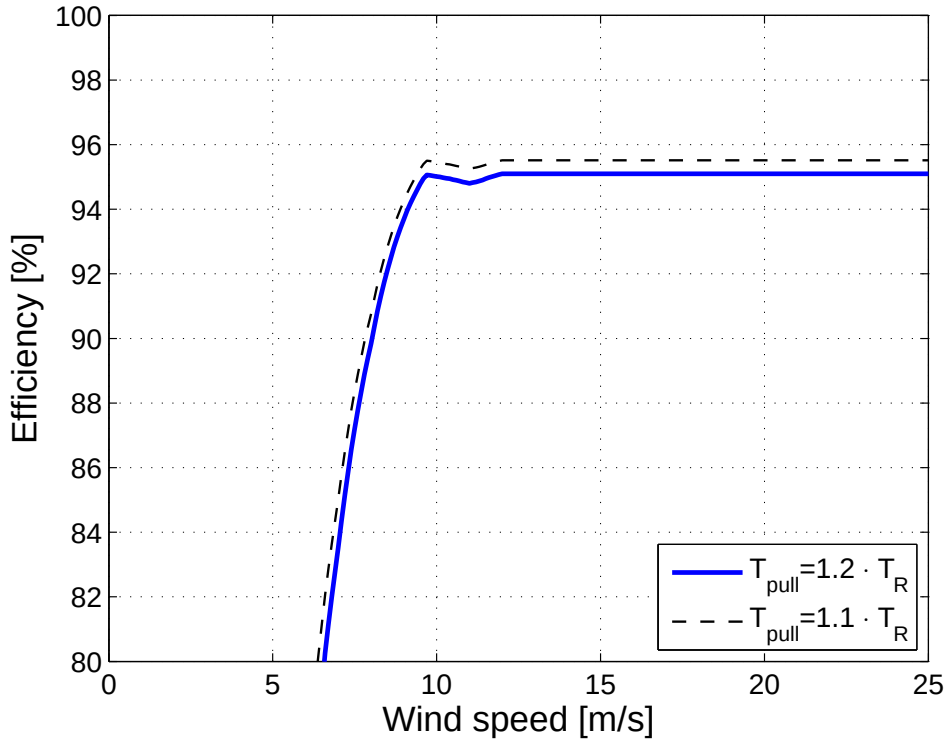

Fig. 6.27: Variation of the efficiency with the power. (Pullout torque T_{pull} per unit of rated torque T_R)

Fig. 6.28 shows the variation of the annual energy efficiency with the minimum EMF for the PDDs with coil excitation and PM excitation. Designs for which constraints (6.15) and (6.16) could not be fulfilled simultaneously over the entire range of the operating wind speeds are rejected in this analysis. In particular for this PDD, the minimum EMF had to be kept below 62% of the rated EMF. It can be seen that the selection of the minimum EMF has a significant effect on the annual energy efficiency and this should be considered, when a control strategy and a converter topology are selected. It can also be seen that the efficiency of a PM excited PDD could exhibit a significantly higher annual energy efficiency, however, the PM excited PDD would also require a significantly larger amount of PMs.

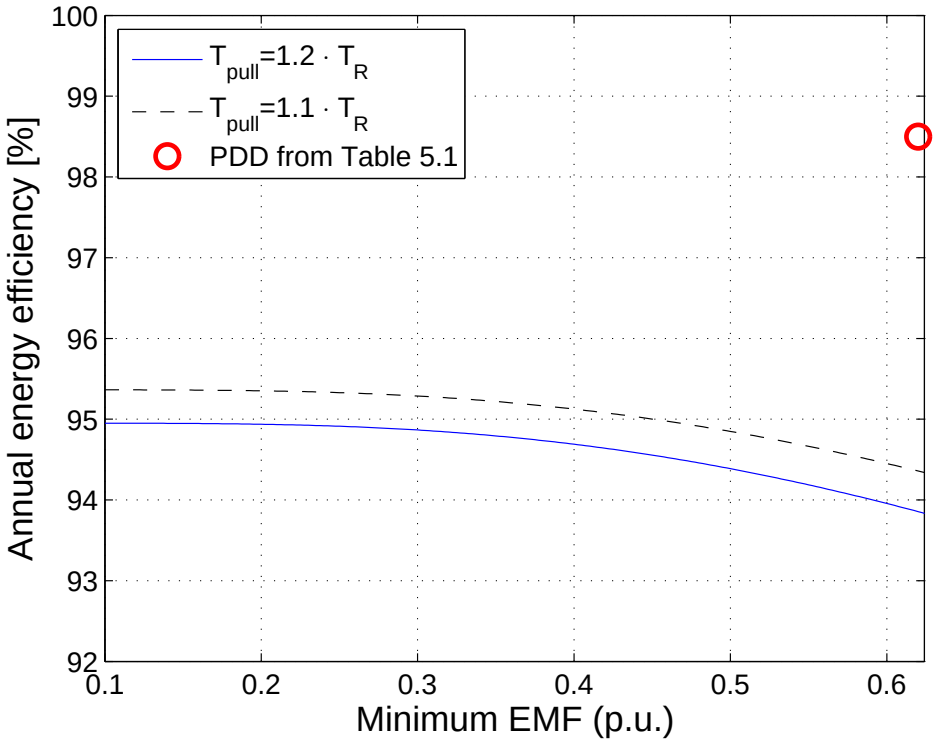

Fig. 6.28: Variation of the annual energy efficiency with the minimum EMF. (Minimum EMF per unit of the rated EMF, and pullout torque per unit of rated torque T_R)

6.5 Conclusions

A model for the analytical prediction of the flux density distribution in the airspaces and PMs of a PDD with a coil excited HS rotor is presented. The developed analytical model is utilised for the optimisation of a PDD for the application in a 10MW wind turbine generator that has the same requirements as the PDD in Chapter 5. The PDD in Table 6.1 has been optimised to minimise the PM and total active mass, whilst achieving a sufficiently high shear stress and efficiency. The PDD has a PM mass of only 4.5$tons$, which is significantly less than for a PM excited PDD, however the rated electromagnetic efficiency is ~95%, and the total active mass is increased, see Table 9.1. The optimised PDD is employed for the comparison of the analytical model with 2D FE studies, and it is shown that a good agreement exists for the flux density waveforms and the transmitted torque. Furthermore, it is also shown that the pullout torque and the EMF can be controlled by the HS rotor

current, however, saturation effects need to be considered. The model is further employed to discuss the effects of the leading design parameters on the main PIs, such as the PM mass. It is shown that leakage flux across the PPs could be an issue and that saturation effects in the HS rotor poles can have a significant effect on the torque. It is shown that the minimum achievable PM mass is limited by the maximum current loading that can be applied without affecting the transmitted torque through saturation effects. An equivalent shear stress in excess of $100kPa$ can be achieved and significant reductions in PM mass, less than $4tons$, can be realized compared to a PDD with HS rotor PM excitation, albeit at the expense of increased total active mass and reduced efficiency. Similarly to the PDD with PM excited HS rotor the active mass could be significantly reduced by selecting a smaller aspect ratio, however this would only be possible at the expese of increased mass/cost of the structural components. Furthermore, for a given equivalent shear stress and total copper loss the minimum achievable PM mass is fairly independent from the number of sections and the gear ratio for a wide range of values, however the copper mass and total active mass may vary significantly. It is also shown that control of the excitation current is required, in order to maximise the annual energy efficiency.

Chapter 7

Scaling of the PDD for large wind turbines

Increasingly large wind turbines have been built in the recent decades [3]. In particular for offshore application a trend towards larger wind turbines has been established due to the cost structure of offshore installations. While the cost for the installation and the electrical infrastructure mainly depend on the number of wind turbines, the cost of operation and maintenance for a given wind farm capacity could also be reduced with an increasing size of the turbine [70]. On the other hand the weight of the turbine may increase unfavourably with upscaling, hence a cost reduction may not be guaranteed [6].

In particular for the turbine generator, scaling rules indicate that the upscaling of wind turbine generators is characterised with the intrinsic challenge of a decreasing power to torque ratio with increasing power rating [6, 7]. Resulting in drive-trains with decreasing power to weight/size ratios. Suitable upscaling rules for predicting the mass/size exist for electrical generator types most used in wind turbines [71, 72]. However, little is known on the scaling behaviour of PDDs and magnetically geared generators in general, which have two airgaps and exhibit differing torques in each airgap. Therefore, in this chapter the scaling behaviour of the PDD is investigated for wind turbine power levels between 5-20MW.

7.1 Theoretical scaling limits

The available shaft power of a wind turbine is given by (5.1). For fixed geometric and aerodynamic characteristics (fixed c_p, $v_{w,R}$ and maximum tip speed v_{tip}) the rated power (5.2) of the turbine is scaled by

$$P_R = \frac{1}{2} m_{air} c_p \pi R_{blade}^2 v_{w,R}^3 \sim s^2 \tag{7.1}$$

where s is the scaling factor [6]. Furthermore, the rated rotational speed would scale as

$$\omega_{PP,R} = R_{blade}^{-1} v_{tip} \propto s^{-1} \tag{7.2}$$

while the rated torque would scale by

$$T_R = P_R \omega_{PP,R}^{-1} \propto s^3 \tag{7.3}$$

From (7.1) and (7.3) it can be seen that the required rated torque increases faster with the scaling factor s than the rated power.

7.2 Scaling of the PDD with PM excited HS rotor

As is shown in section 5.4.1 for a PDD with PMs on the HS rotor the shear stress and Q_{rms} remain constant when applying a scaling factor s. Furthermore, when all radial dimensions of the MG component of the PDD are scaled linearly by a factor s, the torques, the PM mass, and the HS rotor and PP rotor laminated steel mass scale with s^3. Since the airgap diameter is many times larger than the radial stator slot depth it can be assumed that the end winding length also scales linearly with s, thus the copper mass and copper loss increases with s^2 if the current density at rated power is kept constant.

Fig. 7.1 shows the variation of the active masses with the power, where the PDD in Table 5.1 is scaled as described above. It can be seen that while the copper mass per unit power is constant, the PM and laminated steel mass per unit power increase. Fig. 7.2 shows the variation of the copper and iron losses with the rated power. It can be seen that the percentage of copper loss remains constant. However,

the iron losses may decrease as the power increases. Fig. 7.3 shows the variation of the rated efficiency with the rated power. It can be seen that for this particular case the rated efficiency increases with the rated power. Furthermore, design refinements such as adjusting the aspect ratios, see Section 5.4.1, can result in improvements of the PDD.

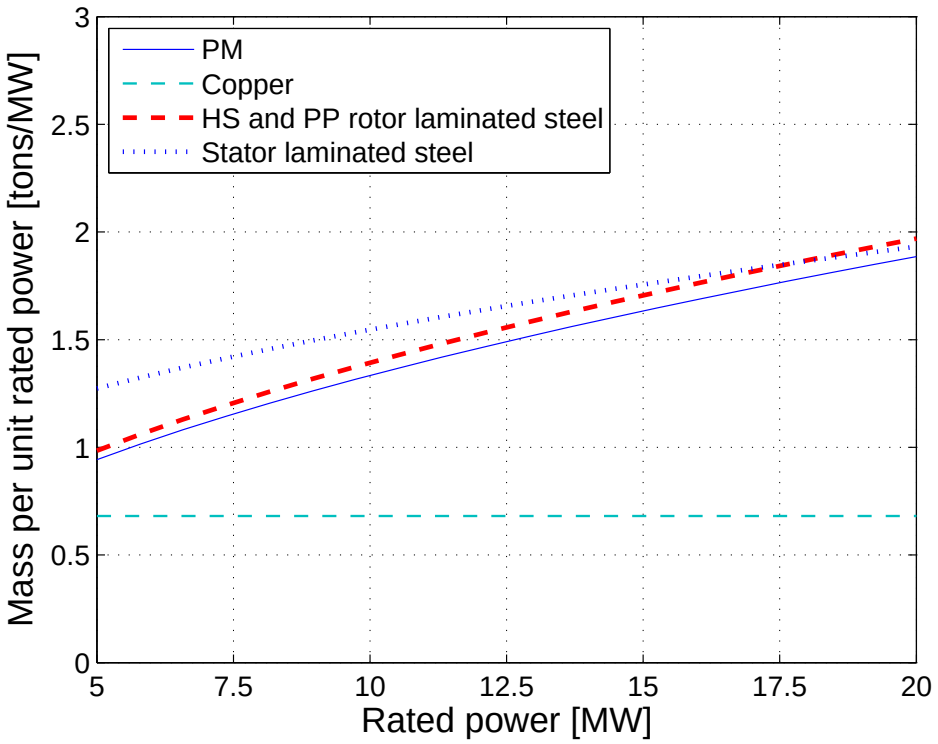

Fig. 7.1: Variation of active masses per unit of rated power with the rated power.

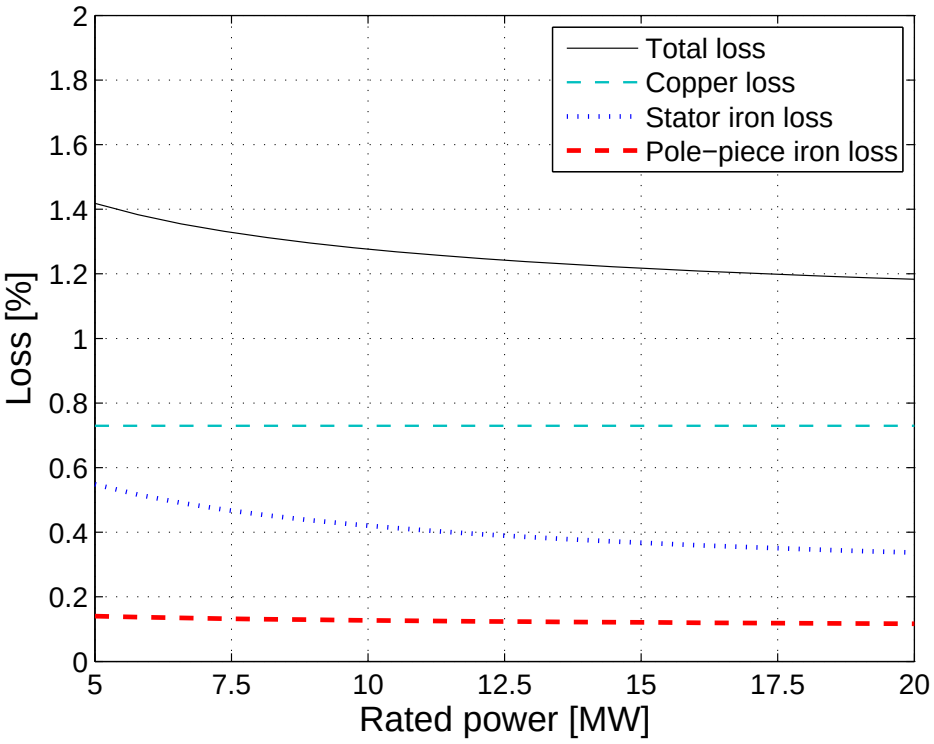

Fig. 7.2: Variation of rated electromagnetic losses with the rated power.

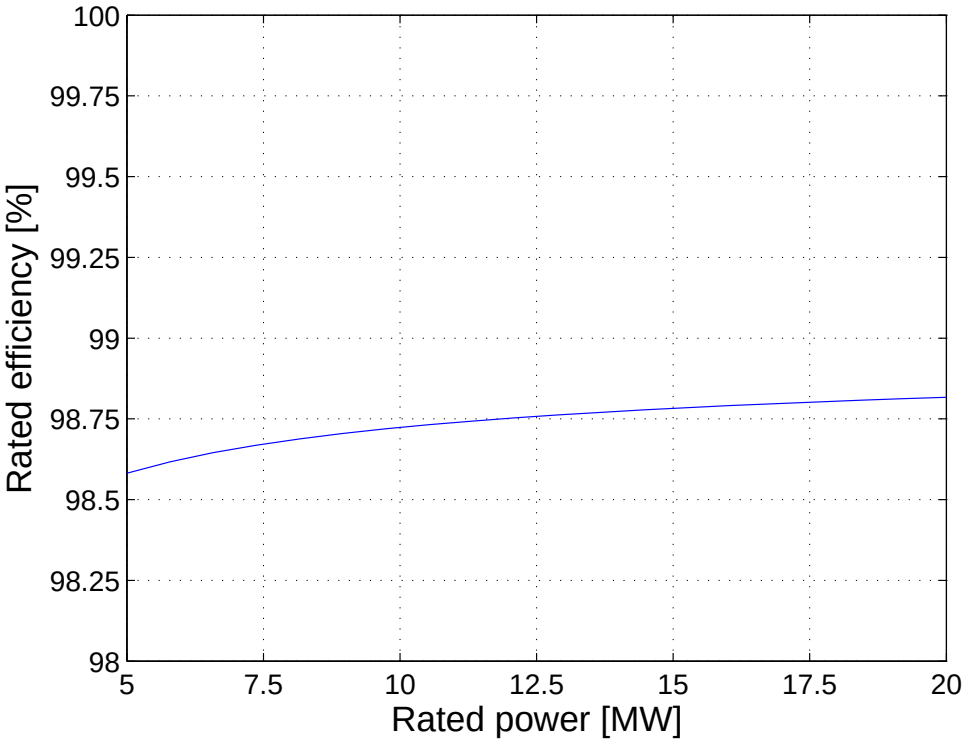

Fig. 7.3: Variation of rated efficiency with the rated power.

7.3 Scaling of the PDD with coil excited HS rotor

For the scaling of the coil excited PDD the rated total copper loss is kept to 4%, $\sigma_{pull} = 100kPa$ and the aspect ratio of the MG component is kept constant. The iron loss is neglected in this analysis since it is the smaller loss component with less than 1%. Similarly to the PM excited PDD the torque increases with s^3, however for the coil excited PDD the required torque can be achieved by varying the PM mass and $Q_{HS,R}$. Figs. 7.4 and 7.5 show the variations of the total copper mass and the total active mass with the PM mass per unit of rated power for several power ratings. It can be seen that the minimum achievable total copper mass per MW remains constant, while the associated PM and total active masses per MW may increase noticeably. Similarly, if only designs with a minimum PM mass are considered, the minimum PM and total active masses per MW may increase significantly, while the copper mass per MW would remain fairly constant.

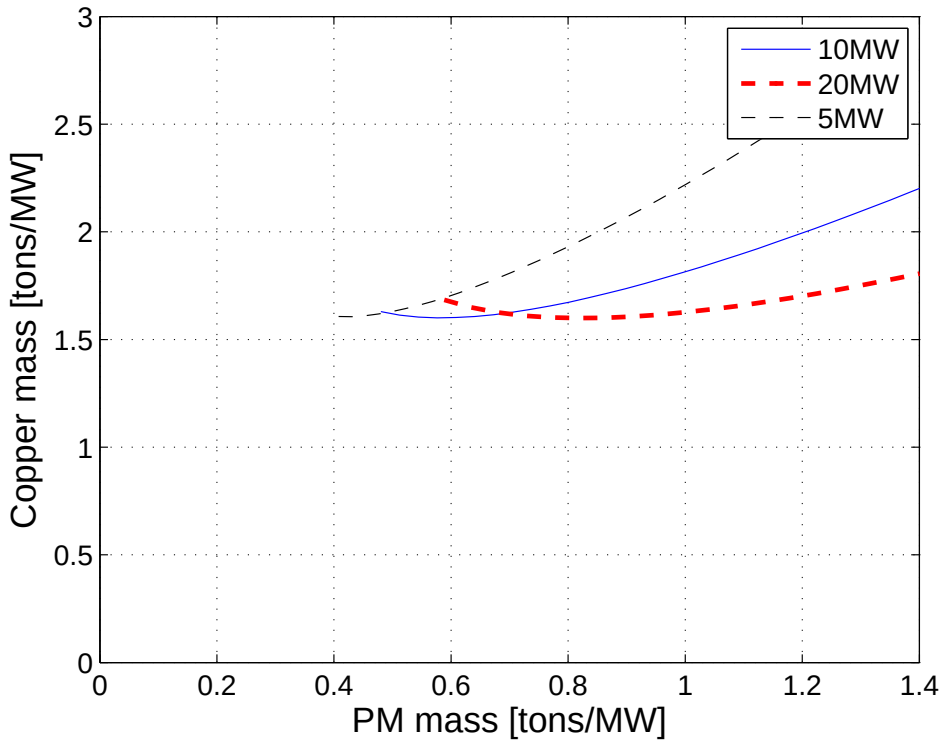

Fig. 7.4: Variation of the total copper mass with the PM mass for several power ratings.

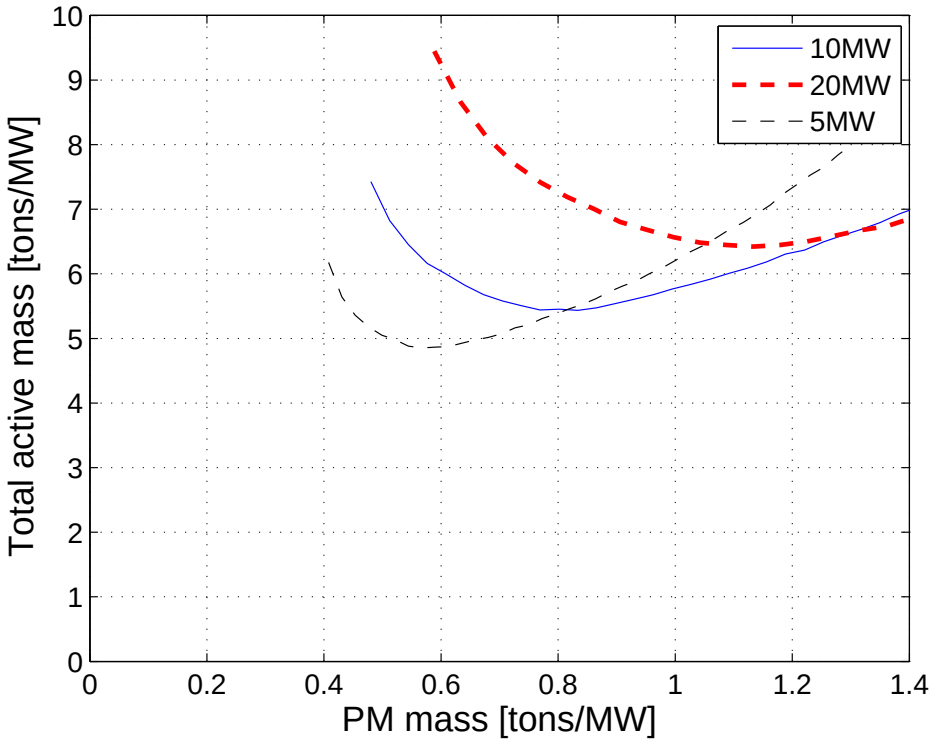

Fig. 7.5: Variation of the total active mass with the PM mass for several power ratings.

As is shown in Section 6.3.3, for a given power rating and for the designs with a minimum PM mass the maximum achievable $Q_{HS,R}$ is limited due to saturation limits in the HS rotor poles. Furthermore, if the design is upscaled with constant values of $i_{HS,R}$ and $Q_{HS,R}$, a decreasing proportion of leakage flux would be produced due to the almost constant radial dimension of the HS rotor coil slot. However, since this would also reduce the maximum flux density in the teeth, at higher power ratings a higher maximum HS rotor current loading can be selected for the designs before reaching the saturation limits in the HS rotor teeth. Fig. 7.6 shows the variations of the maximum achievable $Q_{HS,R}$ and the corresponding values of $Q_{rms,R}$ with the power rating. It can be seen that $Q_{HS,R}$ can be increased, and that this would also result in a decrease of $Q_{rms,R}$. In addition an increase in $Q_{HS,R}$ would also result in an increase of the required PM mass with less than s^3.

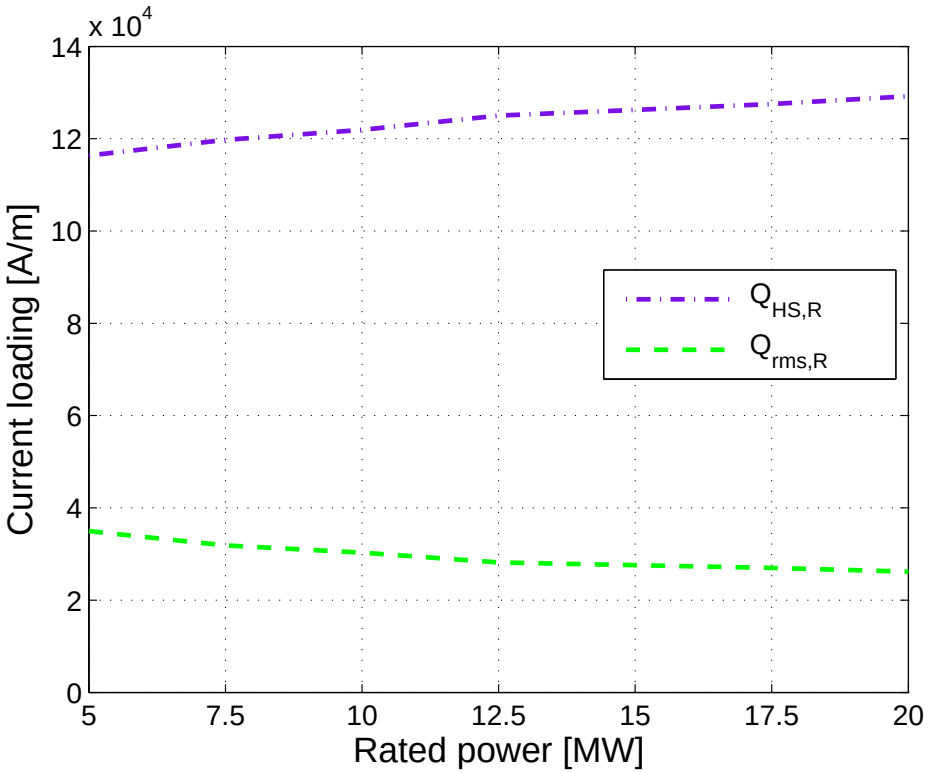

Fig. 7.6: Variation of the rated current loadings with the rated power.

Fig. 7.7 shows the variation of the active masses with the rated power for the designs with minimum achievable PM mass. It can be seen that the copper mass on the HS rotor increases slightly due to the increase of $Q_{HS,R}$ and that the copper mass on the stator decreases slightly due to the decrease of $Q_{rms,R}$. By comparing with Fig. 7.1 it can also be seen that the PM mass per MW increases much slower than for a PDD with a PM excited HS rotor. However, the laminated steel masses increase similiar to the PM excited PDD, Fig. 7.1.

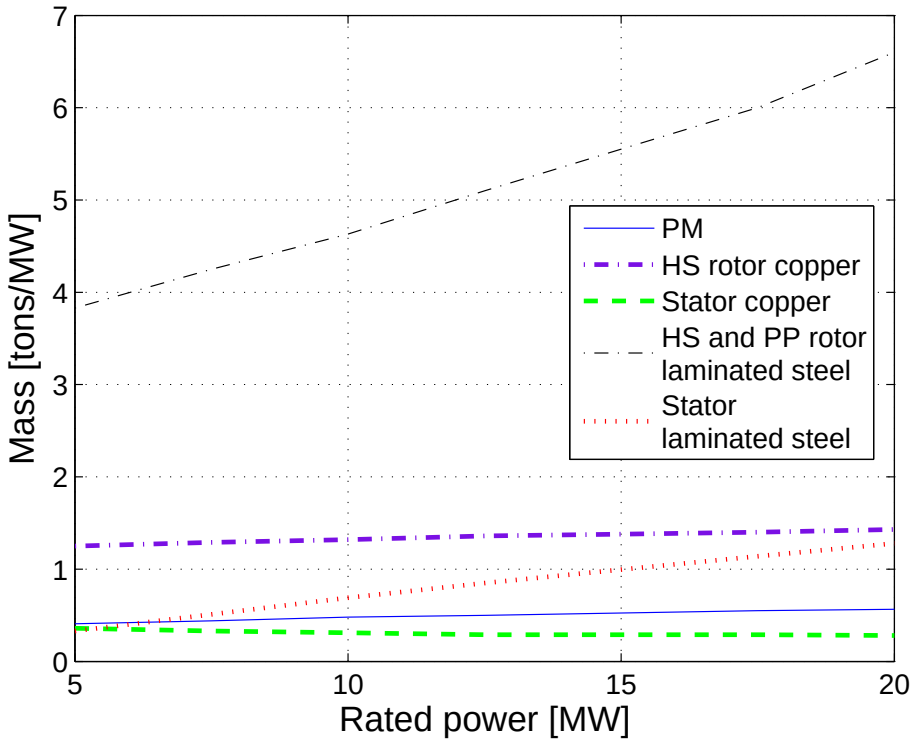

Fig. 7.7: Variation of the active masses with the rated power.

7.4 Conclusions

The scale invariance of the analytical models for a PDD are employed to discuss the scaling behaviour of the complete PDD. It is shown that if the current density is kept constant, the copper mass per MW remains fairly constant. However, it is also shown that the PM and steel lamination masses per MW could increase with the power of the wind turbine, albeit design refinements could minimise such increase. For the coil excited PDD the pullout torque is also controlled by the current loading on the HS rotor. It is shown that this can be exploited when upscaling, in order to allow for a slower increase of the PM mass than it is the case for a PDD with a PM excited HS rotor.

Chapter 8

Experimental results and validation

In order to demonstrate the technical feasibility of a PDD generator and to validate the design tools developed by University of Sheffield, a down-scaled demonstrator with a rated torque of 5kNm has been designed and built by Magnomatics Ltd as part of the INNWIND.EU project [73]. The analytical tools developed in Chapters 2 and 4 are compared to experimental results obtained from the demonstrator in this chapter.

Table 8.1 gives the parameters of the demonstrator PDD. The rated speed and the pole-number of the PDD allow for testing of electrical output frequencies of up to $165Hz$. Fig. 8.1 shows the cross-sectional schematic of the magnetically active components of the demonstrator PDD, while Fig. 8.2 shows a sectional view of the assembled PDD.

	Quantity	Values
T_R	Rated torque (when water cooled)	5 kNm
p_{HS}	Pole-pairs on HS rotor	6
p_S	Pole-pairs on stator	27
m_S	Halbach segments per pole-pair on the stator	4
Q	Pole pieces	33
G	Gear ratio	5.5
	Rated PP rotor speed	300 rpm
	Rated output frequency	165 Hz
	Outer airgap diameter	363 mm
	Airgap lengths	1.5 mm
	Radial thickness of HS rotor PMs	21 mm
	Radial thickness of stator PMs	10 mm
	Radial thickness of PPs	18 mm
	Axial segmentation of the HS rotor PMs	3 mm
	Axial segmentation of the stator PMs	5 mm
l_a	Active axial length	318 mm
	NdFeB magnet grade	N40SH
B_r	Remanence of PMs	1.25 T
μ_r	Relative recoil permeability	1.05
	Coils per turn	6
	Wire diameter	0.95 mm
	Rated current	308 A_{rms}
	Packing factor	0.4

.

Table 8.1: Parameters of the demonstrator PDD designed and build by Magnomatics Ltd.

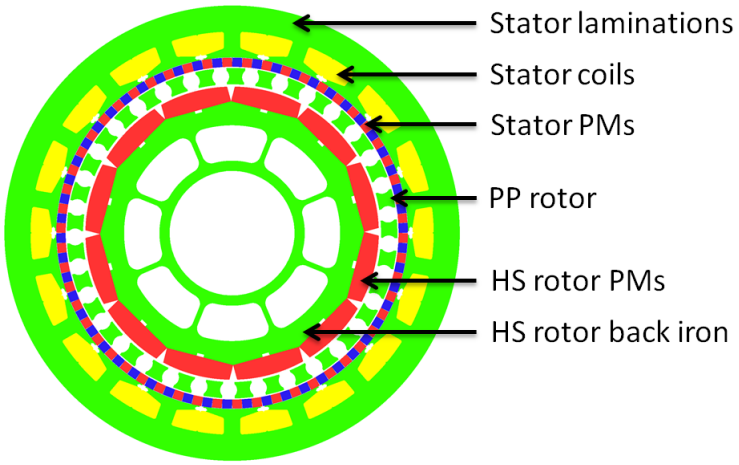

Fig. 8.1: Cross-sectional schematic of the active components of the PDD in axial direction.

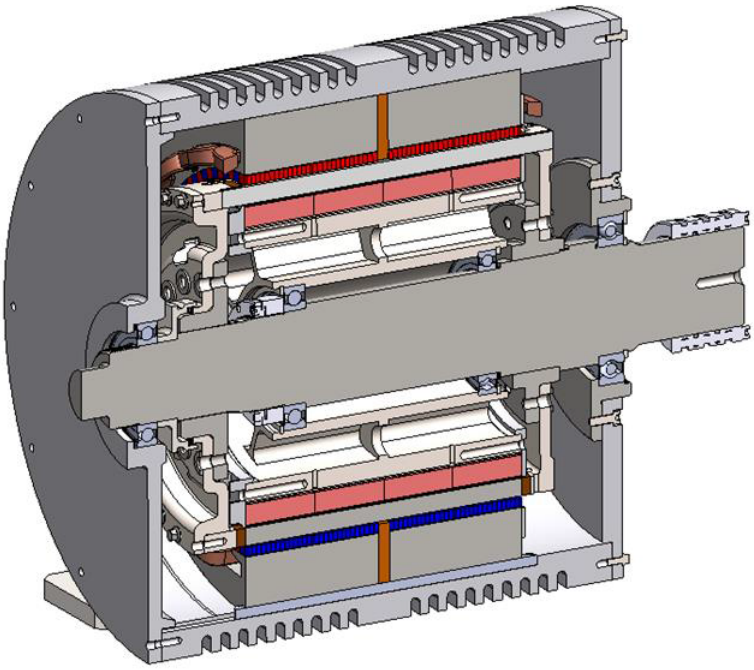

Fig. 8.2: Sectional view of the assembled PDD [73].

Fig. 8.3 shows the stator PMs after a Glass-Fibre liner has been applied to prevent the PMs from detaching from the stator iron. Figs. 8.4-8.5 show the PP rotor and the HS rotor after assembly. As can be seen from Fig. 8.4 magnetically inactive carbon fibre bands have been wrapped around the PP rotor, in order to provide additional mechanical stability.

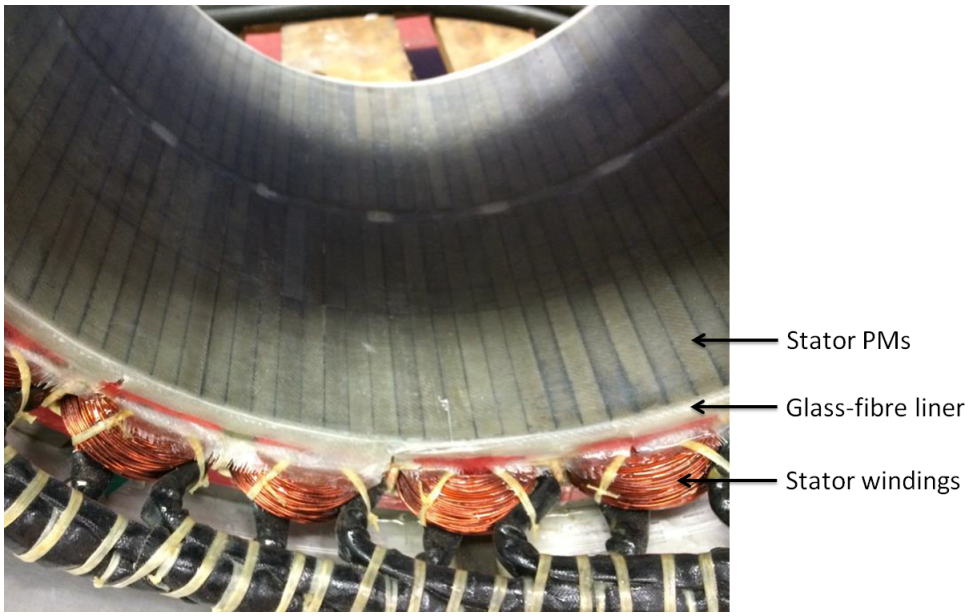

Fig. 8.3: Stator PMs including Glass-Fibre liner [73].

Fig. 8.4: Assembled PP rotor [73].

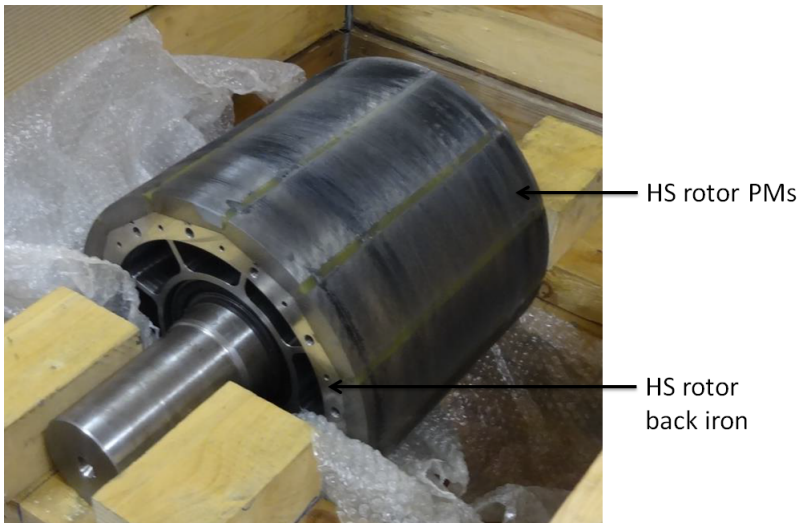

Fig. 8.5: Assembled HS rotor [73].

8.1 Flux measurement at the pole-pieces

In order to validate the predictions of the analytical model for the flux density distributions near the airgaps, search coils have been placed on the PP rotor, see Figs. 8.6 and 8.7. The variation of the flux linking the search coils induces a voltage, which is transmitted using cables and captured by an oscilloscope. The signal is then numerically integrated to derive the variation of the flux through the coils with time.

Coils 1 and 2 measure the radial flux at the PPs, and are placed in grooves in order to avoid contact with the stator and the HS rotor, respectively, Fig. 8.6. However, since the depth of the grooves is very small compared to the PP dimensions their impact on the flux density distributions is assumed to be negligible. Furthermore, coils 3 and 4 measure the circumferential flux at the PPs. As shown in Fig. 8.7 it can be seen that the form of a PP in the demonstrator PDD is slightly different from the form of a PP assumed in the analytical models. Thus, in order to allow a suitable comparison between the experimental results and the analytical predictions, the PP slot opening angle β in the analytical models has been selected to be identical to the opening angle at the outer airgap radius, i.e. the circumferential distance between two PPs at the outer airgap radius.

Figs 8.8 and 8.9 show the variation of the average flux density at the PP faces adjacent to the outer airgap (coil 1) and adjacent to the inner airgap (coil 2) during two consecutive PP electrical cycles. It can be seen that the analytical model agrees well with the FE and experimental results. Figs 8.10 and 8.11 show the average flux density on the faces covered by coils 3 and 4. It can also be seen that despite the geometrical details introduced by the manufacturing requirements, a good agreement still exists between the measurements and the FE and analytical predictions.

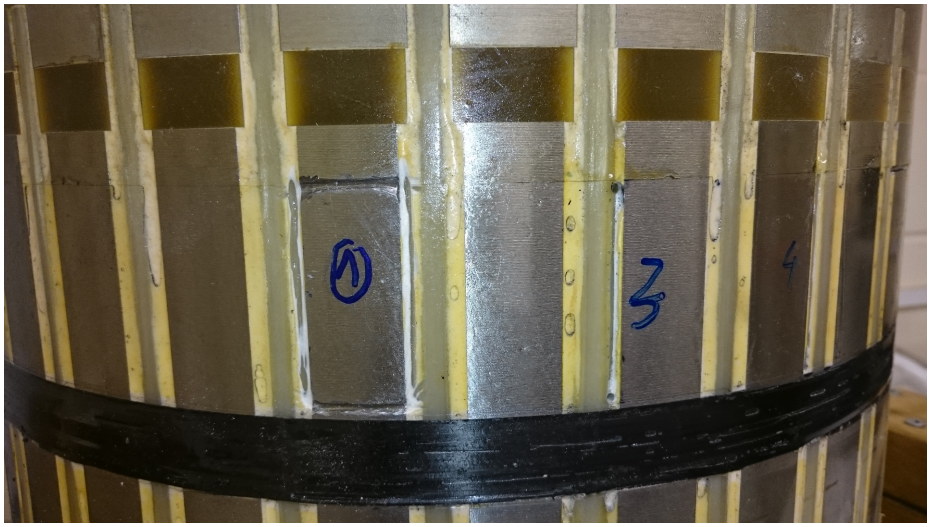

Fig. 8.6: Grooves in which the search coils have been placed.

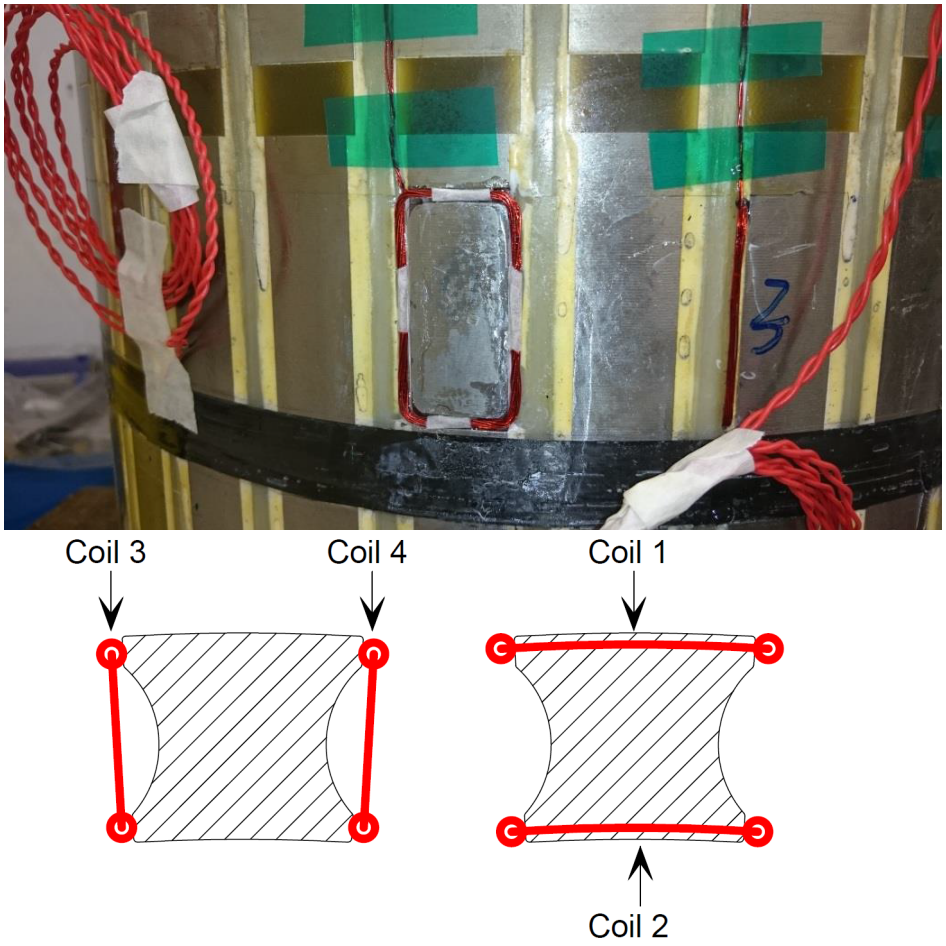

Fig. 8.7: Search coils for the measurement of the flux through the PP surfaces [73].

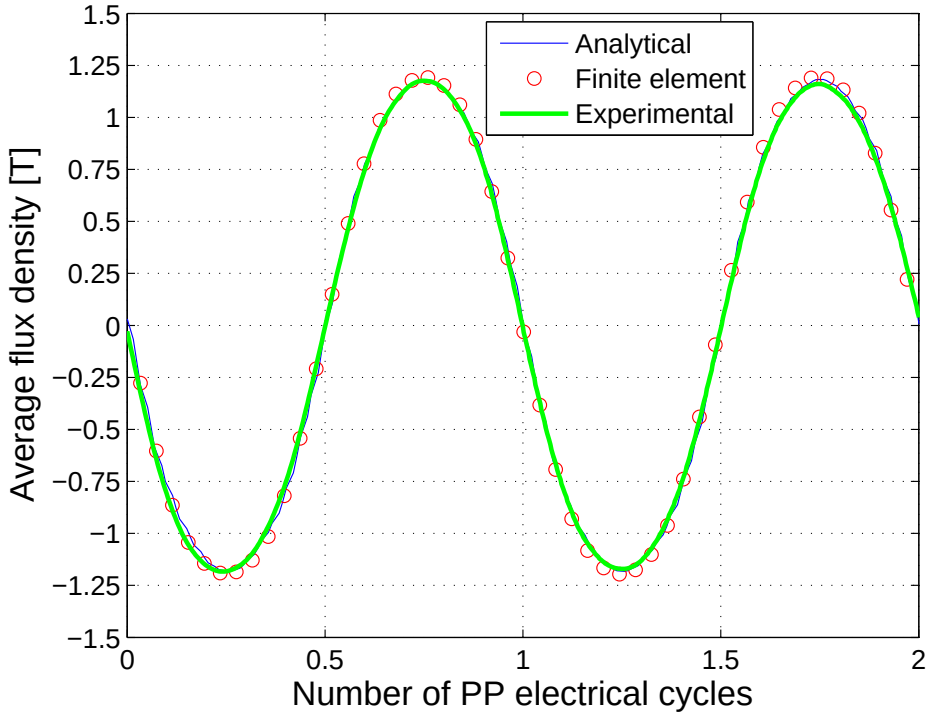

Fig. 8.8: Variation of average flux density distribution at coil 1 during two consecutive PP electrical cycles. Finite element analysis has been performed for steel with non-linear characteristics.

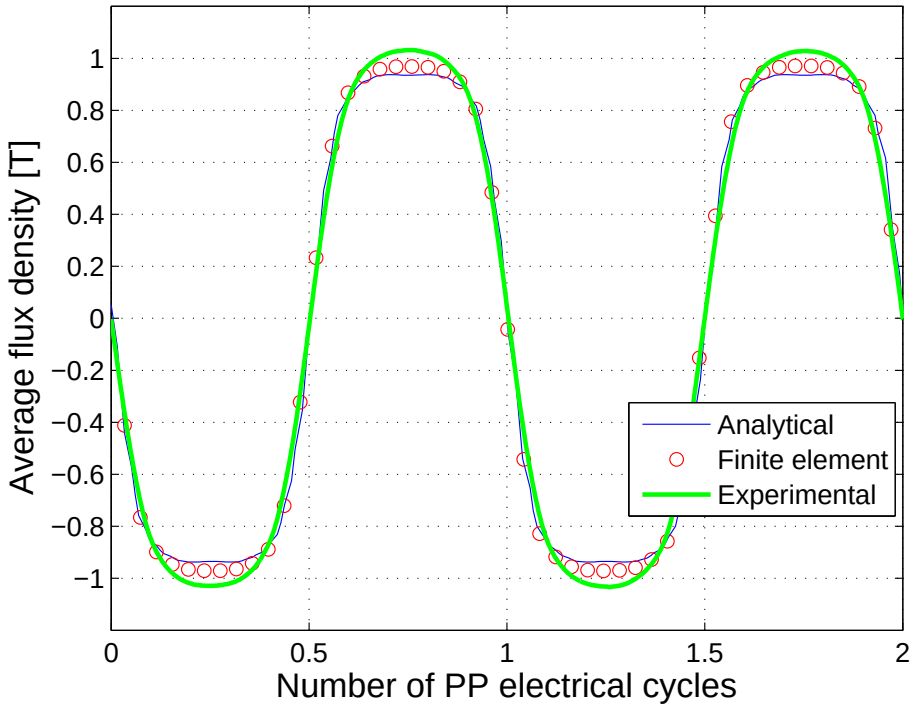

Fig. 8.9: Variation of average flux density distribution at coil 2 during two consecutive PP electrical cycles. Finite element analysis has been performed for steel with non-linear characteristics.

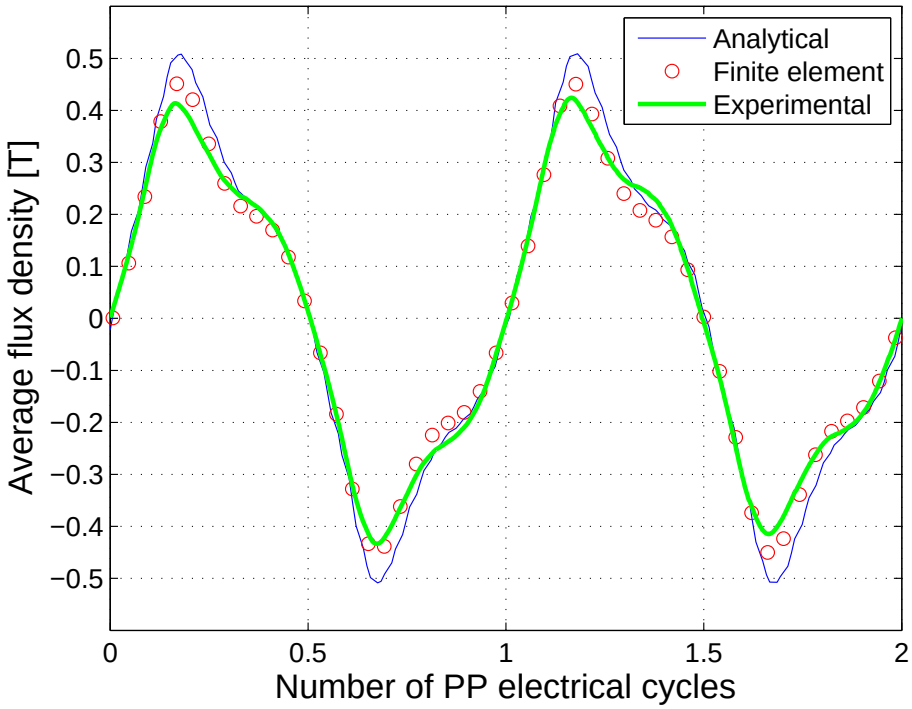

Fig. 8.10: Variation of average flux density distribution at coil 3 during two consecutive PP electrical cycles. Finite element analysis has been performed for steel with non-linear characteristics.

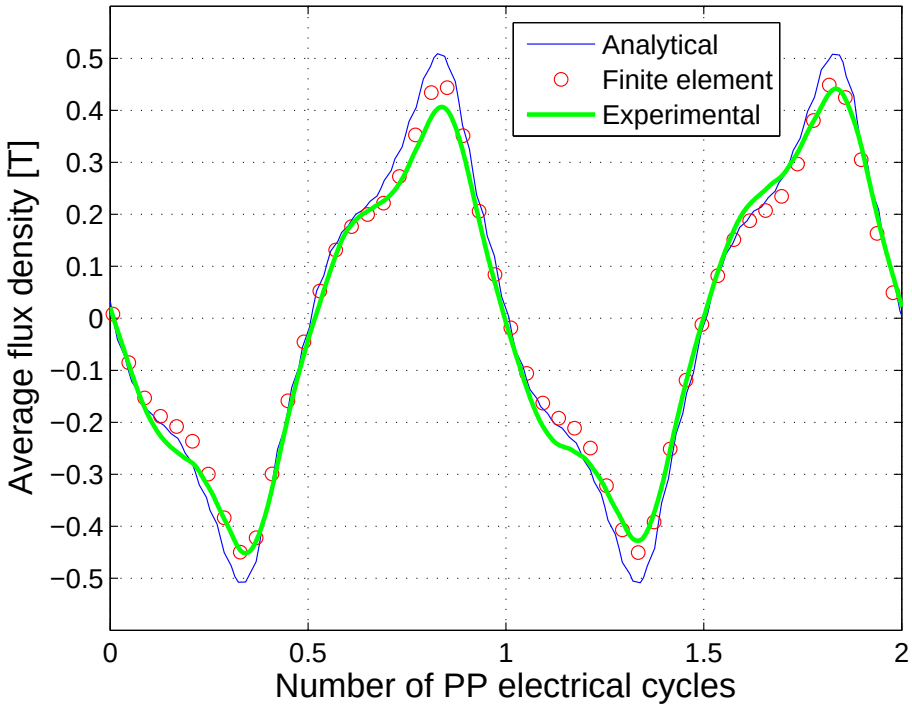

Fig. 8.11: Variation of average flux density distribution at coil 4 during two consecutive PP electrical cycles. Finite element analysis has been performed for steel with non-linear characteristics.

8.2 Dynamometer tests

For the testing of the demonstrator a bespoke dynamometer was commissioned at Magnomatics Ltd as shown in Figs. 8.12-8.13. To achieve the required load torque a 300kW induction machine (1500rpm/2020Nm) is used in series with a mechanical gearbox with a gear ratio of 2.88. Two 150kW Emerson drives are employed in parallel to provide sufficient current for the load induction machine and enable for the full operational range of torque and speed. An Emerson drive is also employed for the PDD. Since the HS rotor shaft is not accessible, an encoder has been mounted on the PP rotor, and the position of the HS rotor which is required for commutation, is derived using a specially developed observer implemented by [74]. The electrical input power P was measured using a power analyser (Newtons4th Ltd PPA1500), the shaft torque was measured by a torque transducer (Datum Electronics M420, size 4 for the range 0-5kNm), and the rotational speed of the PP rotor ω_{PP} was determined by the Emerson drive. The torque could either be monitored by the analogue output through the torque transducer interface (Datum Electronics 400150) or by the digital output of the Datum signal conditioner. During testing the temperatures of key regions have been monitored using K-type thermocouples. The temperature monitoring has been employed to ensure temperature limits are not exceeded and materials are within safe operating limits. The maximum winding and PM temperatures in the PDD have been specified as 120^oC and 110^oC, respectively.

No-load tests

The PDD has been tested at no load to measure the back-EMF. Fig. 8.14 shows the variation of the phase EMF with time when the HS rotor speed is set to 200rpm. It can be seen that the analytical results agree well with the FE and experimental results.

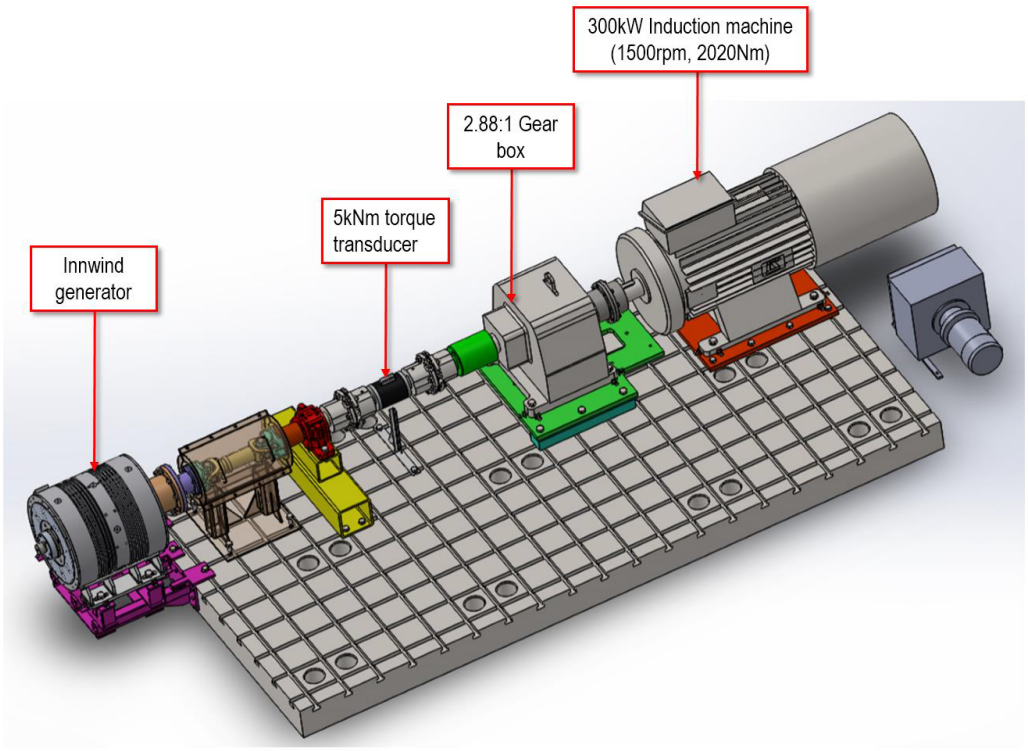

Fig. 8.12: Set-up of the test rig [73].

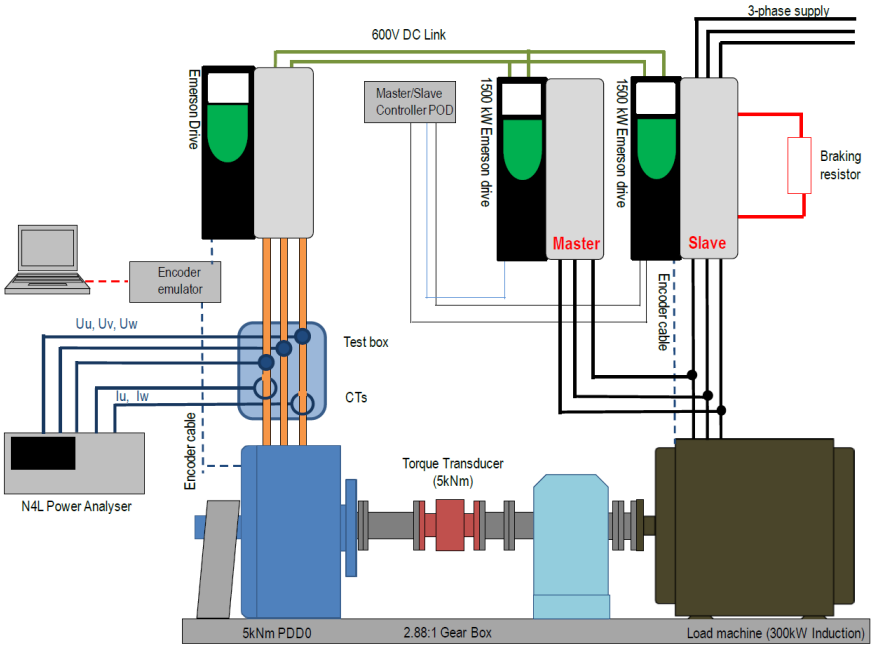

Fig. 8.13: Set-up of the dynamometer with Emerson drives [Magnomatics Ltd].

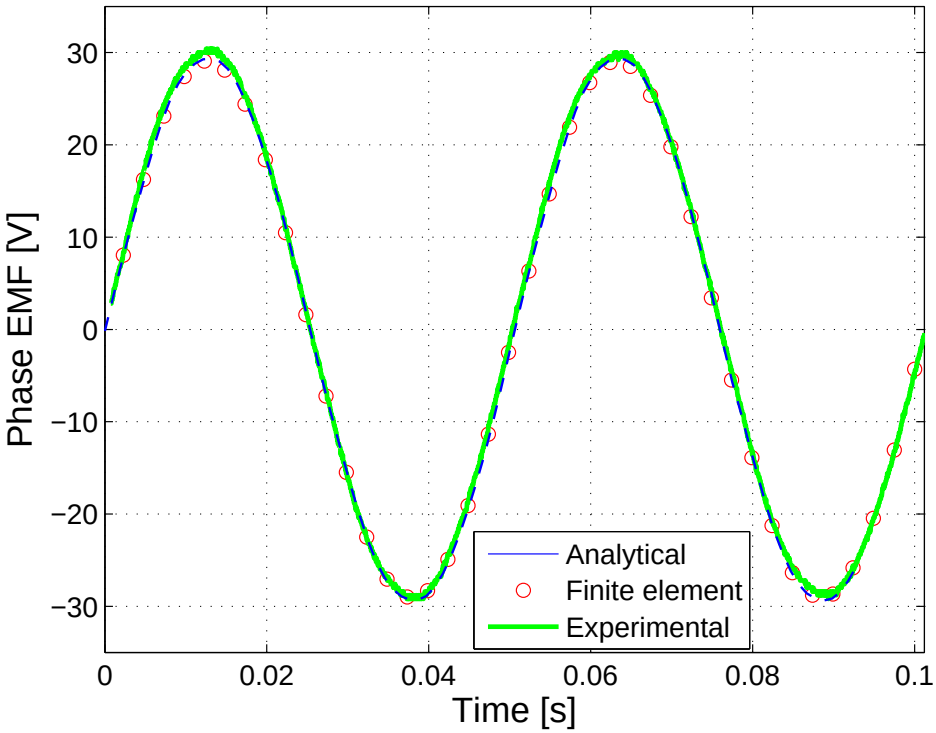

Fig. 8.14: Variation of the phase EMF with time. FE analysis has been performed for steel with non-linear characteristics.

On-load tests

For the testing at load conditions the induction machine is speed controlled while the PDD is torque controlled. As the torque is increased on the PDD, the system attempts to decelerate. In order to maintain constant speed the induction machine then increases the torque to react to the load torque. Fig. 8.15 shows the variation of the torque on the PP rotor with the applied current in the stator windings. It can be seen that the analytically predicted torque is closer to the experimental values for a PM temperature of 110^oC. It can also be seen that in order to predict the torque more accurately nonlinear effects of the steel need to be considered. Furthermore, since the aspect ratio of the PDD is only about $a = 0.88$, end effects could be a source for the decreased torque, however, end effects seem to have no effect on the EMF, see Fig. 8.14.

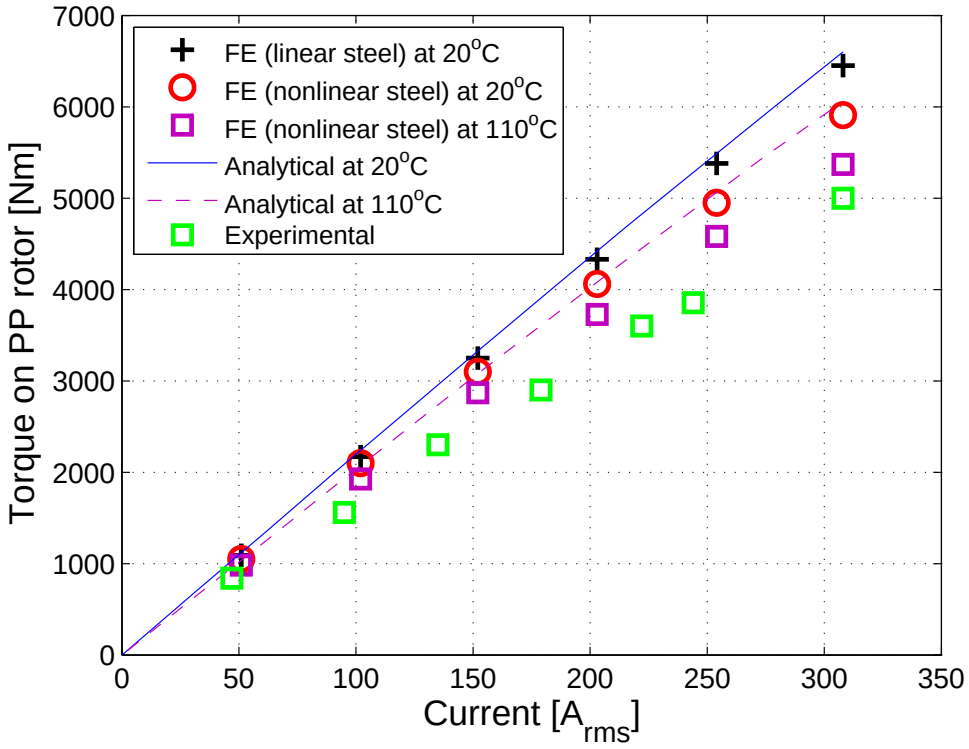

Fig. 8.15: Variation of the torque on the PP rotor with the applied current at a rotational speed of $100rpm$. Torque curves are shown for the analytical and FE predictions with a PM temperature of 20^oC and 110^oC.

From the measured values by the power analyser, the torque transducer, and the encoder the efficiency can be determined, and it is given by

$$\eta = \frac{T_{PP}\omega_{PP}}{P} \tag{8.1}$$

Fig. 8.16 and Fig. 8.17 show the variations of the measured and analytical efficiencies for a PP rotor speed of 150rpm and 300 rpm, respectively. A curve fit is applied to the measured efficiencies, where the fitted curve is given by

$$\eta = \frac{T_{PP}\omega_{PP}}{T_{PP}\omega_{PP} + aT_{PP}^2 + bT_{PP} + c} \tag{8.2}$$

For the curve fit the Root Mean Squared (RMS) error is included. It can be seen that the RMS error of the measured values from the mean curve in terms of total loss is about 1% of the efficiency value, however individual measurements may differ as much as 2%. Each of the measurements, i.e. the measurement of T_{PP}, ω_{PP}, and P, is accompanied by a device specific error. In particular the relative errors provided by the manufacturers are $\Delta P/P = 0.05\%$ for the power analyser, $\Delta T_{PP}/T_{PP} = 0.1\%$

for the torque transducer. Although no value could be determined for the relative error of the speed measurement $\Delta\omega_{PP}/\omega_{PP}$, it is assumed that $\Delta\omega_{PP}/\omega_{PP}$ lies well below 0.5%. The total relative error of the efficiencies is then given by

$$\frac{\Delta\eta}{\eta} = \frac{\Delta T_{PP}}{T_{PP}} + \frac{\Delta\omega_{PP}}{\omega_{PP}} + \frac{\Delta P}{P} \tag{8.3}$$

Since the total relative error by the measurement devices is very small (less than 0.5%) these devices are excluded as the primary source for the observed deviations from the mean curve, and random errors such as noise may be the main source of the deviations. From Fig. 8.16 it can be seen that the analytically predicted efficiency agrees well with the mean measured efficiency for a PP rotor rotational speed of 150rpm, when the electrical frequency is 82.5Hz which is closer to the 10MW PDD operating frequency of 48Hz. However, from Fig. 8.17 it can be seen that at 300rpm when the electrical frequency is about 165Hz, there are larger discrepancies between the predicted and measured efficiencies. This may be due to the relatively larger frequency dependent losses such as eddy current losses, which are not considered in the predictions of the analytical and FE models.

The eddy current losses in the stator PMs are estimated at the rated point employing the methods in [58], which assume resistance limited eddy currents and take into account of the axial and circumferential segmentation of the PMs. In the model the equivalence of the equations which govern the resistance-limited eddy currents and those that govern a magnetostatic field is exploited. Initially the flux density distribution in the PMs is determined through 2D FE. 3D FE software is subsequently employed to solve the equivalent magnetostatic problem in a single PM piece. The eddy currents are then deduced from the equivalent flux density distributions gained from the 3D FE method. For simplicity only the average value of the fundamental flux density in the stator PMs is considered. Furthermore, since the circumferential component of the flux density is much smaller than the radial component, only the radial component of the flux density is considered. The calculated eddy current loss in the stator PMs are $P_{eddy} = 104W$ or 0.13% of the power at rated torque, and $P_{eddy} = 416W$ or 0.27% of the power at rated torque at $150rpm$

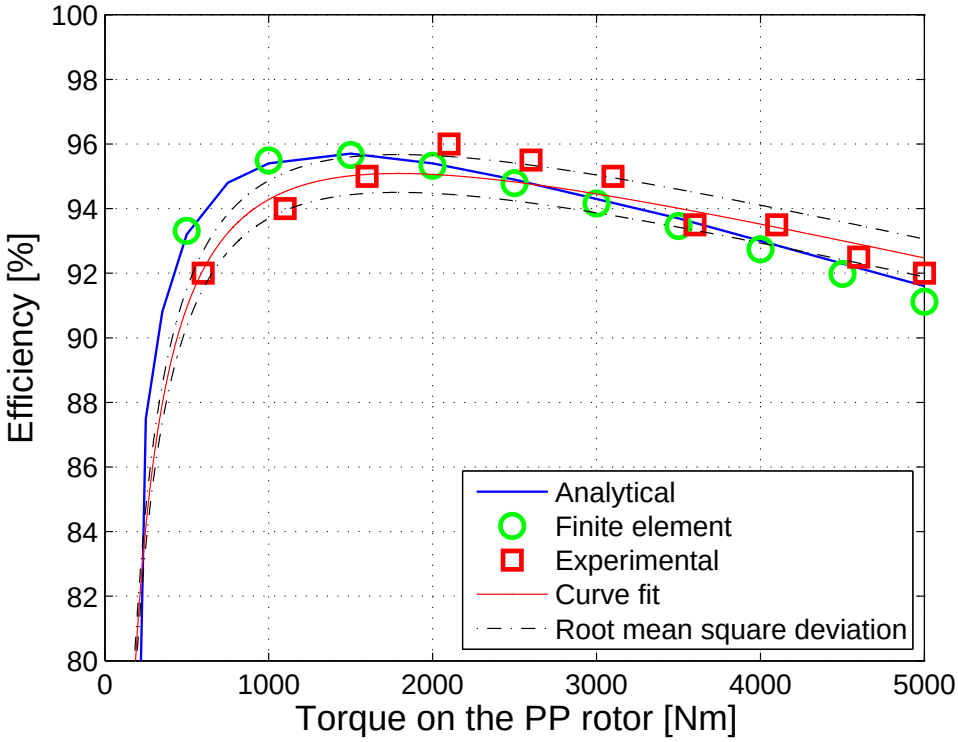

Fig. 8.16: Variation of the measured and analytically calculated efficiencies with the Torque for a rotational speed of the PP rotor of 150rpm. An error analysis is applied to the curve that is fitted to the experimental data.

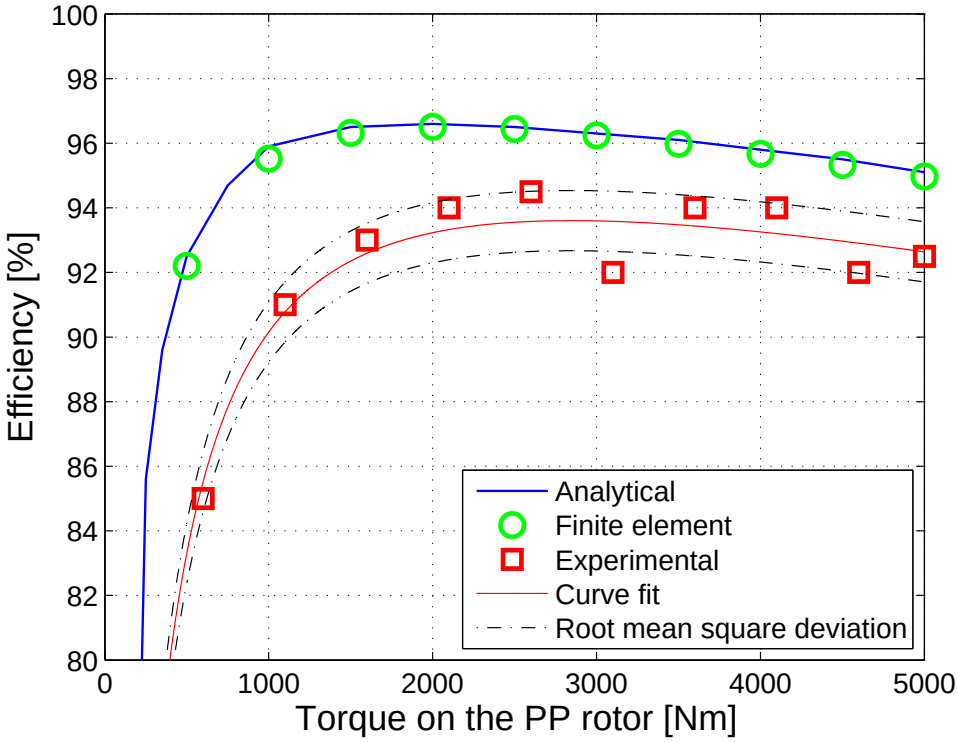

Fig. 8.17: Variation of the measured and analytically calculated efficiencies with the Torque for a rotational speed of the PP rotor of 300rpm. An error analysis is applied to the curve that is fitted to the experimental data.

and $300rpm$, respectively.

Furthermore, for the rotational speeds in the experiment the respective skin depth in the copper wires is large, compared to the wire diameters, about $\delta = 9mm$ at a frequency of $50Hz$ and at a temperature of 120^oC. AC losses in the windings may, therefore, not account for the discrepancy.

As discussed in Section 3.4.1, axial leakage flux exists in the PPs. In order to determine the magnitude of the axial flux, search coils have been placed, Fig. 8.18. Search coil 6 has been placed at the end of a PP, while coil 5 and 7 have been placed with $10mm$ and $60mm$ distance from the end of the PP, respectively, Fig. 8.18. The peak value of the axial component of the average axial flux density in the PPs has been determined to be about $0.2T$ at search coil 7, and $0.35T$ at search coils 5 and 6, Fig. 8.19. Due to the relatively large magnitude of the average axial flux density, the associated eddy current losses may be significant, since the axial flux is perpendicular to the face of the lamination. However, the magnitude of the axial flux density could be further reduced by introducing flux barriers along the PPs, but this is not adopted in the current prototype.

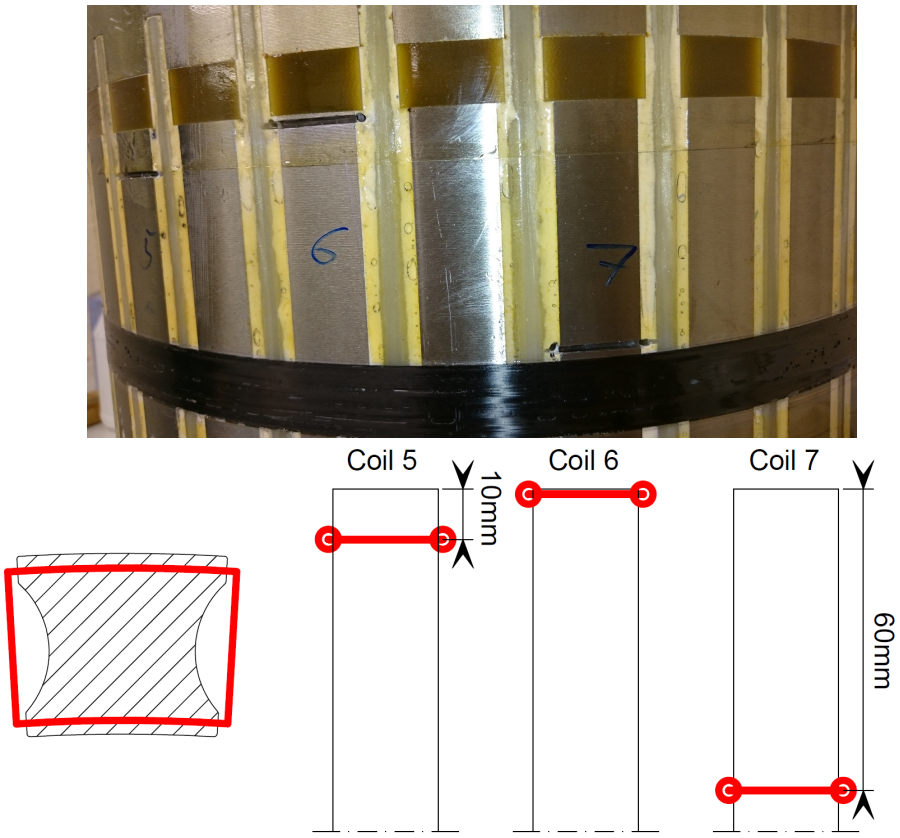

Fig. 8.18: Positions of the search coils 5, 6 and 7.

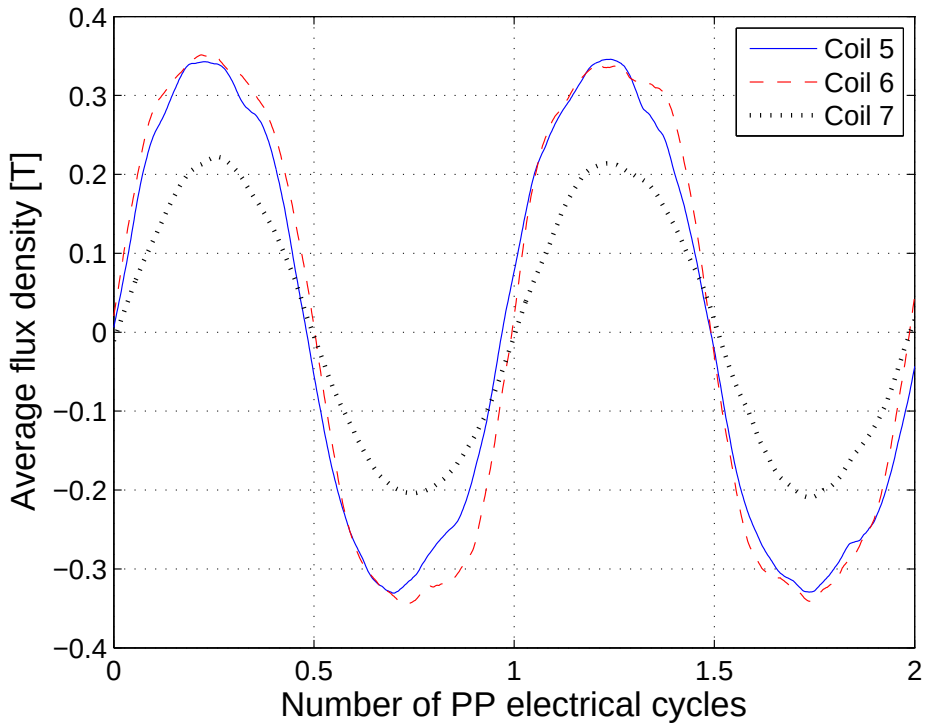

Fig. 8.19: Variation of average flux density distribution at coil 5, 6, and 7 during two consecutive PP electrical cycles.

8.3 Conclusions

A 5kNm PDD has been designed and built, and the analytical design tools developed in Chapter 4 are compared and validated with results obtained from test on the demonstrator PDD. Search coils have been placed on the PPs in order to measure the flux through the PPs. It is shown that a good agreement exists between the analytical and the experimental results. Furthermore, a bespoke dynamometer has been commissioned to test the demonstrator PDD at no-load and on-load conditions. Although there is a good agreement between analytically and FE predicted and measured EMFs, some discrepancy between measured and predicted output torque exists mainly due to the temperature rise in the PMs. The efficiency has been measured for a PP rotor rotational speed of 150rpm and 300rpm. It is shown that a good agreement exists between the analytically calculated values and the experimental results for the electrical frequency that is closer to the one in the 10MW PDD of Chapter 5, and which is $48Hz$.

Chapter 9

Conclusions

Analytical models for the prediction of the flux density distributions in the airgap and PM regions of MGs, with arbitrary magnetisation distributions, are presented and applied for radial and Halbach magnetisation. It has been shown that a good agreement for the analytical models and the FE predictions exists for the flux density distributions and the transmission torques including the ripple component. It has been shown that since large MGs are likely to be constructed using a set of circumferentially identical sections, applying symmetry conditions can result in significant reductions in the computational efforts. Furthermore, a careful selection of the harmonics to be considered can further reduce the computational efforts while achieving a sufficient accuracy. The models have been employed for the analysis and optimisation of large MGs for a 10MW wind turbine application. It has been shown that an MG can be achieved with a PM mass of 13.5tons and an active mass of 35tons. It is also shown that adopting a discrete HM distribution can result in significant increase of the transmitted torque.

In order to investigate the performance of PDDs for wind turbine applications, the analytical models are extended to account for the effects of stator windings on the flux density distributions in the air and PM regions. Furthermore, in order to predict the iron losses, analytical models for the predictions of the average flux density waveforms in the stator core and the localised flux density waveforms in the PPs are proposed, and their predictions are compared with FE. It is shown that a good

agreement with FE analysis exists for the flux density waveforms, the transmitted torque, the torque ripple and the iron loss. It is also shown that for a 10MW direct drive PDD an efficiency of 98.7% can be achieved with a total active mass of only 50 tons. Furthermore, the airgap diameter, the number of sections and the gear ratio can have a significant impact on the efficiency and the active masses of the PDD.

In order to reduce the mass of PMs, a PDD with a coil excited HS rotor is proposed. In order to analyse and optimise the PDD the analytical models developed for a PM excited PDD are refined to suit the requirements for a coil excited PDD. The predictions from the analytical models are also compared with FE, and it is shown that a good agreement exists for the flux density and the average torque. It is shown that significant reductions in PM mass can be realised compared to a PDD with HS rotor PM excitation, albeit at the expense of increased total active mass and reduced efficiency. However, it has also been shown that controlling the excitation current is necessary, in order to maximise the annual energy efficiency.

The analytical models have been employed for the study of the scaling behaviour of the PM excited and the coil excited PDDs. It has been shown for the PM excited PDD, that if the current density is kept constant when scaling, the copper mass per MW remains constant for the PM excited PDD. However, the PM and steel lamination masses per MW increase with the power of the wind turbine. It has also been shown that similarly to a PM excited PDD, for a coil excited PDD the copper mass remains fairly constant, while the laminated steel mass can increase significantly. However, the relative increase of the PM mass per MW could be less than for a PM excited PDD.

A 5kNm prototype PDD has been designed and built by Magnomatics Ltd., and predictions from analytical models are compared and validated with results obtained from tests on the demonstrator PDD. It has been shown that a good agreement exists between the analytical and the measured results for the flux density waveforms at the PPs and the EMF, however some discrepancy between measured and predicted output torque exists, which could be attributed to the temperature of the PMs. Fur-

thermore, it is shown that when operating at a frequency closer to the one in the 10MW PDD, a good agreement exists between the analytically and FE predicted, and the measured efficiencies.

The performance of the PDDs investigated in this thesis are compared with competing technologies, i.e. a PMDD [23] and a superconducting direct drive (SCDD) [75], Table 5.1. Although other direct drive technologies may be considered for large wind turbines, e.g. the 7.6MW ENERCON E-126, to the author's knowledge there is no information available in the public domain which would enable a useful comparison for a wound field synchronous machine. Furthermore, to the author's knowledge the only study concerned with a direct drive DFIG for a 10MW wind turbine is in [76]. However, an airgap length of 1mm on a 6m airgap diameter machine has been assumed, which is not feasible because the static deflection of the bearings due to the rotor mass may be of similar magnitude as the airgap length. Therefore, the performance indicators prediction cannot be considered, especially for induction generators, where the performance is highly sensitive to the length of the airgap. From Table 5.1 it can be seen that the PM excited PDD exhibits the highest efficiency at an active mass and airgap diameter similar to that of the SCDD. Furthermore, due to its relatively small airgap diameter the PM excited PDD would also exhibit a significantly lower structural mass than the PMDD. However, although the PM excited PDD offers a very light drive train solution, this comes at the expense of increased PM mass and complexity. On the other hand, the coil excited PDD offers a drive train solution with a PM mass less than that of the PMDD, but an increased amount of copper and laminated steel is required and the efficiency is lower.

Estimating the price of the generator is difficult. However, in order to attempt to do so it is important to estimate the structural mass of the generator. Therefore, the ratio of structural mass to active mass, is assumed to vary approximately linearly with the airgap diameter [68]. Under these assumptions the structural mass of the

Quantity	PMDD [23]	SCDD [75]	PM excited PDD Tab. 5.1	Coil excited PDD Tab. 6.1
Rated supply frequency	27 Hz	2.6Hz	48 Hz	48 Hz
Airgap diameter	10 m	5.4m	6 m	8 m
Airgap lengths	10 mm	4mm	6 mm	8 mm
Axial lengths	1.6 m	3.1m	1.66 m	1.22 m
Rated electromagnetic efficiency	97 %	97.7%$^{+}$	98.7 %	95 %
Mass of PMs	6 $tons$	—	13.5 $tons$	4.5 $tons$
Mass of copper	12 $tons$	19.4$tons$	7 $tons$	20 $tons$
Mass of laminated steel	47 $tons$	25$tons$	29.5 $tons$	59 $tons$
Superconducting MgB_2 tape	—	474km	—	—
Mass of structural steel	260 $tons$	94 $tons^{\#}$	100 $tons^{\#}$	222 $tons^{\#}$
Total mass	325 $tons$	146 $tons$	150 $tons$	306 $tons$

$^{+}$ Cryogenic losses are not included.
$^{\#}$ The structural masses is calculated assuming a linear relation to the airgap diameter and the active mass. For a 6m airgap diameter PDD the structural mass is assumed to be twice the active mass.

Table 9.1: Comparison of selected PDD designs with a PMDD and a SCDD for a 10MW wind turbine.

coil excited PDD would be significantly larger than the PM excited PDD, while the PM excited PDD would exhibit a similar mass as the SCDD. However, this method may be favourable towards a PDD, due to the presence of two airgaps, which could lead to increased structural mass compared to designs with a single airgap.

An estimate of the cost of the different materials employed in the construction of the generators is given in Table 9.2. These prices are for the manufactured materials, under mass production, and were agreed to be used as basis for comparison of the different generator technologies considered in the INNWIND.EU project. However, it should be noted that the PM cost is likely to depend also on other parameters such as the shape and size of the PMs. It can be seen that although the PM excited PDD employs a significant amount of PMs, due to its size it exhibits the lowest price. It can also be seen that the SCDD would be significantly more expensive assuming the current estimates for the price of the superconducting material. Therefore, in order to reduce the mass of the superconducting material, an alternative SCDD generator topology employing iron poles on the rotor was proposed, and although

	PMDD	SCDD	PM excited PDD	Coil excited PDD
PM material	60 $k€/ton$			
Copper material	15 $k€/ton$			
Superconducting MgB_2 tape	12 $€/m$			
Laminated steel material	3 $k€/ton$			
Structural material	3 $k€/ton$			
Total manufactured cost of active material	0.68$M€$	6.00$M€$	1.00$M€$	0.75$M€$
Total manufactured cost of active and structural material	1.46$M€$	6.28$M€$	1.30$M€$	1.41$M€$

Table 9.2: Manufactured material cost for the direct drive designs in Table 9.1.

it exhibits a similar price as the PM excited PDD, with a similar airgap diameter, it is significantly heavier and less efficient by a few percent.

References

[1] "Annual market update," *Global Wind Energy Council*, 2015.

[2] A. Ho and I. Pineda, "Wind energy scenarios for 2030," *Report by the European Wind Energy Association*, 2015.

[3] N. Fichaux, J. Beurskens, P. H. Jensen, J. Wilkes, and et al., "Design limits and solutions for very large wind turbines," 2011.

[4] H. Polinder, F. van der Pijl, G.-J. de Vilder, and P. Tavner, "Comparison of direct-drive and geared generator concepts for wind turbines," *Energy Conversion, IEEE Transactions on*, vol. 21, pp. 725 –733, sept. 2006.

[5] K. Atallah, S. Calverley, and D. Howe, "Design, analysis and realisation of a high-performance magnetic gear," *Electric Power Applications, IEE Proceedings* -, vol. 151, no. 2, pp. 135–143, 2004.

[6] G. Sieros, P. Chaviaropoulos, J. D. Sarensen, B. H. Bulder, and P. Jamieson, "Upscaling wind turbines: theoretical and practical aspects and their impact on the cost of energy," *Wind Energy*, vol. 15, no. 1, pp. 3–17, 2012.

[7] H. Polinder, J. Ferreira, B. Jensen, A. Abrahamsen, K. Atallah, and R. McMahon, "Trends in wind turbine generator systems," *Emerging and Selected Topics in Power Electronics, IEEE Journal of*, vol. 1, pp. 174–185, Sept 2013.

[8] P. M. Tlali, R. J. Wang, and S. Gerber, "Magnetic gear technologies: A review," in *Electrical Machines (ICEM), 2014 International Conference on*, pp. 544–550, Sept 2014.

[9] K. Atallah and D. Howe, "A novel high-performance magnetic gear," *Magnetics, IEEE Transactions on*, vol. 37, pp. 2844 –2846, Jul 2001.

[10] P. Rasmussen, T. O. Andersen, F. T. Joergensen, and O. Nielsen, "Development of a high performance magnetic gear," in *Industry Applications Conference, 2003. 38th IAS Annual Meeting. Conference Record of the*, vol. 3, pp. 1696–1702 vol.3, 2003.

[11] K. Atallah, J. Rens, S. Mezani, and D. Howe, "A novel 'pseudo' direct-drive brushless permanent magnet machine," *Magnetics, IEEE Transactions on Magnetics*, vol. 44, pp. 4349 –4352, nov. 2008.

[12] K. T. Chau, D. Zhang, J. Z. Jiang, C. Liu, and Y. Zhang, "Design of a magnetic-geared outer-rotor permanent-magnet brushless motor for electric vehicles," *IEEE Transactions on Magnetics*, vol. 43, pp. 2504–2506, June 2007.

[13] C. Armstrong, "Power-transmitting device.," Nov. 26 1901. US Patent 687292.

[14] H. Faus, "Magnetic gearing," 1941. US Patent 2243555.

[15] C. C. Huang, M. C. Tsai, D. G. Dorrell, and B. J. Lin, "Development of a magnetic planetary gearbox," *IEEE Transactions on Magnetics*, vol. 44, pp. 403–412, March 2008.

[16] J. Rens, K. Atallah, S. D. Calverley, and D. Howe, "A novel magnetic harmonic gear," *IEEE Transactions on Industry Applications*, vol. 46, pp. 206–212, Jan 2010.

[17] C. W. Musser, "Strain wave gearing," Sept. 29 1959. US 2906143.

[18] G. Schuesler and J. Lindner, "Exzentergetriebe mit magnetischer drehmomentübertragung - eccentric drive having magnetic torque transmission," Feb. 16 1995. DE Patent App. DE19,944,428,441.

[19] M. Venturini and F. Leonardi, "High torque, low speed joint actuator based on pm brushless motor and magnetic gearing," in *Industry Applications Society Annual Meeting, 1993., Conference Record of the 1993 IEEE*, pp. 37–42 vol.1, Oct 1993.

[20] T. Martin, "Magnetic transmission," Apr. 16 1968. US Patent 3378710.

[21] N. Laing, "Magnetic transmission," Feb. 1972. US Patent 3645650A.

[22] B. Ackerman and L. Honds, "Magnetic drive arrangement comprising a plurality of magnetically cooperating parts which are movable relative to one another," May 1997. US Patent 5633555.

[23] H. Polinder, D. Bang, R. P. J. O. M. Van Rooij, A. McDonald, and M. Mueller, "10 mw wind turbine direct-drive generator design with pitch or active speed stall control," in *Electric Machines Drives Conference, 2007. IEMDC '07. IEEE International*, vol. 2, pp. 1390–1395, 2007.

[24] Y. Chen, P. Pillay, and A. Khan, "Pm wind generator topologies," *IEEE Transactions on Industry Applications*, vol. 41, pp. 1619–1626, Nov 2005.

[25] K. Atallah, J. Wang, and D. Howe, "A high-performance linear magnetic gear," *Journal of Applied Physics*, vol. 97, 2005.

[26] R. Holehouse, K. Atallah, and J. Wang, "A linear magnetic gear," in *Electrical Machines (ICEM), 2012 XXth International Conference on*, pp. 563–569, 2012.

[27] A. Razzell and J. Cullen, "Compact electrical machine," Sept. 21 2004. US Patent 6794781.

[28] K. Atallah, S. Calverley, R. Clark, J. Rens, and D. Howe, "A new pm machine topology for low-speed, high-torque drives," in *Electrical Machines, 2008. ICEM 2008. 18th International Conference on*, pp. 1–4, 2008.

[29] L. Jian, G. Xu, Y. Gong, J. Song, L. J., and M. Chang, "Electromagnetic design and analysis of a novel magnetic-gear-integrated wind power generator using time-stepping finite element method," *Progress In Electromagnetics Research*, vol. 113, pp. 351–367, 2011.

[30] J. Wang, K. Atallah, and S. D. Carvley, "A magnetic continuously variable transmission device," *IEEE Transactions on Magnetics*, vol. 47, pp. 2815–2818, Oct 2011.

[31] K. Atallah, J. Wang, S. D. Calverley, and S. Duggan, "Design and operation of a magnetic continuously variable transmission," in *2011 IEEE International Electric Machines Drives Conference (IEMDC)*, pp. 312–317, May 2011.

[32] J. J. Pyrhönen, Y. Alexandrova, R. S. Semken, and H. Hämäläinen, "Wind power electrical drives for permanent magnet generators; development in finland," pp. 9–16, May 2012.

[33] K. Ding, "The rare earth magnet industry and rare earth price in china," *EPJ Web of Conferences, Joint European Magnetic Symposia 2013*, vol. 75, jul 2014.

[34] O. Anaya-Lara, N. Jenkins, J. Ekanayake, P. Cartwright, and F. M. Hughes, *Wind Energy Generation: Modelling and Control*. West Sussex, UK: John Wiley & Sons Inc, 2009.

[35] R. Qu, Y. Liu, and J. Wang, "Review of superconducting generator topologies for direct-drive wind turbines," *IEEE Transactions on Applied Superconductivity*, vol. 23, pp. 5201108–5201108, June 2013.

[36] R. Fair and et.al., "Superconductivity for large scale wind turbines," *GE Global Research*, vol. Tech. Rep. DE-EE0005143, 2012.

[37] L. Jian, K. Chau, and J. Jiang, "A magnetic-geared outer-rotor permanent-magnet brushless machine for wind power generation," *Industry Applications, IEEE Transactions on*, vol. 45, no. 3, pp. 954–962, 2009.

[38] B. L. J. Gysen, K. Meessen, J. J. H. Paulides, and E. Lomonova, "General formulation of the electromagnetic field distribution in machines and devices using fourier analysis," *Magnetics, IEEE Transactions on*, vol. 46, pp. 39–52, Jan 2010.

[39] H. Tiegna, Y. Amara, and G. Barakat, "Overview of analytical models of permanent magnet electrical machines for analysis and design purposes," *Mathematics and Computers in Simulation*, vol. 90, no. 0, pp. 162 – 177, 2013. {ELECTRIMACS} 2011- {PART} I.

[40] M. Fukuoka, K. Nakamura, and O. Ichinokura, "Dynamic analysis of planetary-type magnetic gear based on reluctance network analysis," *Magnetics, IEEE Transactions on*, vol. 47, no. 10, pp. 2414–2417, 2011.

[41] M. Fukuoka, K. Nakamura, and O. Ichinokura, "A method for optimizing the design of spm type magnetic gear based on reluctance network analysis," in *Electrical Machines (ICEM), 2012 XXth International Conference on*, pp. 30–35, Sept 2012.

[42] K. Nakamura and O. Ichinokura, "Dynamic simulation of pm motor drive system based on reluctance network analysis," in *Power Electronics and Motion Control Conference, 2008. EPE-PEMC 2008. 13th*, pp. 758–762, Sept 2008.

[43] M. Rahman, "Analytical models for exterior-type permanent magnet synchronous motors," *Magnetics, IEEE Transactions on*, vol. 23, pp. 3625–3627, Sep 1987.

[44] A. Hughes and T. J. E. Miller, "Analysis of fields and inductances in air-cored and iron-cored synchronous machines," *Electrical Engineers, Proceedings of the Institution of*, vol. 124, no. 2, pp. 121–126, 1977.

[45] Z. Zhu and D. Howe, "Instantaneous magnetic field distribution in brushless permanent magnet dc motors. ii. armature-reaction field," *Magnetics, IEEE Transactions on*, vol. 29, no. 1, pp. 136–142, 1993.

[46] A. Proca, A. Keyhani, A. El-Antably, W. Lu, and M. Dai, "Analytical model for permanent magnet motors with surface mounted magnets," *Energy Conversion, IEEE Transactions on*, vol. 18, pp. 386–391, Sept 2003.

[47] A. Youmssi, "A three-dimensional semi-analytical study of the magnetic field excitation in a radial surface permanent-magnet synchronous motor," *Magnetics, IEEE Transactions on*, vol. 42, pp. 3832–3841, Dec 2006.

[48] T. Lubin, S. Mezani, and A. Rezzoug, "Exact analytical method for magnetic field computation in the air gap of cylindrical electrical machines considering slotting effects," *Magnetics, IEEE Transactions on*, vol. 46, pp. 1092–1099, April 2010.

[49] A. Bellara, Y. Amara, G. Barakat, and B. Dakyo, "Two-dimensional exact analytical solution of armature reaction field in slotted surface mounted pm radial flux synchronous machines," *Magnetics, IEEE Transactions on*, vol. 45, pp. 4534–4538, Oct 2009.

[50] K. Atallah, Z. Q. Zhu, and D. Howe, "Armature reaction field and winding inductances of slotless permanent-magnet brushless machines," *Magnetics, IEEE Transactions on*, vol. 34, pp. 3737–3744, Sep 1998.

[51] T. Lubin, S. Mezani, and A. Rezzoug, "Analytical computation of the magnetic field distribution in a magnetic gear," *Magnetics, IEEE Transactions on*, vol. 46, pp. 2611 –2621, july 2010.

[52] L. Jian and K.-T. Chau, "Analytical calculation of magnetic field distribution in coaxial magnetic gears," *Progress In Electromagnetics Research*, vol. 92, pp. 1–16, 2009.

[53] L. Jian and K. Chau, "A coaxial magnetic gear with halbach permanent-magnet arrays," *Energy Conversion, IEEE Transactions on*, vol. 25, no. 2, pp. 319–328, 2010.

[54] Z. Zhu and D. Howe, "Halbach permanent magnet machines and applications: a review," *Electric Power Applications, IEE Proceedings* -, vol. 148, pp. 299 –308, jul 2001.

[55] Z. Zhu, D. Howe, and C. Chan, "Improved analytical model for predicting the magnetic field distribution in brushless permanent-magnet machines," *Magnetics, IEEE Transactions on*, vol. 38, pp. 229–238, Jan 2002.

[56] S. Gerber and R. J. Wang, "Analysis of the end-effects in magnetic gears and magnetically geared machines," in *Electrical Machines (ICEM), 2014 International Conference on*, pp. 396–402, Sept 2014.

[57] T. Miller and R. Rabinovici, "Back-emf waveforms and core losses in brushless dc motors," *Electric Power Applications, IEE Proceedings* -, vol. 141, pp. 144–154, May 1994.

[58] J. D. Ede, K. Atallah, G. W. Jewell, J. B. Wang, and D. Howe, "Effect of axial segmentation of permanent magnets on rotor loss in modular permanent-magnet brushless machines," *IEEE Transactions on Industry Applications*, vol. 43, pp. 1207–1213, Sept 2007.

[59] A. Mlot, M. Korkosz, P. Grodzki, and et al., "Analysis of the proximity and skin effects on copper loss in a stator core," *Archives of Electrical Engineering*, vol. 63(2), pp. 211–225, 2014.

[60] J. R. Hendershot and T. J. E. Miller, eds., *Design of brushless permanent-magnet machines*. Motor Design Books LLC, Venice, Florida, USA, 2010.

[61] D. Ionel, M. Popescu, S. Dellinger, T. Miller, R. Heideman, and M. McGilp, "On the variation with flux and frequency of the core loss coefficients in electrical machines," *Industry Applications, IEEE Transactions on*, vol. 42, pp. 658–667, May 2006.

[62] K. Atallah and D. Howe, "The calculation of iron losses in brushless permanent magnet dc motors," *Journal of Magnetism and Magnetic Materials*, vol. 133, pp. 578 – 582, 1994.

[63] J. Lavers, P. Biringer, and H. Hollitscher, "A simple method of estimating the minor loop hysteresis loss in thin laminations," *Magnetics, IEEE Transactions on*, vol. 14, pp. 386–388, Sep 1978.

[64] C. Bak, F. Zahle, R. Bitsche, T. Kim, A. Yde, L. C. Henriksen, M. H. Hansen, J. P. A. A. Blasques, M. Gaunaa, and A. Natarajan, "Description of the dtu 10mw reference wind turbine," *Report Number: DTU Wind Energy Report-I-0092*, Jun 2013.

[65] J. Jonkman, S. Butterfield, W. Musial, and G. Scott, "Definition of a 5-mw reference wind turbine for offshore system development," *Technical Report NREL/TP-500-38060, NREL*, 2009.

[66] E. C. Morgan, M. Lackner, R. M. Vogel, and L. G. Baise, "Probability distributions for offshore wind speeds," *Energy Conversion and Management*, vol. 52, no. 1, pp. 15 – 26, 2011.

[67] I. Bastigkeit, "Database of existing wind parameter measurements for tall atmospheres across europe," *INNWIND.EU, Work package 1: Conceptual designs, Task 1.1: External conditions, Report deliverable D1.11*, Aug 2014.

[68] G. Shrestha, H. Polinder, and J. Ferreira, "Scaling laws for direct drive generators in wind turbines," in *Electric Machines and Drives Conference, 2009. IEMDC '09. IEEE International*, pp. 797–803, May 2009.

[69] M. R. Islam, Y. G. Guo, and J. G. Zhu, "Power converters for wind turbines: Current and future development," *Materials and Processes for Energy: Communicating Current Research and Technological Developments*, pp. 559–571, Aug. 2013.

[70] M. Hofmann and I. B. Sperstad, "Will 10 mw wind turbines bring down the operation and maintenance cost of offshore wind farms?," *Energy Procedia*, vol. 53, pp. 231 – 238, 2014.

[71] V. Honsinger, "Sizing equations for electrical machinery," *Energy Conversion, IEEE Transactions on*, vol. EC-2, pp. 116–121, March 1987.

[72] S. Huang, J. Luo, F. Leonardi, and T. Lipo, "A general approach to sizing and power density equations for comparison of electrical machines," in *Industry Applications Conference, 1996. Thirty-First IAS Annual Meeting, IAS '96., Conference Record of the 1996 IEEE*, vol. 2, pp. 836–842 vol.2, Oct 1996.

[73] R. Clark, S. Calverley, and M. Andrew., "Report, subtask 3.2.2," *INNWIND.EU, Work package 3: , Task 3.2.2: Report deliverable D3.21*, Sep 2015.

[74] M. Bouheraoua, J. Wang, and K. Atallah, "Design and implementation of an observer-based state feedback controller for a pseudo direct drive," *IET Electric Power Applications*, vol. 7, pp. 643–653, September 2013.

[75] A. B. Abrahamsen, N. Magnusson, D. Liu, E. Stehouwer, B. Hendriks, and Polinder, "Design study of a 10 mw mgb2 superconductor direct drive wind turbine generator," *Poster session presented at European Wind Energy Conference & Exhibition 2014*, vol. Barcelona, Spain., 2014.

[76] V. Colli, F. Marignetti, and C. Attaianese, "Feasibility of a 10 mw doubly fed induction generator for direct-drive wind turbines," in *Sustainable Alternative Energy (SAE), 2009 IEEE PES/IAS Conference on*, pp. 1–5, 2009.

Appendix A

Appendix

A.1 Poisson solution for region I for a MG

By employing (2.19) and considering symmetry in z-direction the z-component of the Poisson equation (2.16) can be rewritten by

$$\begin{aligned} \triangle A_I &= \frac{\mu_0}{r}\left(\frac{\partial M_{rad,I}}{\partial \theta} - M_{\theta,I}\right) \\ &= \frac{B_r}{r}\sum_{n=1}^{\infty}\begin{pmatrix} nf_{s,I,n} - g_{c,I,n} \\ nf_{c,I,n} + g_{s,I,n} \end{pmatrix} \cdot \begin{pmatrix} \cos(n\theta) \\ -\sin(n\theta) \end{pmatrix} \end{aligned} \tag{A.1}$$

As described in section 2.2 the solution for A_I can be separated into a general solution $A_{G,IV}$ and a particular solution $A_{P,I}$. Since

$$\begin{aligned} \triangle r^n\cos(n\theta) &= r^{n-2}(n(n-1)+n-n^2)\cos(n\theta) = 0 \quad n>1 \\ \triangle r\cos(\theta) &= r^{-1}(1-1^2)\cos(\theta) = 0 \quad n=1 \\ \triangle r^{-n}\cos(n\theta) &= r^{-n-2}(n(n+1)-n-n^2)\cos(n\theta) = 0 \quad n>1 \end{aligned} \tag{A.2}$$

$$\begin{aligned} \triangle r^n\sin(n\theta) &= r^{n-2}(n(n-1)+n-n^2)\sin(n\theta) = 0 \quad n>1 \\ \triangle r\sin(\theta) &= r^{-1}(1-1^2)\sin(\theta) = 0 \quad n=1 \\ \triangle r^{-n}\sin(n\theta) &= r^{-n-2}(n(n+1)-n-n^2)\sin(n\theta) = 0 \quad n>1 \end{aligned} \tag{A.3}$$

the general solution $A_{G,I}(r,\theta)$ takes the form

$$A_{G,I}(r,\theta) = \sum_{n=1}^{\infty}\begin{pmatrix} A_n' r^n + B_n' r^{-n} \\ C_n' r^n + D_n' r^{-n} \end{pmatrix} \cdot \begin{pmatrix} \cos(n\theta) \\ \sin(n\theta) \end{pmatrix} \tag{A.4}$$

Since

$$\begin{aligned} \triangle r\cos(n\theta) &= r^{-1}(1-n^2)\cos(n\theta) \quad n>1 \\ \triangle r\ln r\cos(\theta) &= r^{-1}(1+(\ln r+1)-\ln r)\cos(\theta) \quad n=1 \end{aligned} \tag{A.5}$$

$$\begin{aligned} \triangle r\sin(n\theta) &= r^{-1}(1-n^2)\sin(n\theta) & n>1 \\ \triangle r\ln r\sin(\theta) &= r^{-1}(1+(\ln r+1)-\ln r)\sin(\theta) & n=1 \end{aligned} \tag{A.6}$$

the particular solution takes the form

$$A_{P,I} = B_r \sum_{n=1}^{\infty} f_n(r) \begin{pmatrix} nf_{s,I,n} - g_{c,I,n} \\ -nf_{c,I,n} - g_{s,I,n} \end{pmatrix} \cdot \begin{pmatrix} \cos(n\theta) \\ \sin(n\theta) \end{pmatrix} \tag{A.7}$$

where $f_n(r)$ is defined in equation (2.39). For the general solution the boundary condition between the interface of region I and the HS rotor back-iron (2.21) reduces to

$$B_{\theta,I}(R_{HS}) = 0 \tag{A.8}$$

Considering orthogonality between $\cos(n\theta)$ and $\sin(n\theta)$ over the interval 2π the following relationships between the coefficients can be deduced:

$$A_n^{'} R_{HS}^n - B_n^{'} R_{HS}^{-n} = 0 \tag{A.9}$$

$$C_n^{'} R_{HS}^n - D_n^{'} R_{HS}^{-n} = 0 \tag{A.10}$$

The general solution can then be rewritten as

$$A_{G,I}(r,\theta) = \sum_{n=1}^{\infty} \frac{R_{mi}}{n} \frac{P_n(r,R_{HS})}{P_n(R_{mi},R_{HS})} \begin{pmatrix} A_{I,n} \\ C_{I,n} \end{pmatrix} \cdot \begin{pmatrix} \cos(n\theta) \\ \sin(n\theta) \end{pmatrix} \tag{A.11}$$

where $P_n(r,v)$ is defined in equation (2.33). The denominator is chosen such that $A_{G,I}$ takes a simple form at the boundary at R_{mi}, while the factor $\frac{R_{mi}}{n}$ is added in order to allow for scale invariance of the coefficientes. Since terms of the order r^{-n} can be added to the n-th term in the particular solution, it can be rewritten to satisfy the boundary condition (2.21) at R_{HS} as

$$A_{P,I} = B_r \sum_{n=1}^{\infty} \left\{ \left(\frac{r}{R_{HS}}\right)^{-n} \begin{pmatrix} G_{I,n} \\ H_{I,n} \end{pmatrix} + f_p(r) \begin{pmatrix} nf_{s,I,n} - g_{c,I,n} \\ -nf_{c,I,n} - g_{s,I,n} \end{pmatrix} \right\} \cdot \begin{pmatrix} \cos(n\theta) \\ \sin(n\theta) \end{pmatrix} \tag{A.12}$$

Solving the Poisson equation for each component results in

$$\begin{pmatrix} G_{I,n} \\ H_{I,n} \end{pmatrix} = \frac{R_{HS}}{n} \left[f_n'(R_{HS}) \begin{pmatrix} nf_{s,I,n} - g_{c,I,n} \\ -nf_{c,I,n} - g_{s,I,n} \end{pmatrix} + \begin{pmatrix} g_{c,I,n} \\ g_{s,I,n} \end{pmatrix} \right] \tag{A.13}$$

Terms of the order $P_n(r,R_{HS})$ can be added to the particular solution without altering the previous constraints and such that the particular solution is zero at the interface

between HS PMs and the inner airgap:

$$A_{P,I}(r,\theta) = B_r \sum_{n=1}^{\infty} \begin{pmatrix} X_{A,I,n}(r) \\ X_{C,I,n}(r) \end{pmatrix} \cdot \begin{pmatrix} \cos(n\theta) \\ \sin(n\theta) \end{pmatrix} \tag{A.14}$$

$$\begin{pmatrix} X_{A,I,n}(r) \\ X_{C,I,n}(r) \end{pmatrix} = \left(\frac{r}{R_{HS}}\right)^{-n} \begin{pmatrix} G_{I,n} \\ H_{I,n} \end{pmatrix} + f_n(r) \begin{pmatrix} nf_{s,I,n} - g_{c,I,n} \\ -nf_{c,I,n} - g_{s,I,n} \end{pmatrix} \tag{A.15}$$
$$-\frac{P_n(r,R_{HS})}{P_n(R_{mi},R_{HS})} \left[\left(\frac{R_{mi}}{R_{HS}}\right)^{-n} \begin{pmatrix} G_{I,n} \\ H_{I,n} \end{pmatrix} + f_n(R_{mi}) \begin{pmatrix} nf_{s,I,n} - g_{c,I,n} \\ -nf_{c,I,n} - g_{s,I,n} \end{pmatrix} \right]$$

A.2 Discrete Halbach magnetisation

The residual magnetisation of a discrete HM may be expressed as (Eqn. (2.98))

$$\overrightarrow{M}(\theta) = \sum_{k=0}^{m-1} \vec{M}_k f_k(\theta) \tag{A.16}$$

where

$$f_k(\theta) = \sum_{q=0}^{p-1} f_{k,q}(\theta) \tag{A.17}$$

The residual magnetisation for the k-th segment is given by

$$\vec{M}_k = \frac{B_r}{\mu_0} \begin{pmatrix} \Re \\ \Im \end{pmatrix} exp(\pm j2\pi\frac{k}{m}) = \frac{B_r}{\mu_0} \begin{pmatrix} \cos(2\pi\frac{k}{m}) \\ \pm\sin(2\pi\frac{k}{m}) \end{pmatrix} \tag{A.18}$$

where$+$ corresponds to an internal field, $-$ corresponds to an external field, and $\Re$ and $\Im$ give the real and imaginary value of a complex variable, respectively. The function $f_{k,q}(\theta)$ given by (2.95) can be expressed in terms of a Fourier series as

$$f_{k,q}(\theta) = \sum_{n=-\infty}^{\infty} c_{n,k,q} e^{jn\theta}$$

If the rotor is in a position where the centre of a radially magnetised PMs is at the angle $\theta = 0$ the coefficients are given by

$$c_{0,k,q} = \frac{1}{2\pi} \int_{\theta=0}^{2\pi} f(\theta) \mathrm{d}\theta = \frac{1}{mp} \tag{A.19}$$

$$c_{n,k,q} = \frac{1}{2\pi} \int_{x(k,q)-y}^{x(k,q)+y} e^{-jn\theta} \mathrm{d}\theta = \frac{\sin(ny)}{n\pi} e^{-jnx(k,q)} \tag{A.20}$$

where

$$x(k,q) = \frac{2\pi}{p}(q + \frac{k}{m}) \tag{A.21}$$

$$y = \frac{\pi}{pm} \tag{A.22}$$

Given the above expressions for the coefficients, $f_k(\theta)$ can be reduced to

$$f_k(\theta) = \frac{1}{m} + \sum_{\substack{n=-\infty \\ n\neq 0}}^{\infty} \frac{\sin(ny)}{n\pi} exp\left(jn\left[\theta - \frac{2\pi}{p}\frac{k}{m}\right]\right) p\varepsilon_{n,p} \tag{A.23}$$

where $\varepsilon_{n,p}$ is given in appendix A.3. Furthermore the residual magnetisation can be expressed as

$$\begin{aligned} \vec{M}(\theta) &= \frac{B_r}{\mu_0}\begin{pmatrix} \Re \\ \Im \end{pmatrix} \sum_{\substack{n=-\infty \\ n\neq 0}}^{\infty} mp\frac{\sin(ny)}{n\pi} e^{jn\theta}\, \varepsilon_{n,p}\, \varepsilon_{n\mp p,mp} && \text{(A.24)} \\ &= \frac{B_r}{\mu_0}\sum_{n=1}^{\infty} h_{n,m,p}\begin{pmatrix} \varepsilon^{+}_{n,m,p}\cos(n\theta) \\ \varepsilon^{-}_{n,m,p}\sin(n\theta) \end{pmatrix} && \text{(A.25)} \end{aligned}$$

where

$$\begin{aligned} h_{n,m,p} &= pm\frac{\sin(n\pi/mp)}{n\pi}\varepsilon_{n,p} && \text{(A.26)} \\ \varepsilon^{+}_{n,m,p} &= \varepsilon_{n\mp p,mp} + \varepsilon_{n\pm p,mp} && \text{(A.27)} \\ \varepsilon^{-}_{n,m,p} &= \varepsilon_{n\mp p,mp} - \varepsilon_{n\pm p,mp} && \text{(A.28)} \end{aligned}$$

An arbitrary shift by an angle Θ_0 may be applied by applying the transformation

$$e^{jn\theta} \longrightarrow e^{jn(\theta-\phi_0)} \tag{A.29}$$

The expression for the residual magnetisation is then given by

$$\begin{aligned} \vec{M}(\theta) &= \frac{B_r}{\mu_0}\begin{pmatrix} \Re \\ \Im \end{pmatrix} \sum_{\substack{n=-\infty \\ n\neq 0}}^{\infty} h_{n,m,p} e^{jn(\theta-\Theta_0)}\, \varepsilon_{n\mp p,mp} && \text{(A.30)} \\ &= \frac{B_r}{\mu_0}\sum_{n=1}^{\infty} h_{n,m,p}\begin{bmatrix} \varepsilon^{+}_{n,m,p}\cos(n\Theta_0) & \varepsilon^{+}_{n,m,p}\sin(n\Theta_0) \\ -\varepsilon^{-}_{n,m,p}\sin(n\Theta_0) & \varepsilon^{-}_{n,m,p}\cos(n\Theta_0) \end{bmatrix}\begin{pmatrix} \cos(n\theta) \\ \sin(n\theta) \end{pmatrix} \end{aligned}$$

A.3 $\varepsilon_{t,s}$

The values of the function

$$\varepsilon_{t,s} = \frac{1}{s}\sum_{n=1}^{s} e^{-jn2\pi t/s}$$

of two integer values t and s can be separated by the two special cases of the modulo function t mod s. For t mod $s = 0$ the following identity is valid:

$$\frac{1}{s}\sum_{n=1}^{s} e^{-jn2\pi t/s} = \frac{1}{s}\sum_{n=0}^{s} 1 = 1 \tag{A.31}$$

Furthermore, for $t \bmod s \neq 0$ the function $\varepsilon_{t,s}$ can be expressed through a geometric series and the value of the function is given by

$$\frac{1}{s}\sum_{n=1}^{s}\left(e^{-j2\pi t/s}\right)^n = \frac{1}{s}\frac{1-e^{-j2\pi t}}{1-e^{-j2\pi t/s}} = 0 \tag{A.32}$$

Hence the function can be simplified to

$$\varepsilon_{t,s} = \begin{cases} 1 & t \bmod s = 0 \\ 0 & t \bmod s \neq 0 \end{cases} \tag{A.33}$$

A.4 Calculation of Fourier coefficients

For an analysis of the amplitudes of the harmonics $\overrightarrow{a}$ of a function $f(\theta)$ a Fourier analysis is applied:

$$\vec{a} = M^{-1}\vec{f}(\theta_i)$$

$$M = \begin{bmatrix} 1 & \cos 1\theta_i & \cdots & \cos N\theta_i & \sin 1\theta_i & \cdots & \sin N\theta_i \\ \vdots & \vdots & \ddots & \vdots & \vdots & \ddots & \vdots \\ 1 & \cos 1\theta_i & \cdots & \cos N\theta_i & \sin 1\theta_i & \cdots & \sin N\theta_i \end{bmatrix}$$

$$\vec{a}' = \begin{pmatrix} a_0, & a_1, & \cdots & a_N, & b_1, & \cdots & b_N \end{pmatrix}$$

A.5 Effects of selected current densities

In order to find the minimum total copper mass the total copper mass is differentiated by one of the rated current densities, equation 6.12. The total copper mass can be expressed in terms of the rated HS rotor current by using equation 6.11 and (4.50) by

$$M_{Cu} = M_{Cu,HS} + M_{Cu,S} = 2\pi m_{Cu}\left[\frac{R_{HS}Q_{HS}}{i_{HS}}(l_a + l_{e,HS}) + \frac{R_S Q_{rms}}{i_{rms}}(l_a + l_{e,S})\right] \tag{A.34}$$

Furthermore, by combining (6.8) , (4.47), and (6.19) the stator current density can be expressed as

$$i_{rms} = \frac{1}{2\pi R_S Q_{rms}(l_a + l_{e,S})}\left[\frac{P_{Cu}}{\rho_{Cu}} - 2\pi R_{HS}Q_{HS}(l_a + l_{e,HS})i_{HS}\right] \tag{A.35}$$

After substituting i_{rms} by this expression, the differentiation of the total copper mass by $i_{HS,R}$ and for a given copper loss, results then in the following expression for the rated HS rotor current

$$i_{HS,R} = \frac{P_{Cu}}{2\pi\rho_{Cu}} \frac{1}{R_{HS}Q_{HS}(l_a + l_{e,HS}) \pm R_S Q_{rms}(l_a + l_{e,S})} \tag{A.36}$$

Using this in equation (A.35) the rated stator current density is given by

$$i_{rms,R} = \pm i_{HS,R} \tag{A.37}$$

Only the solution with the $+$ sign results in a positive value for both $i_{HS,R}$ and $i_{rms,R}$, and therefore the minimum total copper mass is given by

$$\begin{aligned} M_{Cu} &= M_{Cu,HS} + M_{Cu,S} \\ &= 4\pi^2 \frac{m_{Cu}\rho_{Cu}}{P_{Cu}} \left[R_{HS}Q_{HS}(l_a + l_{e,HS}) + R_S Q_{rms}(l_a + l_{e,S})\right]^2 \end{aligned} \tag{A.38}$$